

CRANFIELD UNIVERSITY

Marleen Maartje Kerssens

Study of calcification formation and disease diagnostics utilising
advanced vibrational spectroscopy

Cranfield Health
Translational medicine

PhD thesis
Academic Year: 2009- 2012

Supervisors:
Prof Nick Stone, Prof Pavel Matousek, Prof Keith Rogers
October 2012

CRANFIELD UNIVERSITY

Cranfield Health

PhD

Academic Year 2009 - 2012

Marleen Maartje Kerssens

Study of calcification formation and disease diagnostics utilising
advanced vibrational spectroscopy

Supervisors:

Prof Nick Stone, Prof Pavel Matousek, Prof Keith Rogers

October 2012

This thesis is submitted in partial fulfilment of the requirements for
the degree of PhD

© Cranfield University 2012. All rights reserved. No part of this
publication may be reproduced without the written permission of the
copyright owner.

ABSTRACT

The accurate and safe diagnosis of breast cancer is a significant societal issue, with annual disease incidence of 48,000 women and around 370 men in the UK. Early diagnosis of the disease allows more conservative treatments and better patient outcomes.

Microcalcifications in breast tissue are an important indicator for breast cancers, and often the only sign of their presence. Several studies have suggested that the type of calcification formed may act as a marker for malignancy and its presence may be of biological significance.

In this work, breast calcifications are studied with FTIR, synchrotron FTIR, ATR FTIR, and Raman mapping to explore their disease specific composition. From a comparison between vibrational spectroscopy and routine staining procedures it becomes clear that calcium builds up prior to calcification formation. Raman and FTIR indicate the same size for calcifications and are in agreement with routine staining techniques. From the synchrotron FTIR measurements it can be proven that amide is present in the centre of the calcifications and the intensity of the bands depends on the pathology. Special attention is paid to the type of carbonate substitution in the calcifications relating to different pathology grades.

In contrast to mammography, Raman spectroscopy has the capability to distinguish calcifications based on their chemical composition. The ultimate goal is to turn the acquired knowledge from the mapping studies into a clinical tool based on deep Raman spectroscopy. Deep Raman techniques have a considerable potential to reduce large numbers of normal biopsies, reduce the time delay between screening and diagnosis and therefore diminish patient anxiety.

In order to achieve this, a deep Raman system is designed and after evaluation of its performance tested on buried calcification standards in porcine soft tissue and human mammary tissue. It is shown that, when the calcification is probed through tissue, the strong 960 cm^{-1} phosphate band can be used as a pseudo

marker for carbonate substitution which is related to the pathology of the surrounding tissue. Furthermore, the first study in which human breast calcifications are measured in bulk tissue with a thickness of several millimetres to centimetres is presented. To date, measurements have been performed at 41 specimens with a thickness up to 25 mm. Measurements could be performed through skin and blue dye.

The proposed deep Raman technique is promising for probing of calcifications through tissue but will need refinement before being adopted in hospitals.

Keywords: Breast cancer, apatite, FTIR (Fourier Transform InfraRed), synchrotron FTIR, ATR (attenuated total reflection), Raman mapping, deep Raman, Transmission Raman spectroscopy

ACKNOWLEDGEMENTS

I would like to thank my three professors Nick Stone, Pavel Matousek, and Keith Rogers for their support. I learned a lot from them and I consider myself privileged working with not one but three encouraging supervisors. All three of them excel in their respective fields and I value their guidance and the untiring discussions we had on the different sub disciplines of this research. Furthermore, I would like to thank all collaborators at Central Michigan University, Imperial College, Diamond, IRENI, OCTOPUS, Royal College of Surgeons in Ireland, Gloucestershire Hospitals NHS Foundation Trust and the past and present members of the Biophotonics Research Unit.

This work was funded by a doctoral research fellowship jointly funded by Gloucestershire Hospitals NHS Foundation Trust and the Science and Technology Facilities Council's Biomedical Network (4161234). I would also like to thank the Science and Technology Facility Council for awarding me a Science in Society award which enabled me to share my work with a wider audience and Dr Catherine Kendall for her guidance and help in these outreach activities. Financial support from the Association of British Spectroscopists (ABS), Federation of Analytical Chemistry and Spectroscopy Societies (FACSS), and the British Medical Laser Association (BMLA) Educational Award allowed me to share my work abroad.

Ik wil mijn familie en vrienden bedanken voor alle vakanties die naar Engeland werden gepland, ik kijk ernaar uit om jullie weer vaker te zien nu ik in Nederland ga wonen! Pap en mam, bedankt voor jullie support, zowel tijdens mijn tijd in Gloucester als de verhuizing erna. De vele pakketjes die jullie stuurden werden ook door de rest van het team erg gewaardeerd! Hans, dank je wel voor het steunen van mijn beslissing om naar Engeland te gaan.

TABLE OF CONTENTS

ABSTRACT	iii
ACKNOWLEDGEMENTS.....	v
LIST OF FIGURES.....	xi
LIST OF TABLES	xxi
LIST OF EQUATIONS.....	xxi
GLOSSARY.....	xxiii
1 Introduction	1
1.1 Breast disease and anatomy	1
1.1.1 Breast disease.....	1
1.1.2 Breast anatomy	3
1.1.3 Detection of breast cancer	4
1.1.4 Pathology of breast disease	7
1.2 Breast cancer screening and the clinical need of a new tool.....	10
1.3 Calcifications in the breast	12
1.3.1 Types of breast calcifications	17
1.3.2 Carbonate incorporation in apatites and its relationship to disease...	20
1.4 The use of vibrational spectroscopy to detect breast calcification and cancer.....	23
1.4.1 Vibrational spectroscopy	23
1.4.2 Infrared spectroscopy on calcifications.....	28
1.4.3 Raman spectroscopy on breast calcifications.....	30
1.5 Utilizing deep Raman spectroscopy to detect breast calcifications <i>in vivo</i>	32
1.5.1 Kerr gating.....	34
1.5.2 Spatially Offset Raman Spectroscopy	35
1.5.3 Transmission Raman	38
1.5.4 Surface Enhanced Raman scattering (SERS) combined with SORS (SESORS).....	40
1.6 Summary and outlook	41
1.7 Aims and objectives of the study	42
2 Materials and methods.....	45
2.1 Materials and sample collection	45
2.1.1 Calcification standards	45
2.1.2 Pathology slides for (synchrotron) FTIR mapping	45
2.1.3 Stained pathology slides	46
2.1.4 Pathology slide for ATR imaging and Raman mapping	47
2.1.5 Mineralising breast cell line	47
2.1.6 Breast tissue models for preliminary deep Raman studies.....	48
2.1.7 Nanoparticles	48
2.1.8 Breast tissue for preliminary deep Raman studies	49
2.1.9 Fresh human breast tissue for transmission Raman study.....	49
2.2 Experimental setups.....	51
2.2.1 Benchtop Fourier Transform InfraRed (FTIR).....	51

2.2.2	Raman microscope and imaging	52
2.2.3	Synchrotron beam lines.....	53
2.2.4	ATR FTIR setup	54
2.2.5	Transmission Raman setup.....	54
2.3	Methods	57
2.3.1	Study of breast calcifications (Chapter 3).....	57
2.3.2	Deep Raman system evaluation (Chapter 4).....	64
2.3.3	Deep Raman spectroscopy on breast calcifications and tissue (Chapter 5)	69
3	Results: study of breast calcifications	75
3.1	Study of calcification standards.....	75
3.1.1	Infrared experiments on calcification standards	75
3.1.2	Raman microscope measurements on calcification standards.....	83
3.2	Comparison of spectroscopic techniques with pathology samples staining	85
3.3	Synchrotron FTIR imaging of breast calcifications	94
3.3.1	General observations and challenges	94
3.3.2	Results from Diamond beamtime allocation SM6123.....	96
3.3.3	Results from Diamond beamtime allocation SM6605.....	100
3.3.4	Results IRENI beam time	117
3.4	ATR imaging of breast calcifications	118
3.5	Raman imaging of breast calcifications.....	122
4	Results: Deep Raman system evaluation.....	125
4.1	Comparison porcine soft tissue and human mammary tissue	125
4.2	Sample thickness limits when using transmission Raman setup.....	126
4.2.1	SESORS	128
4.3	Lateral spreading in transmission Raman measurements.....	129
4.4	The originating depth and spatial resolution of transmission Raman signal	132
4.5	Measurements through skin	134
5	Deep Raman spectroscopy on breast calcifications and tissue.....	139
5.1	Use of a pseudo marker to estimate the amount of carbonate substitution	139
5.1.1	Position of the 960 cm^{-1} band.....	140
5.1.2	Width of the 960 cm^{-1} band	144
5.2	SNR limits for using the pseudo marker	147
5.3	Theatre project deep Raman spectroscopy on breast.....	151
6	Discussion.....	157
6.1	Study of breast calcifications.....	157
6.1.1	Study of calcification standards	157
6.1.2	Comparison of spectroscopic techniques with staining	158
6.1.3	Synchrotron FTIR imaging of breast calcifications	159
6.1.4	ATR imaging of breast calcifications	160
6.1.5	Raman imaging of breast calcifications	161
6.2	Deep Raman system evaluation	162
6.2.1	Comparison porcine soft tissue and human mammary	162
6.2.2	Sample thickness limits when using transmission Raman setup.	162

6.2.3	Lateral spreading in transmission Raman measurements.....	163
6.2.4	The originating depth and spatial resolution of transmission Raman signal.....	164
6.2.5	Measurements through skin	164
6.3	Deep Raman spectroscopy on breast calcifications and tissue.....	165
6.3.1	Use of a pseudo marker to estimate the amount of carbonate substitution	165
6.3.2	SNR limits for using the pseudo marker	165
6.3.3	Theatre project deep Raman spectroscopy on breast.....	166
7	Conclusion	167
7.1	Study of breast calcifications.....	167
7.2	Deep Raman system evaluation	168
7.3	Deep Raman spectroscopy on breast calcifications and tissue.....	168
7.4	Recommendations for further work	169
	REFERENCES.....	171
	APPENDICES	183

LIST OF FIGURES

Figure 1.1: Most common cancers among females in the UK in 2009 (Cancer Research UK, 2012b).....	1
Figure 1.2: Number of breast cases per year and age-specific incidence rates per 100,000 women in the UK (Cancer Research UK, 2012b).....	2
Figure 1.3: Anatomy of the human breast (training.seer.cancer.gov accessed August 11, 2010).....	4
Figure 1.4: Example of the range in density visible in mammography. Horizontal views are shown in the upper row and oblique views in the lower row. (Images kindly provided by Prof. Iain Lyburn, radiologist at Cheltenham General Hospital).	5
Figure 1.5: Mammogram versus MRI scan; A) Horizontal view mammogram; B) Oblique view mammogram; C) MRI scan (images kindly provided by Prof. Iain Lyburn, radiologist at Cheltenham General Hospital).	6
Figure 1.6: Amount of recalls in NHSBSP 2009/2010 (based upon numbers of Patnick 2011).	10
Figure 1.7: Overview of the current screening programme (in case an abnormality is detected).	12
Figure 1.8: Mammography of breast with diffuse calcification in left breast A) horizontal view right breast; B) horizontal view left breast; C) Zoom of left breast horizontal view; D) oblique view right breast; E) oblique view left breast; F) Zoom of oblique view left breast (Images kindly provided by Prof. Iain Lyburn, radiologist at Cheltenham General Hospital).	13
Figure 1.9 A) Mammogram with macrocalcification; B) mammogram with microcalcifications (images kindly provided by Prof. Iain Lyburn, radiologist Cheltenham General Hospital).	14
Figure 1.10: A) X-ray image of surgical specimen; B) X-ray machine used in theatres; C) X-ray image of microcalcifications in slice; and D) X-ray image of microcalcifications in core specimens (www.faxitron.com).....	16
Figure 1.11: Mammary mineralisation model proposed by Cox et al. Betaglycerophosphate (β G) of the osteogenic cocktail is hydrolysed to glycerol (G) and phosphate (Pi) by alkaline phosphatase (ALP). Pi is transported into the cell and apatite is formed and up regulation of ALP mRNA takes place. Hydroxyapatite enters the extracellular matrix. Pyrophosphate (PPi) acts as an inhibitor of apatite formation, but the increased ALP may result in PPi hydrolysis to Pi, which can be incorporated in the apatite. Osteopontin (OPN) is also an inhibitor but ALP may take of a phosphate group whereby making it inactive. The apatite crystals in the extracellular matrix enhance the proliferation and migration of the surrounding cells (Cox et al., 2012).....	20
Figure 1.12: Relationship between the different pathology groups and the carbonate percentage (Baker et al., 2010).	21
Figure 1.13: Incorporation of carbonate in the HAP lattice. The location of the carbonate substitution is indicated with a black circle. Oxygen atoms are	

List of figures

depicted in red, calcium in green, phosphorus in pink, hydrogen in white, and carbon in yellow. (Peroos et al., 2006).	22
Figure 1.14: Photo of the Diamond Light Source (www.diamond.ac.uk , accessed 7 December 2010).	25
Figure 1.15: The principle of Raman scattering. S_0 and S_1 correspond to the two lowest electronic states. After excitation (\uparrow), the scattered photon (\downarrow) can have an energy similar (Rayleigh), higher (Anti-Stokes), or lower (Stokes) than the incident photon.	27
Figure 1.16: Average FTIR spectra of calcifications from samples with benign, in-situ and invasive pathology, figure modified from (Baker, 2009).	28
Figure 1.17: Raman spectra of calcium oxalate monohydrate and 0.5 and 6% carbonated HAP.	31
Figure 1.18: Schematic representation of a temporal approach in deep Raman. The time difference between the photons emerging from the different layers is used by only accumulating a fraction of the time. By choosing the delay time between the trigger to start the gating and opening the gate, it is possible to selectively detect one of the signals without a large contribution from another one (Ariese 2009).	33
Figure 1.19: Schematic representation of the Kerr gated setup. Kerr gating is based upon temporal differences. When the 'gate' is opened, the Kerr medium acts as a half-wave plate. As a result, light can enter the spectrometer. When the gate is closed, light cannot reach the spectrometer due to crossed polarizers (Matousek and Stone 2009).	35
Figure 1.20: Principle of SORS. Photons with their origin deeper in the tissue will have a higher chance to travel sideways during their route towards the surface. (See for comparison red (shallow depth) and blue (deeper depth) arrow above each other) By introducing a distance between the excitation and collection it is possible to discriminate between photons from different depths.	36
Figure 1.21: SORS and inverse SORS probe. SORS measurements are applied by exciting in the middle and collecting in a ring with offset Δs around the excitation point. In inverse SORS the excitation and collection positions are swapped around, which means excitation is in the ring and collection in the middle. In this case, the average power can be higher since the beam is spread over a larger surface (Matousek and Stone 2009).	37
Figure 1.22: Raman spectra SORS experiment of 0.5 mm normal breast tissue layer with tumour underneath (Keller 2009). The main changes in the spectra are highlighted in grey.	38
Figure 1.23: Transmission setup with breast model. Upper panel) Not illuminated, Lower panel) When illuminated by laser scattering can be seen in the whole of the breast (Photography by Hans van Schoot).....	39
Figure 1.24: Time line of the current screening programme (in case an abnormality is detected) and where a deep Raman approach would fit in.	42
Figure 2.1: Raman spectra of the four different SERS particles. The crosses depict the characteristic bands used in non-invasive experiments (Stone et al., 2011).	49

List of figures

Figure 2.2: Example of wire localisation A) Mammogram made after wire insertion; B) excised breast specimen with wire.....	50
Figure 2.3: Some of the specimens had blue dye in them and a range of 'blueness' was observed. In the left panel a specimen without blue dye is shown, while in the right panel the most extreme case is shown.	51
Figure 2.4: Illustration of the Perkin Elmer Spotlight 400 (www.perkinelmer.de , accessed 11 October 2012).	51
Figure 2.5: Schematic overview of the Renishaw 1000 system (Clark, 2002)..	52
Figure 2.6: Overview IRENI beamline A) Schematic of the experimental setup; B) FPA image (128x128 pixels) of the 12 beams illuminating an area of ~50x50 μm . Scale bar 40 μm . C) Visible light photograph of the 12 beams projected on a screen in the beam path, dashed box in A, the scale bar has a size of ~1.5 cm; D) Long time exposure photograph showing the combination of the 12 individual beams into the beam bundle (Nasse et al., 2011).....	54
Figure 2.7: Experimental setup used for the transmission Raman study.....	55
Figure 2.8: Photograph of the deep Raman setup, with the different components indicated.....	56
Figure 2.9: Detail of the combination of SORS and transmission Raman on one setup. The path of the laser is depicted in the photograph for both the SORS (orange arrows) and transmission Raman (blue arrows).	56
Figure 2.10: A) Schematic view of the workings of an axicon with the apex angle indicated in red (adapted from www.thorlabs.de , last accessed 11 October 2012); B) Photograph of the output of the axicon used, the point in the middle of the circle is the output of the transmission laser.	57
Figure 2.11: A) Original white light obtained with FTIR setup; B) same figure corrected for unequal distribution of light over each tile.	59
Figure 2.12 Screening procedure of pathology samples A) A white light image was taken; B) Area which is thought to contain microcalcifications was mapped and subsequently a biochemical fit of hydroxyl apatite (0.5% carbonate) performed; C) pixels with a calcification signal higher than threshold are coloured white, and D) Spectra matching to the white pixels.	61
Figure 2.13: White light image of the deparaffinated sample with the ATR FTIR measurement locations indicated with orange boxes and the transmission FTIR locations with red boxes.	63
Figure 2.14: Tissue block (45-50x50x50mm, average thickness 47mm) used for the extended Raman depth measurements.	65
Figure 2.15: Sample orientation in the originating depth experiment.....	66
Figure 2.16: Pathology sample with skin A) photograph of sample; B) sample mounted for deep Raman measurements.	68
Figure 2.17: Pathology sample with skin A) Front view, the arrow indicates the skin patch; B) Side view of mounted sample (thickness 23 mm).....	69
Figure 2.18: Detail of the experimental setup. Left panel: porcine soft tissue wrapped around an optical cell as used in feasibility experiment; right panel: a graphical representation (Kerssens et al., 2010).	70
Figure 2.19: Graphical representation of the spatial resolution experiment.....	71

List of figures

Figure 2.20: Photograph of the SNR experimental setup.	72
Figure 3.1: Mean FTIR spectra from samples prepared by Tecklenburg lab (Central Michigan University). Measurements are normalised and for clarity shown with offset. The blue dotted vertical lines indicate the key positions at 873, 878, 1030, 1410, 1470, and 1537 cm^{-1}	76
Figure 3.2: Infrared spectra measured from Clarkson Chromatography samples and samples provided by Prof. Keith Rogers (Cranfield University, Shrivenham). Measurements are normalised and for clarity shown with offset. The blue dotted vertical lines indicate the key positions at 873, 878, 960, 1030, 1410, 1455, and 1550 cm^{-1}	77
Figure 3.3: Results dilution experiments; Upper panel) Measurements on 0.3 wt% sample; Lower panel) Measurements on 1.8 wt% sample. Data is not normalised.....	79
Figure 3.4: Mean ATR measurements (green) versus mean transmission FTIR (blue) on 2.0% carbonate substituted HAP standard. Spectra are not normalised.....	80
Figure 3.5: Mean spectra of ATR FTIR measurements performed on A- and B-type substituted calcification standards. Measurements are normalised...	80
Figure 3.6: Mean spectra of each dataset performed on the A- and B-type carbonate substituted calcification standards. Measurements are normalised.....	81
Figure 3.7: All ATR measurements on standards. A) Standard with 4.4 wt% A-type and 0.6 wt% B-type substitution; B) Standard with 4.3 wt% A-type and 2.1 wt% B-type substitution; C) Standard with 5.7 wt% B-type substitution.	82
Figure 3.8: ATR FTIR measurements on calcification standard with predominantly A-type substitution. In blue the area under the phosphate curve along the line scan is depicted and in green the position of this band.	82
Figure 3.9: Mean Raman spectra (n=5) of samples Tecklenburg lab, 830 nm laser, 60s accumulation time. Measurements are normalised and for clarity shown with offset. The blue dotted vertical lines indicate the prominent bands discussed in the text located at 432, 440, 445, 960, 1018, 1046, 1071, 1076, and 1106 cm^{-1}	83
Figure 3.10: Mean Raman spectrum (n=5) for samples Rogers lab and Clarkson Chromatography. Key band positions are indicated with blue dotted vertical lines positioned at 432, 445, 960, 1046, and 1076 cm^{-1}	85
Figure 3.11: A) White light image of benign sample with overlaid the intensity fit of hydroxyapatite. Two calcifications are visible which are highlighted by a circle and spectral information is shown; B) Alizarin Red staining of adjacent slide; C) H&E staining of adjacent slide; D) von Kossa staining adjacent slide.	87
Figure 3.12: Measurements on sample with <i>in situ</i> pathology. A) White light image of sample, overlaid is the chemical component map for hydroxyapatite; B) Adjacent slide stained with Alizarin Red; C) Adjacent slide stained with H&E; D) Adjacent slide stained with von Kossa.	88

List of figures

- Figure 3.13: Sample with *in situ* pathology. A) Score plot of the hydroxyapatite; B) Alizarin Red staining of adjacent slide; C) H&E staining of adjacent slide; D) Von Kossa staining of adjacent slide. 89
- Figure 3.14: Invasive sample A) Scores of the chemical component map of hydroxyapatite; B) Alizarin Red staining on adjacent slide; C) H&E staining of adjacent slide; D) Von Kossa staining of adjacent slide. 90
- Figure 3.15: Comparison of intensity of the 1030 cm^{-1} phosphate band characteristic for apatite to biochemical fit of apatite. A) Intensity of the apatite band on benign sample; B) Biochemical fit of apatite on benign sample (same as in A); C) Intensity of the apatite band on *in situ* sample; D) Biochemical fit of apatite on *in situ* sample (same as in C)..... 91
- Figure 3.16: Mineralization of mammary 4T1 cells. A) Alizarin red and von Kossa staining of 4T1 cells grown in the osteogenic cocktail for 14 and 21 days; B) Measurements Diamond synchrotron on 4T1 cells grown for 14, 17, or 21 days in osteogenic cocktail. The blue line indicates the position of the 1026 cm^{-1} band characteristic for apatite. One spectrum displaying apatite was found on the sample that matured for 17 days, while apatite was abundant in the sample matured for 21 days. No apatite was found in the sample matured for 14 days. 92
- Figure 3.17: FTIR mapping 4T1 cell line grown in osteogenic cocktail. A) Apatite fit on map of sample grown for 17 days; B) Apatite fit of map of sample grown for 21 days. 93
- Figure 3.18: Intensity of the phosphate band in the Raman maps of 4T1 cell line grown in osteogenic cocktail for 14, 17, and 21 days. 93
- Figure 3.19: White light image of the same area on three different setups A) Spectrum Spotlight 400 microscope and Spectrum One; B) Bruker 80V FTIR and Hyperion 3000 microscope B22 beamline, Diamond Light Source Ltd (Oxfordshire, UK); C) Vertex 70 FTIR spectrometer and Hyperion 3000 IR/VIS microscope from Bruker, IRENI beamline, Synchrotron Radiation Center (University of Wisconsin, USA). 95
- Figure 3.20: Illustration of sample degradation over a nine month period A) sample in April 2011; B) sample in January 2012. 96
- Figure 3.21: Area sample 4694 (*in situ* pathology) measured on the B22 beam line of Diamond Light Source Ltd and Principal Component Analysis of this measurement. A) White light image of the sample measured; B) Load PC3; C) Score PC3. 97
- Figure 3.22: Measurements sample 4694 (*in situ* pathology) on B22 beamline Diamond Lightsource Ltd. A) Spectra of pixel 1:12 of row 7; B) Area under the phosphate (blue) and amide I (green) curve; C) Spectra of pixel 13:23 of row 7; D) Area under the phosphate (blue) and amide I (green) curve. 98
- Figure 3.23: Transmission of the tested substrates (an air measurement is taken as background). Note that the thickness of the substrates is not equal. 99
- Figure 3.24: Comparison of a $10\times 10\mu\text{m}$ (top panel) and a $100\times 100\mu\text{m}$ aperture (bottom panel). The same $200\times 500\mu\text{m}$ area was measured with both settings on the Perkin Elmer Spotlight. 100

List of figures

Figure 3.25: Sample with benign pathology measured at Diamond Light Source Ltd A) White light image of the sample; B) Intensity plot of the phosphate band (background corrected); C) Intensity plot of the amide I band (background corrected).	101
Figure 3.26: Sample with benign pathology measured at Diamond Light Source Ltd A) score plot of paraffin fit; B) Line scan (row 14) over the calcification.	101
Figure 3.27 Sample with benign pathology measured at Diamond Light Source Ltd. A) White light image of the sample; B) Spectra corresponding to the calcification (top) and its surroundings (bottom panel).	102
Figure 3.28: Sample with <i>in situ</i> pathology (low grade) pathology measured at Diamond Light Source Ltd. A) White light image of the sample; B) Line scan (row 3) over the map.....	103
Figure 3.29: Sample with <i>in situ</i> (low grade) pathology measured at Diamond Light Source Ltd. Spectra of pixel 16-19 of row 3 of the map shown in figure 2.28.	104
Figure 3.30: Sample with <i>in situ</i> pathology (high grade) measured at the Diamond Light Source Ltd. A) White light image of the studied calcification; B) Score plot of the apatite biochemical fit.	105
Figure 3.31: Example of line scan over sample with <i>in situ</i> (high grade) pathology. A) Spectra of row 9; B) Area under the curve for phosphate (blue) and amide I (green) band.....	105
Figure 3.32: Ratio plot of the phosphate: amide of the data shown in figure 3.31 B.....	106
Figure 3.33: Line scan over sample with <i>in situ</i> (high grade) pathology A) All spectra of row 9; B) Spectra 5:13 of row 9.	106
Figure 3.34: White light images of the line scans done over calcifications with <i>in situ</i> pathology A) White light image corresponding to data in figure 3.35 and 3.36; B) White light image corresponding to data in figure 3.37 and 3.38; C) White light image corresponding to data in figure 3.39 and 3.40; D) White light image corresponding to data shown in figure 3.41 and 3.42. .	107
Figure 3.35: A) Spectra correlating to the line scan sample with <i>in situ</i> pathology; B) Area under the curve for phosphate band (blue) and the amide I band (green) over the line map.	107
Figure 3.36: Ratio plot of the data shown in figure 3.35 B.....	108
Figure 3.37: A) Spectra correlating to line scan with <i>in situ</i> pathology; B) Area under the curve for phosphate (blue) and amide I (green) band over the line map.....	108
Figure 3.38: Ratio plot of the data shown in figure 3.37 B.....	109
Figure 3.39: A) Spectra correlating to the line scan with <i>in situ</i> pathology; B) Area under the curve for phosphate (blue) and amide I (green) band over the line map.....	109
Figure 3.40: Ratio plot of data shown in figure 3.38 B.....	109
Figure 3.41: A) Spectra correlating to the line scan with <i>in situ</i> pathology; B) Area under the curve for phosphate (blue) and amide I (green) band over the line map.....	110
Figure 3.42: Ratio plot of the data shown in figure 3.41 B.....	110

List of figures

Figure 3.43: Sample with invasive pathology A) White light image of the measured calcification; B) Spectra corresponding to pixel 7:15 of the line scan.	111
Figure 3.44: Line scan (row 6) over sample with invasive pathology A) Colour coded spectra of the row: tissue depicted in blue, calcification in red, and tissue calcification interface in green; B) Area under the curve of phosphate (blue) and amide I (green) band over the line scan.....	112
Figure 3.45: Ratio plot of the data shown in figure 3.44 B.	112
Figure 3.46: Sample with invasive pathology A) White light image of the map measured; B) Score plot of the apatite biochemical fit.	113
Figure 3.47: Selection of data related to one calcification; Left) Selected pixels are indicated by red box; Right) Spectra of the selected pixels.....	113
Figure 3.48: Horizontal line scan over calcification with invasive pathology A) Colour coded spectra of line scan; red is related to calcification and blue with surrounding tissue; B) Area under the curve for phosphate (blue) and amide I (green) band over the line scan.....	114
Figure 3.49: Ratio plot of the data shown in figure 3.48 B.....	114
Figure 3.50: Vertical line scan over invasive calcification; A) Spectra of the line scan; spectra correlating to the calcification are colour coded with red and spectra of the surrounding tissue with blue; B) Area under the curve of the phosphate (blue) and amide I (green) band.	115
Figure 3.51: Ratio plot of the data shown in figure 3.50 B.....	115
Figure 3.52: Line scan (row 10) through sample with invasive pathology A) Intensity plot of the phosphate region of the spectra on the line scan; B) Spectra relating to the calcification (position 10-20 along the line scan).	116
Figure 3.53: Biochemical fit for apatite on invasive breast pathology sample (1 micron thickness mounted on 1 mm calcium fluoride).....	116
Figure 3.54: Example of a calcification measured at the IRENI beamline. A) Principal component with the line scans analysed indicated in red. B) Data corresponding to the line scans; C) Area under the phosphate (blue) and amide I (green) curve for each line scan (upper panel) and the amide:phosphate ratio (lower panel).	117
Figure 3.55: Example of calcification measured at IRENI beamline. A) PC2 with the locations of the line scans; B) Data corresponding to the line scans; C) Line scans with the area under the curve for phosphate (blue) and amide I (green) per pixel (upper panel) and the amide:phosphate ratio (lower panel).	118
Figure 3.56: Transmission FTIR and ATR FTIR measurements on area 4. A) Intensity of apatite band over transmission FTIR map; B) Intensity of apatite over ATR FTIR map; C) Transmission FTIR spectra of calcification (red) and surrounding tissue transmission (blue); D) ATR FTIR spectra of calcification (red) and surrounding tissue (blue).....	119
Figure 3.57: Line scan over calcification in area 4. A) PC 2 of area 4 and the location of the line scan; B) Area under the curve for the phosphate band (blue) and amide I band (green) over the line scan; C) Spectra relating to the line scan; D) Band shift of the phosphate band over the line scan....	120

List of figures

Figure 3.58: Line scan over calcification in area 8. A) PC 2 and the location of the line scan; B) Area under the phosphate curve (blue) and amide I curve (green) over the line scan.....	121
Figure 3.59: Line scan over calcification in area 9. A) PC 4 and the location of the line scan; B) Area under the phosphate curve (blue) and amide I curve (green) over the line scan.....	121
Figure 3.60: FTIR and Raman mapping on same sample. A) Apatite chemical fit on FTIR map; B) Intensity of the 960 cm^{-1} phosphate band on Raman map; C) Example of Raman spectra of the intensity map showed in panel B. For both measurements a pixel size of ~ 6 micron was chosen.	122
Figure 3.61: Raman mapping with $1\text{ }\mu\text{m}$ steps. A) White light image of the calcification; B) Principal component two with the location of the line map indicated with a red line; C) Spectra corresponding to the pixels on the line scan; D) Amplitude of a fitted Gaussian to the 960 cm^{-1} band.	123
Figure 3.62 Comparison of benchtop transmission FTIR and Raman mapping. A) Benchtop FTIR; B) Raman mapping ($1\text{ }\mu\text{m}$ stepsize) on same area. .	124
Figure 4.1: Comparison Raman spectra of human mammary tissue (blue) and porcine soft tissue (green).....	125
Figure 4.2: Plot of the SNR versus the thickness of the sample. Measurements were done during $3 \times 60\text{s}$ with the cosmic removal function on. The error bars indicate the standard deviation.....	127
Figure 4.3: upper panel: $x403$ (3×10^{10} particles in $50\text{ }\mu\text{l}$) through $45\text{-}50\text{ mm}$ tissue; lower panel: $x403$ (1.8×10^9 particles in $3\text{ }\mu\text{l}$) through 20 mm tissue.	129
Figure 4.4: Mapping of porcine soft tissue breast models with $1\text{ }\mu\text{l}$ $x403$ dye injected as an analyte. A) 5 mm sample thickness; B) 20 mm sample thickness.	130
Figure 4.5: 2D Gaussian fitted to the intensity levels of $x403$ dye. A) 5 mm thick sample; B) 20 mm thick sample.	131
Figure 4.6: mapping of samples with same thickness but different injection depth analyte A) Analyte injected at the front of the 18 mm thick sample; B) Analyte injected at the back of the 18 mm thick sample.....	132
Figure 4.7: 2D Gaussian fitted to the intensity levels of the 1016 cm^{-1} band of $x403$ in 18 mm thick sample injected in front or back (baseline corrected).	133
Figure 4.8: Intensity map of $x403$ dye in a porcine soft tissue sample of 15 mm thick including skin.	134
Figure 4.9: Measurements through skin and through tissue only on a fresh human breast specimen.	135
Figure 4.10: Measurements through skin ($n=3$) and through tissue only ($n=3$) on a fresh breast specimen.	136
Figure 4.11: Measurements through skin ($n=2$) and through tissue only ($n=4$) on a fresh human breast specimen.	137
Figure 5.1: Gaussian fit on calcification standard with 2.3% carbonate substitution.	140
Figure 5.2: Relation of the carbonate substitution and the position of the 960 cm^{-1} band.	141

List of figures

Figure 5.3: Actual versus predicted carbonate substitution based upon the position of the 960 cm ⁻¹ band.	142
Figure 5.4: Band position of the phosphate band depends on the relative amount of A- and B-type carbonate substitution and not on the amount of carbonate substitution.	144
Figure 5.5: Peak with 960 cm ⁻¹ band versus carbonate substitution.	145
Figure 5.6: Predicted versus actual carbonate substitution of the buried material based on the width of the 960 cm ⁻¹ band.	146
Figure 5.7: Gaussian fit on 960 cm ⁻¹ phosphate band on batches of apatites from different suppliers (Tecklenburg lab, Clarkson Chromatography, Rogers lab).....	147
Figure 5.8: Spatial resolution experiment. The sample contains two calcification standards and is translated in steps of 1 mm (60 seconds accumulation time). Spectra of the 960 cm ⁻¹ band (850-1000 cm ⁻¹ region depicted) are shown for each step.	148
Figure 5.9: Mean SNR of measurements (n=5) versus the position.	148
Figure 5.10: Predicted amount of carbonate substitution versus the SNR.	150
Figure 5.11: Mean spectra of specimens with (blue) and without blue dye (green).....	151
Figure 5.12: Mean spectra of calcification rich (red) and calcification poor (blue) specimens.	152
Figure 5.13: Loads of principal component one to twelve.	152
Figure 5.14: Principal component 1, 2, and PC scores of PC1 and PC2 of calcification rich (red) and calcification poor (blue) specimens.....	153
Figure 5.15: Mean spectra of specimens without calcifications (blue), specimens of which it is unsure whether they contain calcification (green), specimens with calcifications present (red) and specimens with a high amount of calcifications (cyan).....	154
Figure 5.16: PC score versus the PC score for the next principal component for specimens without calcifications (green), unknown (blue), calcifications (yellow) and high amounts of calcifications (red).....	154
Figure 5.17: Plot of principal component 1 versus principal component 2 for specimens without calcifications (green) and specimens with a high amount of calcifications (red).	155
Figure 5.18: PCA LDA separation of specimens without calcifications (green) and specimens with a high amount of calcifications (red).	156

LIST OF TABLES

Table 1.1: Overview of TNM (Tumour, Node, Metastasis) staging system, adapted from (Cassidy et al., 2006).	8
Table 3.1: Overview of the techniques used to analyse the time course of 4T1 cell mineralisation and their ability to detect calcifications in the different samples. Staining: + = sparse, ++ = moderate, +++ =extensive, ++++ = very extensive. Detection of calcification: Y = yes, N= no.	93
Table 5.1: Prediction of the percentage carbonate substitution based on the location of the peak.	142
Table 5.2: Prediction of the percentage carbonate substitution based on the width of the peak.	146
Table 5.3: The predicted carbonate range, mean carbonate substitution and SNR for each combination of spectra.....	149

LIST OF EQUATIONS

Equation 1: Calculation of the Nottingham Prognostic Index (NPI).	9
Equation 2: Volume of a sphere.	67
Equation 3: Full-width-half maximum calculation.....	70
Equation 4: FWHM of a Gaussian function.	131
Equation 5: Fit of the relationship between the carbonate concentration (x) of the calcification standard and the location of the 960 cm^{-1} band (y).....	141
Equation 6: Fit of the relationship between the carbonate concentration (x) of the calcification standard and the width of the 960 cm^{-1} band (σ).	145

GLOSSARY

4T1: A mineralising breast cell line.

ACP: Amorphous calcium phosphate.

Adipose tissue: fat.

ALP: alkaline phosphatase.

Amide I: FTIR amide vibration band in the 1600 - 1700 cm^{-1} region.

Amide II: FTIR amide vibration band in the 1500 - 1600 cm^{-1} region.

Anti-Stokes: Inelastic scattering event in which the scattered photon has a higher energy than the incident photon.

Apatite: Hydroxyapatite, material type II calcifications are made of, a phosphate mineral with chemical composition $\text{Ca}_{10}(\text{PO}_4)_6(\text{OH})_2$.

AR: Alizarin Red staining, a routine stain used in pathology to visualise calcified material. Calcium is stained in red.

ATR FTIR: Attenuated total reflection FTIR, a form of FTIR in which a higher spatial resolution is obtained by employing a crystal with a higher refractive index than the material that is investigated.

A-type (substitution): The hydroxygroup of the apatite is substituted by carbonate.

B22: FTIR beamline Diamond synchrotron used for studies.

βG : betaglycerophosphate.

B-type (substitution): The phosphate group of the apatite is substituted by carbonate.

Calcifications (breast calcifications): Calcified material in the breast. See type I and type II.

Carcinoma: Cancer arising from the epithelial cells.

CCD: charge coupled device, a type of detector.

COD: Calcium oxalate dihydrate ($\text{CaC}_2\text{O}_4 \cdot 2\text{H}_2\text{O}$), the material type I calcifications consist of.

COHAP: Carbonate substituted HAP.

COM: Calcium oxalate monohydrate, a standard for COD.

CW: Continuous wave, a non-pulsed laser.

DCIS: Ductal carcinoma *in situ*. Cancer arising in the epithelial cells of the ducts.

Deep Raman: Raman spectroscopy adapted in such a way that photons from deeper depths can be measured.

De-paraffin: The removal of paraffin from slides of a pathology block. In our studies this is done by using hexane.

Elastic scattering: Rayleigh scattering, the energy of the incident photon is equal to the energy of the scattered photon.

Epithelium: Type of cell lining the breast ducts.

Extracellular matrix: Complex network produced and excreted by cells to extracellular space which provides the cells structural support and influences their physiology and development.

Ex vivo (measurements): Measurements done outside an organism, for example on excised tissue.

Glossary

- FPA:** Focal plane array, a type of detector.
- FTIR:** Fourier transform infrared, a vibrational technique that examines the chemical compositions by probing chemical bonds.
- FWHM:** Full width half maximum.
- G:** glycerol.
- GLREC:** Gloucestershire Local Research Ethics Committee.
- HAP:** hydroxyapatite, the material type II calcifications consist of.
- H&E:** Haematoxylin and eosin, a routine staining procedure that stains the nuclei of the cells purple and the surrounding tissue a range of orange hues.
- Horizontal view:** Modality during mammography in which the breast is compressed top to bottom.
- Inactive breast:** No lactation or pregnancy.
- Inelastic scattering:** Scattering event in which the energy of the incident and the scattered photon differs.
- Invasive cancer:** Tumour spreading to other parts of the body.
- Inverse SORS:** SORS measurements in which the excitation is done in a ring, and the collection in the centre of the ring.
- In vivo (measurements):** Measurements done in an intact cell or organism.
- IRENI:** FTIR beamline Synchrotron Radiation Center (WI, USA) used for studies.
- Kerr gating:** A type of deep Raman spectroscopy based on temporal differences of signals from different depths.
- LCIS:** Lobular carcinoma *in situ*. Cancer arising in the epithelial cells of the lobules.
- L-type (carbonate substitution):** The carbonate is within the surface hydration layer of the apatite.
- Macrocalcifications:** Larger calcifications with a size up to several millimetres.
- Mammography:** Screening technique used in the NHSBSP. The breast is examined with X-ray after compression from either top to bottom or left to right.
- Metastasis:** Spread of cancer.
- Mie scattering:** Scattering of photons by a sphere.
- MRI:** Magnetic resonance imaging, a medical imaging technique in which a magnetic field is applied and the alignment of the protons returning to their original state is measured when the field is removed.
- mRNA:** messenger RNA.
- NBSP:** National breast screening programme.
- Near-IR:** Region of the electromagnetic spectrum, $\pm 780 - 3000$ nm.
- NHSBSP:** NHS breast screening programme.
- Oblique view:** Modality during mammography in which the breast is compressed left to right.
- One stop clinic:** Triple assessment consisting of mammogram and/or ultrasound, family history and clinical examination and a biopsy done in one day.
- OPN:** Osteopontin, a bone matrix protein expressed by human breast cancer cells.

Glossary

P_i: Phosphate.

PCA: Principal component analysis, a multivariate data analysis used to decrease the amount of data.

PCA-LDA: Principal component analysis linear discriminant analysis

PCA load: All data is compressed to a smaller amount of loads than spectra. Each load shows the next largest variation in the spectrum.

PCA score: The PCA scores indicate how much of the corresponding load is in the original spectrum of the specimen.

PP_i: Pyrophosphate.

Raman mapping: A combination of microscopy and Raman spectroscopy. By measuring a Raman spectrum on every position, a chemical map can be created.

Raman scattering: Inelastic scattering event of photons.

Raman shift: The shift in wavelength between the incident and scattered photon.

Rayleigh scattering: Elastic scattering event, the energy of the incident photon is equal to the energy of the scattered photon (elastic scattering).

Resonance Raman: A variant of Raman spectroscopy where an excitation wavelength close to an absorption band is used to enhance the probability.

SERS: Surface enhanced Raman spectroscopy. Due to the interactions with a roughened metal surface the Raman signal is dramatically improved by electromagnetic and chemical enhancement.

SESORS: Surface enhanced spatially offset Raman spectroscopy, a combination of SERS and SORS which will increase the Raman signal compared to SORS.

SNR: Signal to noise ratio.

SORS: Spatially offset Raman spectroscopy, a distance is introduced between the excitation and collection.

Spatial approach: Discrimination of signals based on position differences.

Stokes: Inelastic scattering event in which the scattered photon has a lower energy than the incident photon.

Synchrotron: Facility where intense beams of lights are produced by accelerating electrons along a circular trajectory.

Temporal approach: Discrimination of signal based on differences in time.

TNM: Tumour Node Metastasis staging.

Transmission Raman: An extreme form of SORS in which the signal is collected on the opposite end of the sample.

Turbid media: highly scattering media.

Type I calcifications: calcifications consisting of COD

Type II calcifications: calcifications consisting of HAP.

US: Ultrasound, a medical imaging technique, US is often used for biopsy guidance.

VK: von Kossa staining, a routine stain which stains calcified material black.

Whitlockite: calcium phosphate mineral with composition $\text{Ca}_3(\text{PO}_4)_2$.

X-ray: Region of the electromagnetic spectrum, $\pm 0.1 - 10 \text{ nm}$.

1 Introduction

1.1 Breast disease and anatomy

1.1.1 Breast disease

Breast cancer is the most common type of cancer among women and accounts for 30.6% of all cancers among women (figure 1.1). In 2009, 48,417 women were diagnosed (and 371 men) with breast cancer in the UK alone (Cancer Research UK, 2012a).

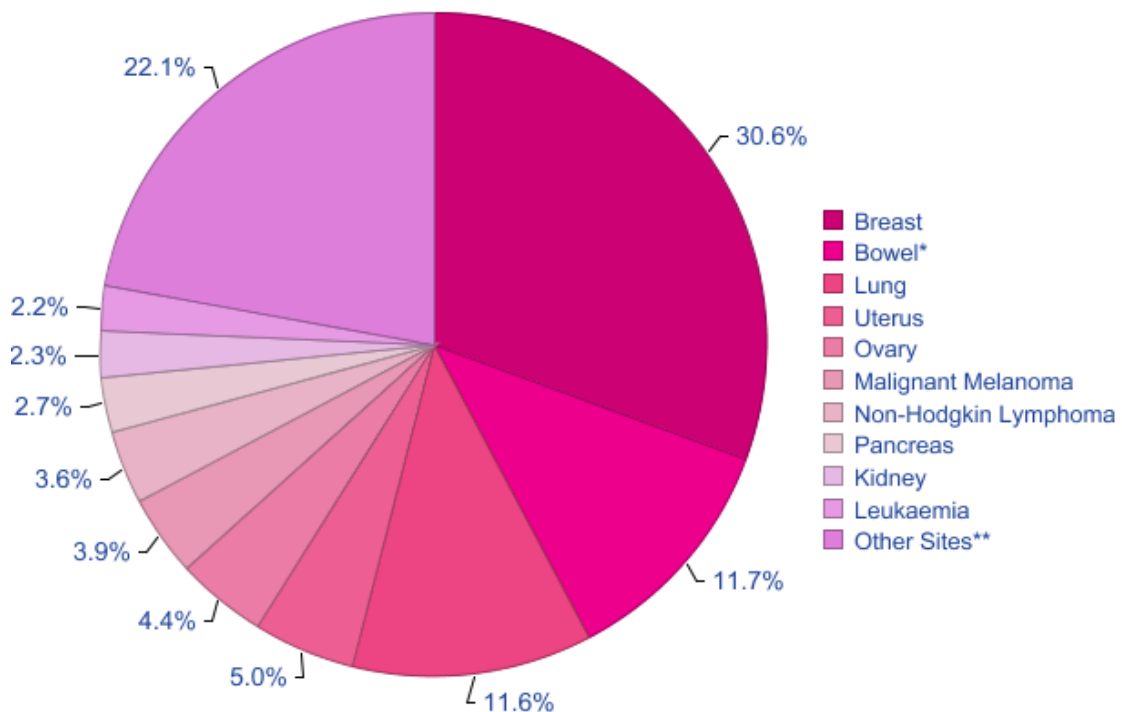


Figure 1.1: Most common cancers among females in the UK in 2009 (Cancer Research UK, 2012b).

Breast cancer incidence in the UK is 124 per 100,000 women (about 1 in every 8 women). There is however a strong relation between age and incidence. In the 20-24 years old age group, the incidence per 100,000 women is 1.4 while for example the incidence in the age group 40-44 years old is 121.4 per 100,000, and 400.1 in the 65-69 age group (Cancer Research UK, 2012b). The incidence numbers per age group are displayed in figure 1.2.

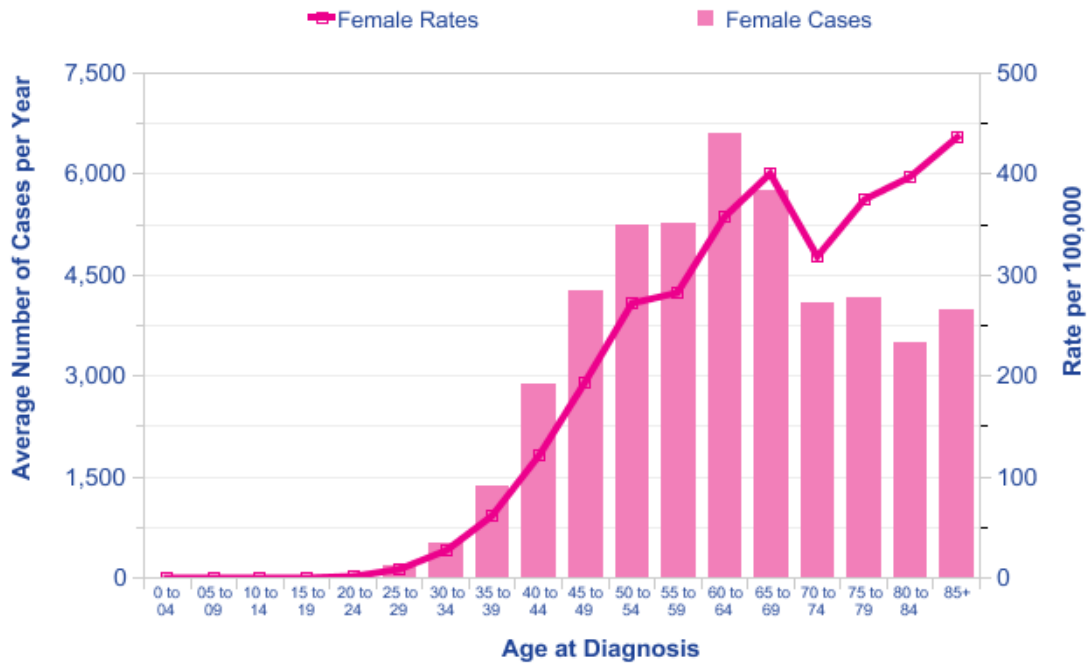


Figure 1.2: Number of breast cases per year and age-specific incidence rates per 100,000 women in the UK (Cancer Research UK, 2012b).

Other important risk factors are a family history of breast cancer (linked to the BRCA1 and BRCA2 genes), previous breast disease, the age at menarche, menopause and the first pregnancy (McPherson, 2000), and the mammographic density. The mammographic density is a measure for the tissue composition. While fat appears dark on a mammogram, epithelium and stroma (connective tissue) are radiographically dense and appear light on a mammogram. The risk of breast cancer increases four to six times for women with dense tissue in 75% or more of the breast compared to women with little or no dense tissue in the breast (Boyd et al., 2007).

Carcinoma, a cancer arising from the epithelial cells, is the most common cancer in the breast and can be divided into several classes and grades according to the tumour node metastasis staging described in section 1.1.4. Carcinoma is often split in ductal and lobular carcinoma named after the believed origin of the cancer i.e. the ducts or the lobules. Although it is now known that both types originate from the terminal duct lobular unit these names are still commonly used (Sainsbury, 2000). Ductal carcinoma is much more common than lobular carcinoma and accounts for 90% of the breast carcinomas

(Cassidy et al., 2006). As the male breast contains ductal epithelium, carcinoma can develop in men as well although the incidence is much lower. Breast cancer accounts for only 0.2% of cancers among men (Cancer Research UK, 2012a).

In situ disease represents the first stage (ductal carcinoma *in situ* or DCIS and lobular carcinoma *in situ* or LCIS) in which the tumour remains within the confines of the ductal basement membrane. It is estimated that the probability of development from DCIS into invasive cancer (when the tumour spreads to other parts of the human body) is between 30 and 50% (Cassidy et al., 2006). Invasive ductal carcinoma (IDC) accounts for 75% of all breast cancers (Cassidy et al., 2006).

1.1.2 Breast anatomy

In women, the breast contains a mammary gland that secretes milk for feeding infants. During the lactation stage, milk is produced in the lobules which are drained into the ducts towards the nipple. Each lobule consists of circa twenty acini which open into the terminal duct. Similar to ducts, the acini are lined with a single layer of epithelial cells and an external layer of myoepithelial cells around the basal membrane (Guinebretiere et al., 2005). The anatomy of the human (female) breast is shown in figure 1.3.

When the breast is inactive (no pregnancy and lactation) the lobules consist almost entirely of branching ducts surrounded by connective and adipose (fat) tissue (Kopans, 2007). During pregnancy the glandular tissue increases in size by growth, branching of the ducts, and formation of acini from the ducts.

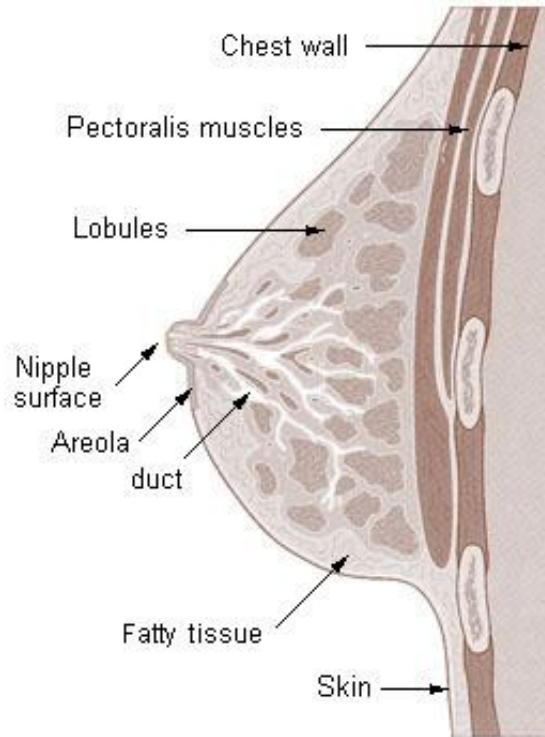


Figure 1.3: Anatomy of the human breast (training.seer.cancer.gov accessed August 11, 2010).

1.1.3 Detection of breast cancer

The prognosis of breast cancer patients is strongly correlated with the stage in which the disease is detected. Early diagnosis allows more conservative treatment and better patient outcomes. Screening will result in detecting cancer in an earlier (and more treatable) phase resulting in lower mortality rates. Mammography is the standard method to screen for breast cancer, the NHS alone screened over 2.1 million women in the year 2009/2010 with this technique (Patnick, 2011). There is no evidence that clinical examination, breast ultrasound, or teaching self-examination are effective tools for early detection (Blamey, 2000).

The UK National Breast Screening Programme (NBSP) offers three-yearly mammography screening. Originally the age range of the women invited for screening was 50-64 years which was in 2002-2004 expanded to 50-70 years.

Chapter 1

Currently the range is further expanded; by the end of 2012 all women between 47 and 73 years old will be invited (Duffy et al., 2010).

During mammography, the breast is examined with X-ray after compression from top to bottom for the horizontal view, and left to right for the oblique view. In general, dense materials such as calcifications (or bone material) would absorb more radiation and are typically displayed in white, while less dense materials such as breast tissue absorb less radiation and appear dark in mammograms. Due to the higher density of breast tissue in breast of young women, the contrast is low and mammography is less sensitive which results in an age restriction on the applicability of this technique. An overview of the techniques that can be applied to improve the contrast is given by Cheng et al. (2003). A typical range of density of mammograms is shown in figure 1.4 for the horizontal view (upper row) and oblique view (lower row).

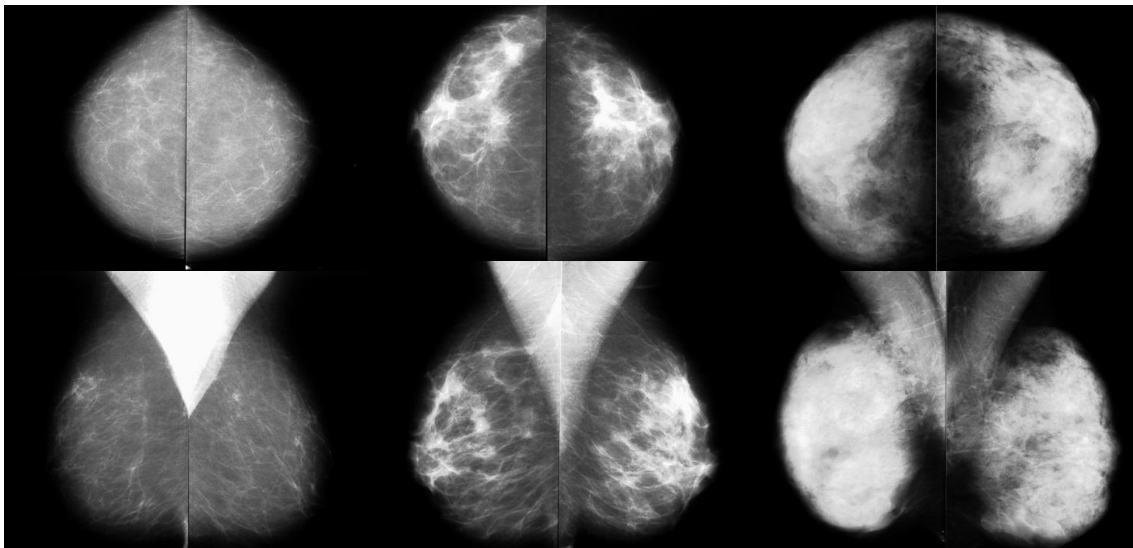


Figure 1.4: Example of the range in density visible in mammography. Horizontal views are shown in the upper row and oblique views in the lower row. (Images kindly provided by Prof. Iain Lyburn, radiologist at Cheltenham General Hospital).

When an abnormality is found during mammography, the patient will be referred to the 'one stop clinic' where a triple assessment will be carried out consisting of the following:

1. Mammogram and/or ultrasound. The combined use of mammography and ultrasound increases the sensitivity (Kuhl et al., 2005; Zonderland et

Chapter 1

al., 1999). Ultrasound is often used to examine young (or pregnant) women who cannot be examined with mammography and can be used to target the location of a biopsy (Nover et al., 2009).

2. Family history and clinical examination by a clinician
3. Biopsy

Women who show symptoms of breast disease, such as a lump felt during breast self-examination, can be referred to the one stop clinic by their GP. Women with a higher-than-average risk of developing breast cancer may be offered additional screening and genetic testing. In the future, the use of molecular markers as a screening tool may be beneficial for this specific group.

A technique suitable for younger women, with symptoms or a family history is magnetic resonance imaging (MRI) (Kuhl et al., 2005). In figure 1.5, a typical example of an MRI image is shown in panel C, alongside the mammogram images in panel A and B.

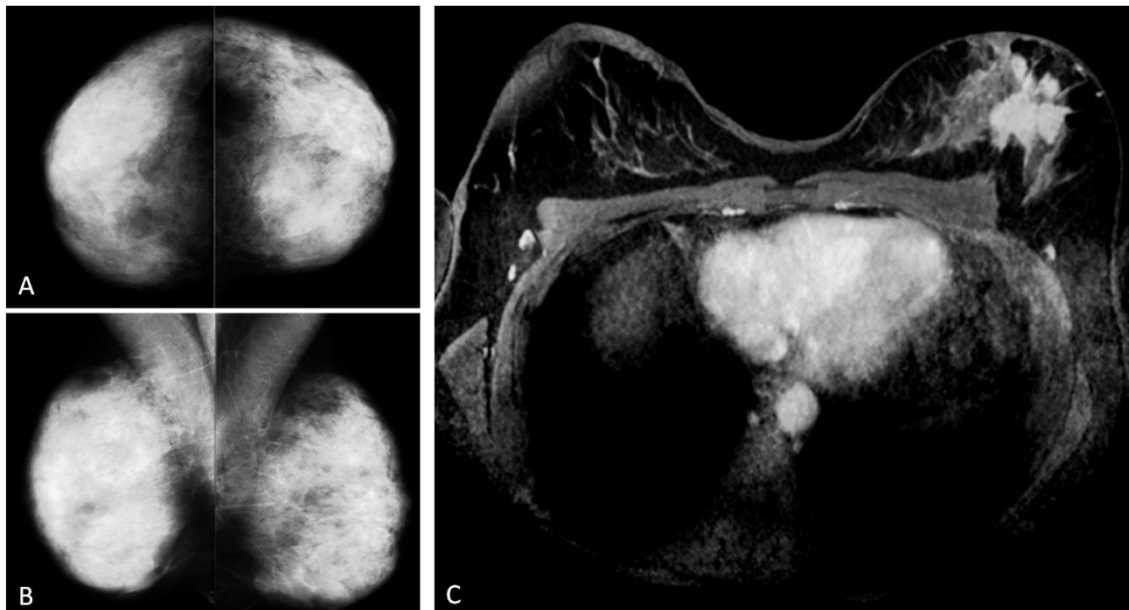


Figure 1.5: Mammogram versus MRI scan; A) Horizontal view mammogram; B) Oblique view mammogram; C) MRI scan (images kindly provided by Prof. Iain Lyburn, radiologist at Cheltenham General Hospital).

MRI is based on the alignment of protons to a magnetic field applied. When the magnetic field is removed, the alignments of the protons return to their original state. A picture is then formed based on the different rates of return to the

equilibrium state (Nover et al., 2009). MRI is typically more sensitive than mammography and therefore used to obtain extra information after a suspicious mammogram (Kriege et al., 2004; Orel and Schnall, 2001). The specificity of MRI is limited (in contrast to the sensitivity which is remarkably high), the technique is costly and the cost-effectiveness is debated and therefore this method is not routinely used in the breast screening programme (Orel and Schnall, 2001).

1.1.4 Pathology of breast disease

When an abnormality is detected, the diagnosis is made based on a tissue biopsy which is examined by pathologists. Biopsy is currently the 'gold standard' for breast cancer diagnosis. Staining of biopsies by a pathologist is a routine procedure in order to pick out differences in pathology more easily. H&E (haematoxylin and eosin) is the first stain performed on almost all (sectioned) specimens in medicine. Haematoxylin stains the cell nuclei blue, the eosin counter stain changes the colour of blue-stained nuclei towards purple and provides a range of orange hues for the surrounding tissue. By providing the different colours to specific elements of the specimen the morphology of cells and tissues is more readily defined by the pathologist.

Pathology samples are staged in order to create a patient specific treatment plan. Breast cancer staging can be done with the 'tumour, node, metastasis' (TNM) staging system. It takes the size of the tumour into account, whether the nodes are affected and whether or not the cancer has spread (metastasis). An overview of the TNM method is given in table 1.1 (Cassidy et al., 2006).

T	Tumour size	Specifics
Tis	In situ disease only	
T1	≤ 2 cm	
	≤0.1 cm	
T1a	0.1 - 0.5 cm	
T1b	0.5 - 1.0 cm	
T1c	1.0 - 2.0 cm	
T2	2.0 - 5.0 cm	
T3	>5.0 cm	
T4	Any size	Involvement of chest wall or skin
T4a	Any size	Spread into chest wall
T4b	Any size	Spread into skin
T4c	Any size	Fixed to chest wall and skin
T4d	Any size	Inflammatory cancer
N	Node assessment	
Nx	Not assessed	
N0	Negative lymph nodes	
N1	Positive mobile axillary lymph nodes (armpit)	
N2a	Positive fixed axillary lymph nodes	
N2b	Internal mammary nodes clinical apparent (behind breast bone)	
N3a	Positive lymph node infraclavical (below collarbone)	
N3b	Positive axillary and internal mammary nodes	
N3c	Positive supraclavicular node (above collarbone)	
M	Metastasis assessment	
M0	No sign of metastasis	
M1	Positive evidence of distant metastasis	

Table 1.1: Overview of TNM (Tumour, Node, Metastasis) staging system, adapted from (Cassidy et al., 2006).

The TNM staging does not take the histological grade into account which is a prognostic factor strongly associated with both breast cancer-specific and disease-free survival (Rakha et al., 2008). The survival rate of patients with grade I tumours is significantly better than that of patients with grade II or III tumours (Elston and Ellis, 1991). The Nottingham Prognostic Index (NPI) combines tumour size, nodal status and histological grade. The NPI is given by the following relationship:

$$NPI = \text{Lymph node stage (1 – 3)} + \text{histological grade (1 – 3)} \\ + 0.2 * \text{tumour size (cm)}$$

Equation 1: Calculation of the Nottingham Prognostic Index (NPI).

A lymph node stage of one means that no lymph nodes are involved. A lymph node stage of two includes patient with up to three lymph nodes involved. When four or more lymph nodes are involved and/ or an internal lymph node the grade equals three. The score of the histological grade equals the grade itself i.e. I=1, II=2, and III=3 (Lee and Ellis, 2008). A NPI value lower than 2.4 indicates an excellent prognosis, between 2.4 and 3.4 equals 'good', 3.4- 5.4 'moderate', and above 5.4 a poor prognosis.

Samples can also be tested for the oestrogen and progesterone receptor status and HER2 expression. 60-75% of breast cancers are oestrogen receptor positive (Cassidy et al., 2006). Oestrogen and progesterone can stimulate the growth of these breast cancers and hormone therapy can block the effect or lower the amount of oestrogen and progesterone in the body. HER2 is a protein that functions as a growth factor receptor and is expressed in 25-30% of breast cancers (Cassidy et al., 2006). When patients are HER2 positive, they can be treated with the antibody Herceptin.

Although pathologists are highly trained and skilled, pathology remains a subjective approach that is time consuming and expensive. In a study by Parham et al. (2010) fifteen H&E slides were examined by seven general pathologists and five pathologists with a special interest in breast pathology. The majority diagnosis of the pathologists with a special interest was used as the gold standard and compared to the diagnosis of the individual general pathologists. The pathologists with a special interest obtained an 85% agreement in the first round and 82% in the second round six months later. The general pathologists reached 75% agreement in the first round and 72% in the second round. An objective and accurate method would clearly mean a leap forward in cancer diagnostics.

1.2 Breast cancer screening and the clinical need of a new tool

Upon examination by pathologists, most biopsies turn out to be negative. A study by Weaver et al. (2006) done at the seven community-based mammography registries located in California, Colorado, New Hampshire, New Mexico, North Carolina, and Washington (USA) indicated that from 26,748 biopsies from the breast cancer surveillance data from 1996-2001, only 8815 were followed by diagnosis of breast cancer (33%). Of the breast cancers, 81% were invasive carcinoma and 19% DCIS. In the UK, the NHSBSP recalled 89,164 women after mammography in the age group 45-74 (4.2% of the total amount of 2,102,870 women) in 2009/2010, of which 16,476 turned out to have breast cancer which is 18.5% of the amount of recalls (Patnick, 2011). The numbers of recalls are displayed in figure 1.6 in orange, and are split into malignant (red) and non-malignant (green).

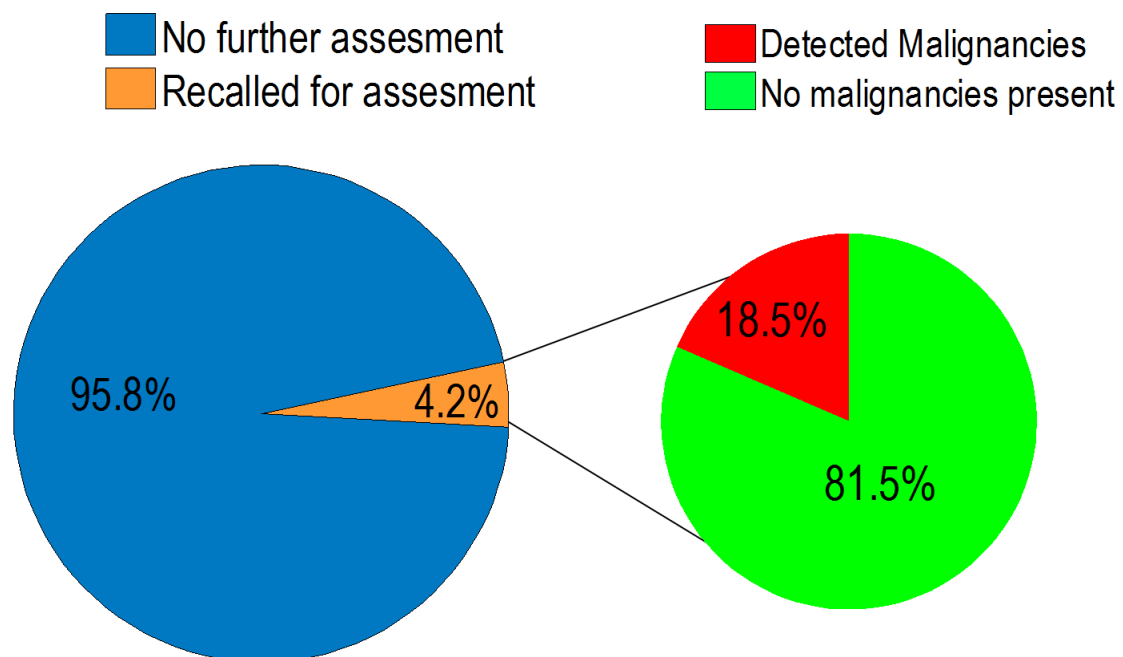


Figure 1.6: Amount of recalls in NHSBSP 2009/2010 (based upon numbers of Patnick 2011).

Due to the time delay between screening, biopsy, and diagnosis, the current procedure is very stressful for the woman involved. A new technique which could be used *in vivo* would not only reduce time delay and stress, but also the amount of biopsies and the costs associated with biopsies. It is estimated that a

Chapter 1

fine needle aspiration cytology costs £35.52, a core biopsy including equipment £49.25, and day case and inpatient excision biopsies including pathology costs £539 and £812, respectively (Dey et al., 2002). It should be noted that the use of fine needle aspiration cytology is not recommended for calcification biopsy as it is not possible to confirm representative sampling (Evans et al., 2002). Vacuum-assisted biopsy has a higher calcification retrieval yield and is the method of choice to biopsy calcifications (Lieberman et al., 1998b). Biopsy costs in the USA were evaluated by Liberman et al. (2001) who found that the costs of a stereotactic biopsy of one site were \$764 (with clip) or \$695 (without clip) and for two sites \$1,345 (with clips) or \$1,234 (without clips). Needle localisation and surgical biopsy costs \$1,502 (with margin analysis) or \$1,435 (without margin analysis) for one site and \$2195 (with margin analysis) or \$2,127 (without margin analysis) for two sites.

In this thesis, the potential incorporation of deep Raman into the breast screening programme is evaluated. Currently, the presence of calcifications in the breast is used as a diagnostic marker but the chemical composition of the calcification is not taken into account. This chemical composition is however related to disease. There is no reliable method to separate different types of calcifications with mammography although several algorithms have been proposed based on for example size, shape, and number (Fandos-Morera et al., 1988; Galkin et al., 1983) but these are not very effective in all situations.

It is estimated that microcalcifications are the primary indication for approximately 50% of the breast biopsies performed for non-palpable mammographic abnormalities (Johnson et al., 1999), although retrospectively most biopsies contain calcifications. This number is in agreement with Gülsün et al. (2003) who state that 30-50% of nonpalpable breast cancers present themselves as microcalcifications alone. National figures regarding the proportion of breast biopsies due to calcifications are unknown for the UK, but it is well known that the recall rate is two times higher in the USA (Elmore et al., 2005) which is thought to be related to extra investigations of calcifications. The number of biopsies due to calcifications in the UK is therefore thought to be

lower. Private communication with Miss Sarah Vesty, breast surgeon at GHNHSFT, revealed that within Gloucestershire Hospitals 15% of the biopsies (group size 400) are solely due to calcifications (Vesty, 2013) which is two times less than the USA figures.

Probing the chemical composition *in vivo* as an adjunct to mammography would reduce the amount of (unnecessary) biopsies and reduce the time delay in clinic; especially in the USA where recall rates are higher. Raman spectroscopy has shown to have the potential to probe the chemical composition of calcifications *ex vivo* (Haka et al., 2002). In figure 1.7 an overview of the current time line is given.



Figure 1.7: Overview of the current screening programme (in case an abnormality is detected).

Over the last few years, breast screening programmes have been criticised in the literature (Kalager et al., 2012). It is often claimed that the high rates of DCIS found are due to over diagnosis with the associated lesions not presenting a clinical problem or threatening patient’s life. Another possibility would therefore be to use deep Raman spectroscopy to monitor disease progress since not in all cases clinical interference would be beneficial.

1.3 Calcifications in the breast

The formation of crystalline and semi-crystalline materials occurs extensively within many types of biological tissues due to natural biological processes (such as bone and tooth growth), but also as a result of disease progression (for example prostate and thyroid cancer), drug therapies and implants. The

presence of calcifications in breast is one of the features screened for during mammographic screening and one of the most common abnormalities identified (Purdie and McLean, 2009). The presence of calcifications is related to high histological grade in both DCIS (Mun et al., 2013) and invasive breast cancer (James et al., 2003).

A typical example of mammography in which calcifications are found is shown in figure 1.8.

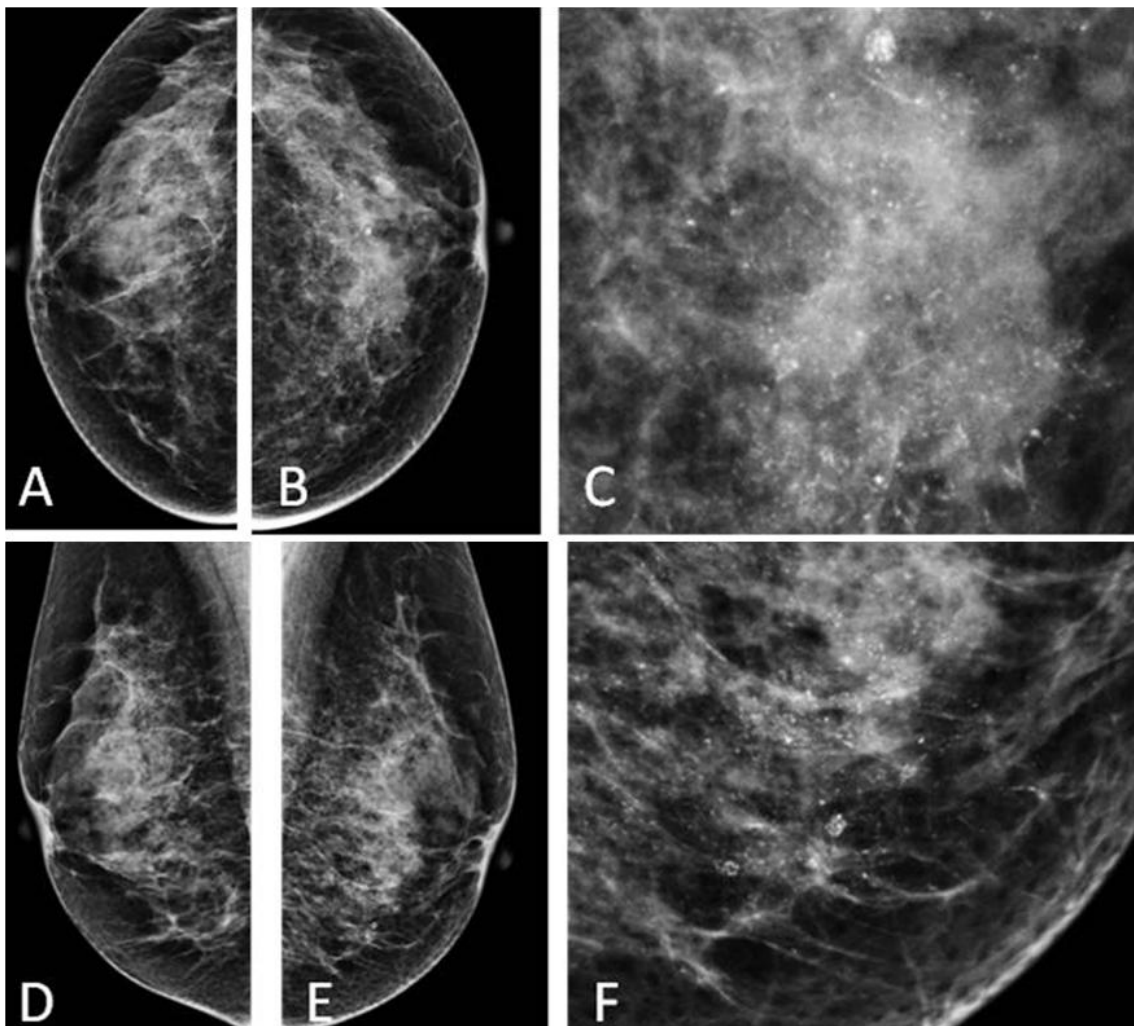


Figure 1.8: Mammography of breast with diffuse calcification in left breast A) horizontal view right breast; B) horizontal view left breast; C) Zoom of left breast horizontal view; D) oblique view right breast; E) oblique view left breast; F) Zoom of oblique view left breast (Images kindly provided by Prof. Iain Lyburn, radiologist at Cheltenham General Hospital).

In panel A and B the horizontal view of the right and left breast are shown, followed by an enlarged version of the left breast in panel C. In this panel

microcalcifications can be distinguished. In panel D and E an oblique view is presented. A zoom of the oblique view of the left breast is shown in panel F in which microcalcifications can be observed again.

The amount of calcifications present in the breast ranges from study to study since it is often not the key research question and the methods of estimating the amount of calcifications range. As previously mentioned, Johnson et al. (1999) estimated that half the biopsies performed after a mammographic abnormality are due to the presence of calcifications, while Evans et al. (2002) estimate that in 80-90% of mammographic abnormalities in DCIS calcifications are present. According to Sickles (1982) 60-80% of cancers are shown to contain calcifications upon histology examination. These numbers cannot be compared since all of the numbers describe another statistic. Although there might not be a standard way of reporting the amount of calcifications in the breast, calcifications are currently the primary guide used in radiology, surgery, and pathology during the diagnostic evaluation (Johnson et al., 1999).

While microcalcifications have a typical size ranging from 50-500 micron (Evans et al., 2002), calcifications can reach sizes of a few millimetres. Figure 1.9 shows an example of a macrocalcification in panel A, and of microcalcifications in panel B.

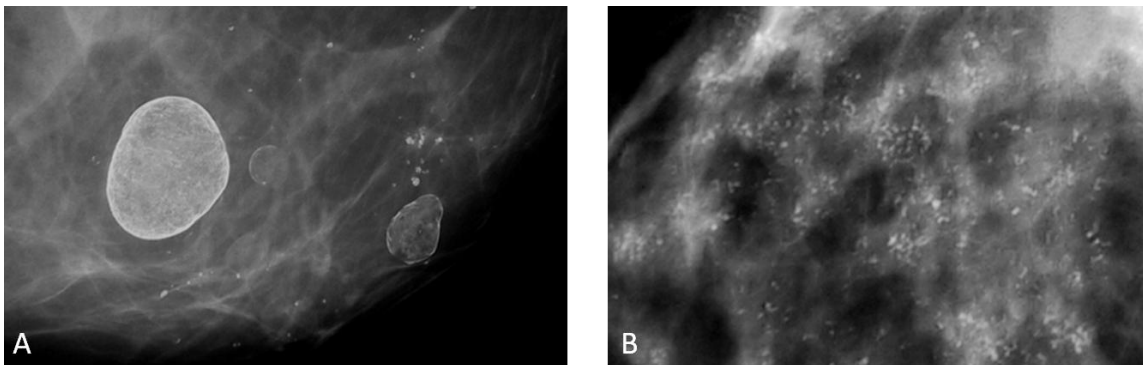


Figure 1.9 A) Mammogram with macrocalcification; B) mammogram with microcalcifications (images kindly provided by Prof. Iain Lyburn, radiologist Cheltenham General Hospital).

A correlation between such large macrocalcifications and cancer has not been found and further monitoring or treatment is not necessary when the macrocalcifications are seen on mammograms. Therefore, for the rest of the

Chapter 1

this macrocalcifications are not discussed and the term 'calcification' will refer specifically to microcalcifications.

Breast calcifications can also be found in men. These calcifications are typically coarser, fewer in number, and more widely scattered than those in female breast cancer (Adibelli et al., 2010). Since breast cancer in males is rare and not routinely screened for, calcifications in the rest of this thesis will refer to calcifications found in the female breast.

The incidence of calcification in carcinoma *in situ* is more common in younger patients and in higher grade lesions (Tse et al., 2007). In a large study by Tabar et al. (2004), the 24-year survival of 714 women with 1-14 mm invasive breast carcinoma was studied. In 7% of the cases calcifications were observed (52 cases) and this was associated with a positive lymph node status (spread to lymph node), poorer histologic grade and a decreased survival rate. It has been reported that removal of calcifications correlates significantly with a lower rate of upgrade from atypical ductal hyperplasia to carcinoma (Nguyen et al., 2010).

Radiography of biopsy specimens is an integral part of the biopsy process (Lieberman et al., 1994). In a study of Margolin et al. (2004) it is shown that biopsy cores containing calcification (based on specimen radiographs) were more likely to enable an accurate diagnosis than cores without calcifications. Furthermore, it was less likely to miss a cancer diagnosis in the samples with calcifications. Radiography is sometimes used to verify the presence of the lesion in the surgical biopsies. If no calcifications are present the surgeon would then be informed and a wider excision would be performed immediately instead of summoning patients back to theatre at a later time (Johnson et al., 1999; Lieberman et al., 1994). In figure 1.10 X-ray images are shown of excised tissue with a wire to target the correct location (panel A), a typical example of an X-ray machine used in theatre (panel B), microcalcifications in a slice (panel C), and microcalcifications in core specimens (panel D).

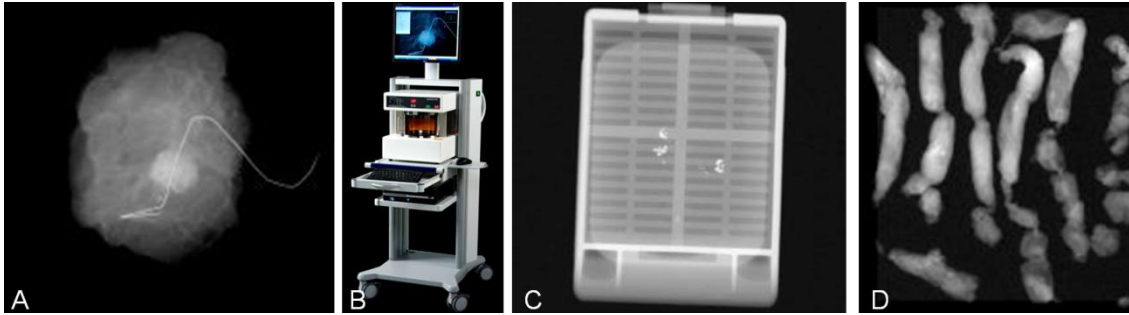


Figure 1.10: A) X-ray image of surgical specimen; B) X-ray machine used in theatres; C) X-ray image of microcalcifications in slice; and D) X-ray image of microcalcifications in core specimens (www.faxitron.com).

Although microcalcifications are relatively common in breast carcinoma, their presence is however also a common feature in benign breast lesions. According to Popli (2002) the amount of cases in which calcifications are found steadily increases with age up to 86% of the mammograms of women between the age of 76 and 79. Since the breast screening programme examines women in the age range from 47-73 years old, the presence of microcalcifications is a frequent occurrence.

In order to distinguish calcifications related to benign and malignant surrounding tissue, several algorithms have been proposed based on, for example, size, shape, and grouping characteristics such as the size and shape of the cluster and the amount of calcifications in the cluster. For example, the shape of most calcification clusters surrounded by breast tissue with benign pathology grade tend to be round or oval, while the majority of clusters associated with 'in situ' breast disease have an irregular shape, 80% of the *in situ* cases, which is sometimes V-shaped (10% of the irregular shapes) (Evans et al., 2002). As a general rule, the smaller the cluster the less characteristic it is for breast disease. In a study by Fondrinier et al. (2002) 44% of the clusters of 25 mm or smaller were malignant, whereas of the clusters larger than 25 mm 69% was malignant. In the same study 42% of the clusters containing 35 calcifications or less were malignant, while 83% of the clusters containing more calcifications were malignant. In contrast, Park et al. (2000) demonstrated in a study of 57 nonpalpable lesions with three different radiologists, that the significance of clustering is lower than 50% and does not necessarily suggest malignancy.

A study by Buchbinder et al. (2002) evaluated the size of the calcifications in a cluster by measuring the length and area of the calcifications. The average length of the calcifications in the malignant group was higher than the length in the benign control group, 0.44 mm versus 0.38 mm. It is however difficult to use this as a tool considering the small size of the calcifications.

Other important features for differentiating benign from malignant mammographic calcifications is the calcification morphology and distribution. Linear calcification morphology has a high positive predictive value for carcinoma (Liberman et al., 1998a). A study by Stomper et al. (2003) indicated that linear calcifications are more often related to invasion than granular calcifications. A common feature of DCIS is that the calcifications are aligned in a ductal distribution (Evans, 2003). When reanalysing previous mammograms from women diagnosed with DCIS, 22% of the mammograms were in retrospect abnormal. The mammograms showed more often predominantly punctate calcifications and less common rod-shaped calcifications (Evans et al., 1999).

1.3.1 Types of breast calcifications

In breast, two major types of microcalcifications are found. These are thought to be related to disease (Frappart et al., 1986, 1984). Type I (calcium oxalate dihydrate, $\text{CaC}_2\text{O}_4 \cdot 2\text{H}_2\text{O}$) is mostly present in benign biopsies and type II (hydroxyl apatite, $\text{Ca}_{10}(\text{PO}_4)_6(\text{OH})_2$) are most often present in proliferative lesions including carcinoma (Foschini et al., 1996; Haka et al., 2002; Singh and Theaker, 1999). Type II micro calcifications frequently indicate the location of the most important abnormality within the breast (Cassidy et al., 2006; Johnson et al., 1999).

Type I calcifications have an amber colour under the microscope and are birefringent under polarised light (Frappart et al., 1986). In contrast, type II calcifications appear greyish under microscope light and are not birefringent under polarised light.

Chapter 1

Although calcifications have a positive predictive value for breast cancer, it is not known how they are formed in mammary tissue and what their exact role in breast cancer formation is. Pathologists often state that calcifications are formed by calcification in necrotic debris or from mucin in extracellular spaces. These claims were however never underscribed by thorough time-studies.

Recent studies suggest that calcifications play an active role in disease development. In a study by Morgan et al. (2001) breast cell lines treated with hydroxyapatite crystals were compared to those treated with latex beads of similar size and concentration and those with no treatment at all. In all the cell lines the addition of hydroxyapatite had a positive effect on mitosis which resulted in a higher cell count compared to the latex bead treatment and control. In a later study by Cox et al. (2012) scratch wound assays were performed on cells treated with hydroxyapatite and controls and an increase in cell migration was found for the cell lines treated with hydroxyapatite. The same assay was performed with calcium oxalate crystals in which no effect was found. Hydroxyapatite crystals were also found to up regulate the production of a variety of matrix metallo proteinases (MMPs)(Morgan et al., 2001). MMPs are associated with degradation of the extracellular matrix and a good correlation between expression of MMPs and the invasive phenotype of tumour cells has been shown (Morgan et al., 2005).

Another indication for the role of calcifications in breast disease is given by a study by Vestergaard (2011) which reported a decreased risk of breast cancer among patients given bisphosphonates. In medicine bisphosphonate medication is used as drugs for various diseases of bone, tooth, and calcium metabolism.

Cox et al. (2012) investigated the effect of several factors on the 4T1 mineralising breast cell line. Inorganic phosphate promotes stabilization of formed hydroxyapatite and inhibits the formation of some other calcium-containing crystals such as calcium oxalate (Terkeltaub, 2001). 4T1 cells stained positively for calcium after treatment with inorganic phosphate. Phosphonoforbic acid inhibited mineralisation with and without inorganic

phosphate. When two inorganic phosphate molecules are joined by an ester bond, inorganic pyrophosphate is formed which is a known inhibitor mineral deposition and growth (Fleisch, 1998; Thouverey et al., 2009). Inorganic pyrophosphate did not have an effect on the 4T1 cell line (Cox et al., 2012). The ratio of pyrophosphate to phosphate is interlinked with alkaline phosphatase which hydrolyzes phosphate esters. Alkaline phosphatase is suggested to have an important role in the calcification formation mechanism (Bonucci, 2007) and was found to enhance 4T1 cell mineralisation (Cox et al., 2012). Levamisole is a known inhibitor for alkaline phosphatase (Cox et al., 2012). Other regulators in breast calcification formation are osteonectin, bone sialoprotein II and osteopontin (OPN) which are all bone matrix proteins expressed by human breast cancer cells (Bellahcène and Castronovo, 1997, 1995; Pampena et al., 2004). Cox et al. (2012) also evaluated the role of OPN on the 4T1 cell line. Similar to the addition of pyrophosphate to the medium, the addition of OPN did not have an effect on the cell line. There was however an increase in OPN mRNA in the 4T1 cell line grown in osteogenic cocktail.

The experiments done by Cox et al. (2011; 2012) resulted in the mammary mineralisation mechanism shown in figure 1.11. Betaglycerophosphate (β G) of the osteogenic cocktail in which the cell line is grown is hydrolysed to glycerol (G) and phosphate (Pi) by alkaline phosphatase (ALP). Phosphate is then transported into the cell and apatite is formed by combining calcium and phosphate in the cell. ALP mRNA is up regulated and the formed apatite enters the extracellular matrix. Pyrophosphate (PPi) acts as an inhibitor of apatite formation, but the increased ALP may result in PPi hydrolysis to Pi, which can be incorporated in the apatite. OPN is also an inhibitor but does not affect an effect on the 4T1 cell line which might be due to the ALP taking of a phosphate group and thus making it inactive. The apatite crystals in the extracellular matrix enhance the proliferation and migration of the surrounding cells.

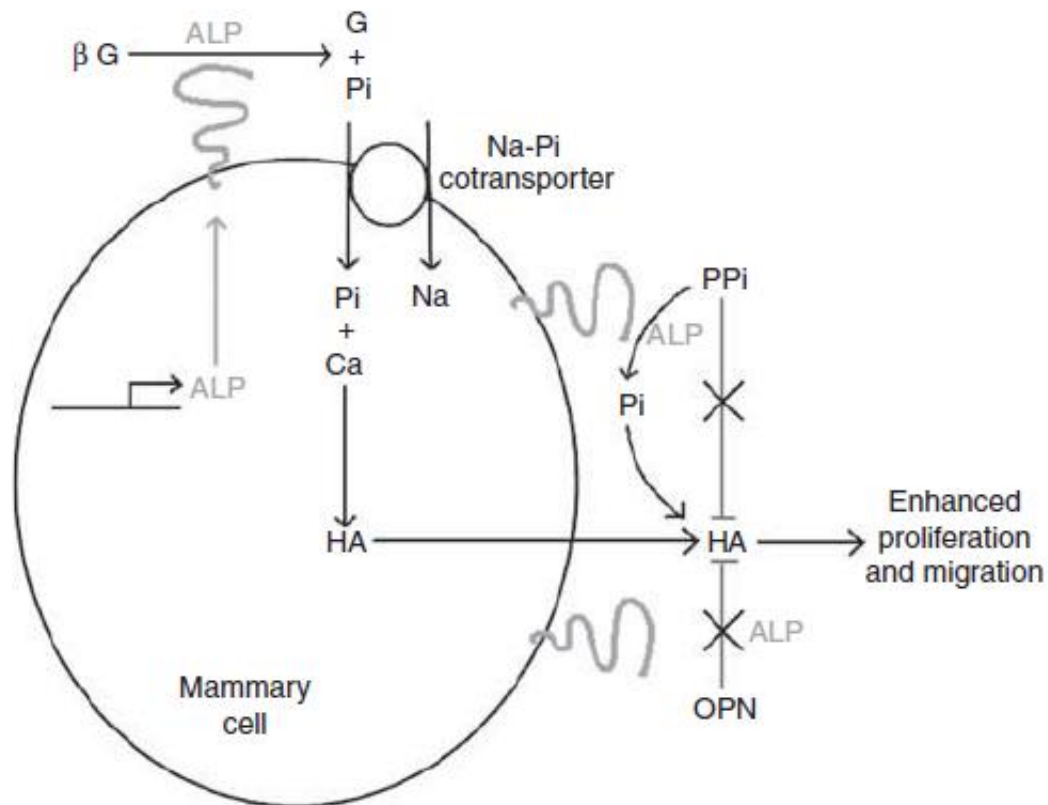


Figure 1.11: Mammary mineralisation model proposed by Cox et al. Betaglycerophosphate (βG) of the osteogenic cocktail is hydrolysed to glycerol (G) and phosphate (Pi) by alkaline phosphatase (ALP). Pi is transported into the cell and apatite is formed and up regulation of ALP mRNA takes place. Hydroxyapatite enters the extracellular matrix. Pyrophosphate (PPi) acts as an inhibitor of apatite formation, but the increased ALP may result in PPi hydrolysis to Pi , which can be incorporated in the apatite. Osteopontin (OPN) is also an inhibitor but ALP may take of a phosphate group whereby making it inactive. The apatite crystals in the extracellular matrix enhance the proliferation and migration of the surrounding cells (Cox et al., 2012).

1.3.2 Carbonate incorporation in apatites and its relationship to disease

Biological apatites are usually described as carbonate substituted hydroxyapatite. Research by Haka (2002) using principal component analysis (PCA) indicated that further subtle differences could be found between type II calcifications associated with benign and malignant tissue. Benign proliferative lesions have shown to have type II calcifications with higher carbonate levels than the more pure hydroxyapatite (HAP) crystals found in malignant lesions.

Chapter 1

A recent infrared study performed by Baker et al. (2010) confirmed that the correlation between carbonate substitutions of type II calcifications (and therefore the chemical composition) and different types of breast lesions is very strong. In this study 236 calcifications on paraffinised pathology samples were measured (10 μm thickness mounted on calcium fluoride). These were separated into three groups; invasive (n=112), *in situ* (n=64), and benign (n=60). These three groups within the cancer spectrum could be separated from each other by the percentage of carbonate substitution and the amide to phosphate infrared band intensity ratio (figure 1.12).

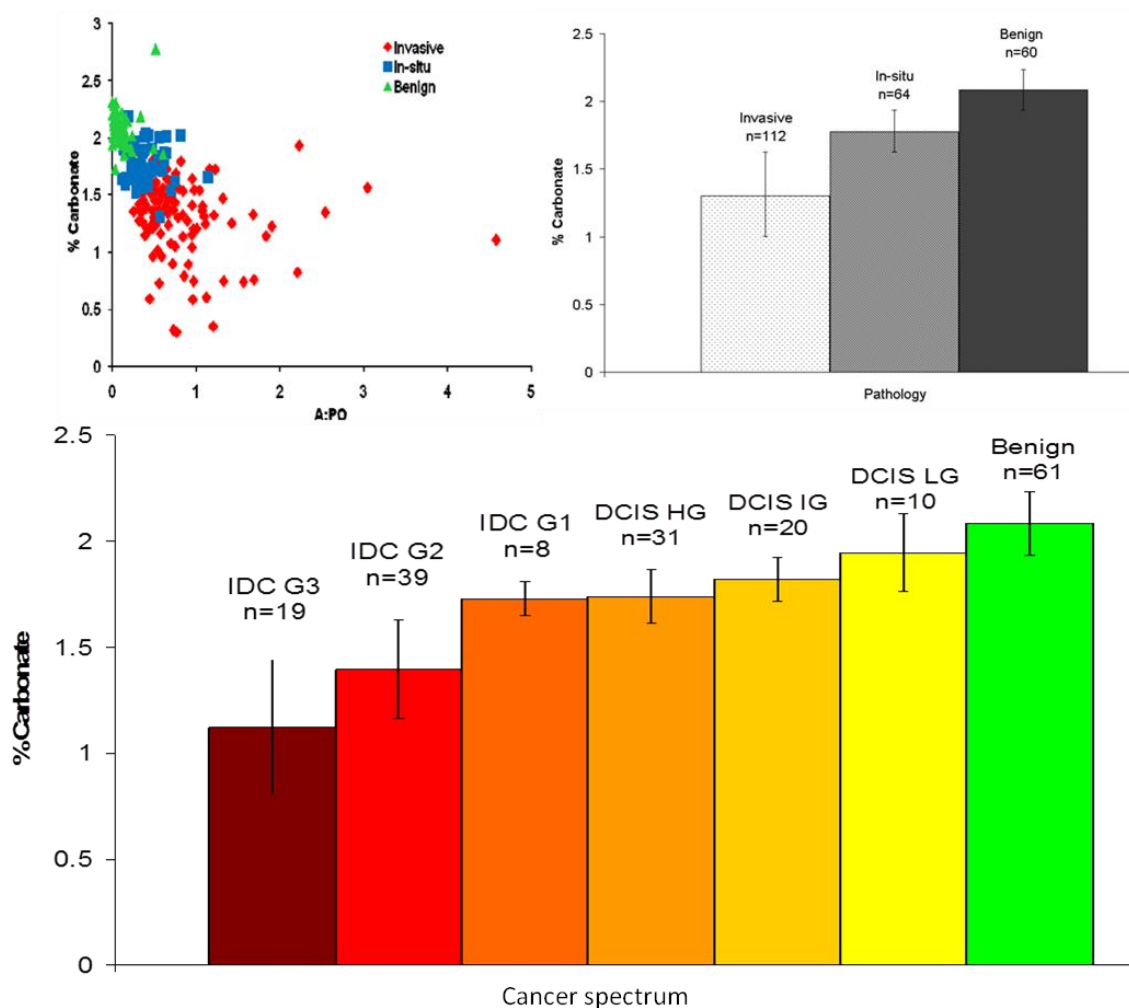


Figure 1.12: Relationship between the different pathology groups and the carbonate percentage (Baker et al., 2010).

Substitution in the apatite lattice slightly changes the structure and often has critical effects on mineral properties such as hardness, strain, crystal size and

dissolution rate. The apatite in bone (7 wt% CO₃) is amenable to dissolution, whereas the slightly different apatite in enamel (3.5 wt% CO₃) resists dissolution (Wopenka and Pasteris, 2005).

Carbonate can be incorporated in the apatite lattice (Ca₁₀(PO₄)₆(OH)₂) in several ways;

- A-type: the hydroxygroup is substituted by carbonate (Peroos et al., 2006)
- B-type: the phosphate group is substituted by carbonate (Peroos et al., 2006)
- L-type (labile); the CO₃²⁻ is within the surface hydration layer of the apatite crystals (Wopenka and Pasteris, 2005)

A representation of the apatite lattice and the apatite lattice with A-type and B-type substitution is given in figure 1.13. The location of substitution is indicated with a black circle.

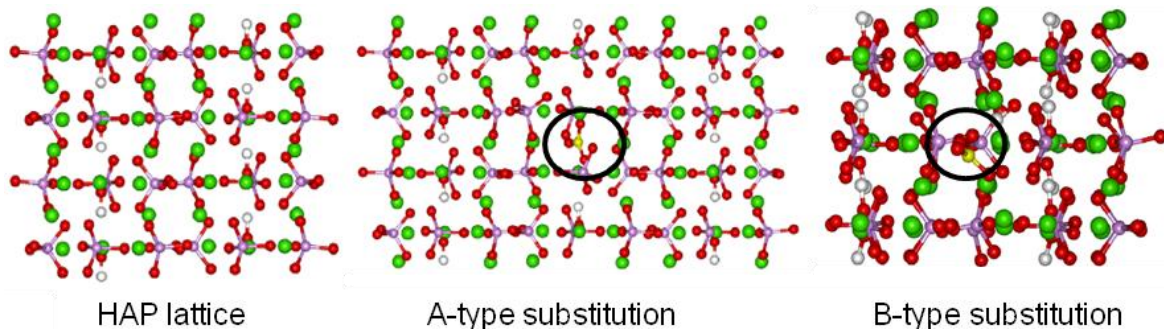


Figure 1.13: Incorporation of carbonate in the HAP lattice. The location of the carbonate substitution is indicated with a black circle. Oxygen atoms are depicted in red, calcium in green, phosphorus in pink, hydrogen in white, and carbon in yellow. (Peroos et al., 2006).

Synthetic and high-temperature apatites often contain A-type defects or a mixture of A- and B-type defects in their lattice. Since the synthesis of A-type carbonated substituted apatites in industry requires high temperatures, it was always thought that apatites in breast tissue (and more general biological apatites) mostly type B would be observed (Baker et al., 2010; Nishino et al., 1981). Although A-type substitution in biological apatites has previously been considered negligible (Wopenka and Pasteris, 2005), more recent studies by

Fleet and Liu (2007) indicate that biological apatites are Na-bearing A-B carbonate apatites, with significant B-type substitution. Calculations of Peroos et al. (2006) showed that type A is the most stable defect structure, but that the B-type defect is also energetically feasible. In a study by Shimoda et al. (1990) a link was found between pH and the type of carbonate inclusion. Apatites were prepared in aqueous systems with a pH of 7.5 or 10.5 at 80°C. At neutral pH the carbonate was incorporated at both the A- and B-positions, while at the alkaline pH the carbonate was only included as B-type.

1.4 The use of vibrational spectroscopy to detect breast calcification and cancer

Probing microcalcifications with Fourier transform infrared (FTIR) can give insight in the disease status of the surrounding tissue (Baker et al., 2010). FTIR is a form of vibrational spectroscopy.

1.4.1 Vibrational spectroscopy

In vibrational spectroscopy, typically, the periodic oscillations of atoms within a molecule (or lattice oscillations) are probed by the absorption (i.e. FTIR spectroscopy) or inelastic scattering of photons (i.e. Raman spectroscopy).

1.4.1.1 FTIR

In an infrared experiment a range of (infrared) frequencies are directed onto the sample and absorption occurs where the energy of the incident radiation matches that of a vibrational mode of the molecule of the sample. The loss of photons from the incident beam after the interaction with the sample is then monitored at different spectral components. Infrared spectroscopy can be done in either transmission (beam passes through the sample), reflection (beam is reflected from the sample), or transflection mode (beam passes through the

sample, is reflected from the substrate, and then passes back through the sample). Water strongly absorbs in the IR fingerprint region, which is why it is not typically possible to apply IR directly *in vivo*. (An exception is NIR which is monitoring overtone and combination vibrational modes which are much weaker.)

FTIR imaging is however a valuable technique to examine the chemical composition of pathology slides on a microscopic scale for its high chemical specificity and high sensitivity. However, work to date has been severely limited by the spatial resolution of the benchtop systems used to study the interface between the calcifications and the breast tissue. To improve spatial resolution synchrotron FTIR can be used to a better effect.

1.4.1.2 Synchrotron IR

In a synchrotron facility, intense beams of lights are produced by accelerating electrons along a circular trajectory (e.g. several tens or hundreds of meters). Synchrotron light is typically 100 – 1000 times brighter than a conventional source and the brightness of the source allows small regions to be probed with an acceptable signal to noise ratio (SNR). Using a synchrotron source instead of a conventional source radically improves the spatial resolution (Miller and Smith, 2005). In figure 1.14, an aerial photo of the Diamond Light Source (Oxfordshire, UK) is shown where part of the synchrotron work described in this thesis was performed.



Figure 1.14: Photo of the Diamond Light Source (www.diamond.ac.uk, accessed 7 December 2010).

The FTIR beam line at Diamond uses conventional confocal arrangements with apertures and a single point collection. When using this type of setup, the aperture dimension determines the spatial resolution (Hirschmugl and Gough, 2012). Apertures only deliver diffraction-limited resolution when the wavelength of the light is larger or equal to the aperture. When a small aperture is used, the signal for the longest wavelengths is below the detection limit since the signal is reduced over the bandwidth. On the other hand, when a larger aperture is chosen the spatial resolution for the shorter wavelengths is sacrificed. The trade off between spatial resolution and SNR may result in long acquisition times (Hirschmugl and Gough, 2012). At the IRENI beamline (Synchrotron Radiation Center, University of Wisconsin, USA), where some measurements presented in this thesis were also performed, a wide field approach is used.

1.4.1.3 Attenuated total reflection (ATR) FTIR

Another way to improve spatial resolution in z-direction (depth) in FTIR is to use attenuated total reflection (ATR). ATR is a form of FTIR in which a higher spatial resolution is obtained by employing a crystal with a higher refractive index than the material that is investigated; commonly used are germanium, silicon, diamond, and zinc selenide with refractive indexes of 4.00, 3.41, 2.41, and 2.40, respectively (Griffiths and De Haseth, 2007). When the angle of incidence is larger than the critical angle total internal reflection takes place. Part of the light penetrates into the sample, the evanescent wave. The penetration depth depends on the wavelength of the light, the incidence angle, and the refractive indexes. Because the penetration depth is independent of the sample thickness, ATR is a suitable technique to measure samples with strong water contributions (Kazarian and Chan, 2006). Due to the wavelength dependence the ATR spectra differ from transmission spectra; the intensity at the high wavenumber end of the spectra is typically lower due to a shorter penetration depth.

1.4.1.4 Raman Spectroscopy

In contrast to FTIR, Raman spectroscopy is based upon inelastic scattering. When light is shone on a sample it can be transmitted, absorbed, or scattered. Most of the scattered light is scattered elastically (no energy is exchanged between the incident photon and the sample) which means the scattered light has the same energy (and therefore wavelength) as the incident light. However, typically, one out of every 10^9 scattered photons or less is shifted inelastically to a longer wavelength (Stokes, the photon transfers a portion of its energy to the sample activating typically a molecular vibrational motion or phonon (crystal lattice) vibration) or to a lower wavelength (anti-Stokes, the photon gains energy from already active vibrational or lattice motion in the sample) as a result of interaction with sample. This effect is called Raman scattering, named after C.V. Raman who first reported the effect (Raman and Krishnan, 1928). On the

theoretical side, the Raman effect was already predicted earlier by Smekal (1923).

During a Raman experiment the incident photons typically raise the energy state of a molecule (the Stokes process) to a so-called 'virtual state' (figure 1.15). This is not a stationary state in a quantum mechanical sense but merely a distortion in the electron distribution. A resonant variant of the Raman scattering process exists with a hugely enhanced probability of the Raman scattering (resonance Raman spectroscopy) where a real electronic absorption state of the molecule coincides with the incident photon energy. This process is however not used in the studies described due to associated absorption and consequently limited penetration depth and therefore not further discussed.

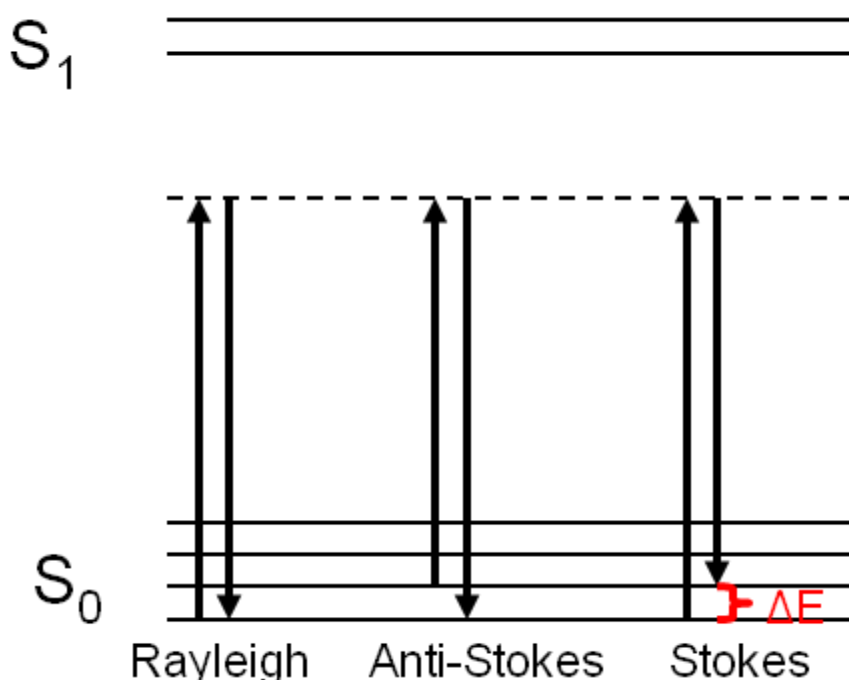


Figure 1.15: The principle of Raman scattering. S_0 and S_1 correspond to the two lowest electronic states. After excitation (\uparrow), the scattered photon (\downarrow) can have an energy similar (Rayleigh), higher (Anti-Stokes), or lower (Stokes) than the incident photon.

The shift in wavelength (Raman shift) is normally given in wavenumbers (cm^{-1}) and directly related to the frequency of the activated mode within the molecule. The frequencies of the modes are highly specific of the chemical constitution. Therefore, molecules can be identified by their spectral pattern, 'Raman

‘fingerprint’. Raman mapping combines spatial information (from the microscope) with spectral information. This spectral information can then be used to derive chemical information and the location of individual sample constituents.

1.4.2 Infrared spectroscopy on calcifications

Baker et al. (2010; 2009) extensively studied breast calcifications in pathology slides with FTIR. As mentioned earlier, Baker et al. (2010) reported a significant correlation between the chemical composition (carbonate content and protein/mineral ratio) of microcalcifications and the pathology grade of the surrounding tissue. Representative spectra for calcifications in tissue with different pathology, benign, *in situ*, and invasive breast disease, are shown in figure 1.16.

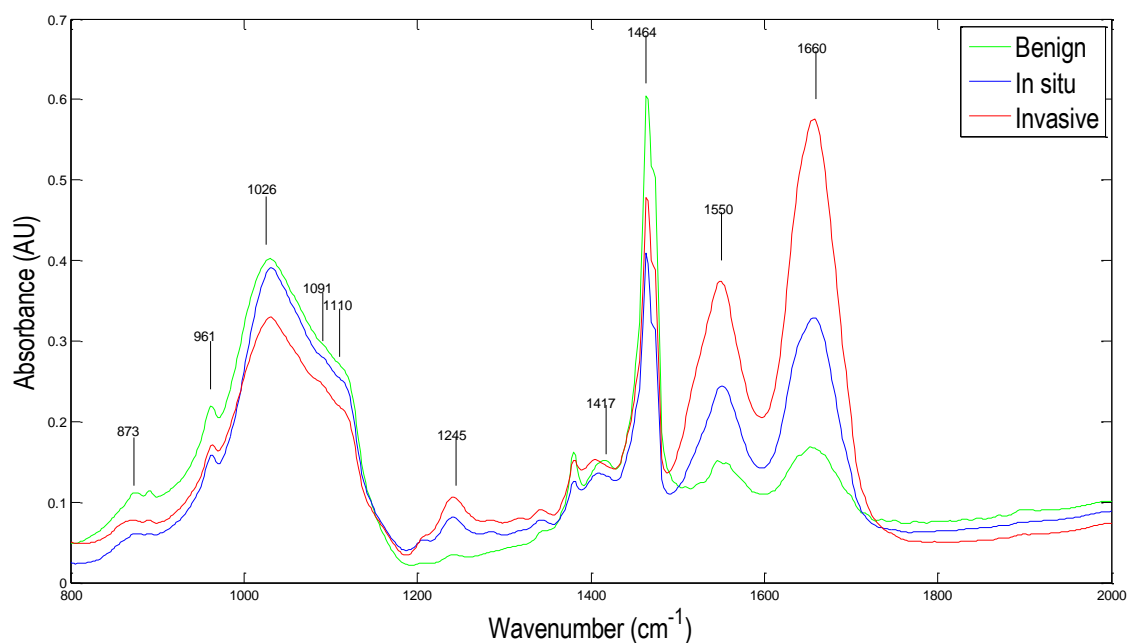


Figure 1.16: Average FTIR spectra of calcifications from samples with benign, *in situ* and invasive pathology, figure modified from (Baker, 2009).

All breast calcifications show a strong band around 1026 cm^{-1} (phosphate) with shoulders $\sim 1091\text{ cm}^{-1}$ and $\sim 1110\text{ cm}^{-1}$. Furthermore bands can be found $\sim 1550\text{ cm}^{-1}$ (amide II protein) and $\sim 1660\text{ cm}^{-1}$ (amide I protein) for all groups, although the intensity differs with pathology. The strong bands around 1464 cm^{-1} and

Chapter 1

1472 cm^{-1} are due to paraffin. Weaker bands can be found in the 870-880 cm^{-1} region (carbonate), ~961 cm^{-1} (phosphate), ~1245 cm^{-1} (amide III), and ~1417 cm^{-1} which is ascribed to carbonate.

A study by Eckel et al. (2001) found that the amide bands in spectra of breast tissue change with pathology. Other FTIR studies evaluate calcified materials such as synthetic standards (Apfelbaum et al., 1992; Fleet, 2009; Gadaleta et al., 1996a, 1996b; Rehman and Bonfield, 1997; Ślósarczyk et al., 1997), urinary stones (Estepa and Daudon, 1997; Maurice-Estepa et al., 2000; Volmer et al., 1993; Wilson et al., 2010), and mineralised tissues (Boskey and Mendelsohn, 2005) such as bone and enamel (Aydin et al., 2011; Miller et al., 2001; Rey et al., 1991a, 1991b).

A synchrotron FTIR study consisting of three maps on frozen breast specimens was performed by Baker (2009). In this study, a lower concentration of amide I and amide II was found in the calcified tissue than in the surrounding tissue. Dessombz et al. (2011) published a synchrotron FTIR study on kidney calcifications.

Both Rehman et al. (2010) and Walsh et al. (2012) performed an ATR study on breast tissue. Increased spatial resolution and reduction of scattering artefacts were reported, but clinical applications are limited due to the required physical contact with tissue and the limited sampling area. When studying bone, Furedi and Walton (1968) found that the mineral component of bones in whole bone sample could be studied without further sample pre-treatment. Gulley-Stahl et al. (2009) used ATR for quantitative analysis of kidney stones which flagged up an important problem using ATR for calcified materials. Linear calibration curves could only be obtained if the particle sizes of the analytes were comparable and considerably less than the sampling area of the ATR crystal. The particle sizes of hydroxyapatite and calcium oxalate monohydrate were measured to be 76 and 20 μm , respectively (Gulley-Stahl et al., 2009).

A detailed list of IR bands in mineralized materials and their assignments can be found in appendix A.

1.4.3 Raman spectroscopy on breast calcifications

It has been shown that type I and type II calcification can be separated with Raman spectroscopy in both fixed tissue samples (Haka et al., 2002) and freshly excised needle biopsy cores (Saha et al., 2011). Baker (2009) performed a Raman mapping study on two areas of a frozen breast tissue sample which indicated protein was present at low concentration in the calcification region compared to the surrounding tissue.

Raman studies with different excitation wavelengths were done by Frank et al. (1994) who found that background luminescence was significantly lower when using an excitation wavelength in the near-IR (691-830 nm used). At these wavelengths, lipid bands were more pronounced and oleic acid appears to be the main component. In a subsequent study by Frank et al. (1995), Raman spectra of normal breast specimens were compared to benign and invasive carcinoma. In this study, a different lipid/protein ratio was found for the pathology groups of which the intensity of the 1439 cm^{-1} band is a marker. The band also shifts to higher wavenumbers (1450 cm^{-1}) for invasive cancer. The intensity of the amide I band (1654 cm^{-1}) changes with the degree of unsaturated fatty acid and Frank et al. (1995) use the 1654/1439 band ratio as a marker for disease.

Shafer-Peltier et al. (2002) modelled the components of human breast tissue of different pathology grades by comparing the spectra of the specimens to chemical components. They found that the amount of fat decreases from normal breast tissue to invasive cancer; the fit coefficient was 83% and 2%, respectively. In contrast, the amount of collagen in the fit increased from normal breast tissue (1%) to invasive breast cancer (40%). Calcifications were not commonly found in their study and only played a minor role in their model. In later studies by the same group the chemical differences of both types of calcifications are probed (Haka et al., 2002), both types of calcifications are incorporated in their biochemical fitting model (Haka et al., 2005), and tested for margin assessment (Haka et al., 2006), freshly excised surgical specimens (Haka et al., 2009) and needle biopsies (Dingari et al., 2012). Deep Raman

studies on breast tissue will be discussed in the relevant technique sections in 1.5.

Most studies on carbonated hydroxyapatites (the material type II calcifications consist of) have been done on bone, dentin enamel, dentine, or synthetic materials (Penel et al., 1998, 2005; Leroy et al., 2002; Antonakos et al., 2007). It is not known to which extent these studies can be used as a basis for breast calcification studies. Spectra of similar materials are expected to be comparable due to the alike chemical composition and therefore similar vibration modes. However, the different properties of the materials indicate different chemical composition which could result in spectral differences.

Wopenka and Pasteris (2005) studied the spectral differences of four different types of apatite; a cross section of a mouse femur, human enamel, geological apatite and synthetic apatite. After exclusion of the bands characteristic for collagen, the spectra looked remarkably similar. However, when spectral regions were enlarged differences could be observed in band position, width, and intensity.

The general shape of the breast calcification spectra will be similar to that of synthetic standards. In figure 1.17, Raman spectra of synthetic standards of calcium oxalate monohydrate (green), and 0.5 (blue), and 6.0% (red) carbonate substituted HAP.

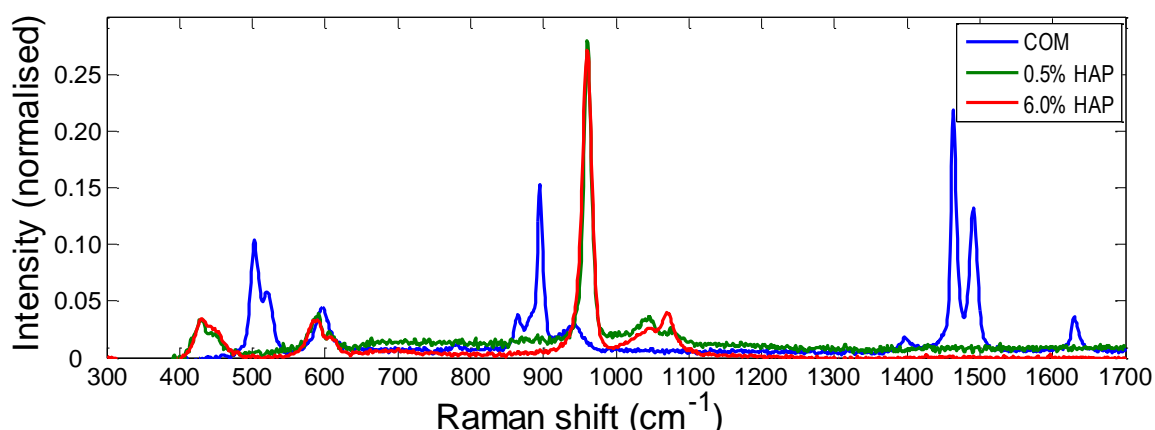


Figure 1.17: Raman spectra of calcium oxalate monohydrate and 0.5 and 6% carbonated HAP.

Calcium oxalate monohydrate (COM) is used as a model for calcium oxalate dihydrate (COD) since the latter cannot easily be obtained as a standard due to its instability (in other studies it is either freshly synthesized or obtained from crushed renal stones). The overall shape of the Raman spectra of COM and COD are very similar due to their chemical similarity. The characteristic Raman bands from COM are observed at 502, 896, 1462, 1489, and 1629 cm^{-1} , and for COD at 508, 912, 1477, and 1632 cm^{-1} (Kontoyannis et al., 1997).

The spectrum of HAP consists of a bands at 430, 448, 591, and 608 cm^{-1} , a strong peak around 960 cm^{-1} , and two broader weaker features at 1047 and 1072 cm^{-1} (Awonusi et al., 2007). The intensity of the 1074 cm^{-1} band increases with increasing carbonate substitution (Awonusi et al., 2007; Penel et al., 1997; Peroos et al., 2006). As a result, the relative intensity of that band and for example the 960 cm^{-1} band (which is a phosphate band) reveals the percentage of phosphate replaced by carbonate (COHAP). As work of Baker et al. (2010) revealed, the percentage of carbonate substitution indicates the state of the disease. Therefore the relative intensities in the spectra can be used to make an indication of the amount of CO_3 substitution, which is related to the state of disease.

An overview of characteristic Raman bands in breast tissue and calcified materials can be found in appendix B.

1.5 Utilizing deep Raman spectroscopy to detect breast calcifications *in vivo*

In order to use Raman spectroscopy for the detection of microcalcifications *in vivo* difficulties concerning depth penetration have to be first overcome, for example measuring through skin and breast tissue. Traditionally Raman is a near-surface technique (Moreira et al., 2008) and cannot be typically applied at depths on more than several hundred micrometers in tissue (Matousek and Stone, 2007). The penetration depth depends in some extent on the wavelength (Stolik et al., 2000) but the choice in wavelength is restricted by the detector

(typically CCD) sensitivity, spectral cut off, and water absorption which increases significantly above 1000 nm. The clinically relevant depth ranges from a few millimetres used for margin evaluation (Keller et al., 2009) to centimetres for probing of calcifications (Stone and Matousek, 2008).

Discrimination of signals with their origin in different layers of a turbid media can be achieved by either a temporal or a spatial approach (Matousek, 2007). With both methods, the relative signal level from the surface is suppressed which enhances the relative signal from the depth of interest (Stone and Matousek, 2008).

Temporal approaches are usually done in backscatter mode (signal collection at the same side of the sample as excitation) which means that photons arriving from greater depths have to travel a larger distance (Matousek, 2007). This will result in a time difference between signals from the surface and deeper layers (figure 1.18). Normally, time differences like these cannot be detected easily since light travels in tissue with a velocity of $\sim 2 \cdot 10^8$ m/s and the differences in distance are minimal. However, due to the diffuse scattering of tissue the path lengths are many times greater than the direct distances and the time differences larger. The time difference can be detected with state-of-the-art equipment such as picosecond Kerr gating (section 1.5.1).

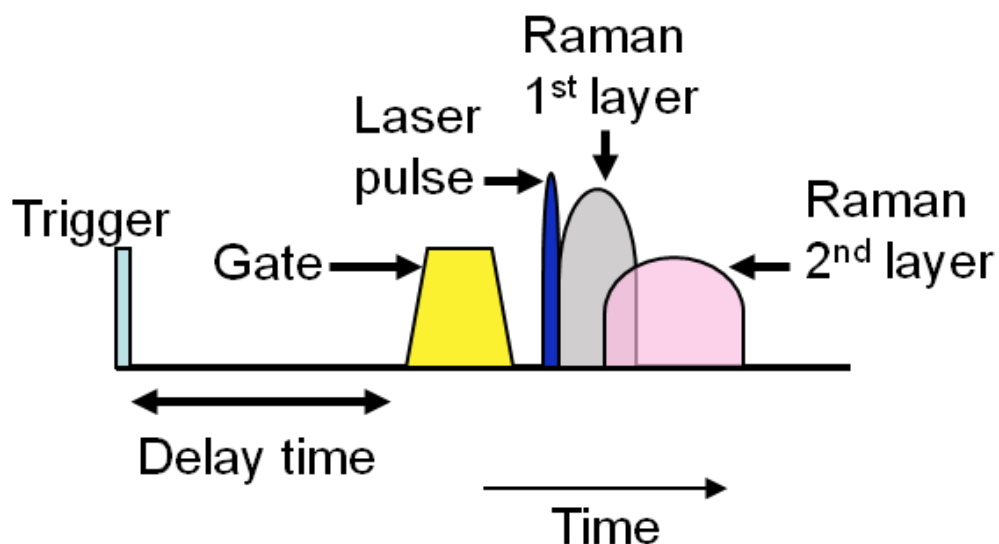


Figure 1.18: Schematic representation of a temporal approach in deep Raman. The time difference between the photons emerging from the different layers is

used by only accumulating a fraction of the time. By choosing the delay time between the trigger to start the gating and opening the gate, it is possible to selectively detect one of the signals without a large contribution from another one (Ariese 2009).

Spatial approaches (for example spatially offset Raman spectroscopy (SORS), section 1.5.2) are based on the fact that photons emerging from deeper depth are spread more sideways than photons emerging from regions closer to the surface (Matousek and Stone, 2009; Matousek, 2007). As a result, the distance between the excitation and the spot where the Raman signal is measured is related to the depth of the origin.

1.5.1 Kerr gating

Kerr gating is based upon sampling light with temporal differences from the illumination pulse. These temporal differences originate from the differences in depth where the Raman signals are originating from. As shown in figure 1.19, the setup consists of two polarisers in crossed orientation. When the gate is closed, all light from the sample is blocked and will not reach the spectrometer. However, when the gate is switched on with the gating pulse (between the polarisers, drawn in red) a transient anisotropy in the Kerr media can be set to act as a half-wave plate. The Kerr media will therefore rotate the polarisation of the Raman signal by 90° and enable it to pass through the cross polariser and reach the detector. The anisotropy is transient, lasting around 4 ps, and consequently the gate automatically closes (due to collisional randomisation of the orientation imposed on molecules of CS_2 by the intense gating pulse) after the passage of the gating pulse. By changing the time delay between the Raman excitation pulse and the gating pulse, different fractions of the Raman spectra (e.g. photons from different depths of the sample) can be measured (Baker et al., 2007; Matousek and Stone, 2009).

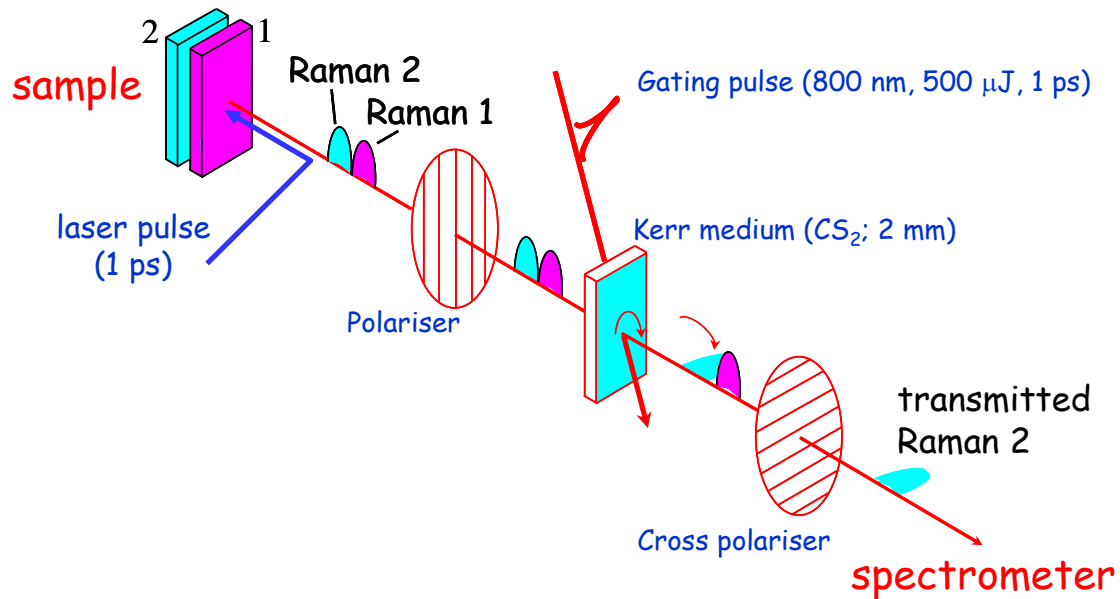


Figure 1.19: Schematic representation of the Kerr gated setup. Kerr gating is based upon temporal differences. When the 'gate' is opened, the Kerr medium acts as a half-wave plate. As a result, light can enter the spectrometer. When the gate is closed, light cannot reach the spectrometer due to crossed polarizers (Matousek and Stone 2009).

Baker et al. (2007) demonstrated that this technique can distinguish synthetic type I and type II material through a layer of both fatty and protein rich tissues. However, the 1 picosecond pulsed laser (490 nm) used combined with a 4 ps Kerr-gate (equal to resolution) was only able to measure through 1 mm of tissue. The combination of the high peak intensity and shallow depth are serious limitations to the use of this technique *in vivo*.

1.5.2 Spatially Offset Raman Spectroscopy

SORS is based upon spatial instead of temporal gating. Spatial gating is achieved by introducing a certain distance between the excitation and collection points of the Raman signals. Photons emerging from deeper areas have to travel a larger distance to the surface and on their way diffuse more sideways than photons from a shallower depth (figure 1.20).

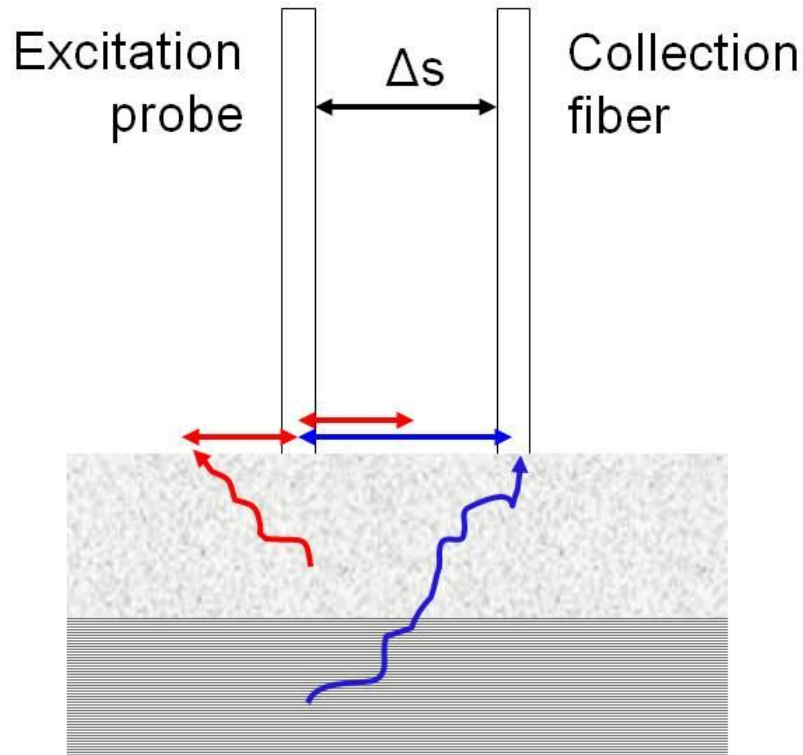


Figure 1.20: Principle of SORS. Photons with their origin deeper in the tissue will have a higher chance to travel sideways during their route towards the surface. (See for comparison red (shallow depth) and blue (deeper depth) arrow above each other) By introducing a distance between the excitation and collection it is possible to discriminate between photons from different depths.

With this concept, low power continuous wave (CW) lasers can be used instead of short laser pulses, which reduces not only the risk of photo degradation but also makes the device instrumentally much simpler and safer. In comparison to the Kerr gated work, the signal quality is typically also higher. This is a result of the fact that the spatial technique integrates scattered light across the entire time domain, unlike the temporal approach (Matousek, 2007). The SORS setup evaluated by Stone et al. (2007) could probe calcified material up to a depth of 10 mm of tissue, which is clinically considerably more relevant than a depth of 1 mm. In addition, with a small modification of the SORS technique it is viable to apply higher laser powers and achieve even higher penetration depths (figure 1.21): in contrast to the conventional SORS setup where the Raman signal is accumulated in a ring around the central excitation fibre, the excitation is within a ring (and thus the light is spread over a larger area) and the Raman signal is

collected in the centre of the ring (Matousek and Stone, 2009). This concept is termed inverse SORS.

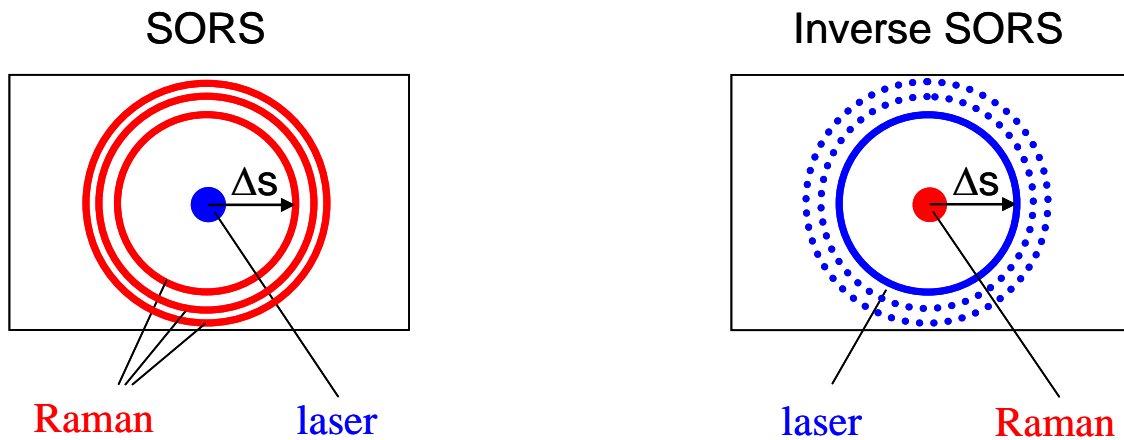


Figure 1.21: SORS and inverse SORS probe. SORS measurements are applied by exciting in the middle and collecting in a ring with offset Δs around the excitation point. In inverse SORS the excitation and collection positions are swapped around, which means excitation is in the ring and collection in the middle. In this case, the average power can be higher since the beam is spread over a larger surface (Matousek and Stone 2009).

Until recently, SORS was only used to detect strong Raman scatterers deep within tissue with a specific fingerprint (for example, microcalcifications and breast tissue have a completely different Raman spectrum) underneath a layer of soft tissue. Keller et al. (2009) recently published a proof of principle study for the use of SORS on layered soft tissue. The authors were able to detect Raman signal of a breast tumour sample based underneath normal breast tissue through up to two millimetres of soft tissue based upon the spectral differences between breast tissue and breast tumour tissue. In figure 1.22, Raman spectra of an experimental run are given. The top spectrum is the pure tumour spectrum and the bottom spectrum a characteristic breast tissue spectrum. The spectra in between are measured on different distances from the excitation fibre and the light grey boxes indicate the spectral regions used for discrimination. In contrast to previous studies (Frank et al., 1995) not the intensity of the 1439 cm^{-1} band is used for the lipid to protein ratio but the ratio of the 1303 to 1265 cm^{-1} band. In a later study (Keller et al., 2011) a SORS probe with multiple offsets was designed and tested.

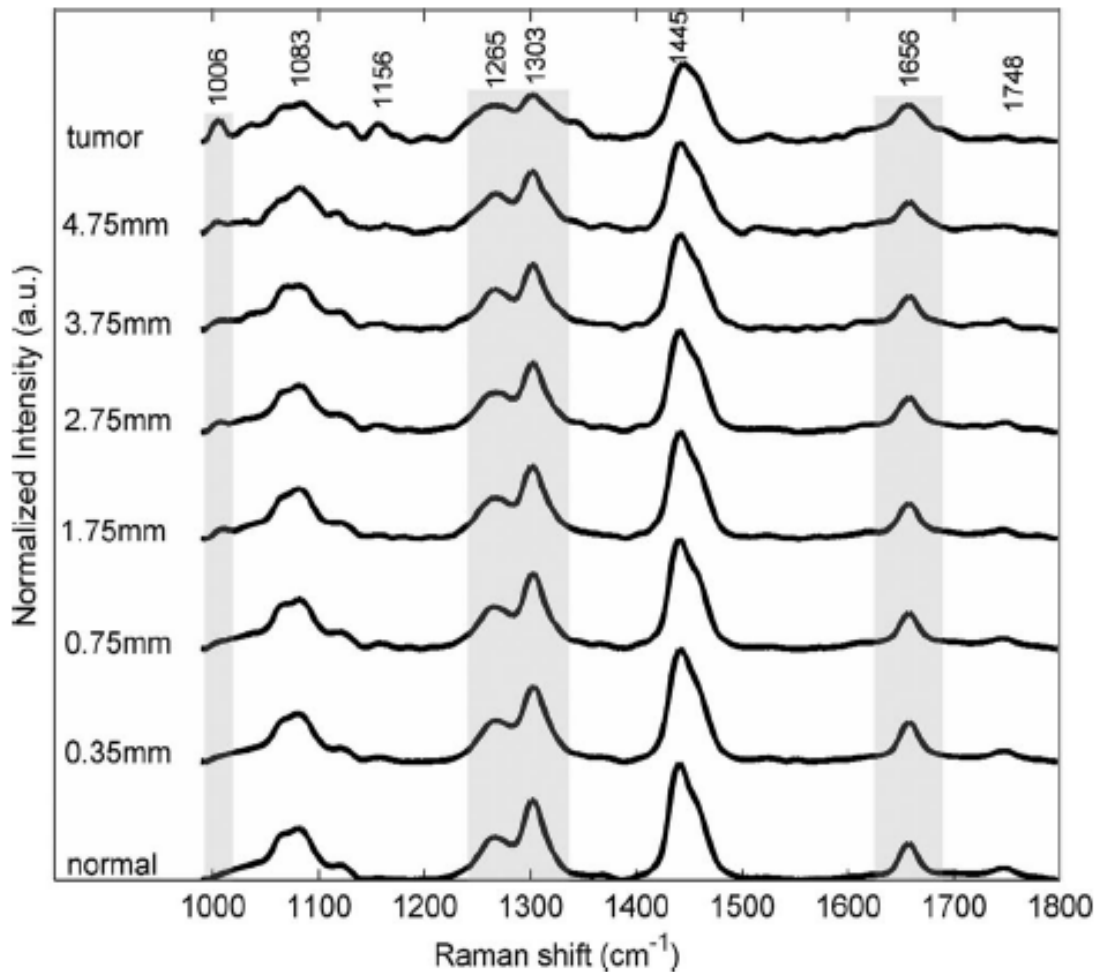


Figure 1.22: Raman spectra SORS experiment of 0.5 mm normal breast tissue layer with tumour underneath (Keller 2009). The main changes in the spectra are highlighted in grey.

1.5.3 Transmission Raman

Transmission Raman can be considered to be an extreme form of SORS in which the signal is not collected in backscatter mode, but at the other side of the tissue - in transmission mode. In this orientation, the overall bulk content is measured instead of an individual layer or microstructure of sample (Matousek, 2007). This issue is illustrated, by figure 1.23 in which the transmission Raman setup used in this thesis is depicted with a breast phantom. The phantom is a triple modality biopsy training phantom (18-229, Imaging Equipment Ltd, Bristol,

UK). Models like this are normally used for needle biopsy training and can be imaged with mammography, MRI, and ultrasound imaging.

The phantom is opaque when it is not illuminated by the laser (upper panel). In the lower panel the same breast phantom is shown during five minutes of illumination (5 minutes shuttertime, ISO 1600, $f=2.8$) and it can be seen that the light travels through the whole of the breast phantom although the transmission Raman signal has shown to have a moderate bias toward the centre of the sample, diminishing outward toward each face (Matousek et al., 2011).

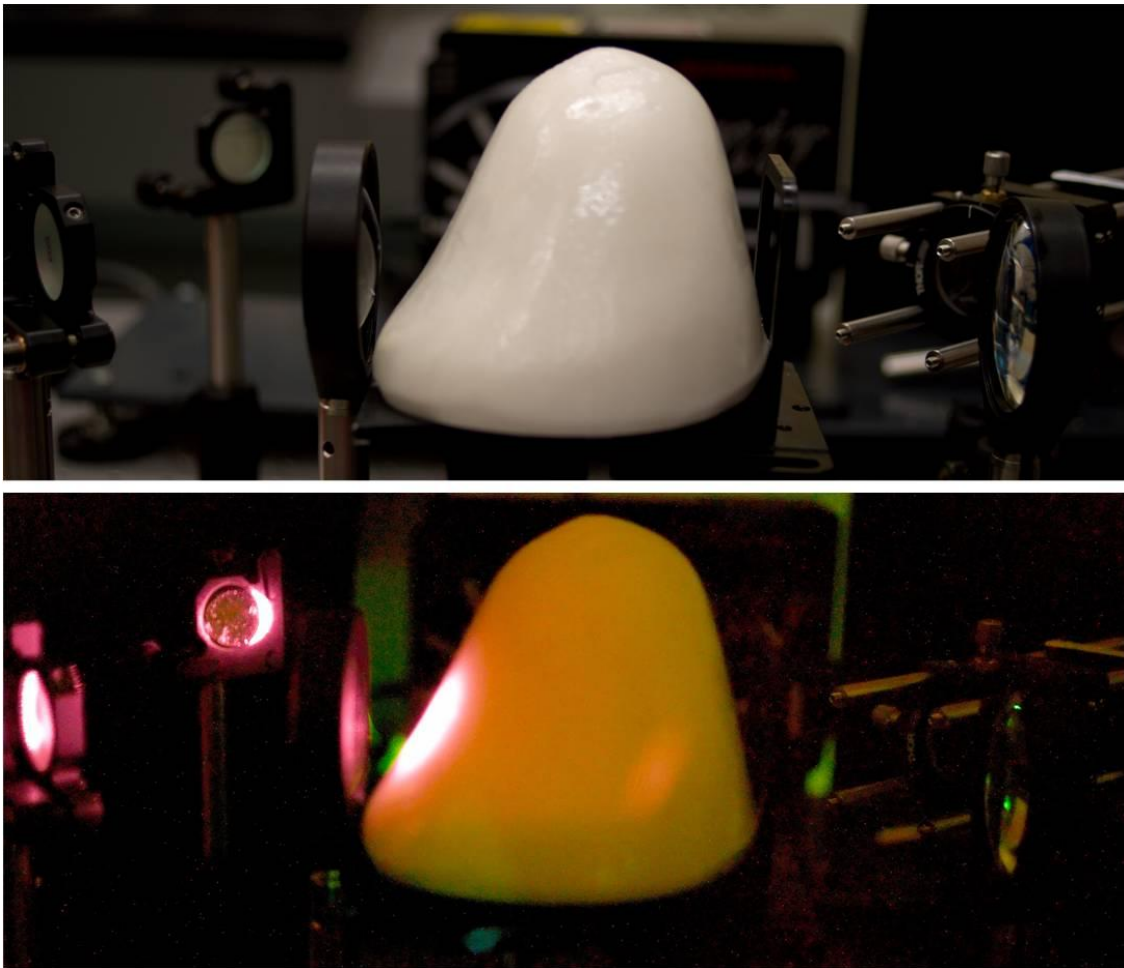


Figure 1.23: Transmission setup with breast model. Upper panel) Not illuminated, Lower panel) When illuminated by laser scattering can be seen in the whole of the breast (Photography by Hans van Schoot).

Stone and Matousek (2007) demonstrated that calcified material at a depth of up to 16 mm in chicken tissue could be detected with transmission Raman, which was about twice the depth that could be achieved with SORS. Only one

year later, with an improved methodology, (Stone and Matousek, 2008) calcified material within mammalian tissue could be detected through 27 mm with transmission Raman. Furthermore, they were able to detect a clinical relevant calcification concentration levels (0.125% volume density ratio HAP, approximately 0.14% relates to benign and 0.05% to malignant) through 20 mm of porcine tissue.

1.5.4 Surface Enhanced Raman scattering (SERS) combined with SORS (SESORS)

The main challenge of Raman spectroscopy, and especially deep Raman, is its low intensity. Only one of every 10^9 photons is typically scattered inelastically. Raman signals can be dramatically improved by using surface enhanced Raman scattering (SERS). The exact mechanism behind SERS is still being discussed although SERS was already observed in the 1970's (Fleischmann et al., 1974). However, it is widely accepted that the major mechanisms are both electromagnetic and chemical enhancement due to interactions with the roughened metal surface (Lin et al., 2009). Electromagnetic enhancement takes place when the exciting radiation interacts with the surface electrons to form a plasmon, a quasiparticle resulting from the quantisation of plasma, essentially an oscillating electron wave on the surface (McNay et al., 2011). Chemical enhancement is sometimes called charge-transfer enhancement because the analyte is bound to the metal surface to form a charge-transfer complex. It is generally acknowledged that the electromagnetic enhancement is typically much larger than the chemical enhancement.

An enhancement factor up to 10^6 or more can be achieved for silver, copper, and gold nanoparticles. Also other metals such as aluminium and a range of transition metals are reported to obtain the surface enhanced Raman effect but these give lower enhancement (Ren et al., 2007). Disease specific signals can be achieved by using specific antibodies to target molecules. This approach is

not entirely non-invasive as it relies on introducing metal nanoparticles into the tissue.

By combining SERS and SORS (SESORS) the SERS signals can be read from deep areas of tissue directly. The first experimental demonstration of SESORS was recently published by Stone et al. (2010). The concept was demonstrated through 25 mm of mammalian tissue in Raman transmission geometry. Disadvantages of this approach include the requirement for injection of metal nanoparticles into tissue and yet unanswered issues about their toxicity. In a later study by Xie et al. (2012) experiments were performed with a tag (bisphosphonate) specific for calcium hydroxyapatite.

1.6 Summary and outlook

Microcalcifications in the breast are related to breast disease. Type I microcalcifications (COD) are mostly present in benign breast disease, while type II calcifications (HAP) are mostly present in proliferative lesions including carcinoma. It has been shown that the level of carbonate substitution in HAP is related to the pathology of the surrounding tissue.

Mammography cannot reliably distinguish between type I and type II calcifications. Raman spectroscopy has the ability to distinguish both types, but is originally a (sub)surface technique. In contrast, Raman spectroscopy has such inherent capability but until recently it could only be applied to the surface or near surface of the specimen of interest. With the introduction of deep Raman techniques there is the potential capability of identifying the lesion type from outside the breast non-invasively. A new generation of non-invasive methods for diagnosis based around transmission Raman and SORS (both deep Raman techniques) have a potential to reduce large numbers of normal biopsies, reduce the time delay between screening and diagnosis and therefore diminish patient anxiety.

The aim of this PhD project is to explore the mechanism of calcification formation, the disease specific composition, and the biochemical interface of the

calcification and the tissue. The ultimate goal is to turn this knowledge into a clinical tool based on deep Raman spectroscopy (especially SORS and transmission Raman) to detect breast disease in vivo and thus reduce the amount of false negatives (which result in a high biopsy rate) and patient stress. An overview of the deep Raman approach and how this could be incorporated in the NHS breast screening programme can be found in figure 1.24.

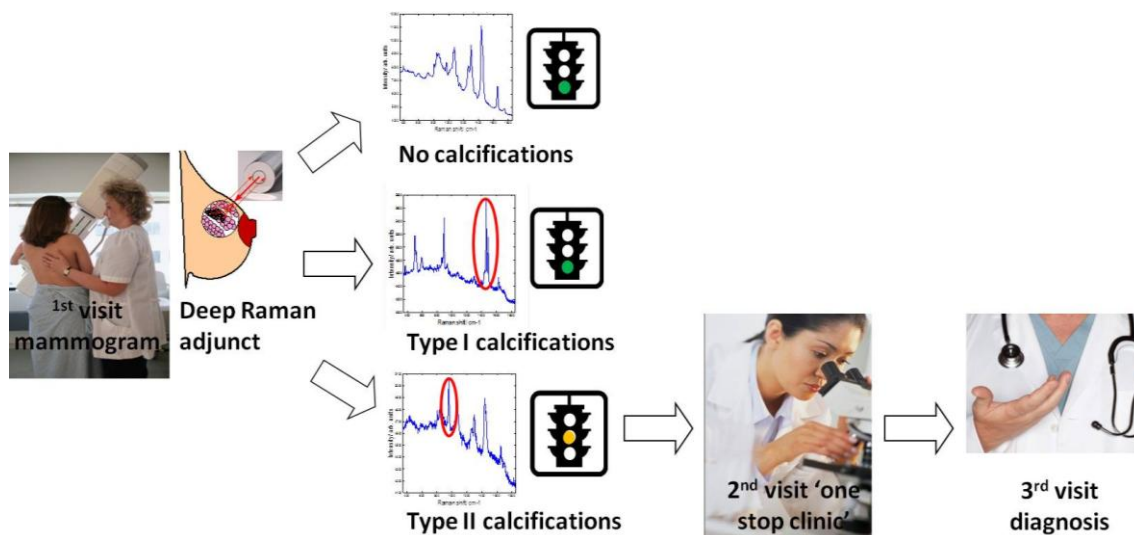


Figure 1.24: Time line of the current screening programme (in case an abnormality is detected) and where a deep Raman approach would fit in.

1.7 Aims and objectives of the study

All work in this thesis can be divided into three categories; 1) study of breast calcifications, 2) study of deep Raman techniques, and 3) deep Raman on breast calcifications. In the first category the following aims are explored: calcification formation, disease specific composition, and biochemical interface of the calcification and the tissue. The other two sections will evaluate the development of a clinical tool for breast cancer diagnosis based around deep Raman spectroscopy.

1) Study of breast calcifications (chapter 3)

- Study known calcification standards to understand the relationship between chemical differences and spectral differences (section 3.1).

Chapter 1

- Infrared experiments (3.1.1)
 - Raman experiments (3.1.2)
 - Compare spectroscopic techniques (FTIR & Raman) to von Kossa (VK), Alizarin Red (AR), and H&E staining to understand how well spectroscopic techniques pick up calcifications in pathology samples (3.2).
 - Detailed mapping of calcifications and surroundings with synchrotron FTIR (section 3.3). Also, an ATR FTIR study is shown (3.4) and a preliminary Raman mapping study (3.5).
- 2) Deep Raman system evaluation (chapter 4)
- To build a deep Raman setup which can be used for proof of principle studies (2.2.5).
 - To evaluate the performance of the system in clinical use by evaluating
 - Sample thickness (4.2)
 - Lateral spreading of Raman signals (4.3)
 - Originating depth of the Raman signals (4.4)
 - Measurements through skin (4.5)
- 3) Deep Raman spectroscopy on breast calcification (chapter 5)
- To test whether the amount of carbonate substitution of calcification standards can be evaluated through tissue (5.1).
 - To detect calcification standards buried in human breast tissue (5.2).
 - To measure fresh human breast tissue with deep Raman system and compare findings with X-ray images of the sample to evaluate detection of microcalcifications (5.3).

2 Materials and methods

2.1 Materials and sample collection

2.1.1 Calcification standards

Standards of 0.5, 1.4, 2.0, 2.3, 3.5, 6.0, and 11.0% COHAP (defined by manufacturer ($\pm 1\%$) with FTIR) were obtained from Clarkson Chromatography (South Williamsport, PA, USA). Calcium carbonate and amorphous calcium phosphate was provided by Prof. Keith Rogers. Calcium oxalate monohydrate was obtained from Aldrich.

Prof. Mary Tecklenburg (Central Michigan University) kindly supplied samples with different amounts and types of carbonate substitution which was monitored with Raman, FTIR, and elemental analysis. The following samples were supplied: type A carbonate substituted apatite (4.4 wt% A-type, 0.6 wt% B-type), AB carbonated apatite (4.3 wt% A-type, 2.1 wt% B-type), and 0.2, 1.1, 2.0, 2.3, 3.5, 5.7, 7.7, and 10.3 wt% B-type substituted apatite.

All samples were used without further sample pre-treatment, except during the IR Diamond experiments and the dilution series for which KBr tablets were pressed. For the diamond experiments 1 wt% tablets were pressed and for the dilution series 0.3, 0.7, 0.8, 1.3, 1.8, and 2.2 wt%.

2.1.2 Pathology slides for (synchrotron) FTIR mapping

Specimens were stored from patients who had undergone biopsy for mammographically suspicious breast lesions at Gloucestershire Royal Hospital between 1996 and 2007. Specimens that were known to contain calcifications, from histopathology reports, were retrieved from storage. Mammographic reports would have been more appropriate, since it is mammographically visible calcifications we are interested in. Unfortunately, mammographic data was not

Chapter 2

available. It should be noted that the resolution of histology for calcification detection is higher than that of mammography.

The paraffin-set biopsy blocks were microtomed to 10 μm thickness and mounted onto calcium fluoride windows (CaF_2) with a thickness of one millimetre (Crystran Ltd, Poole, UK) for the first beam time allocation (Diamond, SM6123).

Four types of substrates were obtained from Crystran Ltd to test for further experiments: calcium fluoride (1mm thickness), barium fluoride (0.5mm), zinc sulphide (0.4mm), and zinc selenide (0.5mm). From these samples the transmittance was measured over the wavelength area of interest.

All the subsequent synchrotron work (SM6605 Diamond synchrotron and direct access IRENI beamline) was carried out with tissue samples microtomed to 6 μm thickness mounted on 0.5 mm barium fluoride windows (Crystran Ltd, Poole, UK).

An ethical approval for this study was obtained from the Gloucestershire Local Research Ethics Committee (GLREC).

2.1.3 Stained pathology slides

Contiguous sections of twelve samples selected for synchrotron work, benign ($n=3$), *in situ* ($n=4$), and invasive breast disease ($n=5$), were stained with H&E, AR, and VK by the pathology department of the Gloucestershire Hospitals. As discussed in chapter 1, H&E stains the cell nuclei purple and the surrounding tissue a range of orange hues.

AR stains specific minerals, a complex with calcium needs to be formed in order to stain. AR forms a salt with calcium and the polarizing effect of the calcium ion results in the colour change (Puchtler et al., 1969). AR staining is affected by the pH of the solution used. Calcium oxalate crystals stain with AR at a pH of 7.0, but not at a pH of 4.2 (Proia and Brinn, 1985). AR staining was performed at a pH of 4.2, which will positively stain apatites red.

VK staining localizes calcium deposits indirectly, it stains the counter ions; normally carbonate or phosphate (Kumar and Kiernan, 2010). For the VK staining, van Gieson was used as a counterstain. The optimal pH for hydroxyapatite is between pH 4.0 and 6.0 (Shoji, 1993). During VK staining calcium cations are replaced by silver, the silver salts are reduced by a light reaction and calcified material is blackened out (Kumar and Kiernan, 2010).

Ethical approval for this study was obtained from the GLREC.

2.1.4 Pathology slide for ATR imaging and Raman mapping

Samples used for the first experiments at the Diamond synchrotron (10 μm thickness mounted on 1 mm CaF_2 , Crystran, Poole, UK) were used for initial ATR experiments. For the Raman mapping and the ATR data presented in this thesis, a sample known to contain calcifications in the ducts was retrieved back from storage and cut to 6 micron thickness and mounted on calcium fluoride (1 mm thickness, Crystran, Poole, UK).

Paraffin was removed by placing paraffin oil on top of the sample for 1 hour and subsequently washed off with 0.5 ml hexane. The protocol was applied twice in order to remove all paraffin and is evaluated in Appendix D. Ethical approval for this study was obtained from the GLREC.

2.1.5 Mineralising breast cell line

A novel *in vitro* model of mammary cell mineralization has previously been established and characterised using the murine mammary adenocarcinoma 4T1 cell line (ATCC). A detailed description of the protocol has been published previously (Cox et al., 2012). Briefly, 4T1 cells were grown on calcium fluoride windows (1 mm thickness, Crystran, Poole, UK) in either osteogenic cocktail (50 $\mu\text{g}/\text{ml}$ ascorbic acid and 10mM beta glycerophosphate) or control media for 7, 11, 14, 17, or 21 days after which they were fixed with 4% paraformaldehyde

by Dr Maria Morgan and Dr Rachel Cox of the Royal College of Surgeons in Ireland. Replicates were stained with AR and VK.

2.1.6 Breast tissue models for preliminary deep Raman studies

Porcine soft tissue was used to mimic human mammary tissue. All models were used fresh and without further sample pre-treatment. For measurements through skin, porcine soft tissue was used with attached skin since porcine skin is known to be similar to human skin (Vardaxis et al., 1997). The epidermis of the porcine skin has been quoted to be in a range similar to that in human, the dermal-epidermal ratio of porcine skin is in the same range as in human skin, and the turnover of the epidermis and the kinetics of epidermal proliferation are similar as well. Porcine tissue has however a large amount of striated muscle which is different than the fibroglandular tissue which makes up the breast.

2.1.7 Nanoparticles

Four different SERS nanoparticles were kindly provided by Cabot (Boston, Massachusetts); x403, x420, x421, and x440. Each nanoparticle consisted of a gold core (~100 nm diameter) surrounded by a reporter molecule (dye) and the whole was encapsulated in a thin silica layer. The nanoparticles were used as a target for several experiments concerning the sample thickness, signal depth and detecting several different analytes (multiplexing). In figure 2.1, the Raman spectra of all nanoparticles are shown. The crosses depict the bands used as marker bands in non-invasive experiments.

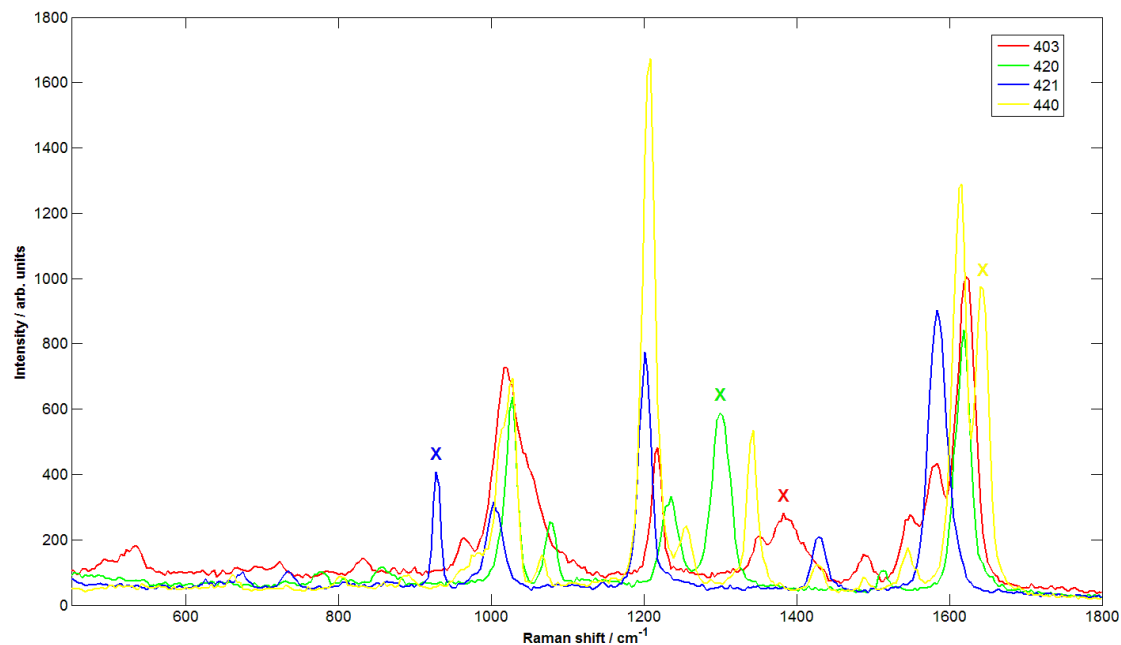


Figure 2.1: Raman spectra of the four different SERS particles. The crosses depict the characteristic bands used in non-invasive experiments (Stone et al., 2011).

2.1.8 Breast tissue for preliminary deep Raman studies

For initial experiments, human tissue collection was done by Mr. J. Horsnell and C. Chan during mammoplasty reduction procedures in Cheltenham General Hospital. Tissue was snap frozen in liquid nitrogen and transported back to Gloucester Royal Hospital and stored at -80°C until used. Ethical approval was obtained from GLREC.

2.1.9 Fresh human breast tissue for transmission Raman study

Breast tissue specimens were collected from 41 patients who underwent a wide local excision or a wire guided local excision at Gloucestershire Royal Hospital during breast lists of Miss Sarah Vesty and Mrs Clare Fowler between March and July 2012. The patients had an age ranging from 35 to 84, with a mean age of 61.

During local excision the affected area and some of the surroundings were removed. For a wire guided local excision a wire is inserted in the breast to mark the location of the breast abnormality which is checked with mammography. In panel A of figure 2.2, a mammogram is shown of a breast with an inserted wire and in panel B the X-ray image of the excised specimen of the same patient.

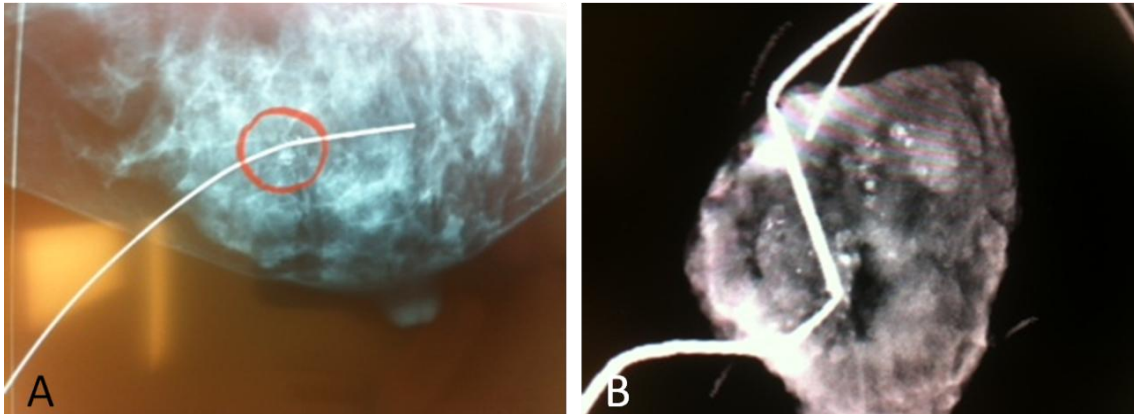


Figure 2.2: Example of wire localisation A) Mammogram made after wire insertion; B) excised breast specimen with wire.

As a routine procedure, X-ray images were captured of each breast specimen in theatre using a faxitron device. X-ray images of every specimen are shown in appendix E3. Four of the 41 specimens had skin attached (specimens 18, 23, 39, and 40) and seven specimens had blue dye in them (specimens 8, 12, 18, 21, 27, 30, and 39). Blue dye is normally injected in combination with technicium near the tumour to locate the sentinel lymph nodes. A range of 'blueness' was found which is illustrated in figure 2.3. The presence of blue dye did not appear to hinder the Raman measurements, although it has been reported it yields a Raman spectrum on its own (Horsnell, 2012).

Ethical approval was obtained from the GLREC and informed written consent was given by the patients involved. A copy of the consent form and patient information leaflet can be found in appendix E1 and E2.

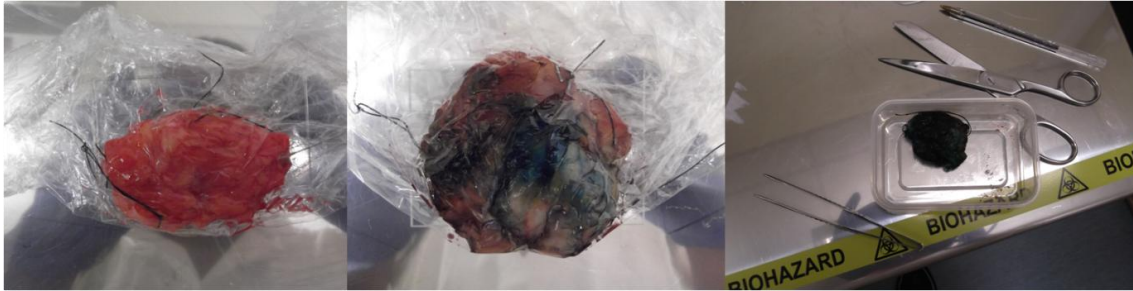


Figure 2.3: Some of the specimens had blue dye in them and a range of 'blueness' was observed. In the left panel a specimen without blue dye is shown, while in the right panel the most extreme case is shown.

2.2 Experimental setups

2.2.1 Benchtop Fourier Transform InfraRed (FTIR)

FTIR measurements for the staining study and the targeting of calcifications for synchrotron experiments were performed on a Spotlight 400 (Perkin Elmer, figure 2.4) at Gloucestershire Hospitals.

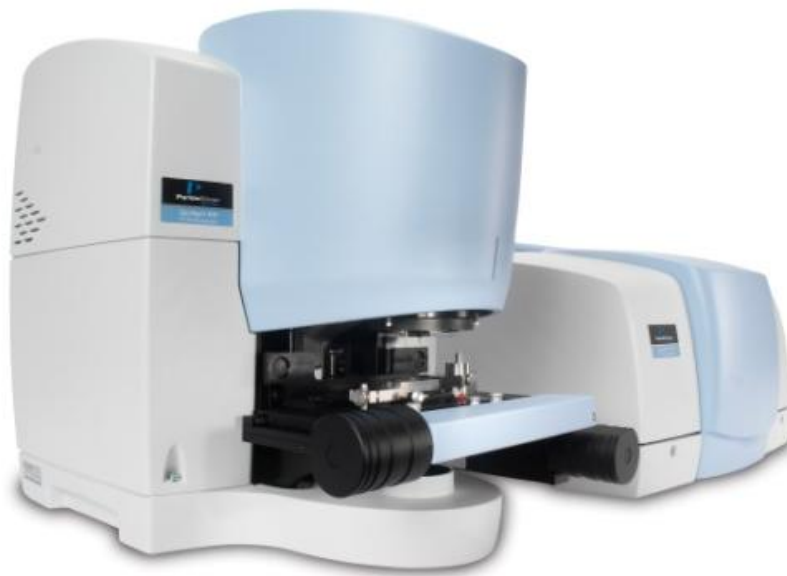


Figure 2.4: Illustration of the Perkin Elmer Spotlight 400 (www.perkinelmer.de, accessed 11 October 2012).

The dilution experiments were performed at the Cranfield Forensic Institute at the Shrivenham campus. For these experiments a Spotlight 200 (Perkin Elmer) was used.

In contrast to the Spotlight 400, a Spotlight 200 cannot be used for imaging. The difference between the two systems lies in the choice of detector; the spotlight 200 has a single element detector while the Spotlight 400 has an 16x1 linear array detector. Both the systems are cooled with liquid nitrogen and have a detection wavelength range of $4000 - 720 \text{ cm}^{-1}$.

2.2.2 Raman microscope and imaging

Measurements were performed on a Renishaw System 1000 using 830 nm as the excitation wavelength. The system is equipped with a xyz-stage and streamline technology which enables Raman mapping. A schematic overview of the system is shown in figure 2.5 below. The laser beam enters the system at the laser turning mirror after which it is directed to the microscope using other mirrors. The scattered light is directed through a filter, removing the spurious laserline, onto a slit. The grating (300 lines/mm) splits the different spectral components of the Raman light before it reaches the CCD detector.

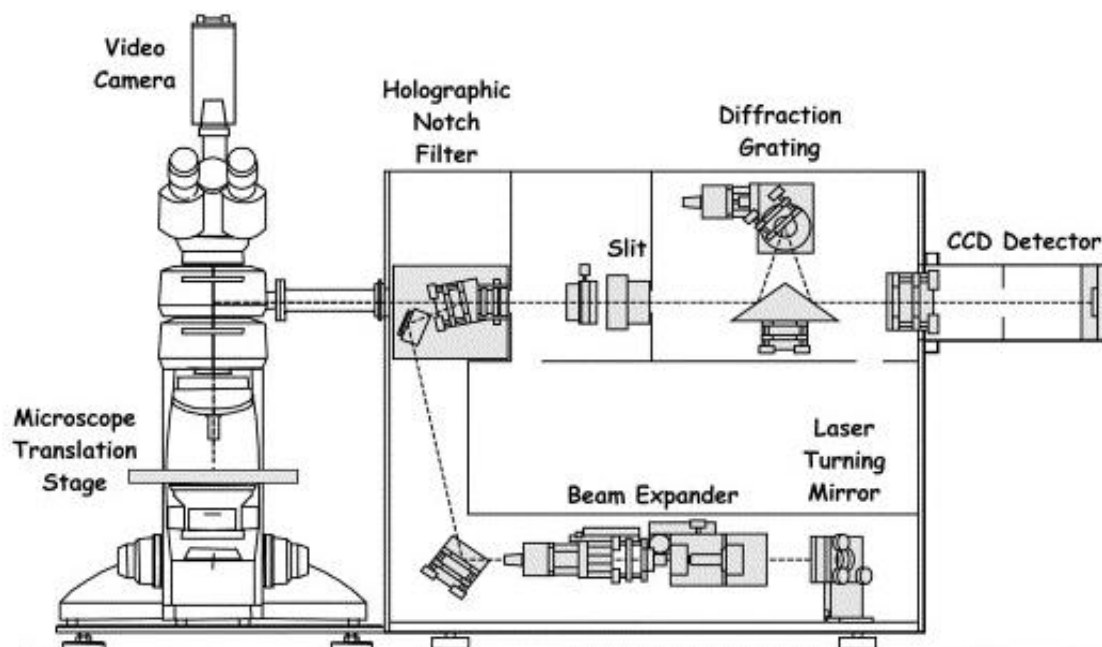


Figure 2.5: Schematic overview of the Renishaw 1000 system (Clark, 2002).

The Raman system is calibrated daily to ensure reproducible measurements. Calibration is performed with an offset calibration based on a measurement of

silicon which has a well defined peak position of 520 cm^{-1} . Furthermore, every day the system is used, standard measurements are performed on a cuvette filled with cyclohexane and a polymer standard (pipette tip) which both have bands over the entire active spectrum. When blocking the laser, a full calibration can be obtained by measuring a neon argon emission spectrum. A measurement done on a piece of green glass is used as a tertiary fluorescent standard. This has been calibrated using a National Physical Laboratory tungsten (W) filament secondary standard calibration lamp.

2.2.3 Synchrotron beam lines

Synchrotron experiments were performed at beam line B22, MIRIAM (Multimode InfraRed Imaging And Microspectroscopy) at the Diamond light source (Harwell Science and Innovation Campus, Oxfordshire, UK) and IRENI (IR ENvironmental Imaging) at the Synchrotron Radiation Center (SRC, University of Wisconsin, USA).

At both the end stations of the B22 beam line, Hyperion 3000 microscopes were used coupled to Bruker Vertex 80V FTIR spectrometers. Synchrotron light is supplied to the beam line by the storage ring. Diamond operates in a 'top up'-mode which means the electron beam is topped up through the day, in contrast to the SRC which gets injected only four times a day.

The IRENI beam line at SRC combines multiple synchrotron beams (3x4) with wide-field detection using a focal plane array (FPA) detector (Nasse et al., 2011). Light is supplied by the Aladdin electron storage ring and mirrors create a 3x4 bundle of synchrotron beams which are directed to the Vertex 70 FTIR spectrometer and FPA detector (Bruker Hyperion 3000). A schematic overview is shown in figure 2.6.

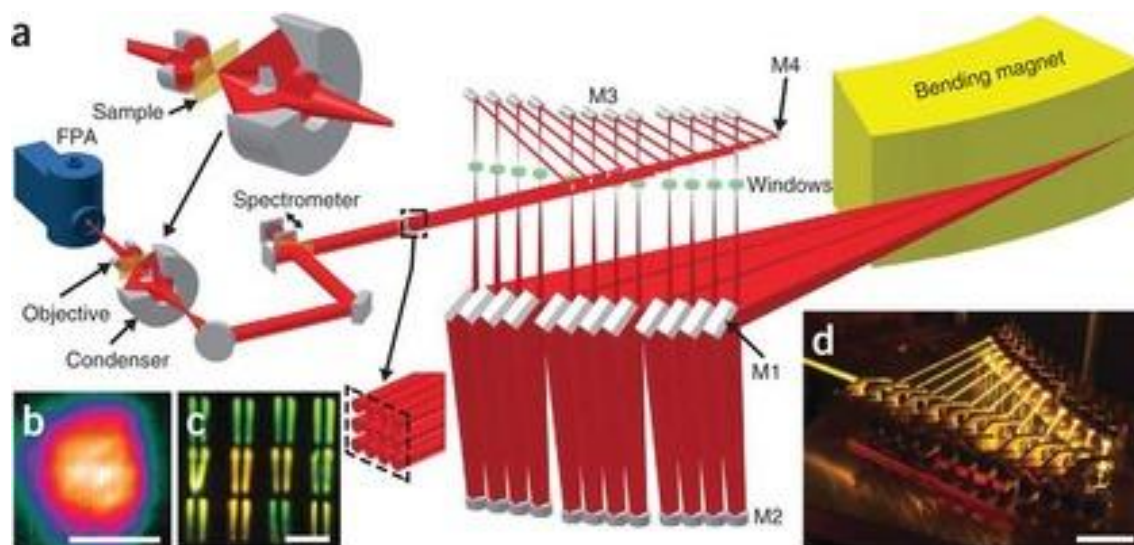


Figure 2.6: Overview IRENI beamline A) Schematic of the experimental setup; B) FPA image (128x128 pixels) of the 12 beams illuminating an area of $\sim 50 \times 50 \mu\text{m}$. Scale bar $40 \mu\text{m}$. C) Visible light photograph of the 12 beams projected on a screen in the beam path, dashed box in A, the scale bar has a size of $\sim 1.5 \text{ cm}$; D) Long time exposure photograph showing the combination of the 12 individual beams into the beam bundle (Nasse et al., 2011).

2.2.4 ATR FTIR setup

ATR experiments on the deparaffinated sample were performed in collaboration with Dr Alina Zoladek and Prof Sergei Kazarian at Imperial College (London, UK). The system comprised a germanium ATR crystal, a Varian 7000 FTIR spectrometer, and a Varian 600 UMA microscope with a 64×64 pixel FPA detector.

2.2.5 Transmission Raman setup

A scheme of the experimental setup is shown in figure 2.7. The emission from a frequency stabilized laser module (830 nm, Innovative Photonics Solutions) is sent from a fibre to a fibre-export collimator (Thorlabs) and passed through a laserline filter (FL830-10, Thorlabs) to suppress off-centre spectral emission from the laser. The generated Raman signal was collected in transmission

mode using an anti reflective coated lens ($f = 60$ mm, dia = 50 mm, INGRYS Laser Systems). The collimated scattered light was passed through a holographic super notch filter (HSPF-830.0 AR-2.0, Kaiser Optical Systems) to remove the elastically scattered light and imaged onto an optical fibre bundle by a second lens of the identical parameters to the collection lens. The output end of the fibre probe was placed at the entrance port of a Holospec VPH system spectrograph (Kaiser Optical systems Inc, HSG-917.4 custom, f-number = 1.8) and a CCD detector cooled to -70°C (Andor Technology, DU420A-BR-DD, 1024 x 255 pixels).

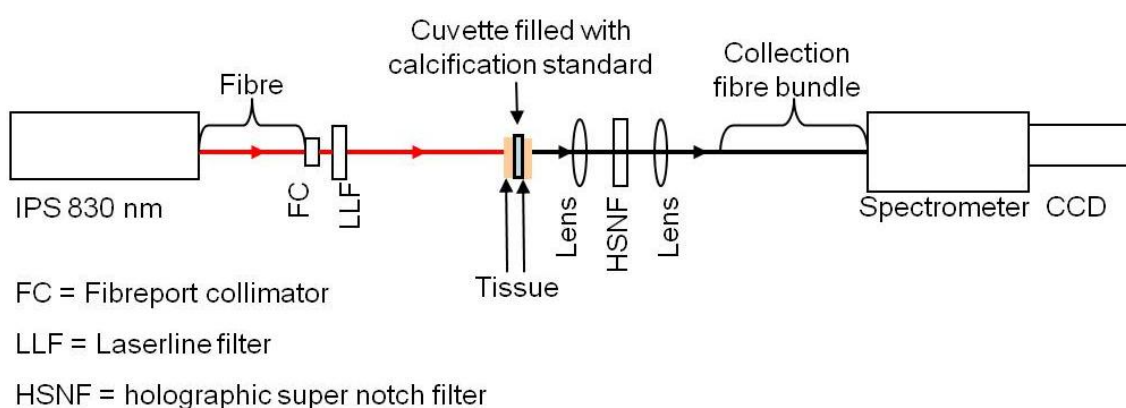


Figure 2.7: Experimental setup used for the transmission Raman study.

During this project, the deep Raman setup was modified to permit both the inverse SORS and transmission Raman modes of operation (figure 2.8 and 2.9). First, a different Innovative Photonics solutions laser was installed for the transmission measurements, with similar excitation wavelength (830 nm), but the output power at the sample was 220 mW. Later this laser was used for the inverse SORS measurement and for the transmission measurements a 830 nm Renishaw laser with an output of 140 mW was utilised.

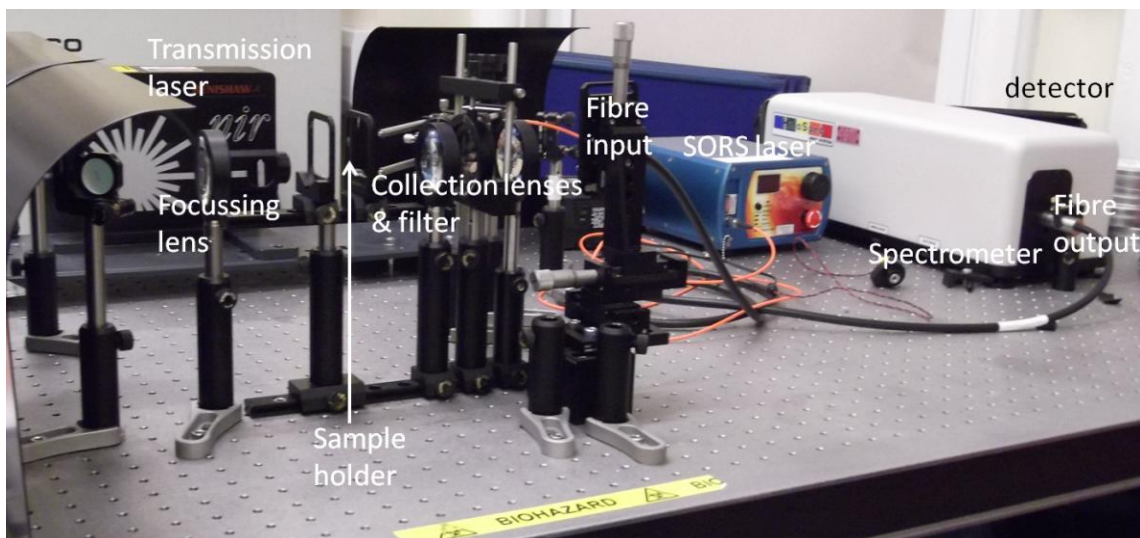


Figure 2.8: Photograph of the deep Raman setup, with the different components indicated.

In figure 2.9, the beam alignments for both SORS and transmission Raman are indicated. The beam used for the transmission Raman (depicted in blue) is steered to the sample using a periscope to adjust the height and mirrors leading the beam to a lens ($f = 7.0$ cm) which focuses the beam onto the sample.

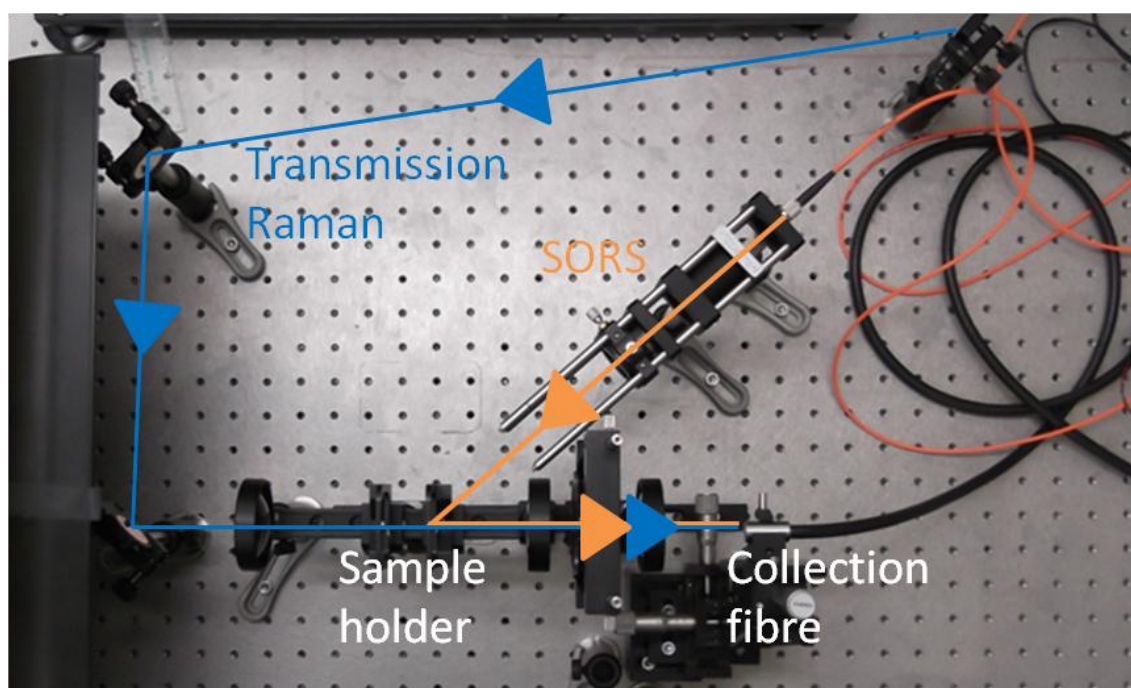


Figure 2.9: Detail of the combination of SORS and transmission Raman on one setup. The path of the laser is depicted in the photograph for both the SORS (orange arrows) and transmission Raman (blue arrows).

A collimated laser beam of the SORS laser (path depicted in orange in figure 2.9) was passed through an axicon (fused silica conical lens, 25.4 mm diameter, 170° apex angle, Topag Lasertechnik, Darmstadt, Germany) transforming the beam into a ring. By changing the separation of the axicon from the sample, the size of the ring could be controlled. In figure 2.10 a schematic overview of the workings of an axicon is shown together with an example of the output.

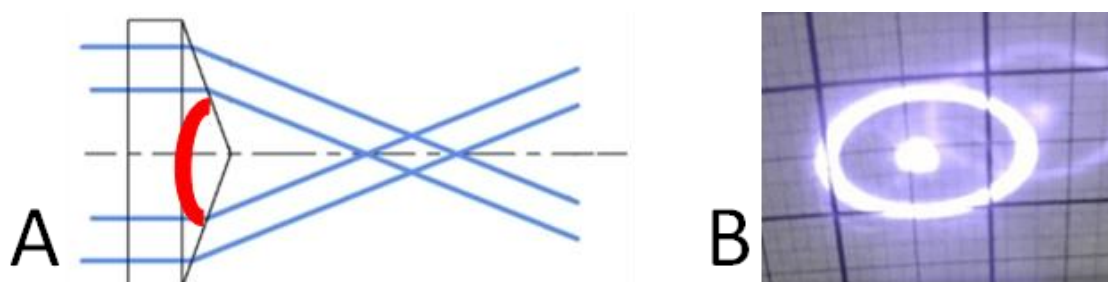


Figure 2.10: A) Schematic view of the workings of an axicon with the apex angle indicated in red (adapted from www.thorlabs.de, last accessed 11 October 2012); B) Photograph of the output of the axicon used, the point in the middle of the circle is the output of the transmission laser.

The system was calibrated using an aspirin tablet (acetylsalicylic acid), using values provided by Boczar et al. (2003). On each day the system was used, an aspirin spectrum was first measured (1 s acquisition time). The pixels relating to the 291, 425, 551, 751, 1045, 1191, 1293, 1606, and 1752 cm^{-1} bands were selected, assigned, and then used to calibrate the system.

2.3 Methods

2.3.1 Study of breast calcifications (Chapter 3)

2.3.1.1 Study of calcification standards

Tablets were pressed from all available standards (KBr, 1wt% analyt) and measured with the MIR light source at Diamond Light Source beamline B22. Measurements were performed without an aperture, 4 cm^{-1} spectral resolution and 256 scans in transmission mode with a blank KBr tablet as background

Chapter 2

(n=3). Data was loaded into Matlab, where the average of each group was taken.

To test what effect the saturation has on the peak shape, KBr tablets were pressed with different amounts of 2% carbonate substituted apatite in them. These tablets were measured on the Spotlight 200 in transmission mode in the 4000-750 cm^{-1} range, 120 scans, 1 cm^{-1} interval, and a 200x200 micron aperture. Measurements were done at five locations on the tablet. This part of the study was performed at the Cranfield Forensic Institute at Shrivenham.

A comparison between ATR and transmission FTIR was made by measuring a 2.0% carbonate substituted HAP sample with both settings. These measurements were performed by Dr Alina Zoladek at Imperial College. All measurements were performed with a 40x objective, but due to the different nature of the measurements the interrogated area differs. ATR measurements were performed at a 64x64 μm area with 64x64 data grid, in contrast to transmission FTIR measurements which interrogated a 350x350 μm area with a 64x64 data grid. For the ATR measurements 50 scans were used and for the transmission FTIR 25 scans.

Raman measurements were performed on a Renishaw 1000 Raman microscope. Powders were measured on a calcium fluoride slide without further sample preparation. Five areas were measured with an acquisition time of 60 seconds and a 50x magnification.

2.3.1.2 Comparison of spectroscopic techniques with pathology staining

The unstained, AR stained, H&E stained, and VK stained sections of all specimens were registered on the Perkin Elmer Spotlight 400 system and corresponding areas were selected. Obtaining a white light image with the FTIR setup results in intensity discrepancies which are visible as 'tiles' in the montaged image. An example is shown in figure 2.11A.

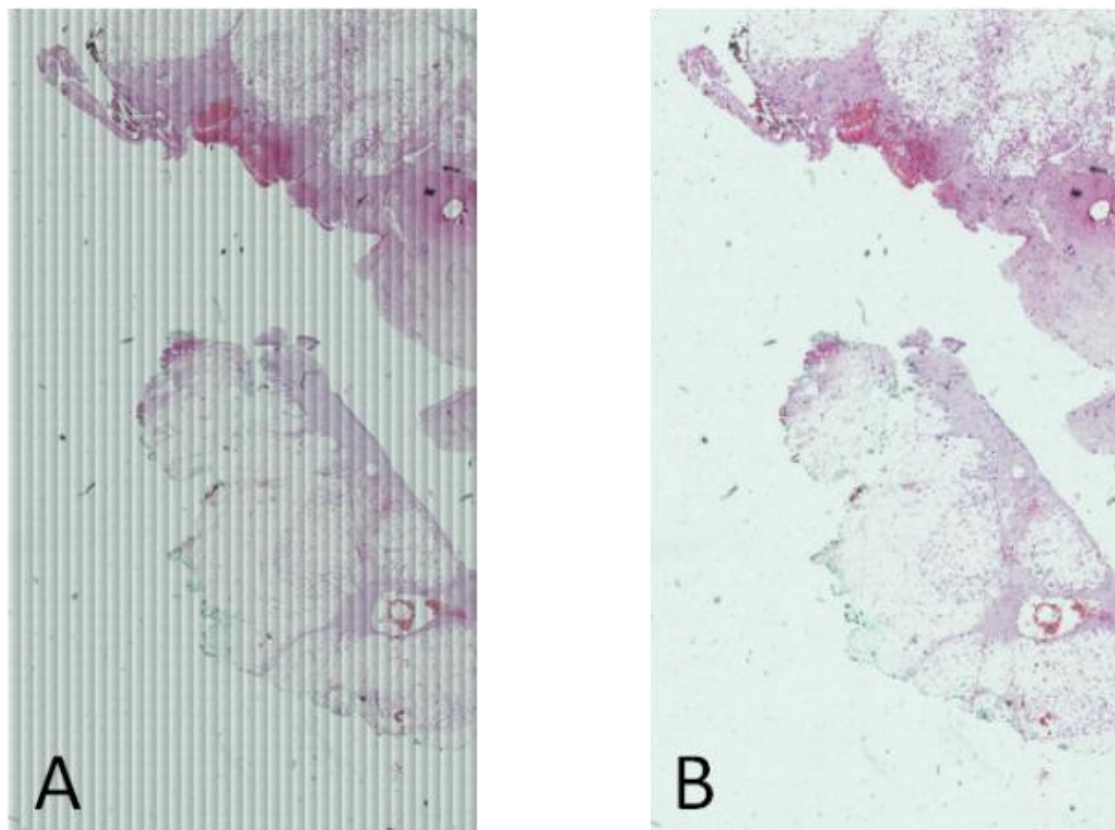


Figure 2.11: A) Original white light obtained with FTIR setup; B) same figure corrected for unequal distribution of light over each tile.

This tiling can be removed by using a blending algorithm (Rankov, 2005). By selecting a blank area of the size of one tile on the slide, a Gaussian filter can be created which reduces the differences in lighting conditions. This filter is then applied to the whole of the image. In panel B of figure 2.11 the image is shown after applying the algorithm.

All FTIR measurements were done on the unstained slides in transmission mode, with a spatial resolution of 4 cm^{-1} and pixel size of $6.25\text{ }\mu\text{m}$. The FTIR data was loaded into Matlab and biochemical component spectra were fitted against the spectral maps of the samples using ordinary least squares. The simplest approach to detect calcifications with FTIR, would be to plot the intensities of a characteristic apatite band, such as the $\sim 1030\text{ cm}^{-1}$ band, over all the maps. However, due to the complexity of the spectra, a fit would be more appropriate to identify calcifications. Biochemical fitting enabled estimations of the relative concentrations of these components at each location in the

Chapter 2

measured map. Hydroxyapatite (0.5% carbonate), DNA, RNA, actin, collagen IV, oleic acid, palmitic acid, paraffin, and triolein were fitted and the first derivative was used because previous research shows that works best (Baker, 2009). The false colour map indicating the fit coefficient (or relative level) of the hydroxyapatite was compared to the images of the different stains on adjacent slides of the sample.

Raman and IR mapping of cell lines

Samples grown in osteogenic cocktail for 7, 11, 14, 17, and 21 days, and samples grown for 11 and 14 days in control media were measured at the B22 beamline of Diamond Light Source Ltd (Harwell Science and Innovation Campus, Oxfordshire, UK) with a Bruker 80 V Fourier Transform IR Interferometer coupled to a Hyperion 3000 microscope. A grid of 145x145 micron was evaluated (10x10 point measurements) on the samples grown in osteogenic cocktail in order to capture different phases in calcification growth. Measurements consisted of 128 scans with a resolution of 4 cm^{-1} performed in transmission mode with a $15\text{ }\mu\text{m}$ aperture and a 36x objective. The background was measured every 10 measurements. Additional FTIR measurements were performed on a Perkin Elmer Spotlight 400 system on larger areas with a spectral resolution of 4 cm^{-1} , pixel size of $6.25\text{ }\mu\text{m}$ and 120 scans per pixel. Raman maps were acquired with a step size of $2.2\text{ }\mu\text{m}$ and an 15s exposure time on a Renishaw System 1000 with streamline technology using 830 nm excitation on samples grown for 14, 17, and 21 days.

2.3.1.3 Synchrotron FTIR imaging of breast calcifications

Localisation of calcifications

White light images of the pathology samples were taken on an IR Spotlight 400 system (Perkin Elmer). Sections which were thought to contain microcalcifications were subsequently mapped. All the measurements were carried out in transmission mode, with a resolution of 4 cm^{-1} , pixel size of 6.25

μm , and up to 16 scans per pixel. Background measurements (120 scans per pixel) were taken on a blank piece of slide. The location of microcalcifications was then marked on the white light image in order to find these regions back easily during synchrotron experiments. Biochemical fitting was used in order to investigate whether a sample contained calcifications. Once the data was loaded into Matlab, biochemical component spectra were fitted against the spectral maps of the samples as described in section 2.3.1.2. A fit of one indicates the spectrum is purely that compound. A mixture of at least protein, paraffin, and apatite is expected for a calcification. The threshold set for the apatite signal was 0.1 to ensure the spectra relating to the pixels do show apatite features. An overview is shown in figure 2.12.

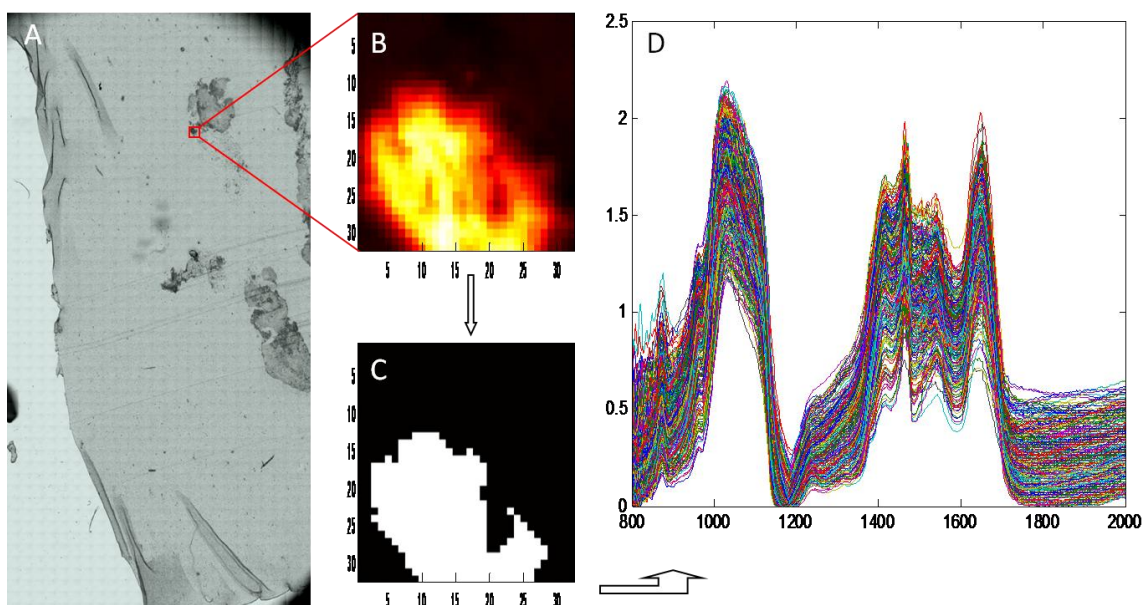


Figure 2.12 Screening procedure of pathology samples A) A white light image was taken; B) Area which is thought to contain microcalcifications was mapped and subsequently a biochemical fit of hydroxyl apatite (0.5% carbonate) performed; C) pixels with a calcification signal higher than threshold are coloured white, and D) Spectra matching to the white pixels.

Diamond experiments

During the first beamtime allocation at Diamond (SM6123) regions of interest were mapped in transmission mode with a 36x objective, 15x15 micron aperture, 128 scans, and a 4 cm^{-1} spectral resolution. During the second

Chapter 2

allocation (SM6605) both line maps and maps were taken using a 36x objective, aperture of 10x10 μm , 4 cm^{-1} spectral resolution, 128 scans and 10 μm steps except for the last map which was measured in a step sizes of 3.5 μm . Data collection at Diamond is performed with OPUS software. In order to load these measurements into Matlab, 'ImportOpus' can be used (modified by Dr Jacob Filik, B22 beamline, Diamond Light Source) and free to use and distribute. When loaded into Matlab, the spectra were analysed and the amount of phosphate and carbonate was evaluated using the area under the curve. In order to test the feasibility of using thinner samples, pathology samples were cut to 1, 2, and 5 μm thickness and mounted on calcium fluoride. The samples were then mapped with the Spotlight benchtop system in transmission mode with a spectral resolution of 4 cm^{-1} , pixel size of 6.25 μm and the background measured on a blank piece of the slide. A biochemical fit was then performed on the datasets.

IRENI experiments

At the IRENI beamline, measurements were performed in transmission mode. For initial experiments (to target locations) a lower amount of scans was used, but for the maps obtained measurements were performed with 128 scans and a spectral resolution of 6 cm^{-1} .

Due to the vast size of the data, original maps had to be compressed using self organising maps (SOMs) before loading into Matlab. In Matlab, PCA was applied and regions with calcifications were selected and saved for further analysis.

Additional measurements were performed in September-October 2012 in transmission mode with 128 scans and a spectral resolution of 6 cm^{-1} .

2.3.1.4 ATR imaging of breast calcifications

ATR measurements were performed by Dr Alina Zoladek (Imperial College, London, UK) on deparaffinised tissue samples. The locations of the measurements are indicated in figure 2.13 the transmission FTIR locations are indicated by the red boxes and the ATR FTIR measurements with the orange boxes. Raw data was provided for measurements at position 3,4,8, and 9 which was loaded into Matlab. The data was interpolated from 900 to 1200 cm^{-1} , using a 1 cm^{-1} step size. PCA was then performed in order to distinguish the calcification area from the surrounding tissue in the 64×64 pixel maps. Line scans were then carried out over the calcified area and the area under the curve for the phosphate and amide I band was analysed.

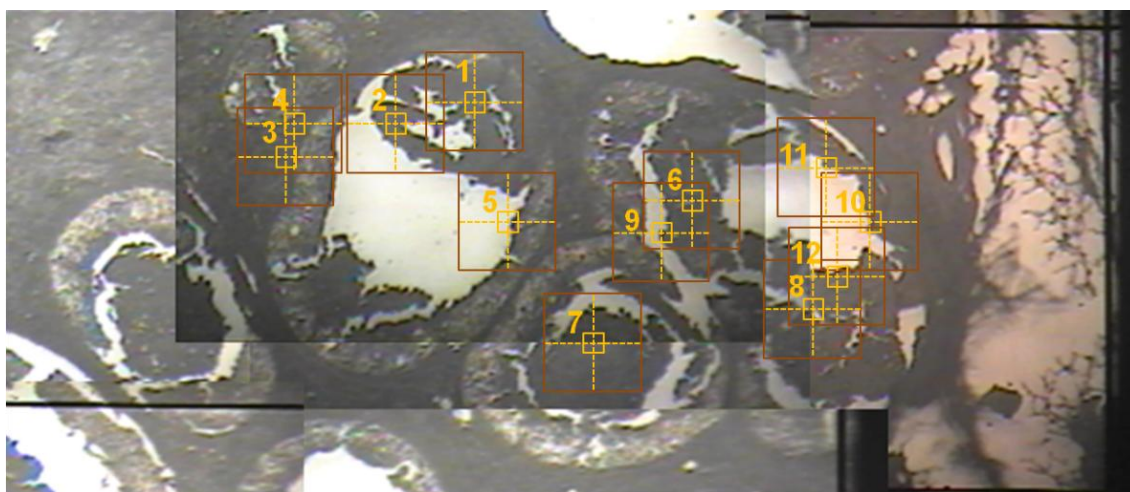


Figure 2.13: White light image of the deparaffinated sample with the ATR FTIR measurement locations indicated with orange boxes and the transmission FTIR locations with red boxes.

2.3.1.5 Raman imaging of breast calcifications

Measurements were performed on a Renishaw 1000 system (830 nm laser, 50x objective, stepsize 6.3 micron) equipped with a xyz stage and Streamline software which enabled mapping experiments. The y-bin was set to 6 and the measurements done with 15s exposure time, 'slalom setting' on and centred

around 1250 cm^{-1} . A higher resolution map was taken on a smaller area on the same sample with stepsize $1\text{ }\mu\text{m}$, the y-bin set to 1 and a 15s exposure time.

Cosmic rays were removed by applying a median filter over all spectra. The Raman measurements were compared to the FTIR measurements taken on the same area. The FTIR map was performed with a spectral resolution of 4 cm^{-1} , pixel size of $6.25\text{ }\mu\text{m}$, scan speed of 1 cm/s and two scans per pixel. As a background measurement a blank piece of slide was measured 120 times with the same settings.

2.3.2 Deep Raman system evaluation (Chapter 4)

2.3.2.1 Comparison porcine soft tissue and human mammary tissue

For a study comparing porcine soft tissue and human mammary tissue, stored breast tissue was retrieved from the freezer and left at room temperature to defrost. To provide stability the tissue was placed inside a polymer tube with a diameter of 2.5 cm . Raman spectra were taken in transmission mode with accumulation times $5 \times 60\text{ s}$ (cosmic ray removal on) on the transmission Raman setup. Measurements of sample with comparable thicknesses (see sample thickness section below) were used to compare porcine soft tissue and human breast tissue.

2.3.2.2 Sample thickness limits when using transmission Raman setup

Freshly frozen breast specimens and porcine soft tissue specimens of different thicknesses were measured on the transmission Raman setup with the same setting described in the section above. The breast specimens had a thickness of 8, 10, 12, 15, 20, 22, and 25 mm and the porcine soft tissue specimens had thicknesses of 10, 18, 27, 40, and 49 mm, respectively.

During the measurements done on freshly excised breast pathology specimens the thickness of each specimen was recorded (section 2.3.3.3). This data was analysed to investigate the effect of sample thickness. The SNR was calculated

Chapter 2

by taking the height of the Gaussian fit to the 1440 cm^{-1} band as the signal and taking the noise as being half the difference of the highest and lowest point between 350 and 450 cm^{-1} .

For extended depth measurements, nanoparticle x403 (described in section 2.1.7) was injected (approximately 3×10^{10} particles) in the centre of the porcine muscle tissue block of $45\text{-}50 \times 50 \times 50\text{ mm}$ (approximate thickness 47 mm) shown in figure 2.14. Raman spectra were collected over $5 \times 60\text{ s}$ (cosmic rays removal on) in transmission mode.

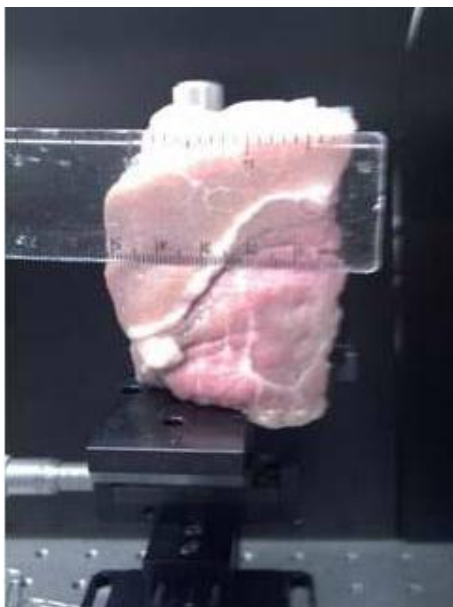


Figure 2.14: Tissue block ($45\text{-}50 \times 50 \times 50\text{ mm}$, average thickness 47 mm) used for the extended Raman depth measurements.

2.3.2.3 Lateral spreading in transmission Raman measurements

To study the spread of Raman signal through the specimens of a certain thickness, one microliter of x403 nanoparticle suspension was pipetted in the middle of a piece of porcine soft tissue with a thickness of 5 mm . Translational x-y stages were used in a range of 20 mm to translate the sample in steps of 2 mm , to construct an image of 11×11 data points. Raman spectra were collected for 10 s at each of these points. After construction of this image, an extra layer of porcine soft tissue was attached to the sample with surgical pins which made

the total thickness of the sample 20mm. Again an image of 11x11 data points was created. Both images were loaded into Matlab where an image was created based on the baseline corrected (1152 cm^{-1}) most prominent band (1016 cm^{-1}) of the x403 spectrum. A 2D Gaussian function was fitted to this data to indicate how much the intensity spread over the pixels depends on the thickness of the sample.

2.3.2.4 The originating depth and spatial resolution of transmission Raman signal

To understand the effect the depths of the calcifications have on the Raman signal quality, measurements were performed with analytes on different depths while keeping the thickness and the size of the analyte static.

Porcine soft tissue of 15-20 mm thick (average 18 mm, figure 2.15) was carved the size of a large microscope slide. It was wrapped into cling film to provide stability needed to mount it upright. Then a microliter of x403 was injected into the tissue block.

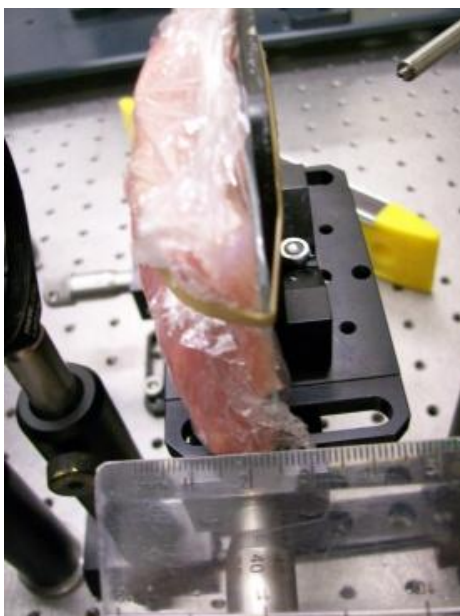


Figure 2.15: Sample orientation in the originating depth experiment.

Chapter 2

Translational x-y stages were used in a range of 20 mm to translate the sample in steps of 1 mm, to construct an image 21x21 datapoints. Raman spectra were collected for 10s at each point. Then the sample was unwrapped, rotated 180 degrees, wrapped again and an image of 21x21 datapoints was constructed while the sample was translated in steps of 1 mm. By doing this, the thickness of the sample is exactly the same, and only the depth of the signal is changed. All data was loaded into Matlab where an image was created based on the most prominent peak of the x403 (1016 cm⁻¹, baseline corrected) spectrum. A 2D Gaussian was then fitted to this data in order to investigate the effect of the depth from which the signals originate on the lateral spreading of the Raman signals.

2.3.2.5 Measurements through skin

In order to use transmission Raman as a non-invasive tool, it should be possible to do measurements through skin. In order to test the capability of the system to achieve this, measurements were performed on porcine soft tissue with skin and human breast tissue with attached skin.

Porcine soft tissue was sectioned to a thickness of 0.5 cm, placed against a large microscope slide and then wrapped in cling film to provide enough stability to position the sample upright. One microliter x403 dye was pipetted into the centre of the sample. A volume of one microliter corresponds to a sphere with a diameter of 0.6 mm, assuming no leeching into the surrounding tissue (see equation below for calculation of radius r).

$$Volume = \frac{4}{3}\pi r^3$$

Equation 2: Volume of a sphere.

Translational xy-stages were used in a range of 20 mm to translate the sample in steps of 2 mm, to construct an image 11x11 data points. Raman spectra were collected for 10s at each point. Then, porcine skin and fat was attached to the sample with surgical pins, which forced the two parts to be in contact. The

Chapter 2

thickness was 15 mm. Again, a 11x11 measurement grid was created in order to construct an image. All data was loaded into Matlab where an image was created using colour scale of one of the prominent peaks of x403. Furthermore, a 2D Gaussian was fitted to this data matrix in order to estimate how much the signal spreads through the sample.

Measurements through skin were also performed on the fresh human breast specimens. During the theatre experiments, four samples had skin attached. The specimens were wrapped in cling film and placed between two large silica microscope slides as described in section 2.3.3.3. In figure 2.16, photographs of the first specimen (10 mm thickness) are shown.

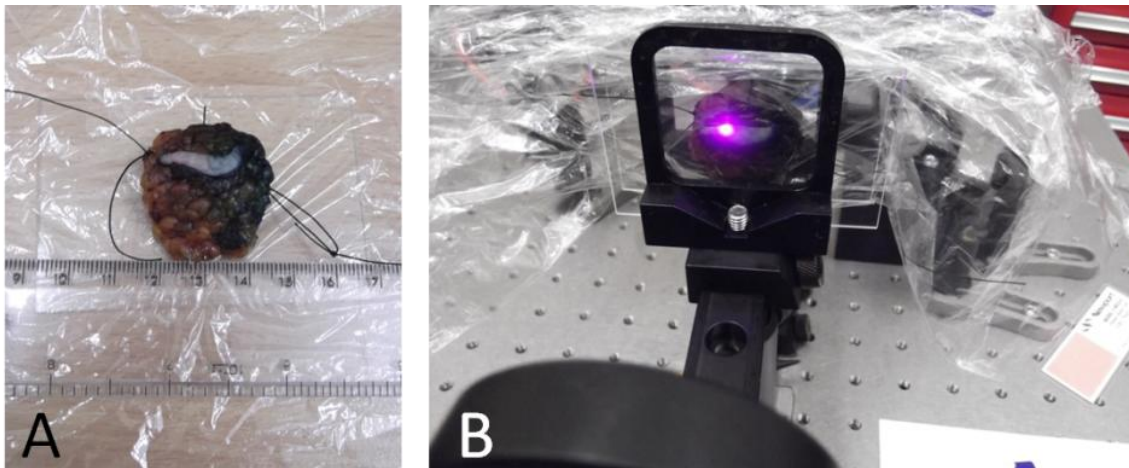


Figure 2.16: Pathology sample with skin A) photograph of sample; B) sample mounted for deep Raman measurements.

The blue colour of the specimen is due to blue dye used in theatre, as explained in material section 2.1.9. On this specimen three measurements were done through skin and five through tissue only.

The second specimen with attached skin had a thickness of 23 mm and did not contain blue dye (figure 2.17). On this specimen six measurements were performed; three on the skin patch and three on an area without skin.

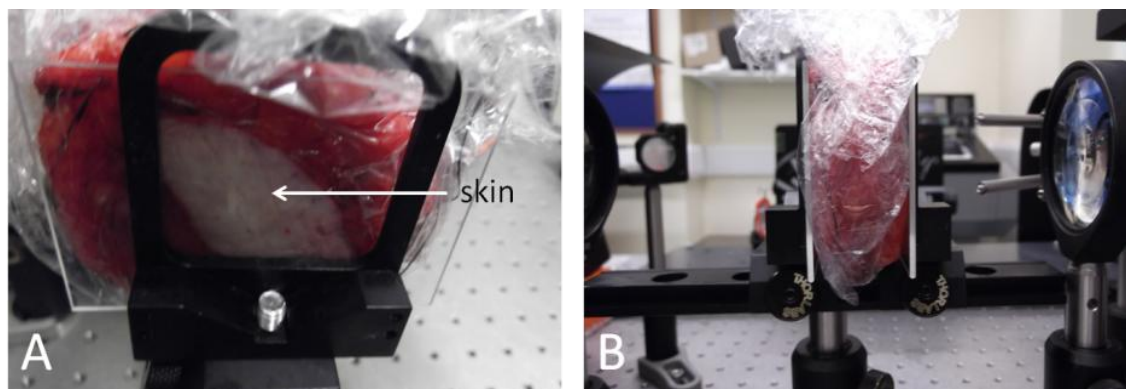


Figure 2.17: Pathology sample with skin A) Front view, the arrow indicates the skin patch; B) Side view of mounted sample (thickness 23 mm).

The third specimen with attached skin had a thickness of 10 mm and blue dye was visible (image not shown). All measurements on this sample were performed through skin. The fourth specimen had a thickness of 21 mm and had no visible blue dye (image not shown), on this specimen two measurements were performed on skin and on the tissue alone.

During all Raman measurements performed on the fresh tissue samples the experimental settings were similar to those of the other measurements in the theatre study (Section 2.3.3.3); all measurements were done in transmission mode with an accumulation time of 3x60 seconds and the cosmic ray removal function on.

2.3.3 Deep Raman spectroscopy on breast calcifications and tissue (Chapter 5)

2.3.3.1 Use of a pseudo marker to estimate the amount of carbonate substitution

Calcification standards with 0.5, 1.4, 2.0, 2.3, 3.5, 6.0, and 11.0% carbonate substitution were placed in quartz cuvettes with a path length of 2 mm (Starna, Hainault, UK). The samples were each measured five times in random order for 20 seconds and these measurements were used as standards.

For a non-invasive proof-of-principle feasibility study the cuvettes were wrapped in porcine tissue (figure 2.18) to evaluate the carbonate substitution through a

layer of tissue. Tissue with a mix of fat and protein was chosen to mimic bulk human breast tissue. The thickness of the porcine tissue was 1.8 mm for the proof of principle experiments on both sides of the cuvettes (overall thickness porcine tissue 3.6 mm + 2 mm cuvette = 5.6 mm). The measurement was also performed with an overall thickness of 16 mm in order to evaluate the clinical relevance of the method. During all measurements ($n=3$ for each standard) the signal was accumulated over 5x60 seconds and the cosmic ray removal option of the detector software was used.

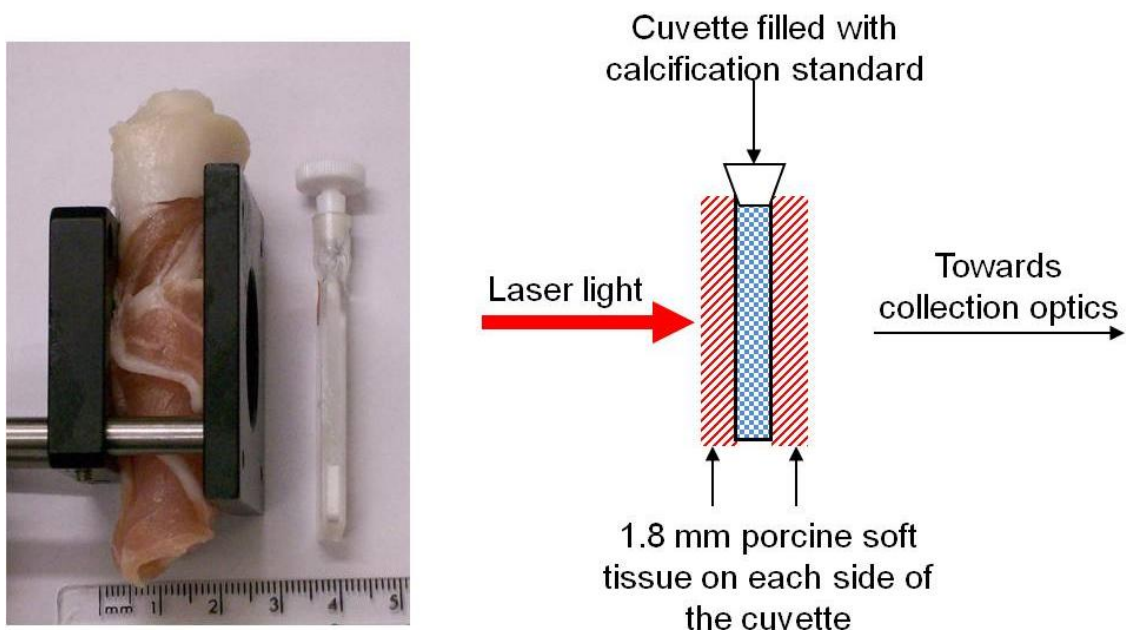


Figure 2.18: Detail of the experimental setup. Left panel: porcine soft tissue wrapped around an optical cell as used in feasibility experiment; right panel: a graphical representation (Kerssens et al., 2010).

All data was loaded into Matlab7 in which an in-house written tool fitted a Gaussian function to the peak located at 960 cm^{-1} after which the characteristics of this fit were evaluated. This yielded four parameters to analyse; the position of the Gaussian, the height of the baseline, the sigma of the Gaussian, and the maximum of the Gaussian. In our analysis the position and the sigma of the fitted Gaussian were used to separate the different samples. The σ is related to the width of the peak:

$$FWHM = 2\sqrt{2 \ln 2} \sigma$$

Equation 3: Full-width-half maximum calculation.

In a later stage of the project, apatite standards were kindly provided by Prof. Mary Tecklenburg (section 2.1.1). All apatite samples were measured on the Raman microscope (n=5) with an accumulation time of 60 seconds to test the effect of substitution type on the position of the apatite band. Since elemental analysis was performed on the new samples, the amount of carbonate substitution could be defined with a higher accuracy. The samples were used to validate measurements performed on the samples from Clarkson Chromatography and the Rogers lab.

2.3.3.2 SNR limits for using the pseudo marker

For the spatial resolution measurements two cuvettes filled with calcification standards with a carbonate substitution range found in breast calcifications (Baker et al., 2010). One standard had a carbonate substitution of 1.4%, which would be a breast calcification relating to invasive breast cancer, and the other calcification standard a carbonate substitution of 2.0%, which would relate to a benign breast calcification. The standards were oriented next to each other and wrapped in porcine soft tissue (figure 2.19).

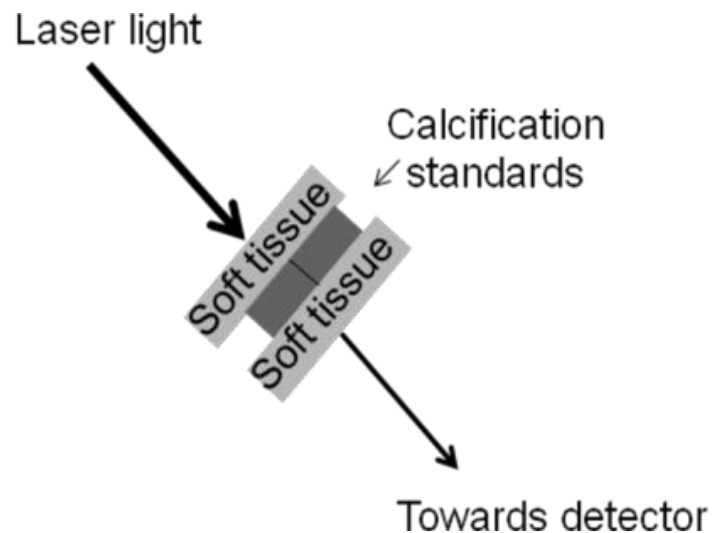


Figure 2.19: Graphical representation of the spatial resolution experiment.

The xy-translational stage was used to move the sample in steps of 1 mm. The overall sample thickness was 7 mm and the sample was measured five times

Chapter 2

(60 s accumulation time) on every location. A signal to noise tool was employed to estimate the SNR. The height of the fitted Gaussian was taken as the signal and the noise was estimated as half the difference between the highest and lowest signal between 800 and 900 cm^{-1} .

Human breast tissue was retrieved from the freezer and left in room temperature to slowly defrost. After defrosting the tissue did not maintain its shape, so stability was provided by mounting the tissue in a syringe tube. A calcification standard containing 2% carbonate substitution was measured with different amounts of breast tissue around it (varying from 5 mm to 20 mm).

To get an idea about the SNR needed for an accurate estimation of the amount of carbonate substitution the study described below was designed and performed.

Human breast tissue was retrieved from the freezer and left in room temperature to slowly defrost. After defrosting the tissue was positioned on top of a glass plate and wrapped in cling film to provide stability. A calcification standard (0.5, 1.4, or 6% COHAP) was put in front of the sample. Figure 2.20 shows a photograph of the sample mounting.

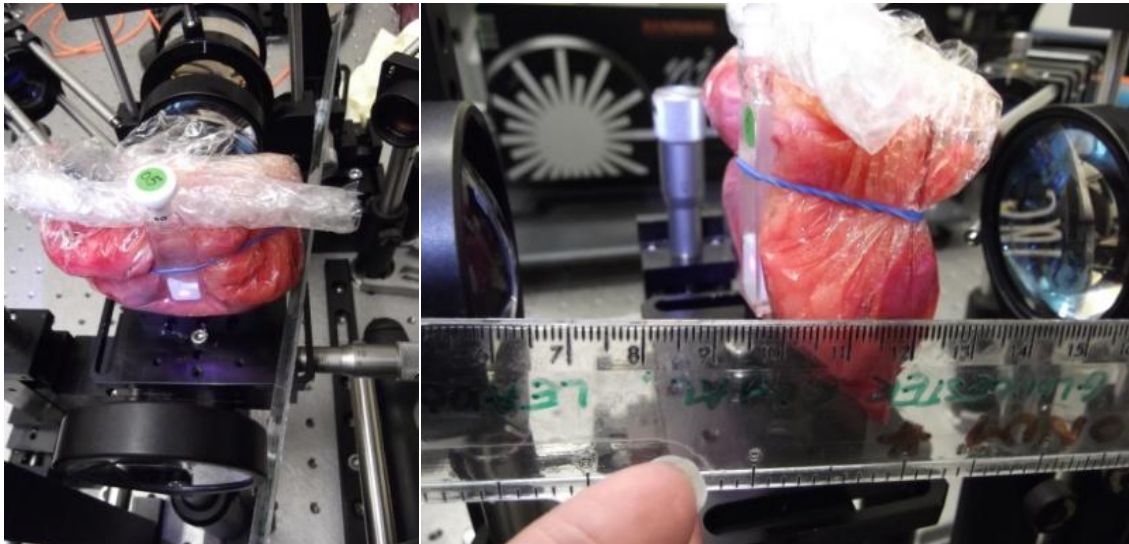


Figure 2.20: Photograph of the SNR experimental setup.

Each sample was measured 12 times (accumulation time 2x30s, cosmic ray removal on). The data was loaded into Matlab, where a matrix was constructed

with all combinations of the spectra. For $n=3$ the combinations would be: 0 0 0 (none of the spectra), 1 0 0 (only the first spectrum), 0 1 0 (only the second spectrum), 0 0 1 (only the third spectrum), 1 1 0 (spectrum 1 and 2), 1 0 1 (spectrum 1 and 3), 0 1 1 (spectrum 2 and 3), and 1 1 1 (all three spectra).

With twelve measurements, 2^{12} (4096) combinations can be constructed since there are two options for each of the twelve measurements; incorporation or not. The combination of none of the spectra is removed, and from all the other (4095) combinations the mean spectra of every combination is calculated. The Gaussian fitting routine is applied over all new spectra and the amount of carbonate substitution is calculated (the range of each group, mean, and standard deviation) and the SNR.

The SNR is calculated by using the highest intensity between 940 and 980 cm^{-1} as a measure for the signal which is lowered by the lowest intensity in this region as a method of background subtraction. The noise is calculated by taking the highest and lowest intensity between 760 and 800 cm^{-1} , which is an area of the spectrum which does not show Raman bands. The difference between the highest and the lowest intensity is then calculated and divided by two, to give an indication of the noise level. The signal is then divided by the noise to obtain the SNR.

2.3.3.3 Theatre project deep Raman on breast

Specimens were collected from theatre and transported to the Biophotonics Research Unit. As a routine procedure, patients might get injected with a radioactive tracer ($^{99\text{m}}\text{Tc}$) which is why radiation protection advice was sought from the GlosRad team and local rules were set up. In short, the lab was designated as a 'supervised area' when a radioactive breast specimen is present. Warning signs were fitted to the door whilst the sample was in the room or waste was stored with a measured activity level exceeding the disposal limits. Radiation was measured with a Thermo Type 44A scintillation monitor SN5023 and records of the measurements retained.

Chapter 2

At the Biophotonics lab, the breast specimens were placed in cling film and mounted between two 51x76x1.2-1.5 mm microscope slides (Logitech Ltd, Glasgow, UK). The sample was then mounted in the sample holder and the thickness of the sample was recorded which ranged from 3-25 mm. Five measurements were taken from each sample (different positions) with an accumulation time of 3x60s with the cosmic ray removal function on. After the measurements the specimens were brought back into the standard clinical pathway. Records of the whereabouts of each sample were kept in both theatre and the lab.

All data was loaded into Matlab and interpolated in order to have the same x-axis for each sample in the dataset and background subtracted. All specimens were coded for the presence of calcification; '0' when no calcifications were clearly seen on the image and '1' when calcifications were present. The presence of the calcifications was evaluated by X-ray images of all specimens. Access to the original data has not been secured yet, but low resolution images are depicted in appendix E3 for all specimens used in the study together with the raw Raman data per sample. It should be noted that this was not done by a radiologist and not based on the high quality images. As a result the classifications of both groups is limited. Calcifications were present in 19 specimens and 22 specimens did not have calcifications.

PCA was performed and the scores for each component were plotted versus the scores for the next principal component for both groups. The model was then changed to four groups: specimens with many calcifications (n=6), specimens with calcifications (n=11), specimens without calcifications (n=8), and an 'unknown' group in which specimens were put with unclear X-ray images. By introducing the 'unknown' group all specimens which were previously borderline calcification/ no calcification will be treated as a separate group which decreases the subjectivity.

3 Results: study of breast calcifications

3.1 Study of calcification standards

In this section, a study involving hydroxyapatites in a range of carbonate substitution (0-11%) with transmission FTIR and Raman spectroscopy, as well as calcium carbonate and amorphous calcium phosphate is presented. By studying the spectra of samples with known chemical composition the effect this composition has on the spectra can be derived. This knowledge can then be used to translate spectral differences to chemical information within tissue specimens. Furthermore, the effect of dilution is studied with transmission FTIR to assess the effect of signal saturation on the measured spectra and a comparison is made between transmission FTIR and ATR FTIR and Raman spectroscopy.

3.1.1 Infrared experiments on calcification standards

Transmission FTIR experiments were performed on the standards as described in section 2.3.1.1. The mean spectra of the samples provided by the Tecklenburg lab (Michigan University) are shown in figure 3.1.

For clarity, the spectra are offset. Key band positions are indicated with blue lines (873, 878, 1030, 1410, 1470, and 1537 cm^{-1}).

The key signature of the apatite spectrum consists of a intense broad band $\sim 1030 \text{ cm}^{-1}$ with a shoulder $\sim 1070 \text{ cm}^{-1}$ and a lower intensity band at 960 cm^{-1} .

The position of the band in the $870 \text{ cm}^{-1} - 880 \text{ cm}^{-1}$ region is different for both types of carbonate inclusion, type A and B. Samples with A-type substitution show a band $\sim 878 \text{ cm}^{-1}$, and samples with B-type substitution show a band $\sim 873 \text{ cm}^{-1}$ which is in agreement with previous studies (Antonakos et al., 2007; Fleet and Liu, 2007; Fleet, 2009).

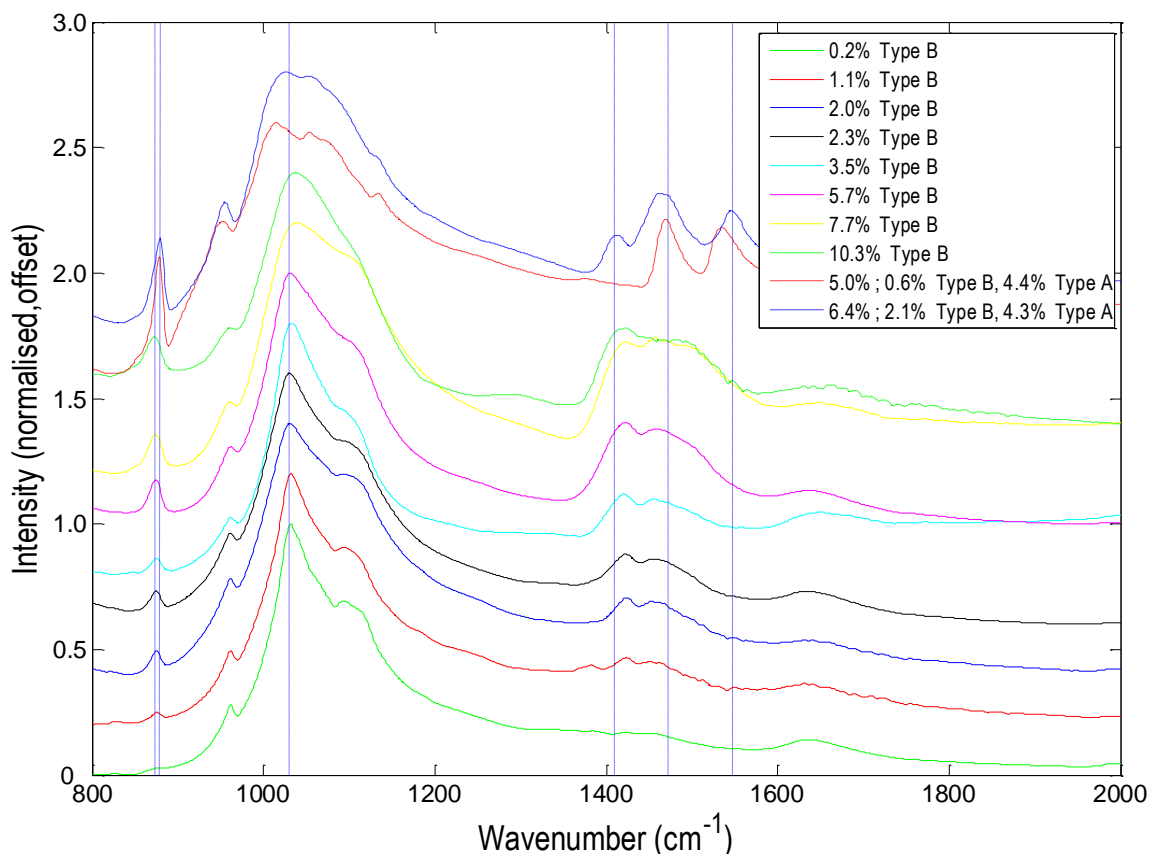


Figure 3.1: Mean FTIR spectra from samples prepared by Tecklenburg lab (Central Michigan University). Measurements are normalised and for clarity shown with offset. The blue vertical lines indicate the key positions at 873, 878, 1030, 1410, 1470, and 1537 cm^{-1} .

Samples with (partly) A-type substitution showed furthermore bands at 1134 cm^{-1} and 1537 cm^{-1} , which were not observed for B-type substituted apatite samples. The phosphate region (900 cm^{-1} -1200 cm^{-1}) shows subtle differences due to environment of the phosphate due to for example pH differences during formation, maturation, carbonate substitution. Rey et al. (1991b) observed a band $\sim 1134 \text{ cm}^{-1}$ in a brushite spectrum. Brushite, $\text{CaHPO}_4 \cdot 2\text{H}_2\text{O}$, is a mineral with a chemical composition fairly similar to hydroxyapatite ($\text{Ca}_{10}(\text{PO}_4)_6(\text{OH})_2$). The band located $\sim 1537 \text{ cm}^{-1}$ can be assigned to A-type carbonate substitution. According to literature, A-type substitution is characterised by a doublet $\sim 1545 \text{ cm}^{-1}$ and 1450 cm^{-1} (Fleet, 2009), although in the same manuscript several orientations of A-type substitution are discussed which alter the band positions to 1540 cm^{-1} (a band was observed $\sim 1537 \text{ cm}^{-1}$ in the spectrum above) and 1449 cm^{-1} and 1569 cm^{-1} and 1507 cm^{-1} . An additional band $\sim 1470 \text{ cm}^{-1}$ was

observed in the A-type substituted samples, which was not observed in the B-type substituted samples, which is most likely a combination of the 1450 and 1545 cm^{-1} doublet described by Fleet.

In figure 3.2 the mean spectra of the samples provided by Prof. Rogers and Clarkson Chromatography are shown. For clarity, the spectra are normalised and shown with offset. Again, key band positions are indicated with blue vertical lines positioned at 873, 878, 960, 1030, 1410, 1455, and 1550 cm^{-1} .

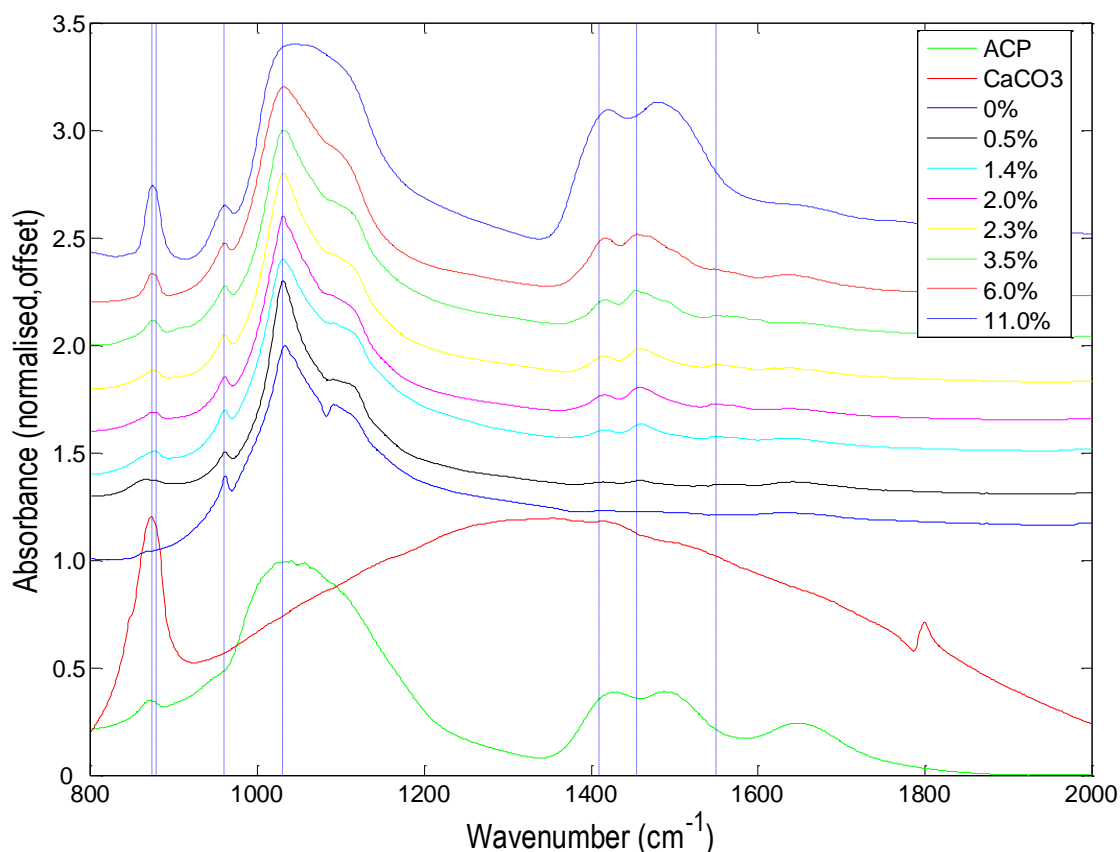


Figure 3.2: Infrared spectra measured from Clarkson Chromatography samples and samples provided by Prof. Keith Rogers (Cranfield University, Shrivenham). Measurements are normalised and for clarity shown with offset. The blue vertical lines indicate the key positions at 873, 878, 960, 1030, 1410, 1455, and 1550 cm^{-1} .

All apatites are said to be B-type carbonated. However, the band between 870 cm^{-1} and 880 cm^{-1} contains features for both A- and B-type carbonate substitution. Although the relative amount of both substitution mechanisms cannot be evaluated with FTIR, it is clear that the samples do not contain solely B-type substituted carbonate as claimed by the manufacturer.

Chapter 3

The phosphate band ($\sim 1030\text{ cm}^{-1}$) is slightly broader for amorphous calcium phosphate (ACP) and hydroxyapatites in which a larger amount of carbonate is incorporated which is due to distortion of the lattice. In contrast to the samples prepared in the Tecklenburg lab, no bands were observed $\sim 1134\text{ cm}^{-1}$. Bands characteristic for B-type carbonated substituted apatite are observed $\sim 1410\text{ cm}^{-1}$ and $\sim 1455\text{ cm}^{-1}$ (Fleet, 2009), although also a small band $\sim 1550\text{ cm}^{-1}$ which can be assigned to A-type carbonate substitution. Although carbonate substituted HAP and calcium carbonate (CaCO_3) both contain calcium and carbonate, it can be seen that the FTIR spectra do not show the same bands and therefore not the same chemical bonds are probed with FTIR.

In appendix A an overview of FTIR band assignments of calcified materials can be found.

3.1.1.1 Dilution experiments

The effect of sample dilution upon the shape of the spectral bands was tested by pressing KBr tablets with different amounts of apatite in them and measuring the FTIR spectrum. In figure 3.3, the measurements are shown for the 0.3 wt% and 1.8 wt% samples. Similar results were obtained from the samples with different amounts of calcification standard (data not shown).

Both samples show the characteristic phosphate band shape in the $1000\text{-}1200\text{ cm}^{-1}$ region. In the lower panel (1.8 wt% sample), a signal saturation artefact is seen in the spectrum displayed in cyan. The top of the band is flat with noise on top, and the bands in the $1400\text{-}1600\text{ cm}^{-1}$ region are much stronger than the other measurements on the same sample. The broadening of the phosphate band of the purple spectrum indicates saturation as well, although not in the same amount as the cyan spectrum.

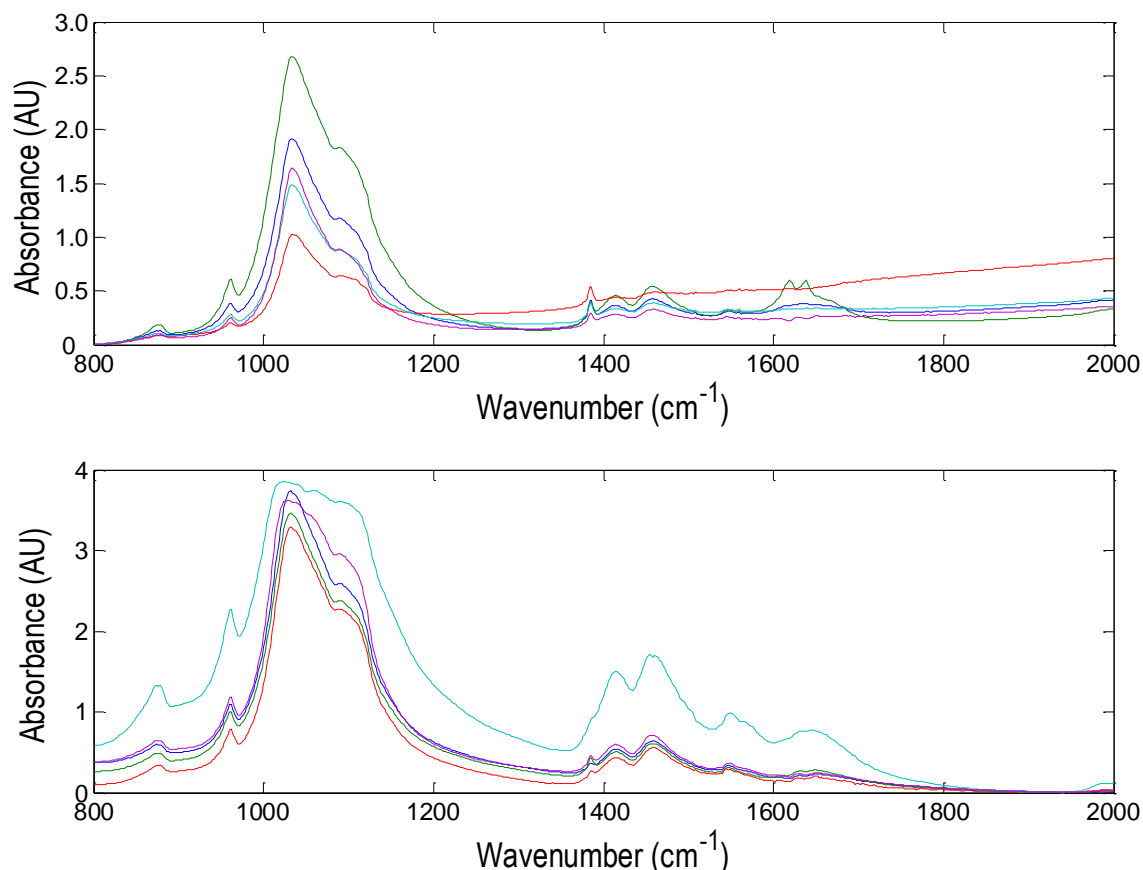


Figure 3.3: Results dilution experiments; Upper panel) Measurements on 0.3 wt% sample; Lower panel) Measurements on 1.8 wt% sample. Data is not normalised.

All spectra, when not saturated, showed the characteristic phosphate band shape consisting of one band $\sim 1030 \text{ cm}^{-1}$ with a strong shoulder $\sim 1090 \text{ cm}^{-1}$. During analysis it should be kept in mind that a spectrum is saturated in case this characteristic shape is lost.

3.1.1.2 Transmission FTIR versus ATR FTIR

In figure 3.4, the mean spectra of the transmission FTIR and ATR measurements on a 2.0% carbonate substituted apatite standards are shown. The carbonate bands in the $1400\text{-}1500 \text{ cm}^{-1}$ region of the transmission FTIR spectrum are much stronger than those in the ATR FTIR measurements. This could indicate that saturation is present in the transmission FTIR measurements. In the raw data, saturation is indeed visible (data not shown).

However, it should be noted that the intensity at higher wavenumbers is lower for ATR due to the wavelength dependence.

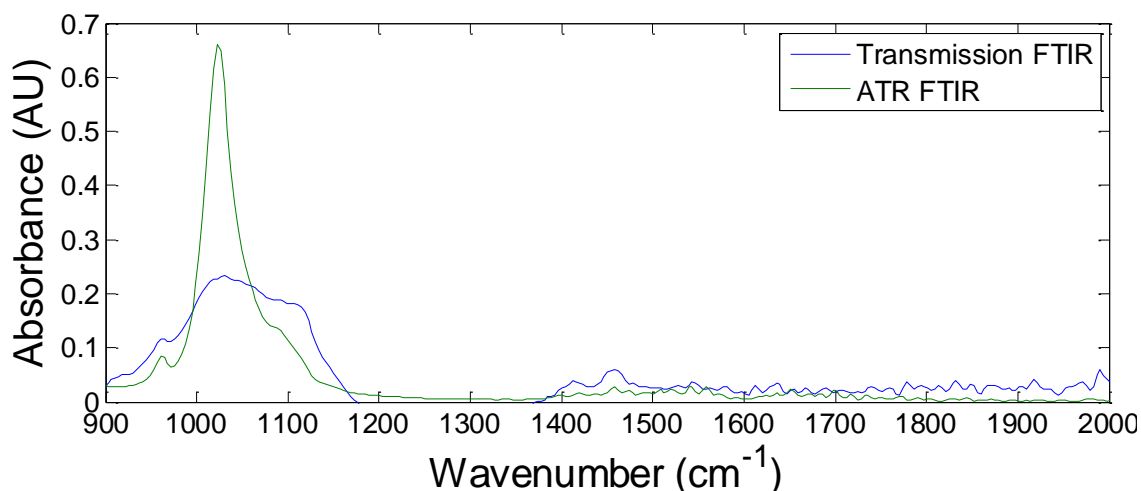


Figure 3.4: Mean ATR measurements (green) versus mean transmission FTIR (blue) on 2.0% carbonate substituted HAP standard. Spectra are not normalised.

Saturation would also explain the difference in the phosphate bandwidth (900-1200 cm^{-1}). During transmission FTIR measurements, light goes through the whole of the sample while the penetration depth during an ATR experiments is typically between 0.5 and 2 μm . The difference in penetration depth is related to the presence or absence of signal saturation.

ATR FTIR measurements were performed on the A- and B-type substituted samples, mean spectra are shown in figure 3.5.

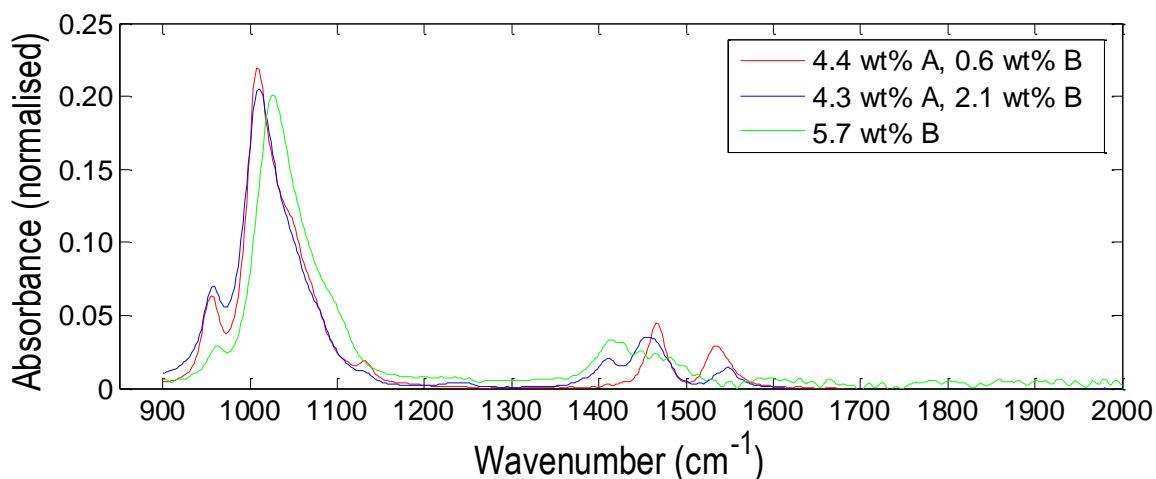


Figure 3.5: Mean spectra of ATR FTIR measurements performed on A- and B-type substituted calcification standards. Measurements are normalised.

Chapter 3

The location of the phosphate band shifts position depending on the type of carbonate substitution. The phosphate band of the fully B-type substituted sample is positioned $\sim 1027 \text{ cm}^{-1}$ (same as previously observed in 2.0% carbonate substituted sample), while the position of the partly A-type substituted sample is $\sim 1008 \text{ cm}^{-1}$ for the red spectrum and $\sim 1010 \text{ cm}^{-1}$ for the blue spectrum.

Considering the different ratio of A- and B-type substitution of both mixed samples (red and blue, respectively) one would expect a more pronounced difference in location of the phosphate band. This is however not visible in the mean spectra.

When plotting the different data sets, two for 4.4 wt% A and 0.6 wt% B (red) and three for 4.3 wt% A and 2.1 wt % B (blue), significant differences in band locations are found between measurements of the same sample (figure 3.6).

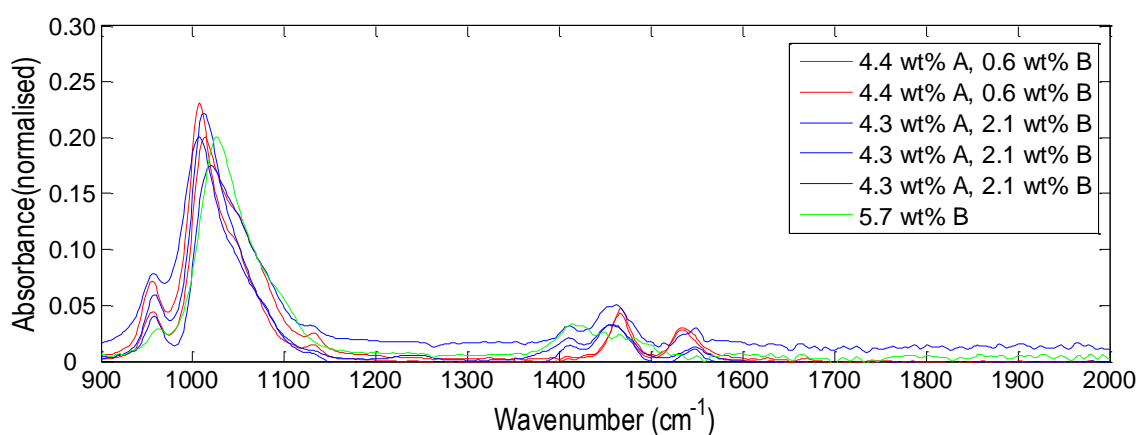


Figure 3.6: Mean spectra of each dataset performed on the A- and B-type carbonate substituted calcification standards. Measurements are normalised.

The band shift between the different samples seems to be a real phenomenon when plotting all data (figure 3.7).

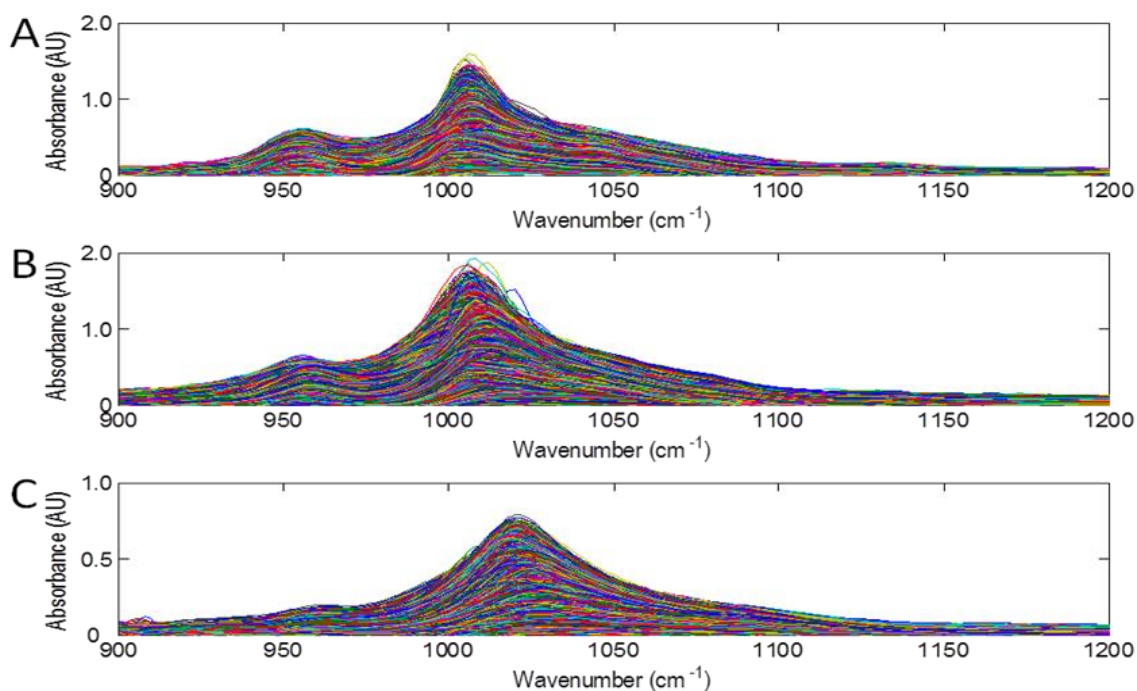


Figure 3.7: All ATR measurements on standards. A) Standard with 4.4 wt% A-type and 0.6 wt% B-type substitution; B) Standard with 4.3 wt% A-type and 2.1 wt% B-type substitution; C) Standard with 5.7 wt% B-type substitution.

However, when plotting the position and the area under the curve of the phosphate band over a line scan across a calcification (figure 3.8), it can be seen that the shift is related to the position of the measurement on the calcification.

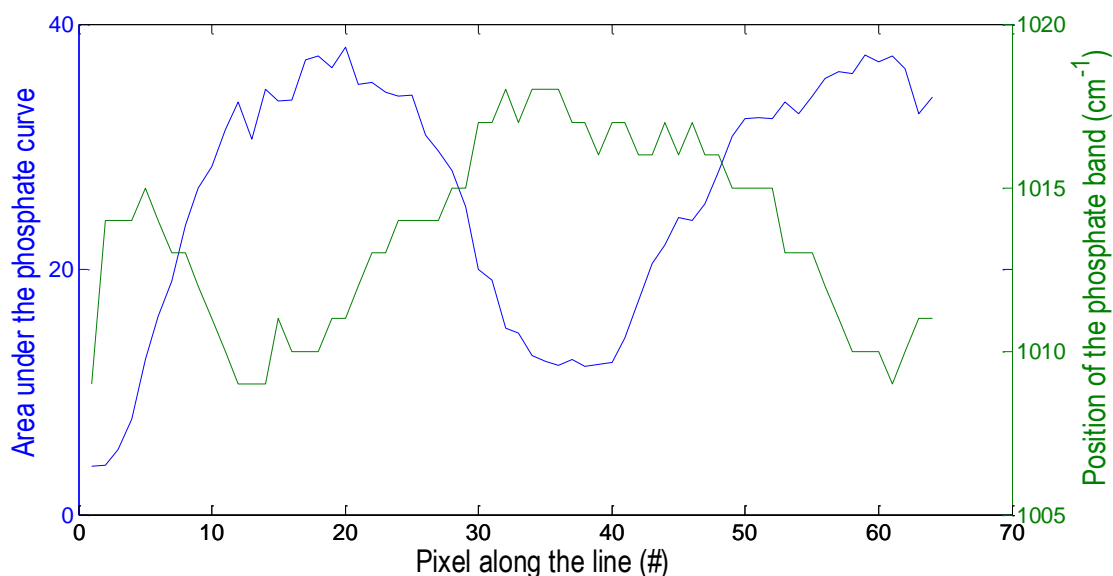


Figure 3.8: ATR FTIR measurements on calcification standard with predominantly A-type substitution. In blue the area under the phosphate curve along the line scan is depicted and in green the position of this band.

3.1.2 Raman microscope measurements on calcification standards

The Raman spectra of the samples prepared by the Tecklenburg lab were loaded into Matlab and the mean was plotted in figure 3.9. The percentages in the legend indicate the amount of B-type carbonate substitution, except for the samples depicted by the dotted red and blue line for which first the total amount of carbonate substitution is given followed by the amount of B- and A-type carbonate substitution.

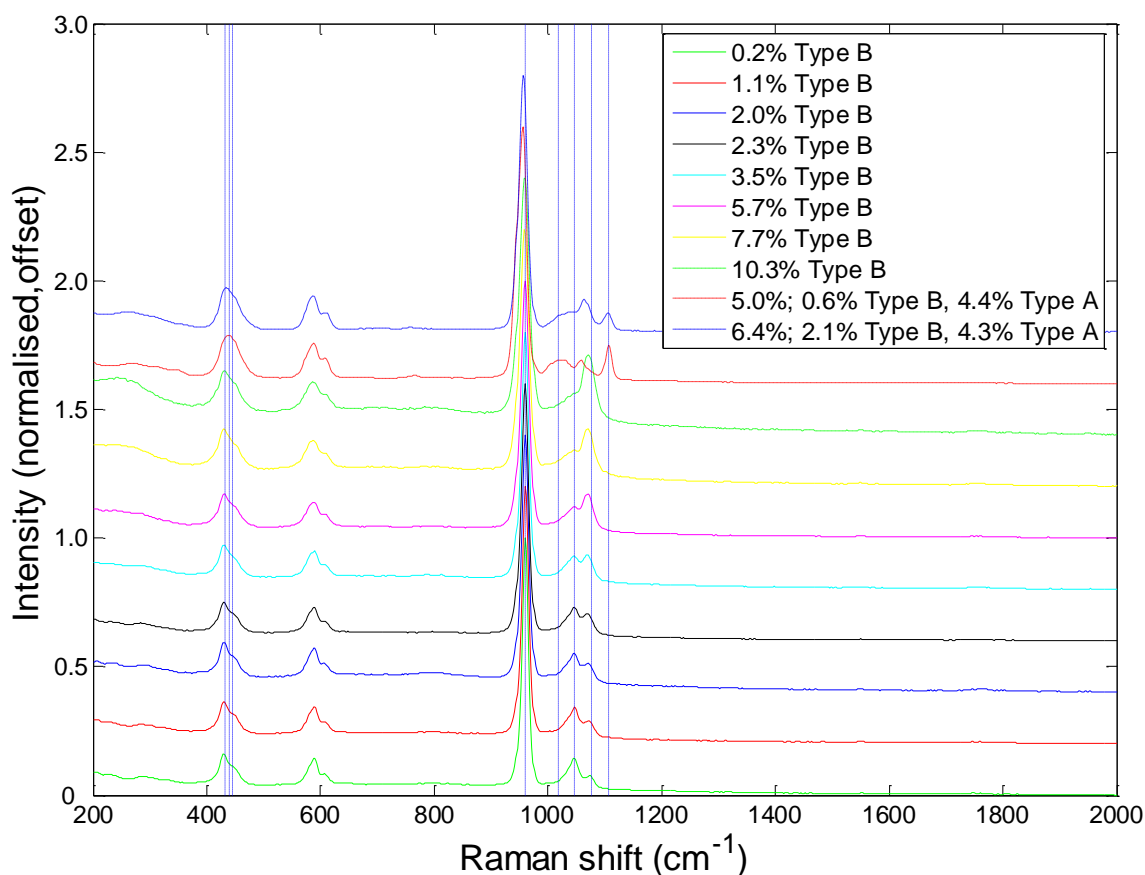


Figure 3.9: Mean Raman spectra (n=5) of samples Tecklenburg lab, 830 nm laser, 60s accumulation time. Measurements are normalised and for clarity shown with offset. The blue vertical lines indicate the prominent bands discussed in the text located at 432, 440, 445, 960, 1018, 1046, 1071, 1076, and 1106 cm^{-1} .

The most prominent band is the phosphate band in the 960 cm^{-1} region. The amount of calcium substitution for the B-type carbonate (carbonate for phosphate) substituted apatites reflects in the relative intensities of bands relating to carbonate and phosphate. The relative intensity of the 1046 cm^{-1} (phosphate) and $\sim 1071 \text{ cm}^{-1}$ (carbonate and phosphate) strongly depends on

the amount of carbonate substitution. For samples with a low amount of carbonate substitution the 1046 cm^{-1} band is the strongest, while for samples with higher amounts of carbonate substitution the intensity levels of the two bands are reversed.

Furthermore, a peak shift can be observed due to a change in intensity of underlying carbonate (1070 cm^{-1}) and phosphate (1076 cm^{-1}) modes (Awonusi et al., 2007). The samples with A-type substitution (CO_3 for OH, spectra with dotted lines) show an additional band $\sim 1106\text{ cm}^{-1}$, which is a carbonate mode characteristic for A-type substitution (Penel et al., 1998) and $\sim 1018\text{ cm}^{-1}$ which is a characteristic phosphate mode for A-type substituted apatite. In the lower wavenumber regions the phosphate band shifts depending on the type of substitution, the maximum for B-type substitution is located ~ 432 and $\sim 445\text{ cm}^{-1}$, while the maximum for A-type substitution would be $\sim 440\text{ cm}^{-1}$. Furthermore, it can be seen that the maximum of the sample with 4.4% A-type substitution with 0.6% B-type substitution (red dotted spectrum) is more shifted towards the maximum characteristic for A-type substitution in this region, than the sample with 4.3% A-type substitution and 2.1% B-type substitution.

Another batch of samples was prepared by Clarkson Chromatography and kindly provided by Prof. Keith Rogers. The apatites (all spectra except amorphous calcium phosphate (ACP) and CaCO_3) all exhibit B-type carbonate substitution and the mean (normalised) spectra are shown in figure 3.10. For clarity, the spectra are shown with offset. Again, key band positions are indicated with blue vertical lines. These lines are located at 432, 445, 960, 1046, and 1076 cm^{-1} . These positions are similar to those in the previous plot, although positions related to the A-type substitution are not displayed.

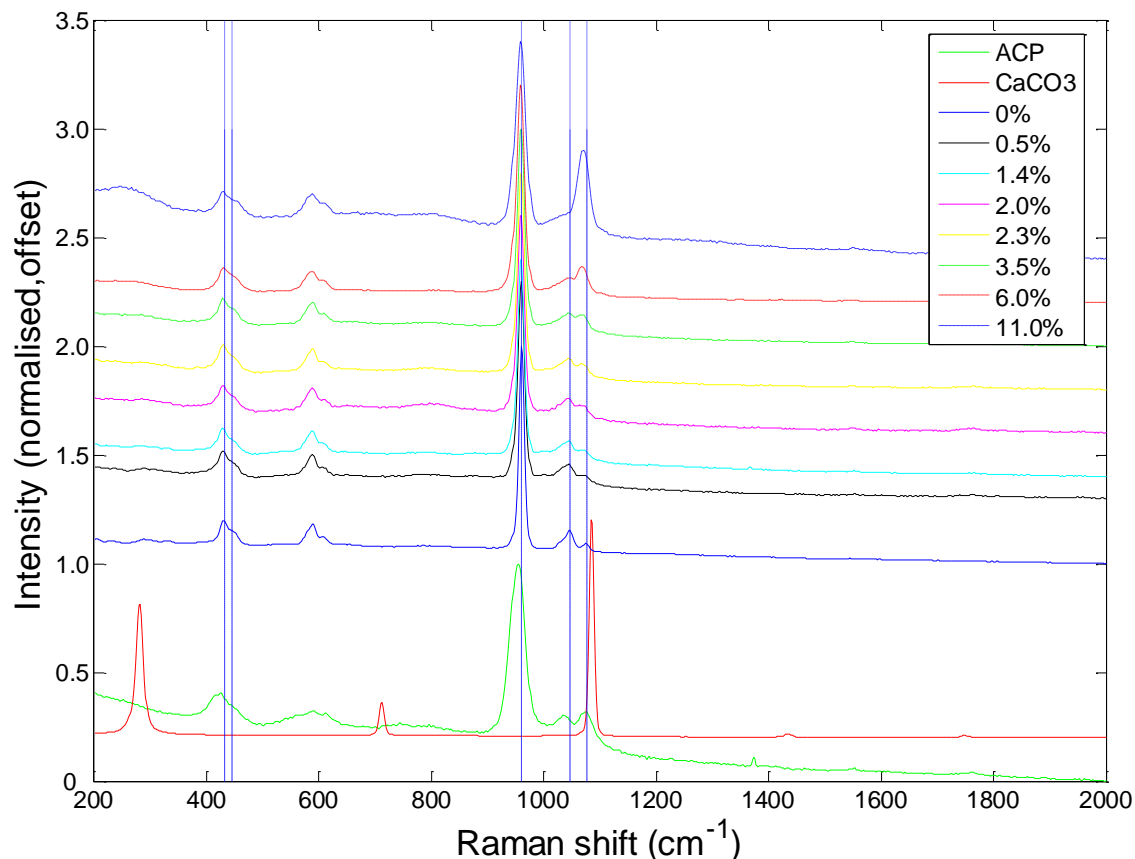


Figure 3.10: Mean Raman spectrum (n=5) for samples Rogers lab and Clarkson Chromatography. Key band positions are indicated with blue vertical lines positioned at 432, 445, 960, 1046, and 1076 cm^{-1} .

Amorphous calcium phosphate (ACP, depicted with solid green line) has bands very similar to apatite, while calcium carbonate (depicted with red solid line) does not show any of the characteristic apatite bands. Similar to the previous bands the relative intensities of the carbonate and phosphate bands change with increasing amount of (B-type) carbonate substitution. Although from the FTIR experiment it is known that these standards contain A-type substitution, this is less readily derived from the Raman experiments.

3.2 Comparison of spectroscopic techniques with pathology samples staining

In this study H&E, VK and AR staining is compared with FTIR mapping on pathology samples. FTIR provides both molecular and crystalline identification of calcified materials such as urinary stones (Volmer et al., 1993; Wilson et al.,

2010), kidney crystal deposits (Estepa and Daudon, 1997), and breast calcifications (Baker et al., 2010). A comparison between FTIR, Raman and the different stains could not be made here since the paraffin embedded tissue samples exhibited sufficient background signals in the Raman to prevent detailed analysis. Therefore, the performance of Raman spectroscopy is compared to FTIR, VK and AR staining on samples from a 4T1 mammary adenocarcinoma cell line in which calcifications are formed. Since these samples are grown for a specific amount of days, the calcifications are 'time stamped' and it can be investigated how soon the different techniques pick up the presence of calcifications.

FTIR imaging picked up additional calcification in all benign samples, in one case no positive staining was obtained with both AR and VK while calcifications were visible in the score plot of hydroxyapatite (figure 3.11). At these positions were indeed calcification spectra found in the original FTIR map (spectra depicted in figure 3.11). Additional measurements on benign samples can be found in appendix C.

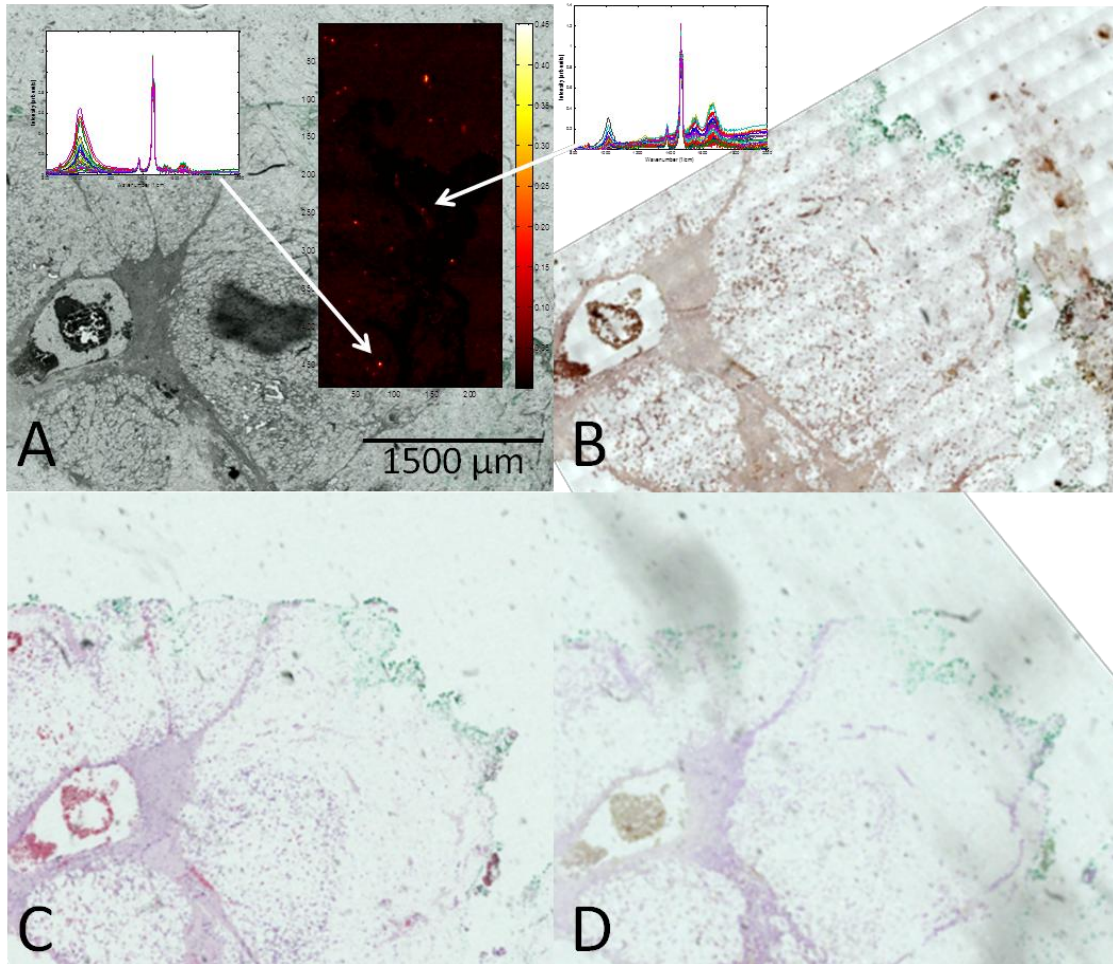


Figure 3.11: A) White light image of benign sample with overlaid the intensity fit of hydroxyapatite. Two calcifications are visible which are highlighted by a circle and spectral information is shown; B) Alizarin Red staining of adjacent slide; C) H&E staining of adjacent slide; D) von Kossa staining adjacent slide.

More calcifications were found within the *in situ* pathology samples than in the benign samples, although one sample was excluded from the dataset since it did not contain calcifications. In figure 3.12, an example of one of the *in situ* pathology samples is shown.

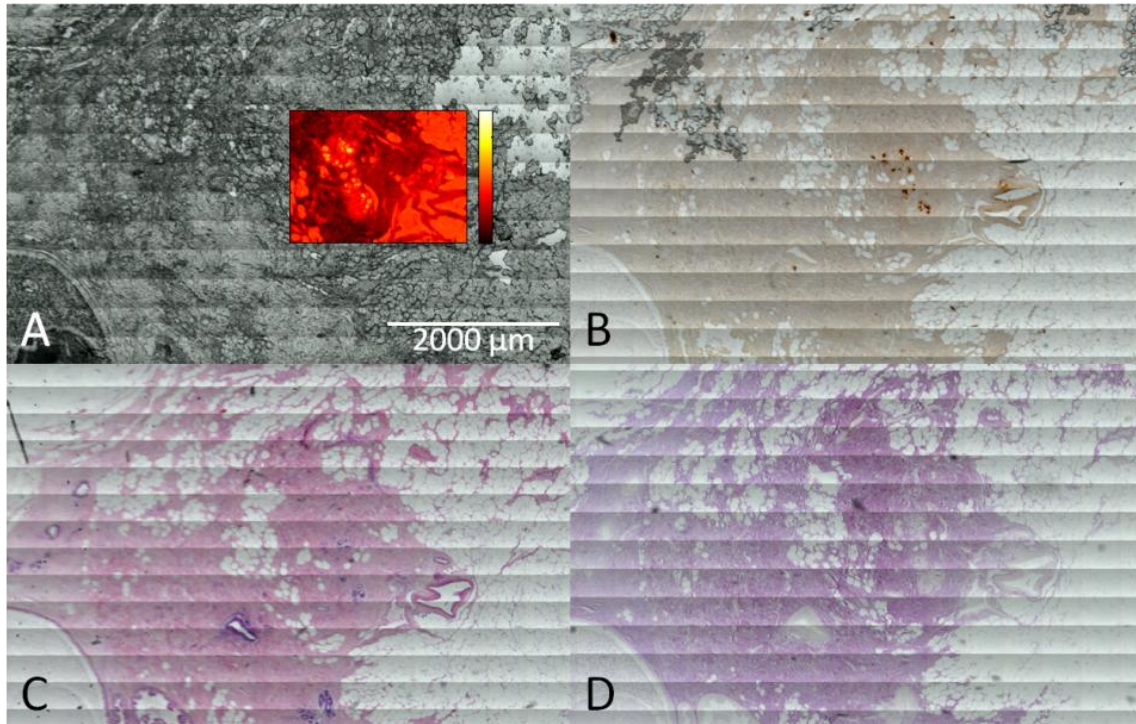


Figure 3.12: Measurements on sample with *in situ* pathology. A) White light image of sample, overlaid is the chemical component map for hydroxyapatite; B) Adjacent slide stained with Alizarin Red; C) Adjacent slide stained with H&E; D) Adjacent slide stained with von Kossa.

Calcifications were stained positively by both AR (panel B) and VK (panel D) and were demonstrated in the score plot of HAP (panel A, yellow/white). In all *in situ* samples the calcifications are more readily recognized in the AR staining than VK, which is mainly due to the area stained. Calcifications which appear as one larger calcification in AR are displayed as a cluster of smaller calcifications when stained with VK. In the FTIR map the calcifications are also a cluster of smaller inclusions.

In figure 3.13, a pronounced example of the extended stained area in AR staining is shown. The AR staining fills the whole of the ducts while von Kossa staining and FTIR show more localized calcifications.

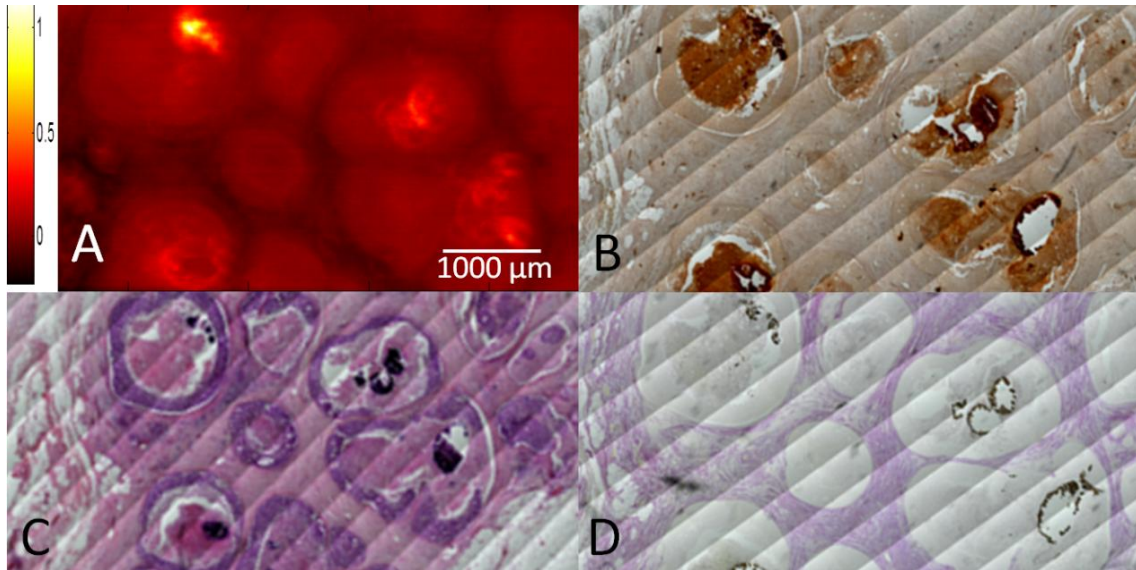


Figure 3.13: Sample with *in situ* pathology. A) Score plot of the hydroxyapatite; B) Alizarin Red staining of adjacent slide; C) H&E staining of adjacent slide; D) Von Kossa staining of adjacent slide.

The calcifications are stained by the H&E (purple) as well, but it should be noted that H&E only gives structural and no chemical information – the walls of the ducts are stained purple as well (figure 3.13). Most of the calcifications within the *in situ* pathology samples are located in the ducts of the breast and are more clearly visible by AR staining and FTIR imaging than VK staining. Additional measurements on samples with *in situ* pathology can be found in appendix C.

In the set of invasive samples studied here (additional measurements in appendix C), the number of calcifications was larger than in the samples with *in situ* or benign pathology. Furthermore, the calcifications were not located solely in the ducts but distributed across the whole of the sample (figure 3.14).

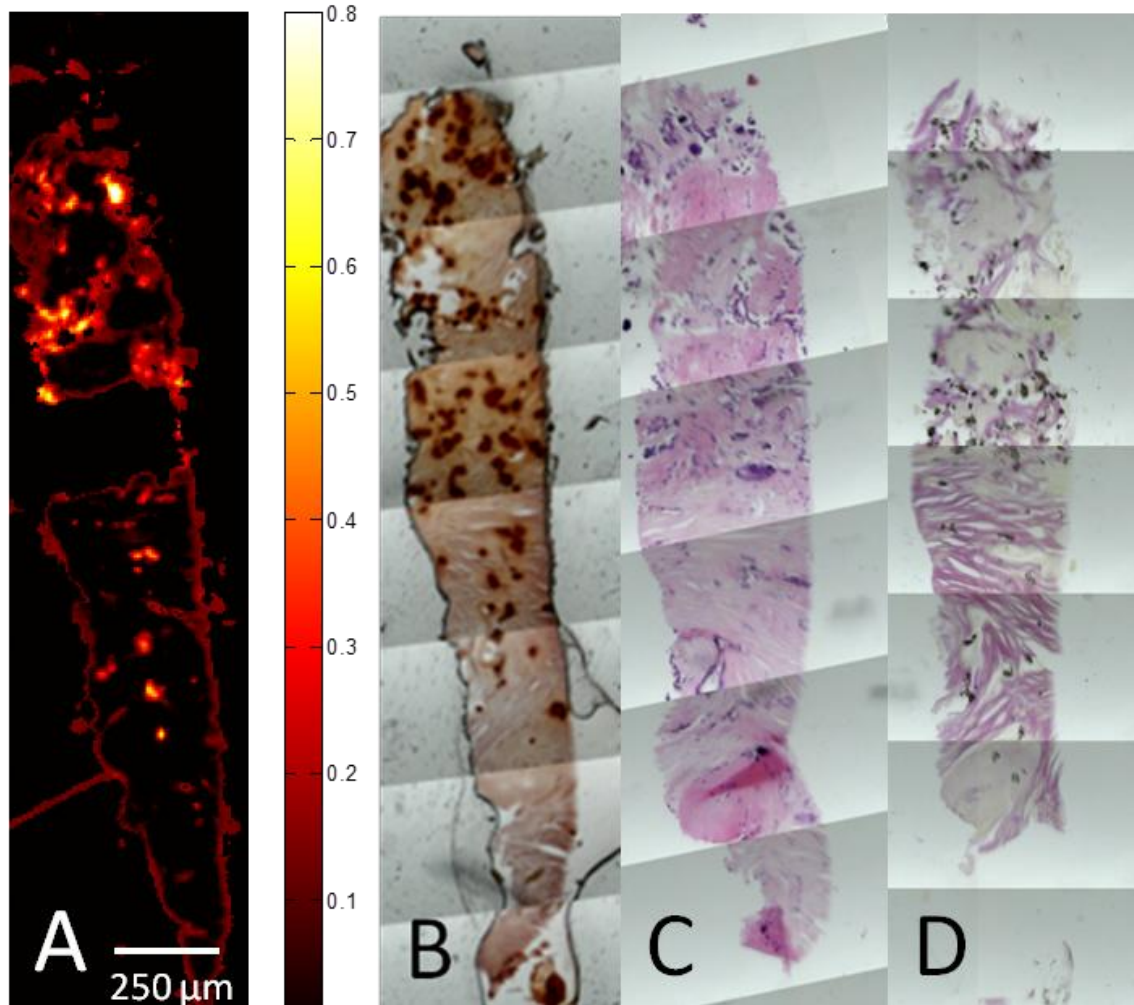


Figure 3.14: Invasive sample A) Scores of the chemical component map of hydroxyapatite; B) Alizarin Red staining on adjacent slide; C) H&E staining of adjacent slide; D) Von Kossa staining of adjacent slide.

In figure 3.15, the displaying method of the FTIR maps (biochemical fit) is compared to simply displaying the intensity of the characteristic apatite band centred $\sim 1030\text{ cm}^{-1}$ for the benign (panel A and B) and in situ sample (panel C and D) shown in figure 3.11 and 3.13. In general, displaying the intensity will be sufficient when the calcification signals have a high intensity. With lower intensity artefacts such as scattering on the edge of the sample and slightly varying background signals will dominate and result in a large number of false positives.

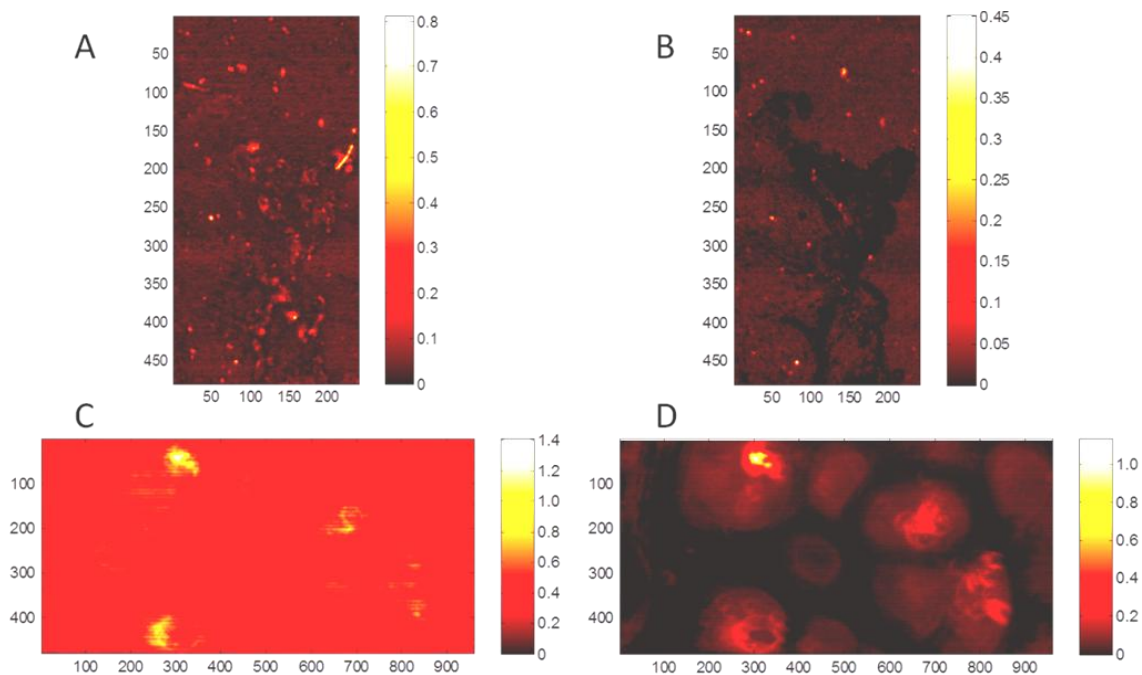


Figure 3.15: Comparison of intensity of the 1030 cm⁻¹ phosphate band characteristic for apatite to biochemical fit of apatite. A) Intensity of the apatite band on benign sample; B) Biochemical fit of apatite on benign sample (same as in A); C) Intensity of the apatite band on in situ sample; D) Biochemical fit of apatite on in situ sample (same as in C).

The 4T1 *in vitro* mineralisation model allows temporal analysis of mammary cell mineralisation to take place. Positive AR staining was first observed in osteogenic cocktail treated 4T1 cells after 11 days and the intensity and extent of staining increased with time (figure 3.16 A). Positive VK staining of replicate samples was consistently more discrete and less extensive than AR staining. However, when replicate samples were analyzed using the B22 beamline, no calcifications were detected at 11 or 14 days. One very small calcification was present in the area measured of the cells grown for 17 days and calcifications were also present in samples grown for 21 days in osteogenic cocktail (figure 3.16 B).

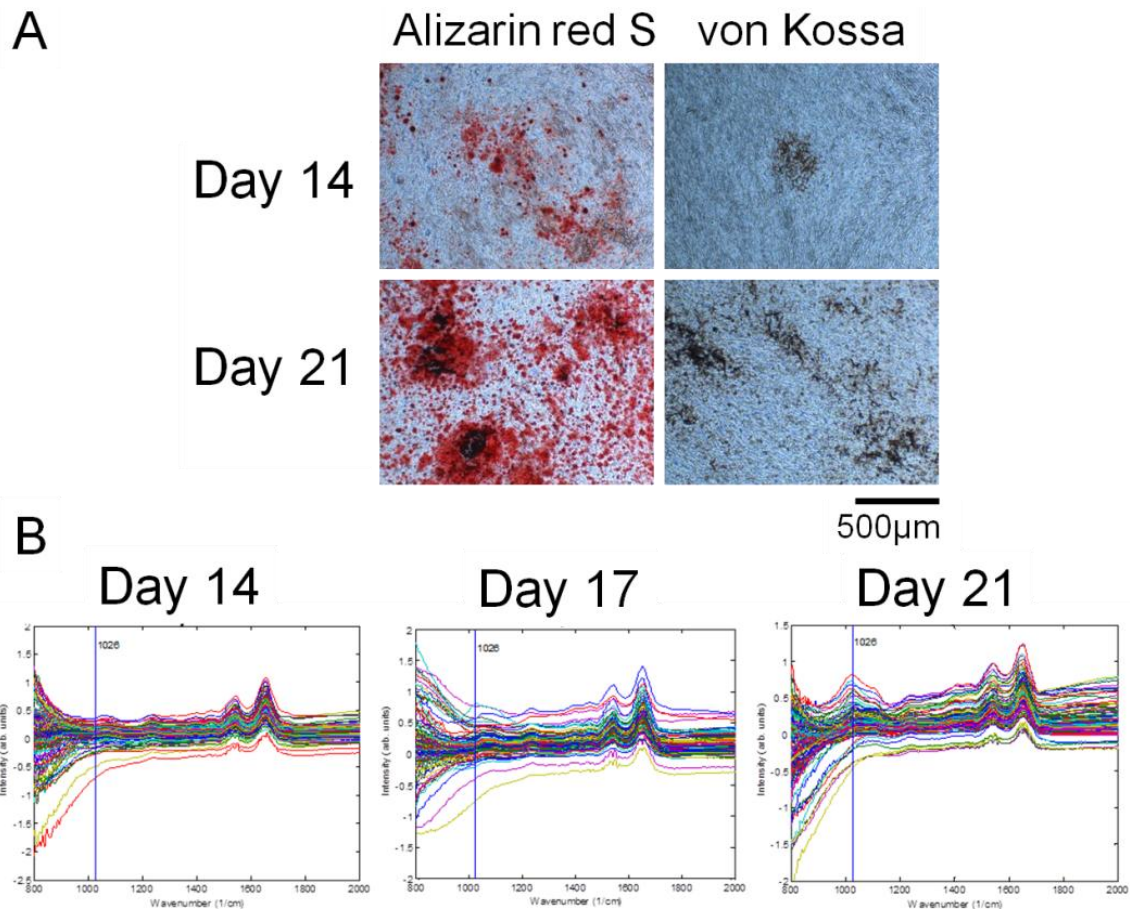


Figure 3.16: Mineralization of mammary 4T1 cells. A) Alizarin red and von Kossa staining of 4T1 cells grown in the osteogenic cocktail for 14 and 21 days; B) Measurements Diamond synchrotron on 4T1 cells grown for 14, 17, or 21 days in osteogenic cocktail. The blue line indicates the position of the 1026 cm^{-1} band characteristic for apatite. One spectrum displaying apatite was found on the sample that matured for 17 days, while apatite was abundant in the sample matured for 21 days. No apatite was found in the sample matured for 14 days.

Additional measurements were undertaken on the FTIR Spotlight system. Measurements on the sample grown for 17 days (figure 3.17 A) showed only one pixel with the characteristic calcification band $\sim 1030 \text{ cm}^{-1}$. On the map taken on a sample grown for 21 days large numbers of calcifications were found (figure 3.17 B).

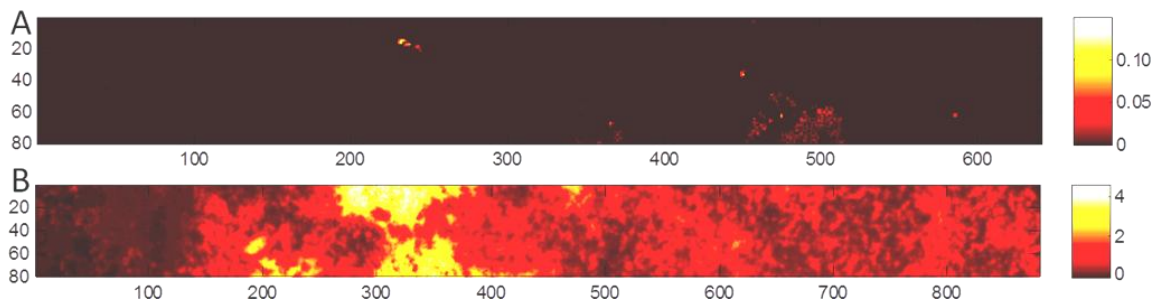


Figure 3.17: FTIR mapping 4T1 cell line grown in osteogenic cocktail. A) Apatite fit on map of sample grown for 17 days; B) Apatite fit of map of sample grown for 21 days.

Raman imaging (figure 3.18) was consistent with FTIR imaging, although no calcifications were found on samples grown for 17 days. This is probably due to the low density of calcifications in the samples (in IR mapping experiment 1 pixel in a map-size of 51840 pixels). In the 21 days matured sample, abundant calcifications were also found with Raman.

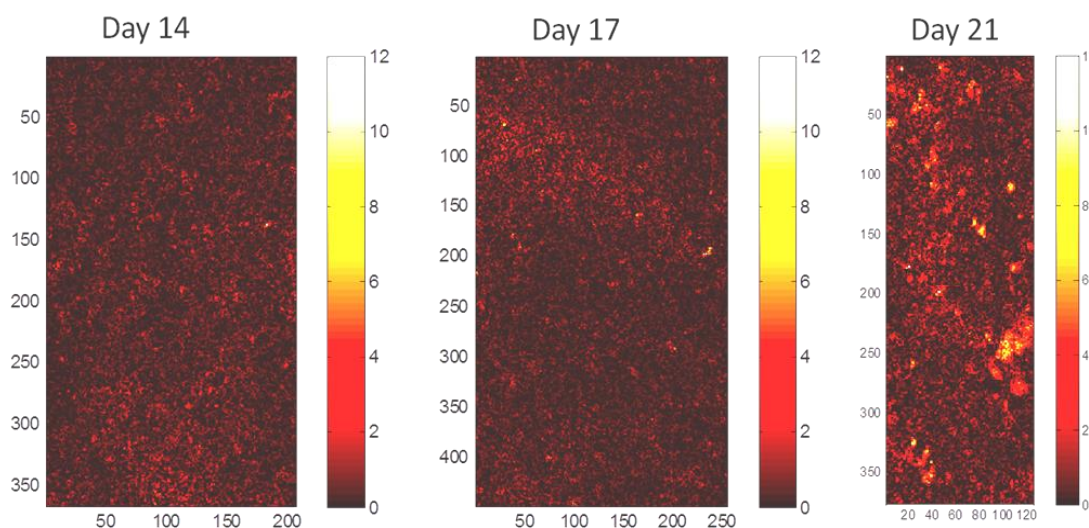


Figure 3.18: Intensity of the phosphate band in the Raman maps of 4T1 cell line grown in osteogenic cocktail for 14, 17, and 21 days.

An overview of the different techniques and their outcome is shown in table 3.1.

	14 days	17 days	21 days
Alizarin Red stain	++	+++	++++
Von Kossa stain	+	++	+++
Raman mapping	N	N	Y
FTIR	N	Y	Y
Synchrotron FTIR (Diamond)	N	Y	Y

Table 3.1: Overview of the techniques used to analyse the time course of 4T1 cell mineralisation and their ability to detect calcifications in the different samples.

Staining: + = sparse, ++ = moderate, +++ =extensive, ++++ = very extensive.
Detection of calcification: Y = yes, N= no.

3.3 Synchrotron FTIR imaging of breast calcifications

In this study the composition of breast calcifications in tissue from different ranges from the pathology spectrum (benign, *in situ*, and invasive) and their surroundings are studied with synchrotron FTIR. Synchrotron FTIR provides a higher signal intensity (and thus higher sensitivity) and spatial resolution than that available from a benchtop FTIR system.

3.3.1 General observations and challenges

Targeting of calcifications for the synchrotron studies proved difficult. It was attempted to localise calcifications on the FTIR benchtop system and marking their position in the white light images before samples were taken over to synchrotron facilities. The distance between the calcification and different features of the pathology slides, for example ducts, could then be used to find the calcifications on a different system. Especially for the pathology samples mounted on barium fluoride this is difficult, due to the circular shape of the substrate which makes it harder to mount the sample in the same orientation every single measurement. Furthermore, it was hard to distinguish paraffin deposits from calcifications, since both resulted in darker areas when using the transmission illumination and glowing areas in the reflection illumination. Recently, the illumination at the IRENI beam line has been adapted to fibre optics. This enhanced the contrast significantly and when the reflection mode is applied paraffin patches glow up (depending on thickness) while the calcification patches did not. When taking white light images with both the transmission and the reflection settings, paraffin can thus be distinguished from calcification patches.

Another challenge was that all systems obtained slightly different white light images. In figure 3.19, an example of the differences is shown. The white light

images of one of the used pathology samples (*in situ* pathology) are shown. The same region is shown in each panel which is measured on the Spotlight benchtop system (panel A), UK's Diamond synchrotron (Bruker system, panel B), and USA's IRENI beamline (Bruker system, panel C). Again, the new illumination at the IRENI beamline improved the contrast significantly compared to the data shown in figure 3.19.



Figure 3.19: White light image of the same area on three different setups A) Spectrum Spotlight 400 microscope and Spectrum One; B) Bruker 80V FTIR and Hyperion 3000 microscope B22 beamline, Diamond Light Source Ltd (Oxfordshire, UK); C) Vertex 70 FTIR spectrometer and Hyperion 3000 IR/VIS microscope from Bruker, IRENI beamline, Synchrotron Radiation Center (University of Wisconsin, USA).

One of the other drawbacks of using white light images measured on the benchtop system as a reference is that the samples degrade over time which means the sample is not always in the same condition as it was when previously mapped. In figure 3.20, the same *in situ* sample is shown measured twice with nine months in between. In this time the sample was shown to lose substantial calcification content, likely due to mechanical vibrations from handling and transportation.

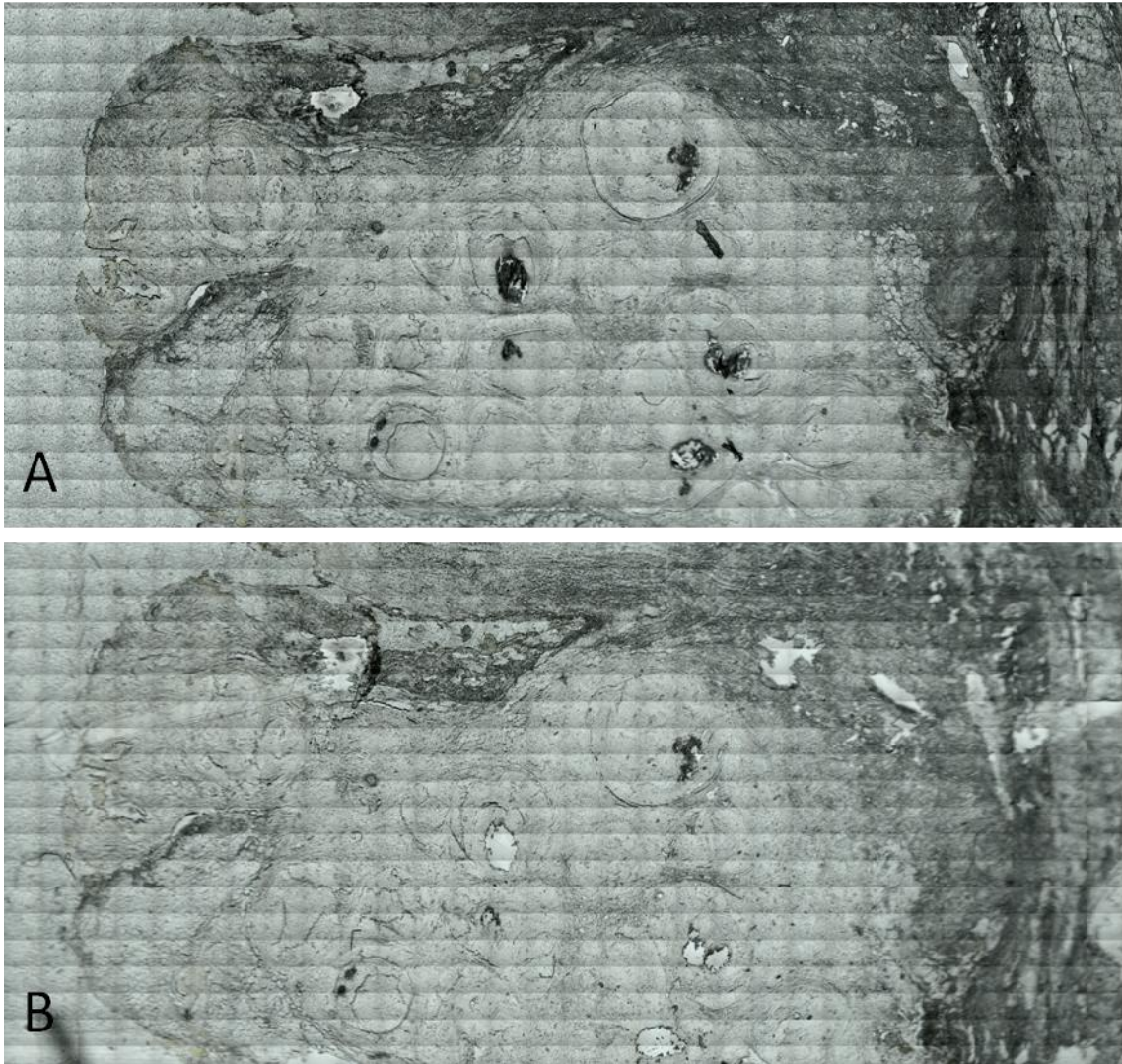


Figure 3.20: Illustration of sample degradation over a nine month period A) sample in April 2011; B) sample in January 2012.

3.3.2 Results from Diamond beamtime allocation SM6123

Larger patches of calcifications were found to be extremely dense in terms of IR transmission and saturated the FTIR absorption. This feature was not observed in the measurements done on the benchtop IR imaging system which is likely due to the use of an aperture at the Diamond beam line while measurements at the benchtop system are done without an aperture and light can potentially bypass the calcification and consequently not provide a true account of its absorption on the benchtop system.

It was therefore attempted to measure some of the less dense calcifications which would show less saturation, shown in figure 3.21. PCA was applied to this dataset and line scans were analysed on this map based on principal component 3 which showed a characteristic apatite band in the positive direction (calcification intensity high in red on score plot shown in panel C).

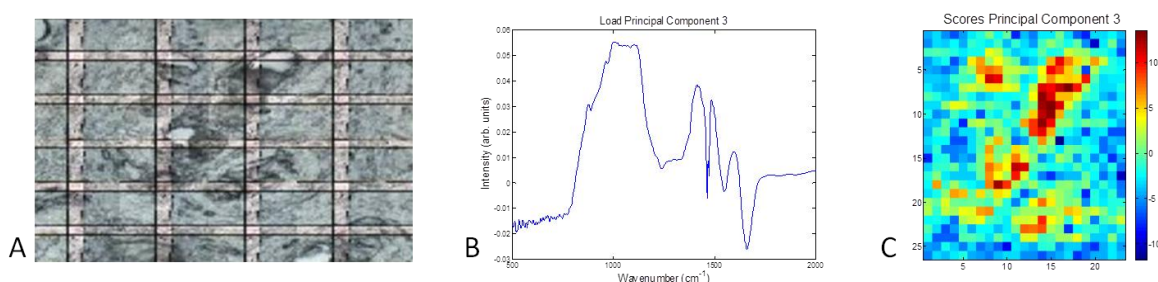


Figure 3.21: Area sample 4694 (*in situ* pathology) measured on the B22 beam line of Diamond Light Source Ltd and Principal Component Analysis of this measurement. A) White light image of the sample measured; B) Load PC3; C) Score PC3.

One feature of interest is the mineral content which is commonly given by the phosphate: amide I ratio (Faibish et al., 2005). In benchtop studies by Baker (2010) an increase in amide:phosphate ratio was observed in calcifications from increasingly malignant tissue. When the different grades were grouped together, the mean amide:phosphate ratio were 0.8278, 0.3717, and 0.1114 for ‘invasive’, ‘*in situ*’, and ‘benign’, respectively. However, it is unknown whether the observed differences in amide intensity are due to higher amide concentration in the calcification or to higher contributions of amide from the surrounding tissue (Baker et al., 2010; Haka et al., 2002).

A linescan (row 7) was selected from the map and broken into two linescans, pixel 1-12 and pixel 14-23, each covering one calcification area. Both the phosphate band and the amide I band were selected in Matlab and the area under the curve was calculated for each pixel. In figure 3.22, the raw data of both lines (panel A and C) are shown together with the area under the curve for both the phosphate and the amide I band (panel B and D). The maxima of the phosphate bands are visible at pixel 9 and 16. The phosphate band of the second calcification (panel C) is heavily saturated and a reliable area under the curve cannot be obtained. The score plot in figure 3.21 shows that the first

Chapter 3

calcification is less dense, and the spectra in panel A from figure 3.22 are indeed less saturated. From the area under the curve calculation can be seen that at the position of the calcification a local minimum is found for the area under the amide I curve. There is however amide present in all calcification spectra.

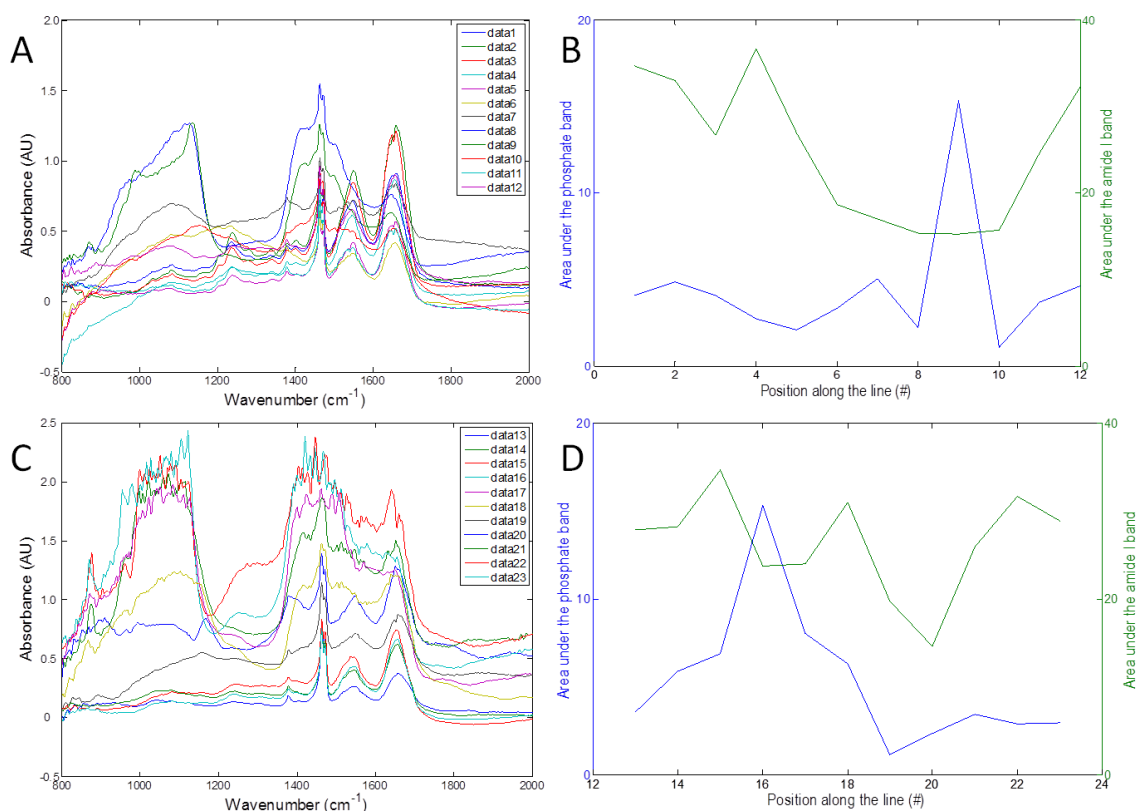


Figure 3.22: Measurements sample 4694 (in situ pathology) on B22 beamline Diamond Lightsource Ltd. A) Spectra of pixel 1:12 of row 7; B) Area under the phosphate (blue) and amide I (green) curve; C) Spectra of pixel 13:23 of row 7; D) Area under the phosphate (blue) and amide I (green) curve.

The data resulting from the first beam time allocation was rather limited, as was the quality. Therefore, the calcification/tissue interface could not be studied and a new proposal was submitted. To improve the quality of future data the transparency of different windows was tested. The transmission of zinc selenide (ZnSe), barium fluoride (BaF₂), calcium fluoride (CaF₂), and zinc sulphide (ZnS) were tested on the Perkin Elmer Spotlight benchtop system for use in a new sample batch. All measurements were done in transmission and point mode

(120 scans) with the auto correction function on, and an interval of two wavenumbers. Measurements on the slides are shown in figure 3.23.

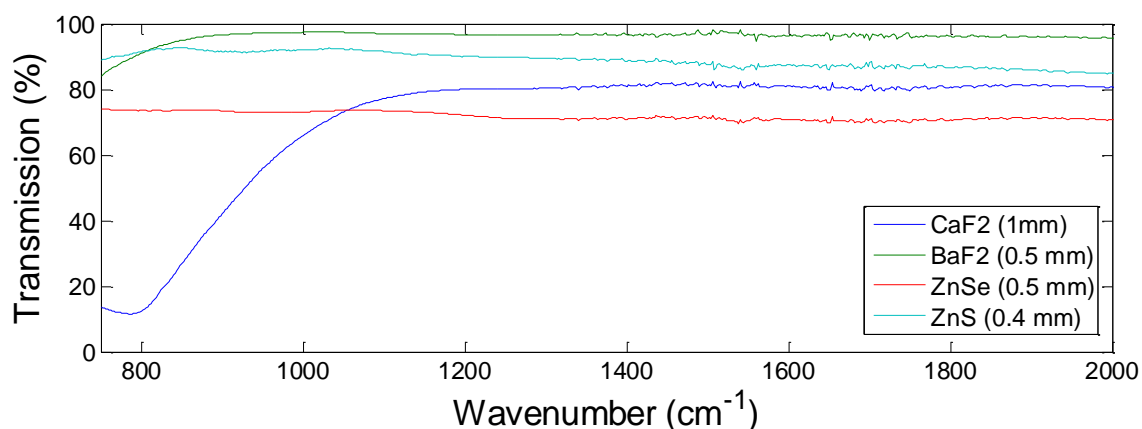


Figure 3.23: Transmission of the tested substrates (an air measurement is taken as background). Note that the thickness of the substrates is not equal.

From the experiments on the different windows it became clear that calcium fluoride (dark blue line) absorbs strongly under 1000 cm^{-1} . Therefore, it was decided that for future experiments barium fluoride windows with a thickness of 0.5 mm would be used which have a greater transparency over the calcification region ($\sim 1030\text{ cm}^{-1}$). Furthermore, the pathology samples themselves would be cut thinner ($6\text{ }\mu\text{m}$) in order to enhance the light intensity transmitted throughout of the sample.

When using the imaging mode of the Spotlight benchtop system no aperture was applied. On the experiments carried out at the Diamond synchrotron an aperture of $15\times 15\text{ }\mu\text{m}$ (in later experiments $10\times 10\text{ }\mu\text{m}$) was used, which yielded a saturated signal on most of the studied calcifications. Experiments were done on the Spotlight benchtop system to investigate the signal quality when similar aperture settings were performed. Brightness of the synchrotron is not due to higher total power but due to a higher flux density (higher power/area) which is due to the small effective source size and the narrow range of angles the light is emitted into. Therefore, a higher throughput is measured through a small aperture compared to a global source with a comparable aperture.

In figure 3.24, spectra are shown which are measured on the Spotlight benchtop system with a $10\times 10\text{ }\mu\text{m}$ and $100\times 100\text{ }\mu\text{m}$ apertures. The spectra

obtained with a 10x10 μm aperture on the Spotlight benchtop system show saturation in the phosphate region, albeit not in the same degree as the measurements performed at the Diamond synchrotron, while when the same area is measured with a 100x100 μm aperture on the same instrument no saturation is observed.

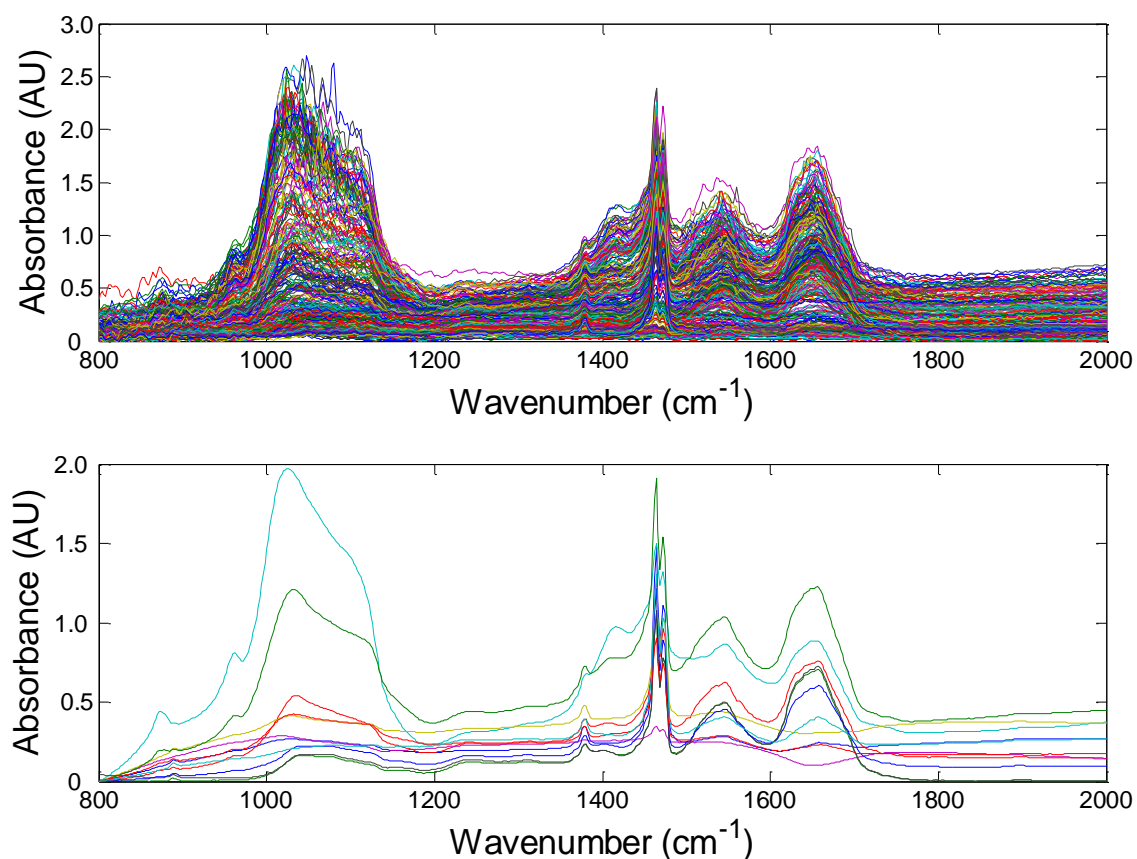


Figure 3.24: Comparison of a 10x10 μm (top panel) and a 100x100 μm aperture (bottom panel). The same 200x500 μm area was measured with both settings on the Perkin Elmer Spotlight.

3.3.3 Results from Diamond beamtime allocation SM6605

During the second beam time allocation samples from different range of the pathology spectrum (benign, *in situ*, and invasive) and their could be studied. Two calcifications from a patient with benign breast disease (pathology report: fibroadipose connective tissue with focal microcalcifications) were mapped. The white light image of the first calcification is depicted in panel A of figure 3.25. In

panel B and C the intensity plot of the phosphate band (characteristic for apatite) and the amide I band are depicted, respectively.

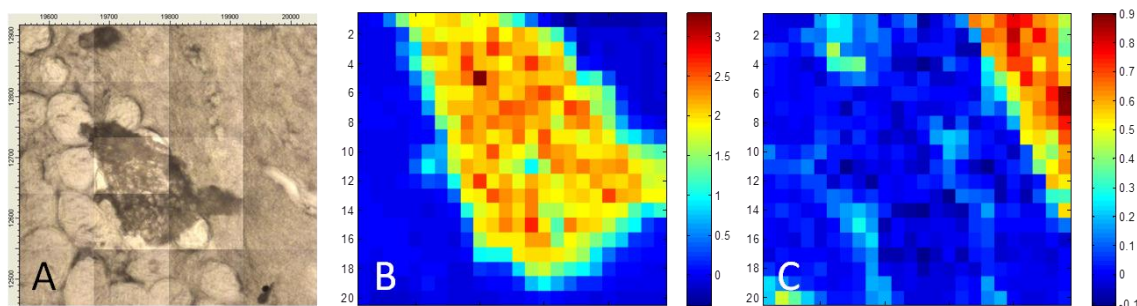


Figure 3.25: Sample with benign pathology measured at Diamond Light Source Ltd A) White light image of the sample; B) Intensity plot of the phosphate band (background corrected); C) Intensity plot of the amide I band (background corrected).

It can be seen that the intensity (absorption) of the amide band is highest directly next to the calcification patch, although not all around it. From the biochemical fitting of paraffin and line scans through the map it becomes clear that all other sides of the calcification patch are surrounded by paraffin (figure 3.26).

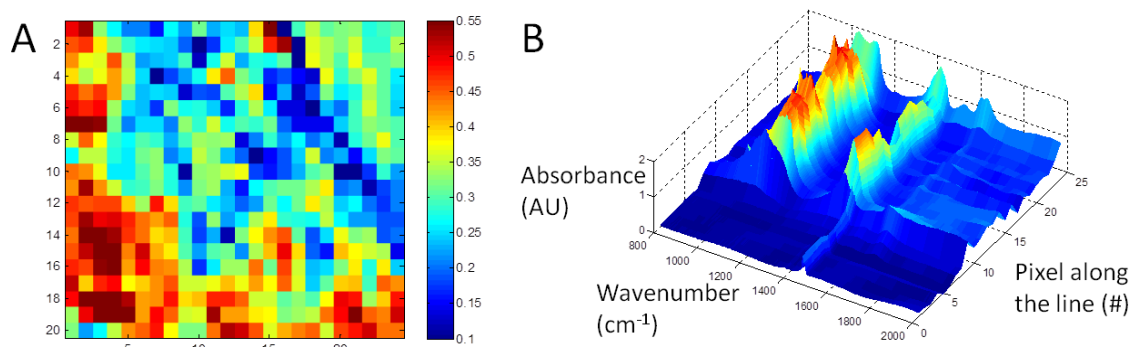


Figure 3.26: Sample with benign pathology measured at Diamond Light Source Ltd A) score plot of paraffin fit; B) Line scan (row 14) over the calcification.

In panel B, the line scan over row 14 is shown. The first seven pixels only show the characteristic paraffin spectrum; a single band $\sim 1378 \text{ cm}^{-1}$ and a doublet $\sim 1462 \text{ cm}^{-1}$ and $\sim 1472 \text{ cm}^{-1}$. Amide I and amide II bands ($\sim 1660 \text{ cm}^{-1}$ and $\sim 1550 \text{ cm}^{-1}$, respectively) were only observed on the edges of the calcification, in the interior a band was observed $\sim 1624 \text{ cm}^{-1}$. This band is one of the characteristic COM (calcium oxalate monohydrate) peaks (Maurice-Esteva et al., 2000) or OH vibration due to water inclusion in apatite (Seregin and Coffey, 2006; Wilson et al., 2010). The latter seems more probable, considering none of

the other characteristic COM peaks; such as the 1316 cm^{-1} band (Maurice-Esteva et al., 2000) are observed and water bands are observed in the 3000 cm^{-1} region. The characteristic phosphate band has its maximum $\sim 1110\text{ cm}^{-1}$ in the middle of the calcification area, but the phosphate maxima of the outermost spectra of the calcification region are found more towards lower wavenumbers. According to Rey (1991b) bands at 1110 and 1125 cm^{-1} are present in newly precipitated apatite, which will disappear progressively during maturation. Furthermore, a strong band $\sim 1440\text{ cm}^{-1}$ is found in the calcification spectra. Biological apatites are usually described as carbonate substituted hydroxyapatite. Carbonate can be included in the lattice in several ways; in type A the hydroxygroup is substituted by carbonate and in type B the phosphate groups is substituted by carbonate (Peroos et al., 2006). According to Akonakos et al. (2007) a band $\sim 1444\text{ cm}^{-1}$ is characteristic for A-type carbonate substitution, while bands ~ 1409 and $\sim 1427\text{ cm}^{-1}$ are characteristic for B-type substitution.

The second calcification in the benign specimen is found in the area shown in panel A of figure 3.27. The spectra corresponding to the calcifications and the rest of the (10×13) map are shown in panel B. The calcification is surrounded by paraffin and no interface with tissue can be studied. The $1010\text{-}1020\text{ cm}^{-1}$ phosphate band is assigned to non-stoichiometric apatite in the formative phase (Chiou et al., 2010).

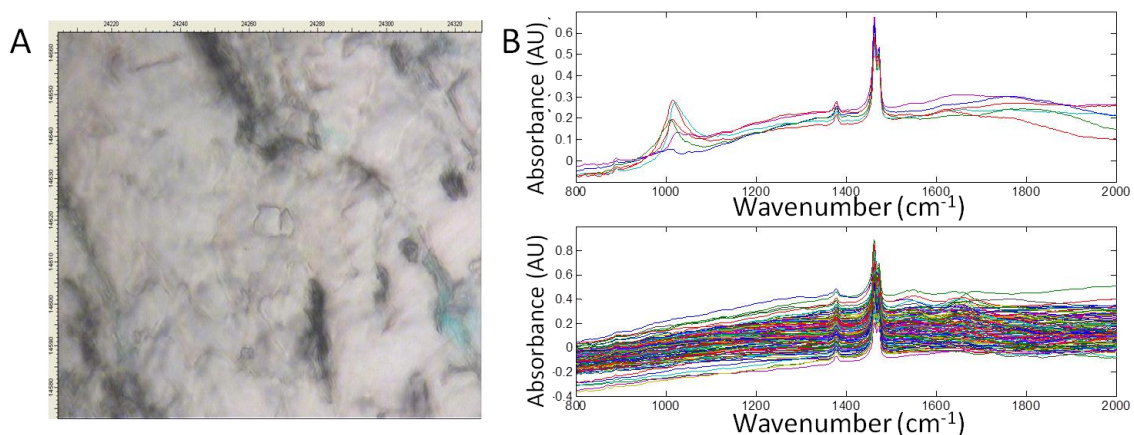


Figure 3.27 Sample with benign pathology measured at Diamond Light Source Ltd. A) White light image of the sample; B) Spectra corresponding to the calcification (top) and its surroundings (bottom panel).

Chapter 3

During the beam time allocation three maps were taken on samples DCIS. Two maps were taken on a sample with low grade DCIS and one on a sample with high grade DCIS. Furthermore, line scans were done on four other calcifications in the high grade DCIS sample.

The first map on the low grade DCIS is shown in figure 3.28A. On this map several calcifications are present, but they are quite small and scattered all over the map. A line scan which consisted calcifications (row 3) is shown in panel B.

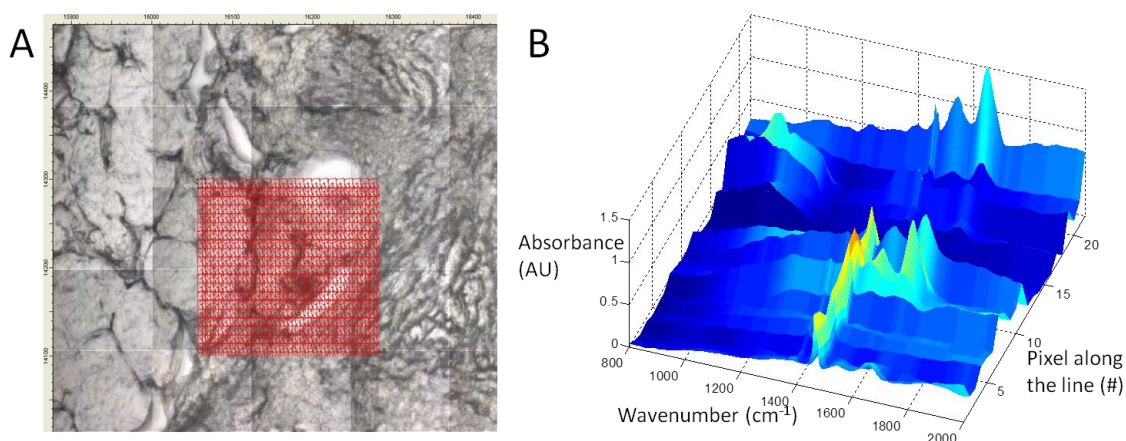


Figure 3.28: Sample with *in situ* pathology (low grade) pathology measured at Diamond Light Source Ltd. A) White light image of the sample; B) Line scan (row 3) over the map.

The spectra corresponding to pixel 16-20 are shown in figure 3.29. These spectra do show amide I and amide II bands. The phosphate bands are all distorted which indicates that the edge of the calcification is measured which results in an artefact due to the scattering of the light on a sphere with a size very similar to the wavelength of the light (Mohlenhoff et al., 2005). When measuring both tissue and calcification a mix of both signals is expected.

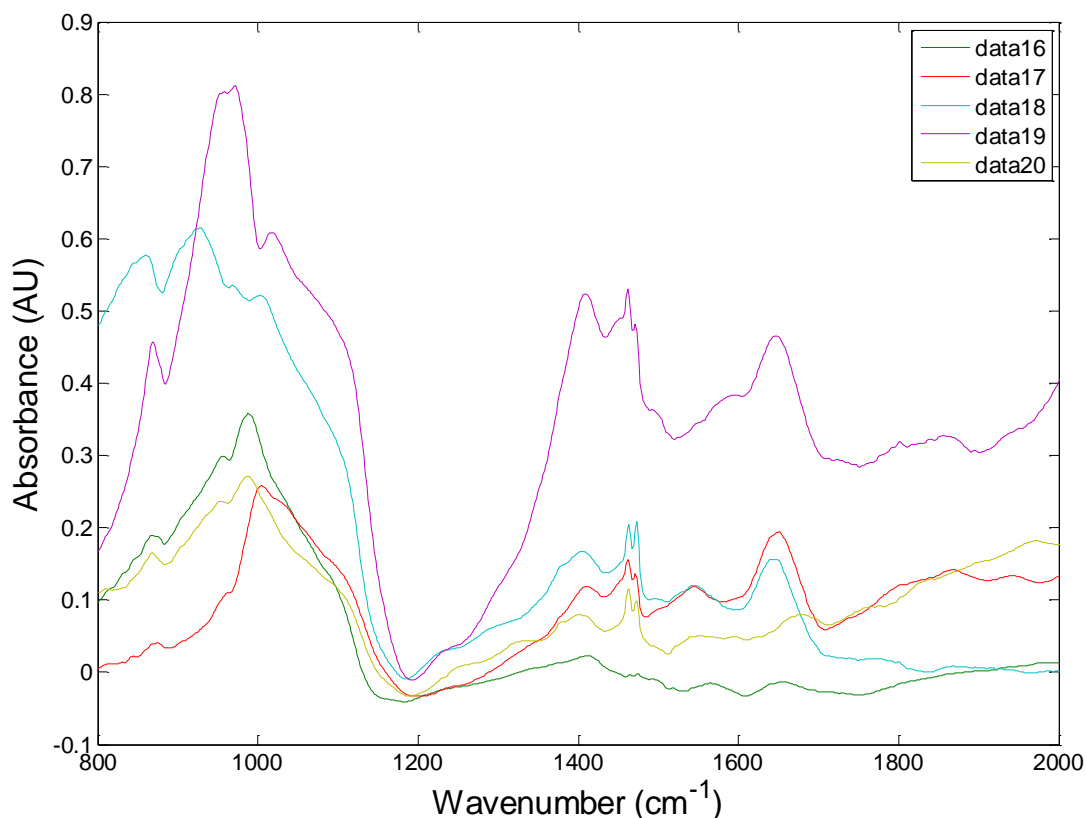


Figure 3.29: Sample with *in situ* (low grade) pathology measured at Diamond Light Source Ltd. Spectra of pixel 16-19 of row 3 of the map shown in figure 2.28.

A strong band is visible left of the paraffin doublet. In contrast to the previous sample, the position is not $\sim 1440 \text{ cm}^{-1}$ but $\sim 1408 \text{ cm}^{-1}$ which is characteristic for B-type carbonate substitution (Antonakos et al., 2007).

Findings from the second map measured (16x22) on the sample with low grade *in situ* pathology were similar to the previous map; a strong band $\sim 1408 \text{ cm}^{-1}$ is found in spectra showing a phosphate band. Again the phosphate bands are distorted and pixels corresponding to calcifications are spread over the map (data not shown).

The third map was measured on a sample with high grade *in situ* pathology. The white light image of the calcification is shown in panel A of figure 3.30. In contrast to the other *in situ* samples, this is a localized larger calcification or cluster of smaller ones which results in less distortion in the spectra. The score plot of the biochemical fit of apatite over the map is shown in panel B of the same figure.

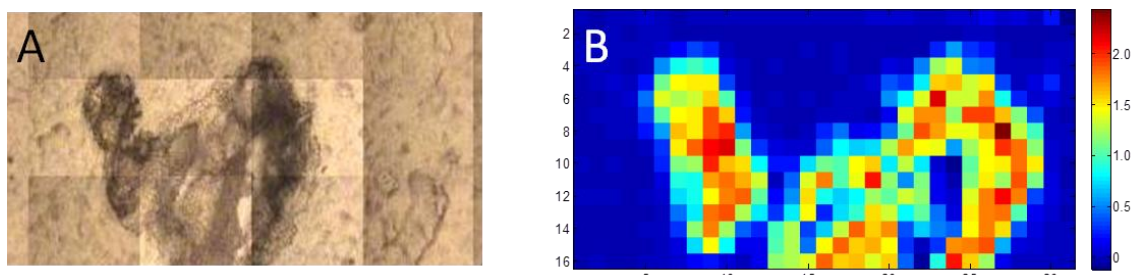


Figure 3.30: Sample with *in situ* pathology (high grade) measured at the Diamond Light Source Ltd. A) White light image of the studied calcification; B) Score plot of the apatite biochemical fit.

Line scans were selected from the map and the area under the curve for the phosphate and amide I band were plotted. In contrast to the benign samples, all spectra in which the phosphate band was present also showed the amide I and amide II bands. An example of one of the line scans (row 9) is shown in the figure below. The area under the curve is given for both the phosphate (blue) and amide I (green) band in panel B. The area under the curve for the phosphate band is not reliable in all cases, due to saturation of the phosphate band which influences the area under the curve.

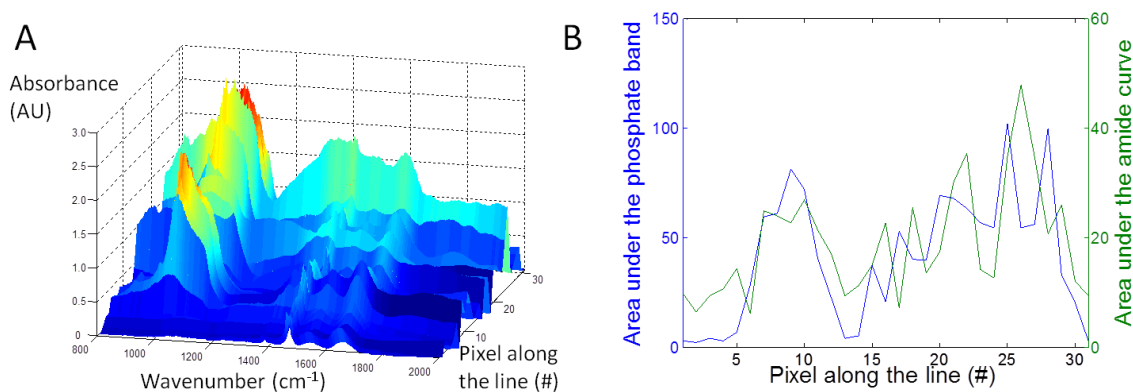


Figure 3.31: Example of line scan over sample with *in situ* (high grade) pathology. A) Spectra of row 9; B) Area under the curve for phosphate (blue) and amide I (green) band.

A ratio plot of the amide and phosphate is shown in figure 3.32 which will compensate for variations in sample thickness and scattering artefacts of the background.

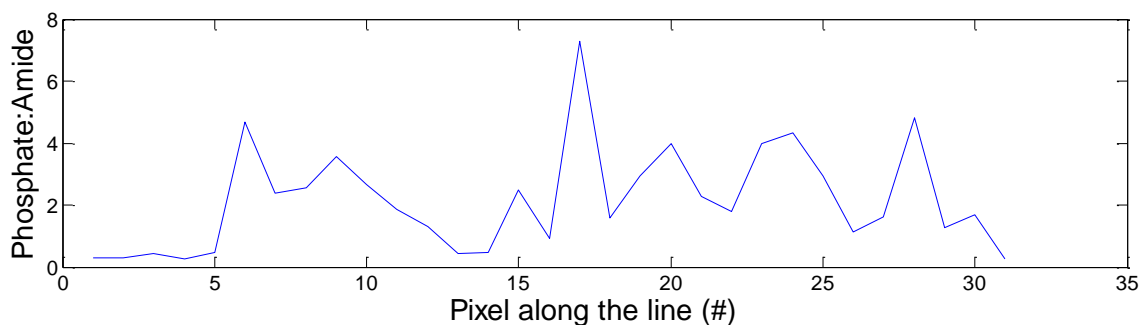


Figure 3.32: Ratio plot of the phosphate: amide of the data shown in figure 3.31 B.

The amount of spectra showing saturation in the characteristic phosphate band is significant; which is more clearly displayed in figure 3.33A where the spectra of row 9 are shown. In panel B of the same figure the spectra of pixel five to thirteen are shown which correspond to the first calcification area and only show minor saturation in the phosphate region. The shape of the phosphate band seems to be different at the edges of the calcifications compared to the middle, although it is unclear at this point in time whether this is genuine or an artefact. The band in the $1410\text{-}1420\text{ cm}^{-1}$ region is characteristic for B-type carbonate substitution. In contrast, the spectra of the second calcification area also show a band (1440 cm^{-1}) characteristic for A-type carbonate substitution.

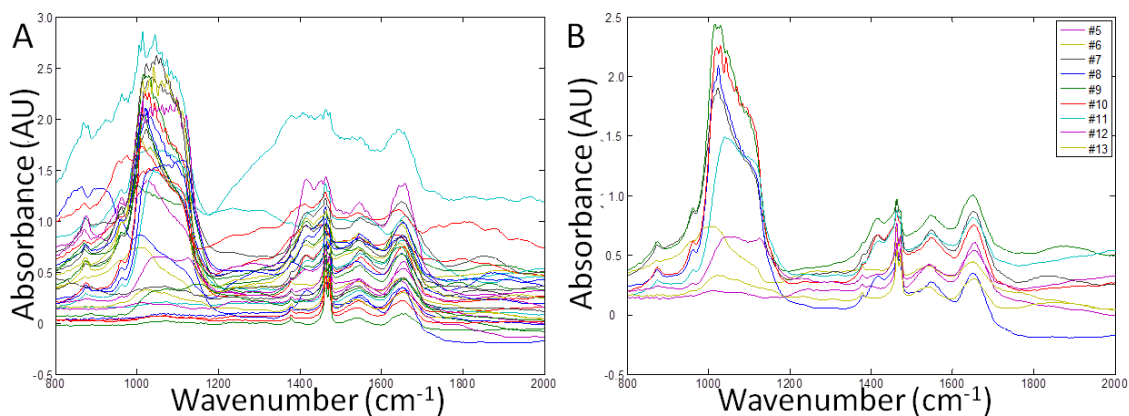


Figure 3.33: Line scan over sample with *in situ* (high grade) pathology A) All spectra of row 9; B) Spectra 5:13 of row 9.

Additional line scans were done on four calcifications in the last sample. White light images of these calcifications are shown in figure 3.34.



Figure 3.34: White light images of the line scans done over calcifications with *in situ* pathology A) White light image corresponding to data in figure 3.35 and d 3.36; B) White light image corresponding to data in figure 3.37 and 3.38; C) White light image corresponding to data in figure 3.39 and 3.40; D) White light image corresponding to data shown in figure 3.41 and 3.42.

The first line scan is shown in figure 3.35 below. The spectra are shown in panel A and the area under the curve for the phosphate (blue) and amide I (green) band in panel B. The area under the curve for the phosphate band shows a maximum between pixel 25 and 35, which indicates the position of the calcification area. Again, the phosphate band is saturated on multiple occasions so the value of the area under the curve should not be used for quantitative purposes. On both sides of the calcifications of the calcification patch (pixel 10-25, and pixel 35-40, respectively) a minimum can be found for the area under the curve of the amide I band. When investigating the spectra in panel A, it becomes clear that these pixels only show a paraffin spectrum and no tissue contribution is present. The area under the curve for the amide I band at the calcification path (pixel 25-35) is similar to the intensities found at the tissue (pixel 0-10, and pixel 40-50, respectively).

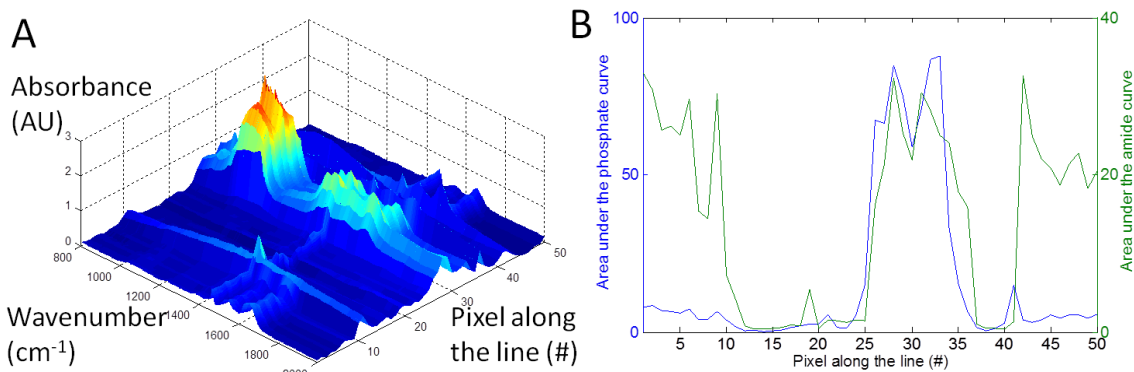


Figure 3.35: A) Spectra correlating to the line scan sample with *in situ* pathology; B) Area under the curve for phosphate band (blue) and the amide I band (green) over the line map.

In figure 3.36 the phosphate:amide ratio of the data is displayed.

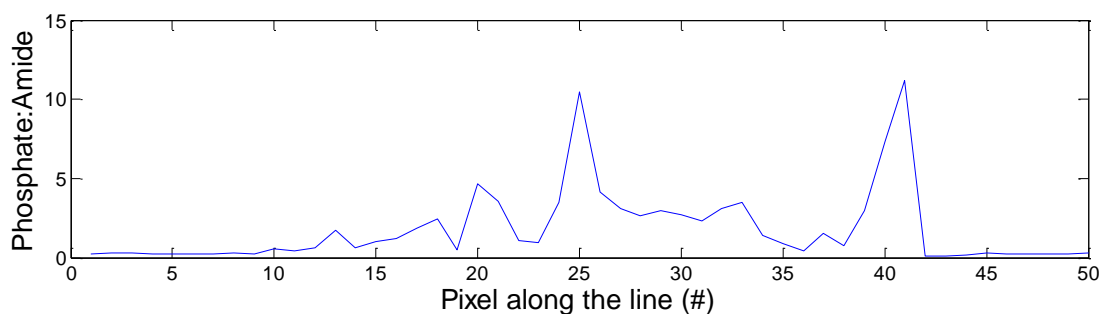


Figure 3.36: Ratio plot of the data shown in figure 3.35 B.

Both bands characteristic for A- and B-type carbonate substitution were present in the calcification spectra, although the intensity of the bands characteristic for B-type were higher than those characteristic for A-type carbonate substitution.

Similar results were found in the second line scan. The spectra of this line scan and the area under the curve for the phosphate (blue) and amide I (green) curve are shown in figure 3.37 and the relative intensity (phosphate:amide ratio) in figure 3.38. Again the calcification was surrounded by paraffin and not by tissue which resulted in the minimum value found for the area under the amide I curve both left and right of the calcification (pixel 12-24, and pixel 36-38, respectively).

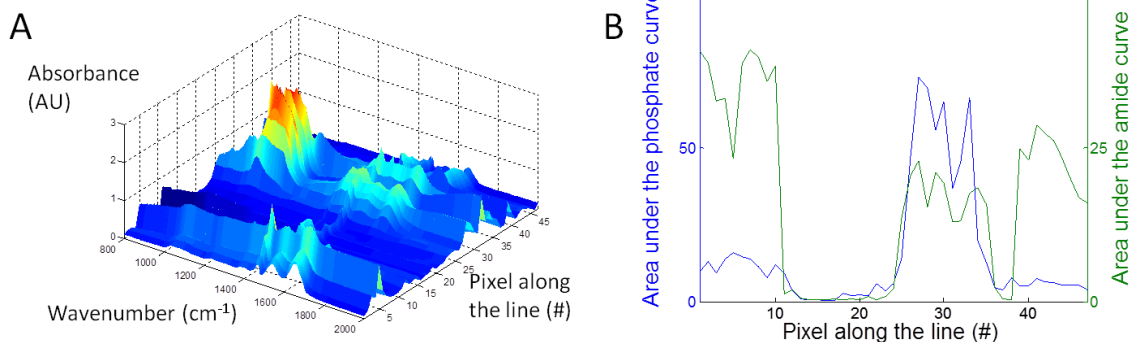


Figure 3.37: A) Spectra correlating to line scan with *in situ* pathology; B) Area under the curve for phosphate (blue) and amide I (green) band over the line map.

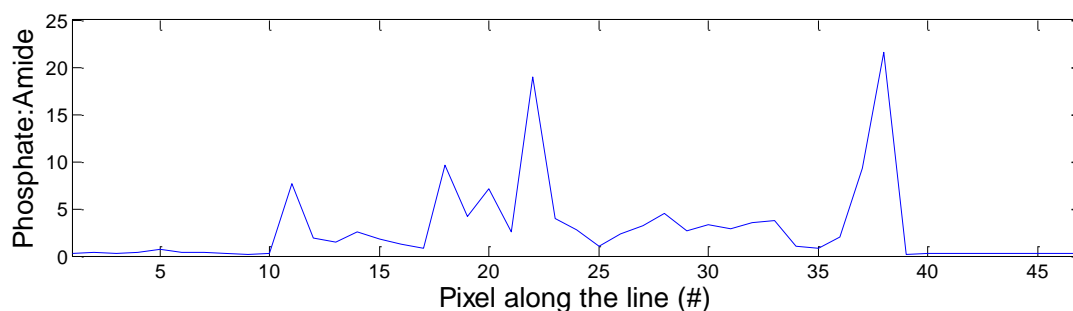


Figure 3.38: Ratio plot of the data shown in figure 3.37 B.

The third line scan is taken over a calcification embedded in tissue. The spectra of this line scan (panel A) and the area under the curve for the phosphate (blue) and amide I (green) curve (panel B) are shown in figure 3.39 and the phosphate:amide ratio in figure 3.40. The calcification is located at pixel 30:70. Unfortunately, most of the phosphate bands are saturated so the area under the curve for the phosphate band cannot be used quantitatively. The area under the curve of the amide I is very similar in the area of the calcification and the surrounding tissue.

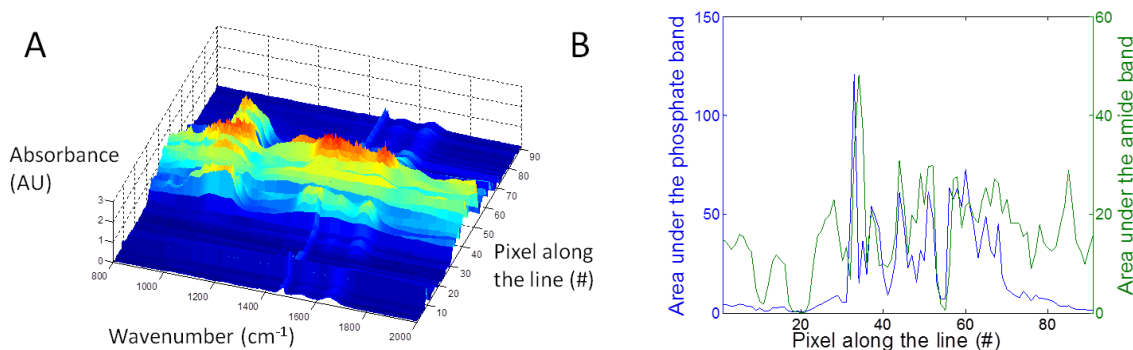


Figure 3.39: A) Spectra correlating to the line scan with *in situ* pathology; B) Area under the curve for phosphate (blue) and amide I (green) band over the line map.

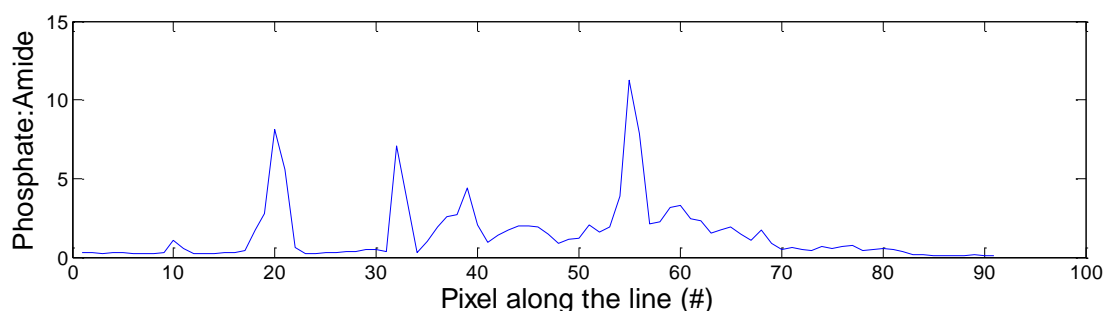


Figure 3.40: Ratio plot of data shown in figure 3.38 B.

The spectra and the area under the curve for the phosphate (blue) and amide I (green) band of the last line scan are shown in figure 3.41. In this line scan, two

calcification areas are visible, the first from pixel 7 to 34, the second from pixel 58 onwards, with in the middle one weak calcification (pixel 42:51). The phosphate:amide ratio is shown in figure 3.42. Unfortunately all calcifications are surrounded by paraffin, most likely due to the calcifications keeping their size during paraffin embedding while the tissue does not. As a result, the empty space between calcifications and tissue is filled by paraffin and the tissue/calcification interface is distorted.

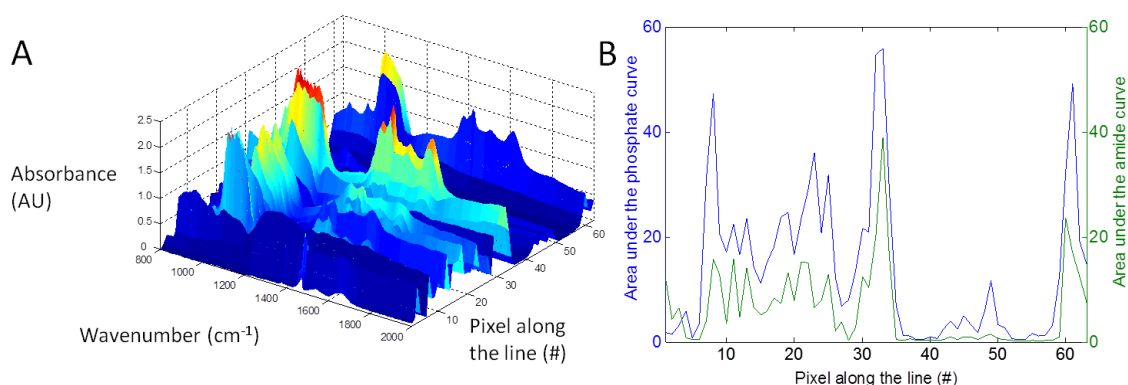


Figure 3.41: A) Spectra correlating to the line scan with *in situ* pathology; B) Area under the curve for phosphate (blue) and amide I (green) band over the line map.

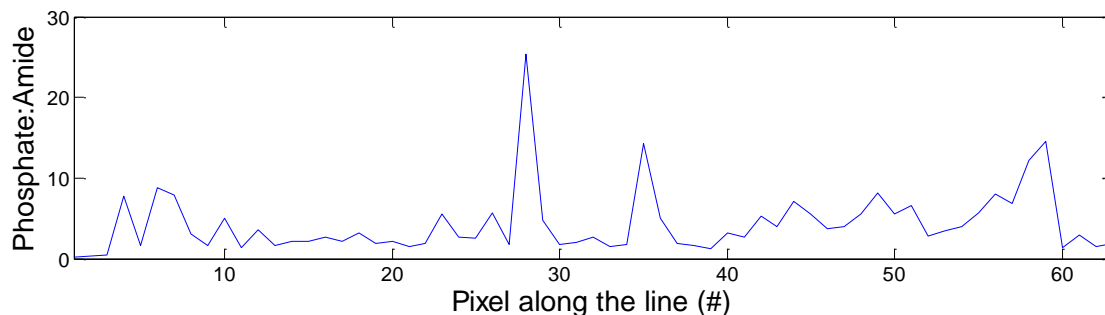


Figure 3.42: Ratio plot of the data shown in figure 3.41 B.

In contrast to the benign calcifications, the *in situ* calcifications do show amide bands. The 1444 cm⁻¹ band is visible as a shoulder of the paraffin peak and a new band ~1414 cm⁻¹ is observed. This band is a combination of the 1409 and 1427 cm⁻¹ band which are both specific for B-type carbonate substitution.

During the beam time allocation four maps were taken on samples with invasive pathology and six line scans. The white light image of the first calcification is shown in figure 3.43. On this calcification with invasive lobular carcinoma a line

scan and a map were measured. In panel B the spectra corresponding to pixel 7 to 15 from the line scan are shown.

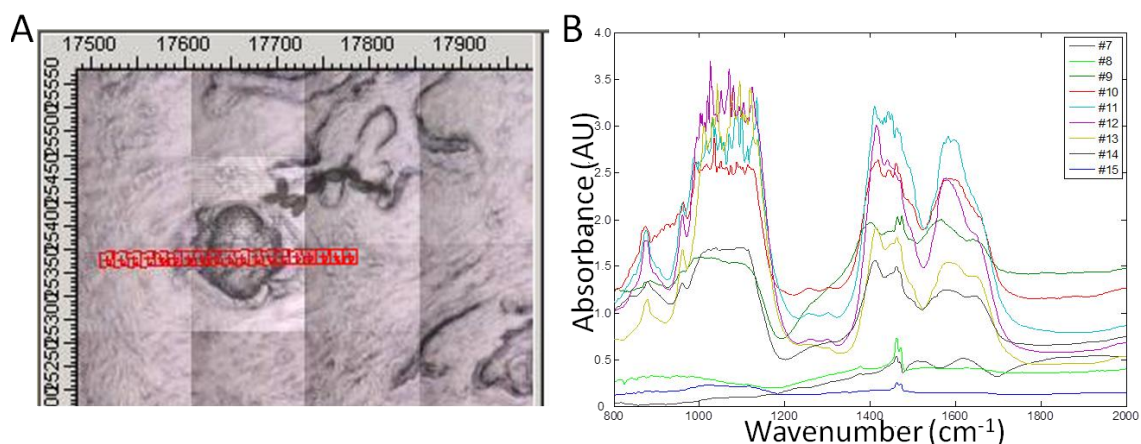


Figure 3.43: Sample with invasive pathology A) White light image of the measured calcification; B) Spectra corresponding to pixel 7:15 of the line scan.

Similar to the data obtained from the samples with *in situ* pathology, most of the phosphate bands are saturated. Furthermore, amide bands ($1500 - 1700 \text{ cm}^{-1}$ region) can be seen in the spectra corresponding to the calcification. However, the amide I and II band seem to have merged into one band with a maximum around 1590 cm^{-1} in the centre of the calcification. In the $1410 - 1460 \text{ cm}^{-1}$ region two bands can be observed, related to both A- and B-type carbonate substitution. On the same calcification a map was taken, data not shown, which had a data quality similar to the line scan shown.

The second map was measured on the same sample (other calcification). Again, line maps were analysed of which an example is shown in figure 3.44. In panel A, the spectra of line 6 are shown, and in panel B the area under the curve for the phosphate (blue) and amide I (green) band. The area under the amide I curve is significantly higher for the spectra corresponding to the surrounding tissue than for those corresponding to calcification. To emphasise this is a real phenomenon and not due to inconsistencies in the area under the curve routine used, the spectra in panel A are colour coded so differences in signal intensities are more readily picked up. Spectra correlated to tissue are depicted in blue, spectra showing the characteristic apatite band are depicted in

red, and spectra correlating to the calcification tissue interface (Mie scattered) in green. The phosphate: amide ratio is displayed in figure 3.45.

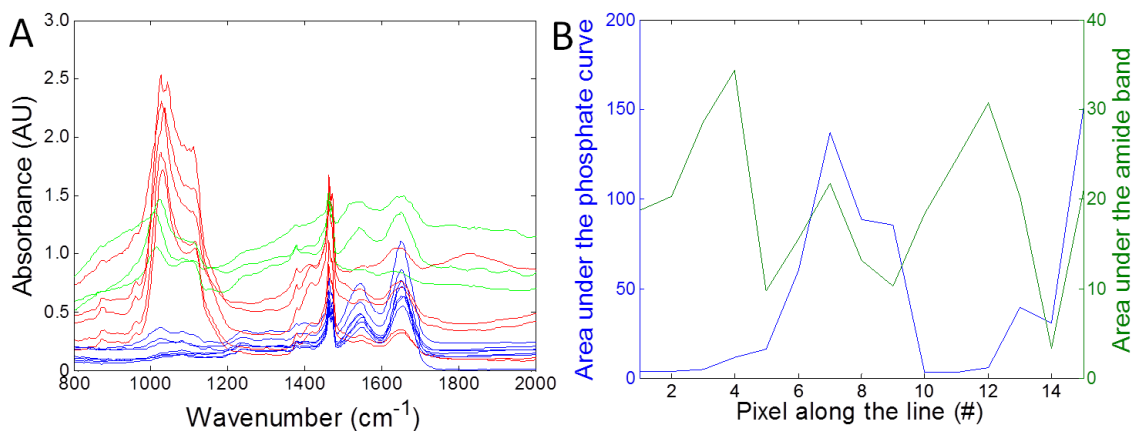


Figure 3.44: Line scan (row 6) over sample with invasive pathology A) Colour coded spectra of the row: tissue depicted in blue, calcification in red, and tissue calcification interface in green; B) Area under the curve of phosphate (blue) and amide I (green) band over the line scan.

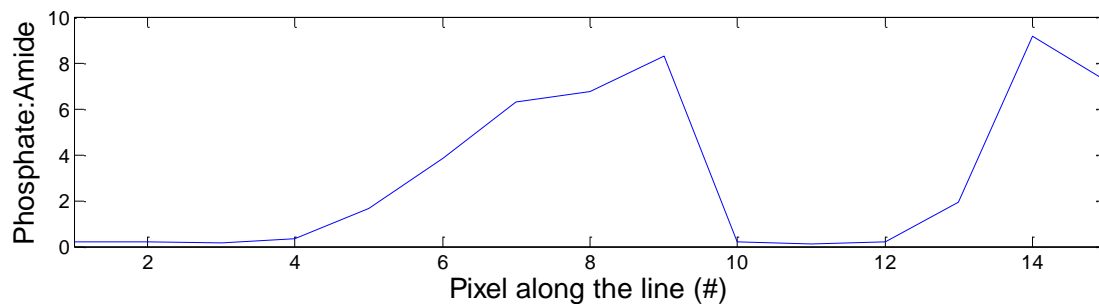


Figure 3.45: Ratio plot of the data shown in figure 3.44 B.

A third map was measured over a new sample with invasive pathology. The white light image of the sample is shown in figure 3.46 with the area of the map indicated in red. In panel B the score plot for the biochemical fit of apatite is shown. From this figure it becomes clear that the map consist of several smaller calcifications.

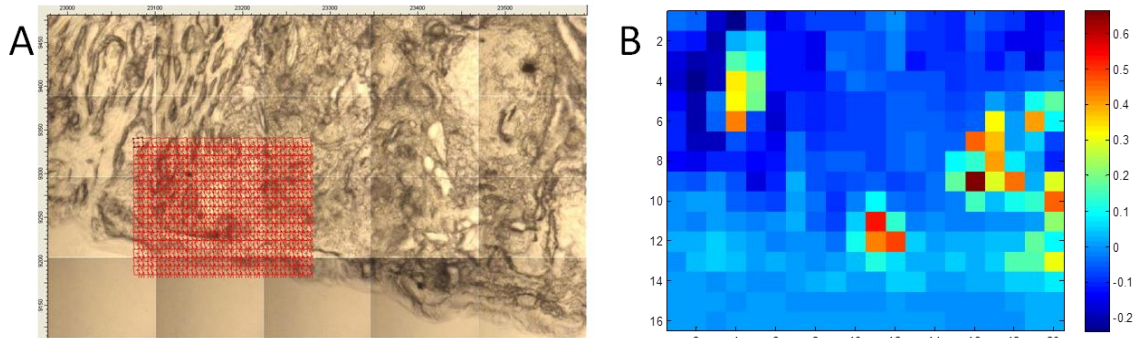


Figure 3.46: Sample with invasive pathology A) White light image of the map measured; B) Score plot of the apatite biochemical fit.

When the spectra relating to one calcification are selected, figure 3.47, it can be seen that the shape of the characteristic phosphate band changes over the calcification patch. In all previous samples the 960 cm⁻¹ band characteristic for phosphate is present as a relatively weak band compared to the phosphate moiety ~1030 cm⁻¹. In contrast, in the spectra shown in figure 3.47 the 960 cm⁻¹ is much stronger and in most cases even stronger than the phosphate moiety ~1030 cm⁻¹. Furthermore, there is a doublet, one band is located ~960 cm⁻¹ and the other ~972 cm⁻¹, instead of a single band. No information about a band positioned ~972 cm⁻¹ could be found in literature, and it is likely this phenomenon is due to saturation.

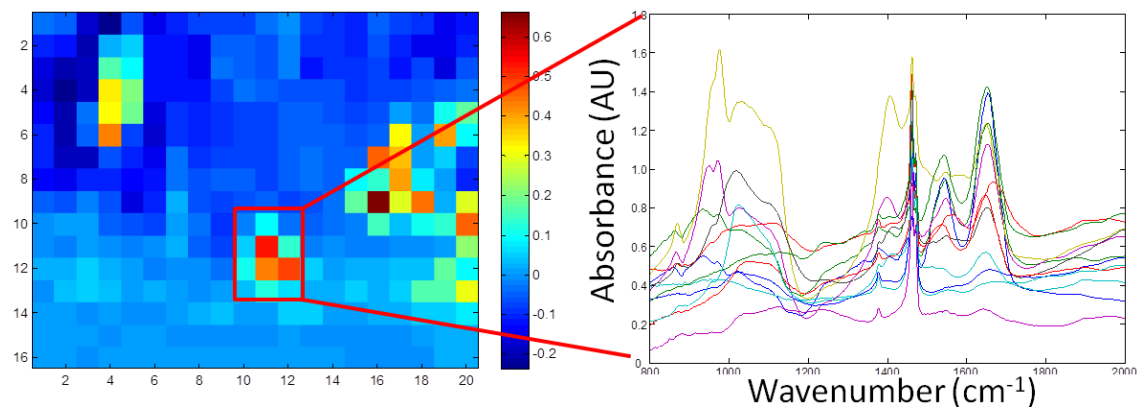


Figure 3.47: Selection of data related to one calcification; Left) Selected pixels are indicated by red box; Right) Spectra of the selected pixels.

On a separate calcification, white light image not shown, a horizontal and vertical line scan was done. Colour coded spectra of the horizontal line are shown in panel A of figure 3.48. The spectra correlating to apatite are depicted in red and the spectra correlating to the surrounding tissue in blue. The area under the curve for the amide I (blue) and phosphate curve (green) was

calculated and plotted against each other in panel B. Both line scans show a local minimum in the area under the amide I curve on the location of the calcification, and a local maximum directly next to the calcification which would suggest a protein rich capsule around the calcification.

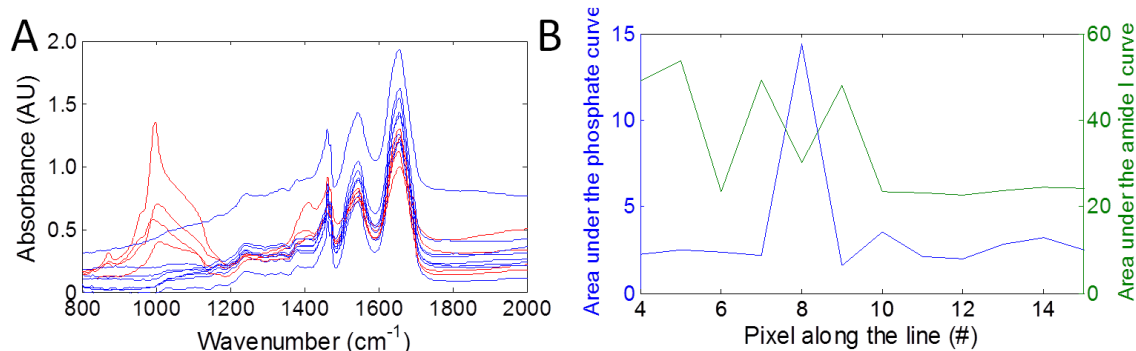


Figure 3.48: Horizontal line scan over calcification with invasive pathology A) Colour coded spectra of line scan; red is related to calcification and blue with surrounding tissue; B) Area under the curve for phosphate (blue) and amide I (green) band over the line scan.

The phosphate: amide ratio is displayed in figure 3.49. From the ratio can be seen (lower than one) that the area under the amide curve larger is than the area under the phosphate curve even though the amide has a local minimum in figure 3.48 B at the pixel (number eight) of the maximum of the area under the phosphate curve.

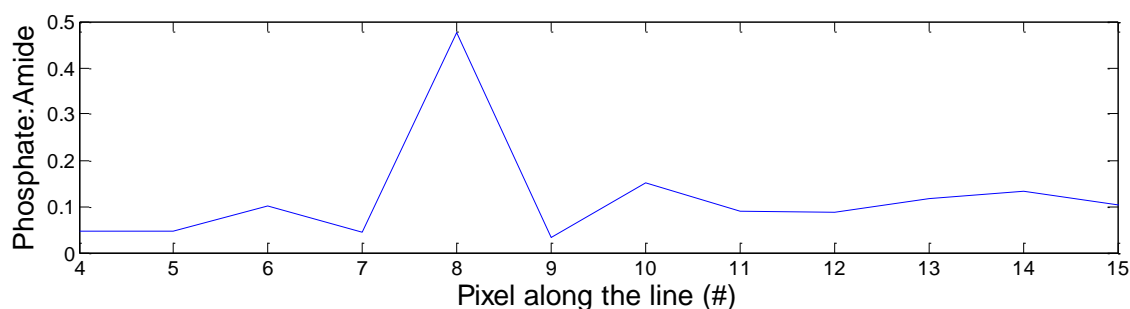


Figure 3.49: Ratio plot of the data shown in figure 3.48 B.

Findings were similar for the vertical line scan. The spectra of the vertical line scan are shown in panel A of figure 3.50. Again the spectra are colour coded; the spectra correlating to the calcifications are depicted in red and the spectra relating to the surrounding tissue in blue. The area under the curve for the phosphate (blue) and amide I curve (green) are shown in panel B. Similar to the horizontal line scan, the spectra relating to the calcification contain less amide I

than the surrounding tissue and the calcification seems to be surrounded by a protein dense capsule.

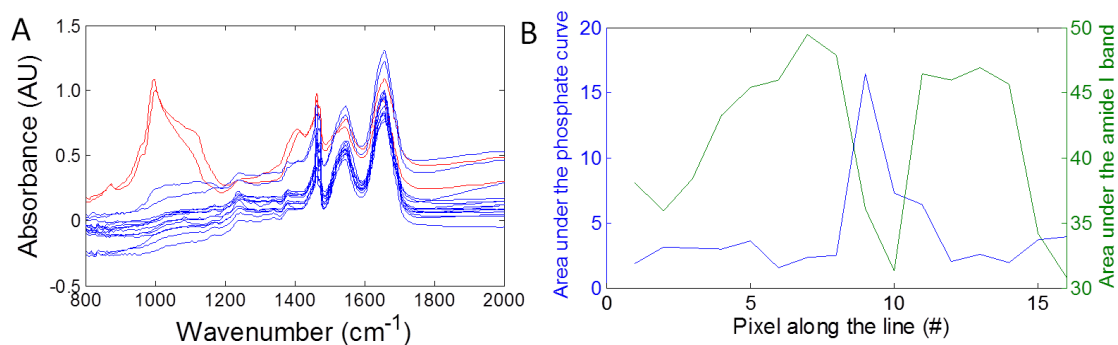


Figure 3.50: Vertical line scan over invasive calcification; A) Spectra of the line scan; spectra correlating to the calcification are colour coded with red and spectra of the surrounding tissue with blue; B) Area under the curve of the phosphate (blue) and amide I (green) band.

In figure 3.51 is the phosphate:amide ratio displayed. In the figure can be seen that the area under the curve for the amide band larger is than that of the phosphate curve (phosphate:amide ratio lower than one).

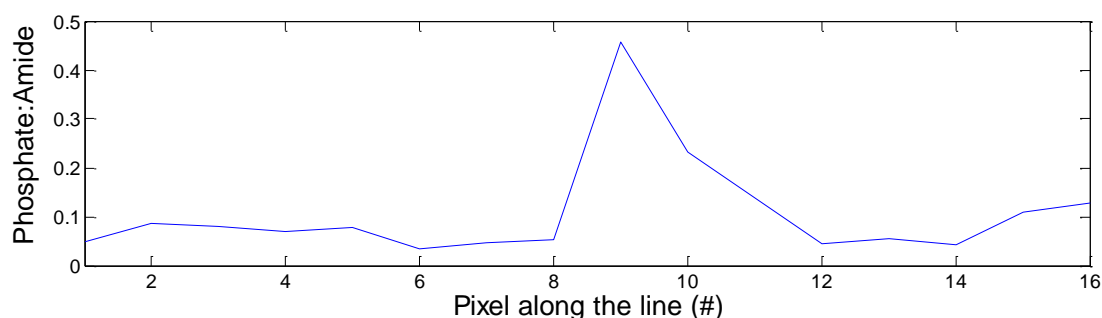


Figure 3.51: Ratio plot of the data shown in figure 3.50 B.

Another line scan was done on the same sample but on a different calcification (white light image not shown). The phosphate bands in the spectra relating to the calcification were heavily saturated and the intensity of the amide I bands was similar over the line scan (data not shown).

On a new sample two line scans were performed on a calcification (horizontal and vertical), followed by a map over the same calcification. In both line scans the area under the curve for the amide I band is constant over the line. When line scans are derived from the map the same is observed. Furthermore no carbonate bands were visible in the 1400 cm^{-1} region of both line scans and line

scans on the map. Similar to the calcification shown in figure 3.52, the intensity of the 960 cm^{-1} band is very high, and the position changes dramatically over the map. As an example an intensity plot is shown of row 10 on which the shift is indicated with a black circle in panel A, and the corresponding spectra are shown in panel B. As can be seen, the location of the band changes; from $\sim 990\text{ cm}^{-1}$ in the centre to $\sim 970\text{ cm}^{-1}$ at the edges of the calcification.

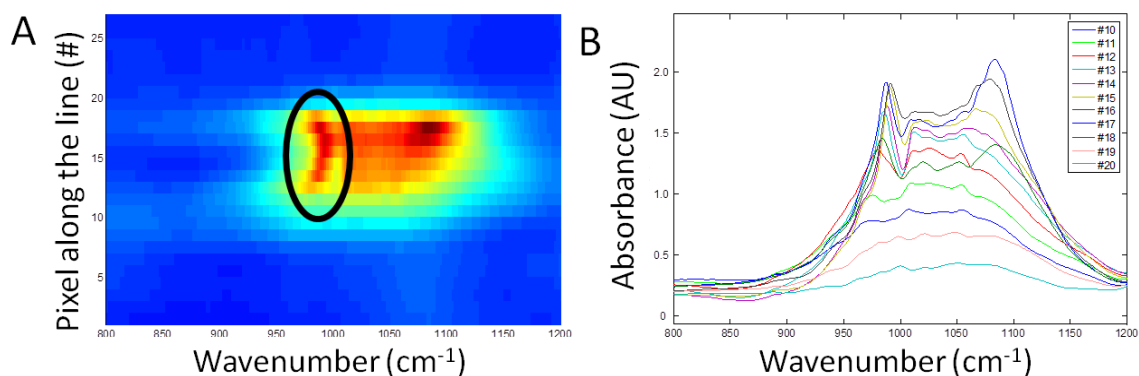


Figure 3.52: Line scan (row 10) through sample with invasive pathology A) Intensity plot of the phosphate region of the spectra on the line scan; B) Spectra relating to the calcification (position 10-20 along the line scan).

In the centre of the calcifications no spectra could be obtained due to the high absorbance leading to saturation. This could be avoided by reducing the thickness of the samples by thinner slicing of the biopsy blocks. It was feared that thinner slicing of pathology samples would force the calcifications out, but as can be seen in figure 3.53 calcifications are still present in a $1\text{ }\mu\text{m}$ thick slice.

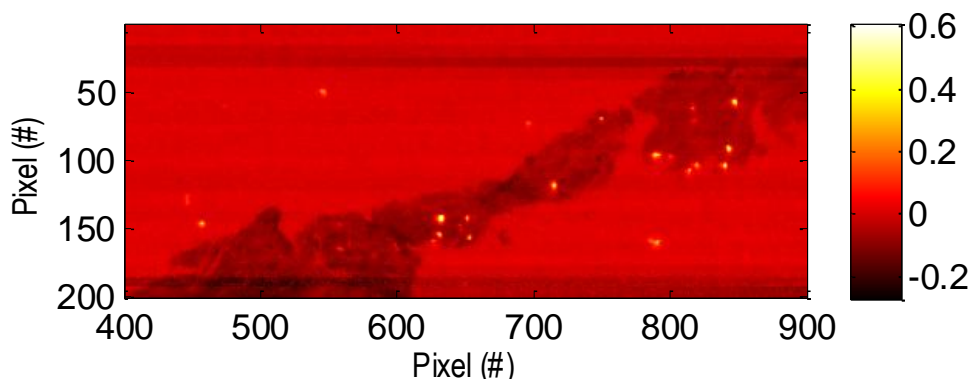


Figure 3.53: Biochemical fit for apatite on invasive breast pathology sample (1 micron thickness mounted on 1 mm calcium fluoride).

3.3.4 Results IRENI beam time

During this PhD project, beam time was obtained at the IRENI beam line at SRC, Wisconsin, USA. Due to the vast amount of data, analysis of all maps taken is beyond the scope of this PhD project and a new PhD project is planned to continue this line of research.

Two maps of calcifications are shown to get an idea about the capabilities of this synchrotron facility. In figure 3.54, a map of a calcification within a sample with invasive pathology is shown.

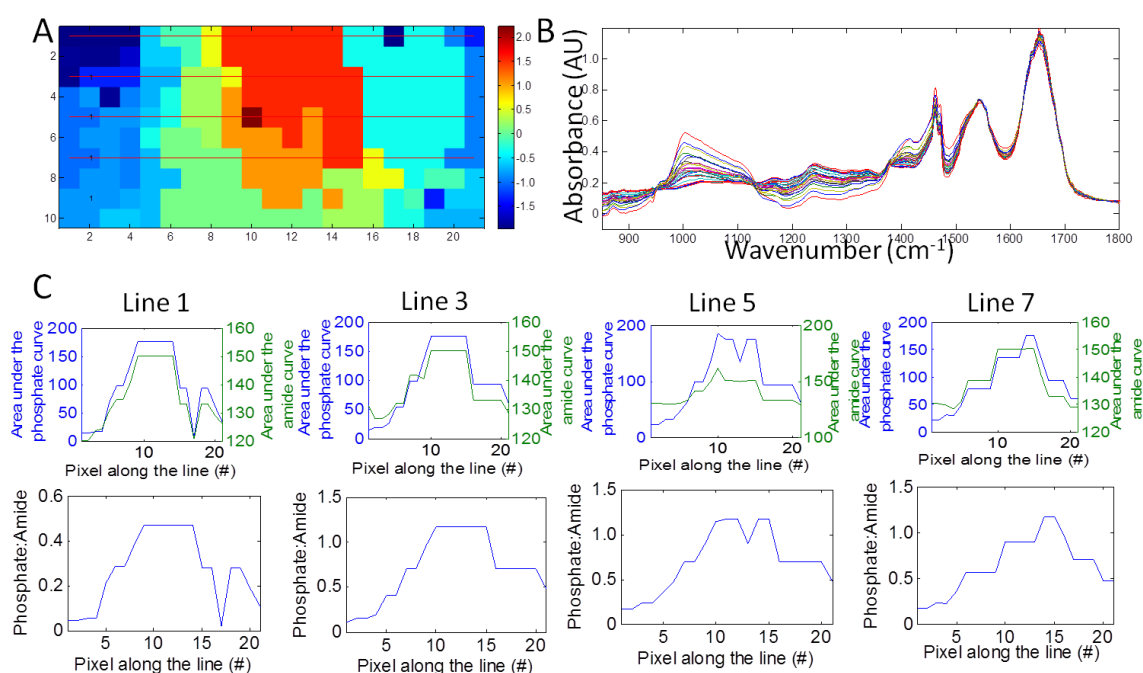


Figure 3.54: Example of a calcification measured at the IRENI beamline. A) Principal component with the line scans analysed indicated in red. B) Data corresponding to the line scans; C) Area under the phosphate (blue) and amide I (green) curve for each line scan (upper panel) and the amide:phosphate ratio (lower panel).

On this calcification several line scans are performed, which are indicated in panel A. In panel B the data corresponding to these line scans are displayed. For every spectrum of the line scans, the area under the curve of the phosphate and the amide I band are calculated. These values are plotted versus the position along the line. In contrast to the measurements on the B22 beamline, the amount of amide does not decrease over the line scan.

Chapter 3

In figure 3.55, the same analysis is shown for a larger calcification in a sample with invasive pathology. On this calcification, four line scans were performed, of which the locations are indicated in panel A. In panel B, the data corresponding to the line scans is shown. Panel C shows the area under the phosphate (blue) and amide I (green) curve. Similar to the smaller calcification, the amount of amide I does not decrease over the calcification as it did for the Diamond measurements.

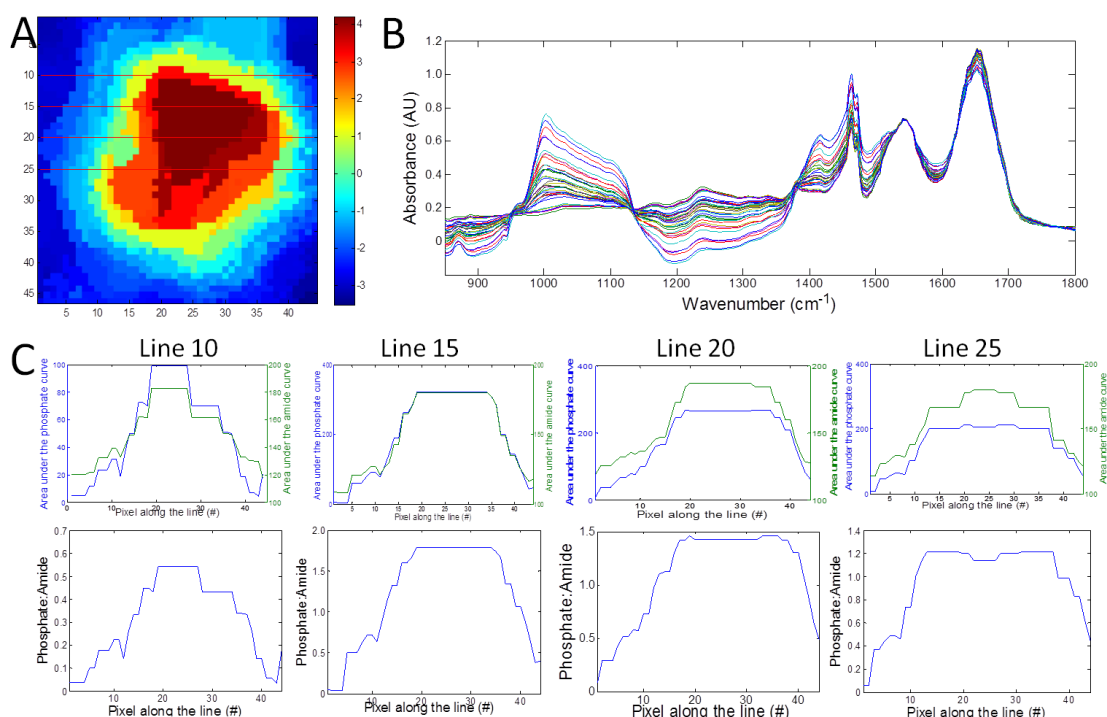


Figure 3.55: Example of calcification measured at IRENI beamline. A) PC2 with the locations of the line scans; B) Data corresponding to the line scans; C) Line scans with the area under the curve for phosphate (blue) and amide I (green) per pixel (upper panel) and the amide:phosphate ratio (lower panel).

3.4 ATR imaging of breast calcifications

In this section, the ATR experiments performed on a deparaffinised breast pathology sample are discussed. The effect of the paraffin removal protocol is discussed in appendix D.

Chapter 3

Data was obtained from the measurements at location 3,4,8, and 9. No calcifications were present in the ATR and transmission FTIR measurements of area 3 (data not shown).

In figure 3.56, the transmission and ATR FTIR measurements of area 4 are shown. In panel A, the intensity of the phosphate band over the transmission FTIR map is displayed and in panel B the intensity of the phosphate band over the ATR FTIR map. In both transmission and ATR FTIR measurements the area measured consist of 64x64 pixels, which correspond to an area of ~350x350 μm for the transmission FTIR and ~64x64 μm for the ATR FTIR measurements. In panels C and D, spectra of both the calcification (depicted in red) and the surrounding breast tissue (blue) are shown for the transmission FTIR (panel C) and ATR FTIR measurements (panel D).

It can be seen that the relative intensity of the lower wave number region is higher in ATR measurements than that of the higher wave numbers.

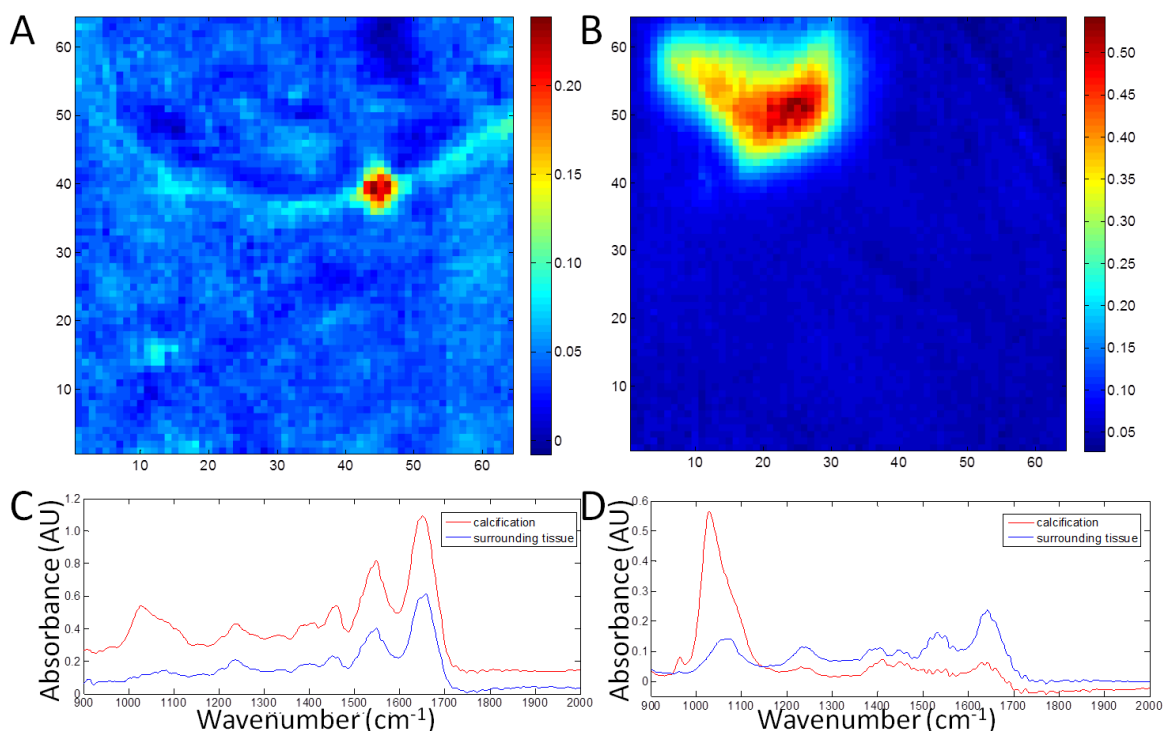


Figure 3.56: Transmission FTIR and ATR FTIR measurements on area 4. A) Intensity of apatite band over transmission FTIR map; B) Intensity of apatite over ATR FTIR map; C) Transmission FTIR spectra of calcification (red) and surrounding tissue transmission (blue); D) ATR FTIR spectra of calcification (red) and surrounding tissue (blue).

Chapter 3

A line scan was performed over the ATR FTIR data. The location of the line scan is depicted in panel A of figure 3.57. In panel B, the area under the curve are depicted for the phosphate band (blue) and amide I band (green). It can be seen that the amount of amide I decreases in the calcification and has a minimum in the centre of the calcification. The spectra of the pixels on the line scan are depicted in panel C and a band shift can be observed. In panel D, the location of the phosphate band over the line scan is shown and it can be seen that the position in the centre of the calcification is close to 1020 cm^{-1} and shifts towards higher wavenumbers when increasing the distance to the centre of the calcification. A similar finding was observed in the ATR measurements of standards. In the case of breast calcifications the shift is larger which is probably caused by mixing in the tissue band located $\sim 1060\text{ cm}^{-1}$.

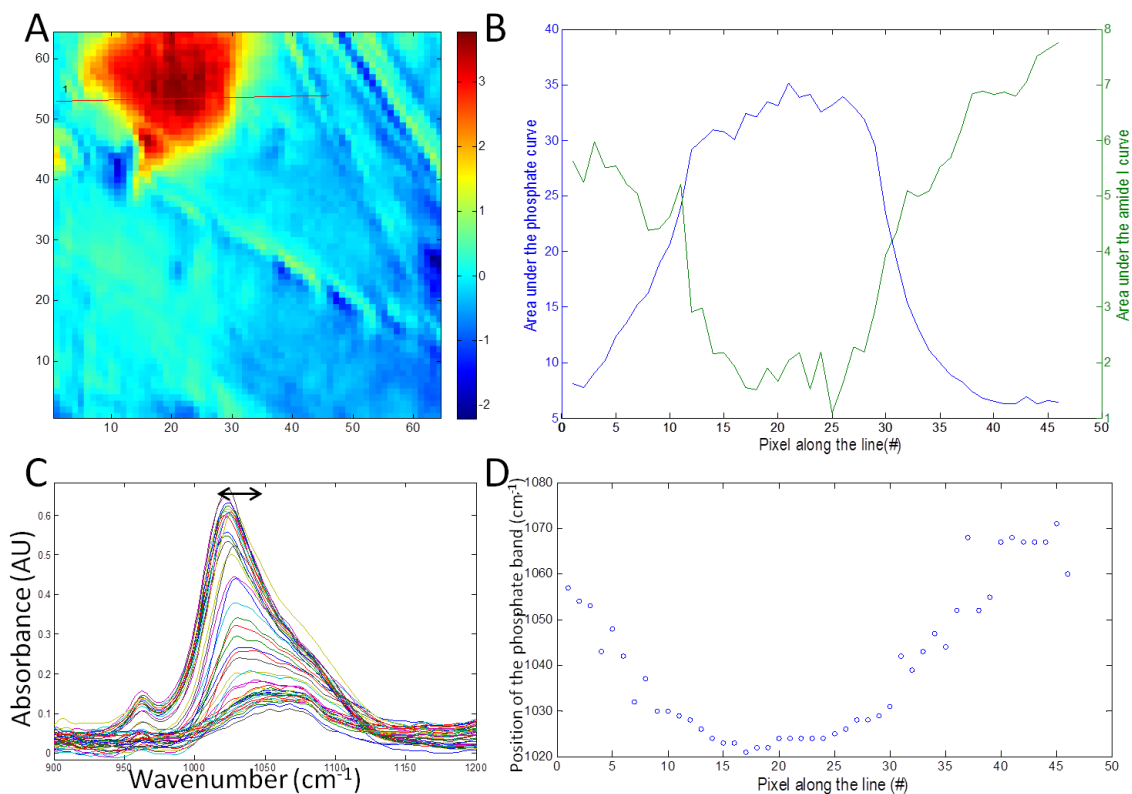


Figure 3.57: Line scan over calcification in area 4. A) PC 2 of area 4 and the location of the line scan; B) Area under the curve for the phosphate band (blue) and amide I band (green) over the line scan; C) Spectra relating to the line scan; D) Band shift of the phosphate band over the line scan.

In the ATR FTIR measurements of area 8 similar findings were observed (figure 3.58). The amide I decreased over the calcification and had a minimum in the centre of the calcifications.

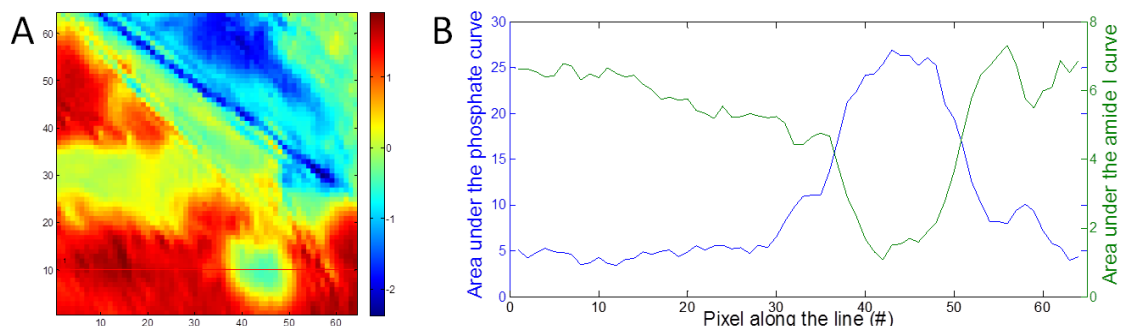


Figure 3.58: Line scan over calcification in area 8. A) PC 2 and the location of the line scan; B) Area under the phosphate curve (blue) and amide I curve (green) over the line scan.

The phosphate band shift was observed as well (data not shown). The position of the phosphate band in the spectra corresponding to the centre of the calcification was $\sim 1023\text{ cm}^{-1}$ and shifted towards higher wavenumbers in measurements relating to position more outwards from the centre.

A similar analysis was done on the calcification in area 9. Also in this measurement the intensity of the amide I band decreases over the calcification, with a minimum in the centre (figure 3.59).

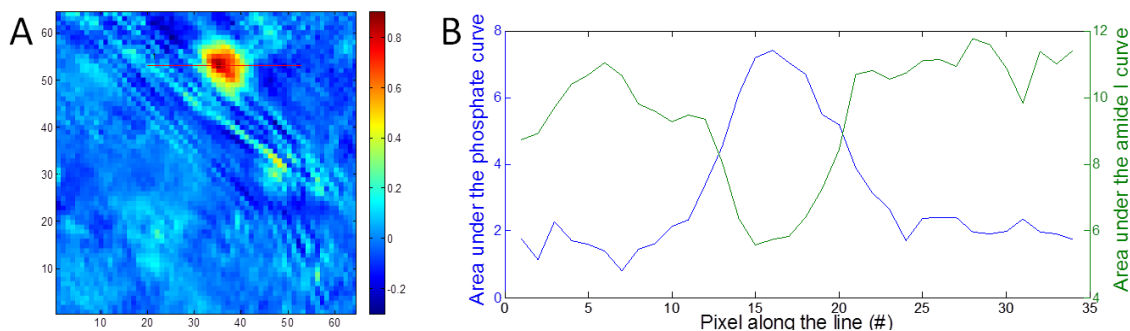


Figure 3.59: Line scan over calcification in area 9. A) PC 4 and the location of the line scan; B) Area under the phosphate curve (blue) and amide I curve (green) over the line scan.

3.5 Raman imaging of breast calcifications

In this section, a proof of principle Raman mapping study is performed on a paraffin embedded sample of which the paraffin is removed with the protocol discussed in section 2.1.4. The effect of the de-paraffin protocol is discussed in the appendix D.

The same area was measured on the Raman Streamline setup and compared to the FTIR measurements (similar pixel size) by plotting the chemical fit of the apatite of the FTIR map versus the intensity of the characteristic $\sim 960\text{ cm}^{-1}$ phosphate band (background subtracted) of the Raman map (figure 3.60).

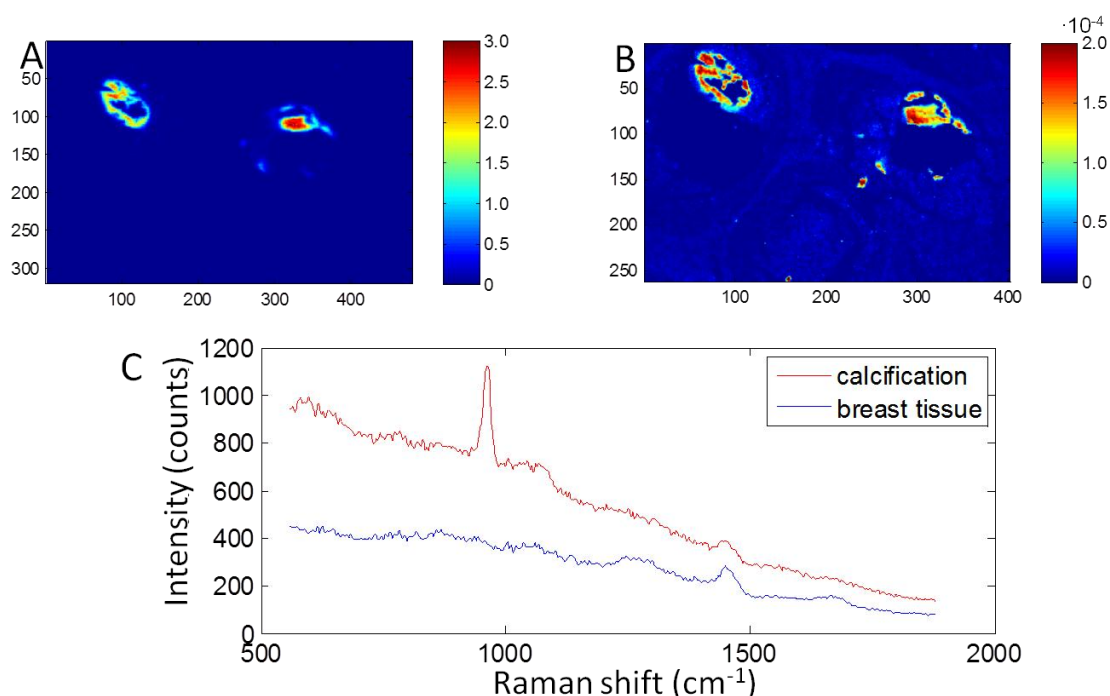


Figure 3.60: FTIR and Raman mapping on same sample. A) Apatite chemical fit on FTIR map; B) Intensity of the 960 cm^{-1} phosphate band on Raman map; C) Example of Raman spectra of the intensity map showed in panel B. For both measurements a pixel size of ~ 6 micron was chosen.

Although the locations do not match exactly, due to alignment differences, it can be seen the shape and size of the calcified areas is the same on both maps. In the Raman map it can be seen that the calcification patch is made up from several smaller calcification, a feature that could not be distinguished in the FTIR mapping due to lower spatial resolution.

Raman mapping can be done with smaller pixel sizes than FTIR imaging. In figure 3.61, a Raman map is shown on the left calcification of the previous figure. In panel A, the white light image is displayed, followed by principal component two and the location of the line map in panel B, in panel C the spectra corresponding to the pixels of the line scan are shown. In panel D, a Gaussian fit of the intensity of the 960 cm^{-1} band is shown. The presence of several smaller calcifications instead of one larger one is obvious in both panel B and D.

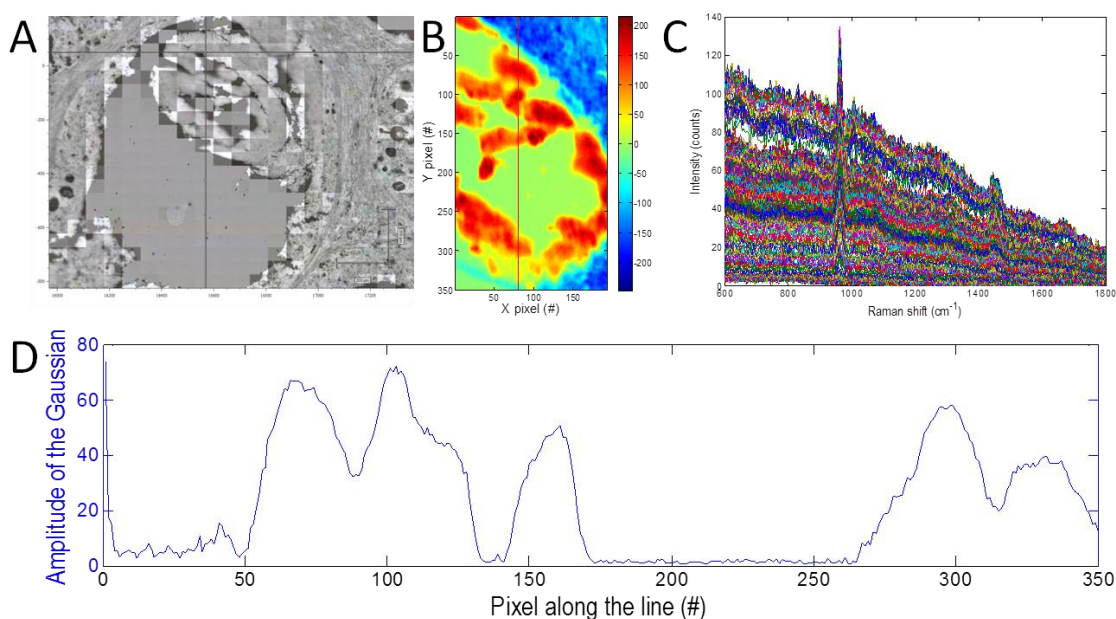


Figure 3.61: Raman mapping with $1\ \mu\text{m}$ steps. A) White light image of the calcification; B) Principal component two with the location of the line map indicated with a red line; C) Spectra corresponding to the pixels on the line scan; D) Amplitude of a fitted Gaussian to the 960 cm^{-1} band.

In figure 3.62, the area of the Raman measurement is shown together with the corresponding area of the FTIR measurement to give an indication of the resolution enhancement that can be obtained. The same calcification is measured with ATR FTIR (area one and two) and measurements should be compared as soon as the raw data is available.

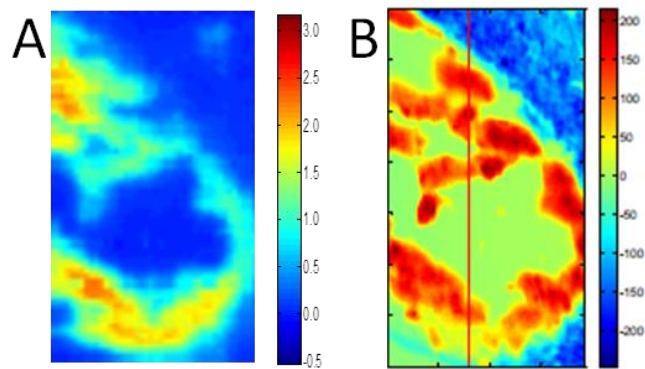


Figure 3.62 Comparison of benchtop transmission FTIR and Raman mapping. A) Benchtop FTIR; B) Raman mapping (1 μm stepsize) on same area.

4 Results: Deep Raman system evaluation

One of the aims of this PhD project is to translate knowledge obtained about breast calcification to the development of a new clinical tool that could be used *in vivo*. To facilitate this, a transmission Raman setup was built (described in the materials and method chapter) and its performance is tested in this chapter.

4.1 Comparison porcine soft tissue and human mammary tissue

In this chapter, porcine soft tissue is routinely used as a model for human mammary tissue. From literature it is known that the biochemical composition, such as the protein to lipid ratio, of porcine and human tissue is very similar (Vardaxis et al., 1997) and the Raman spectra of porcine soft tissue and fresh frozen human breast tissue are therefore expected to be similar too.

In order to test the validity of using porcine soft tissue as a model for human breast tissue, similar thicknesses of porcine soft tissue and snap frozen human breast tissue were measured on the transmission Raman system (figure 4.1).

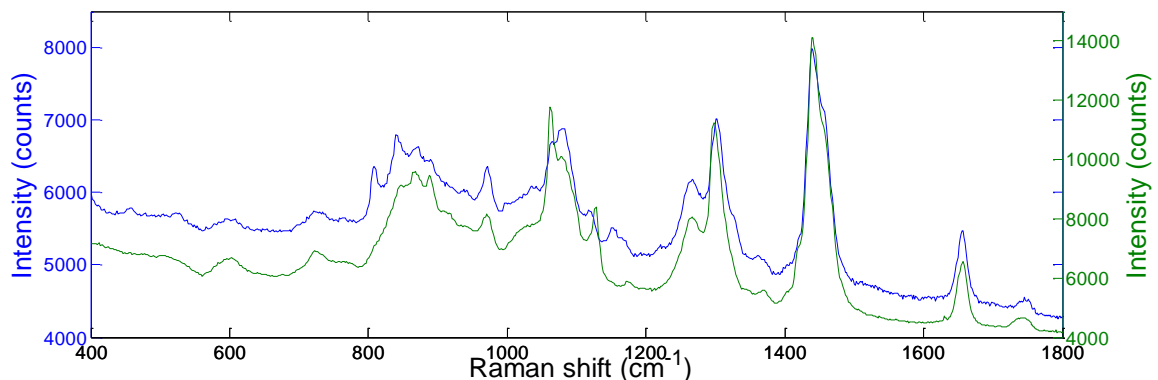


Figure 4.1: Comparison Raman spectra of human mammary tissue (blue) and porcine soft tissue (green).

When comparing the Raman spectra of both samples (figure 4.1), it can be seen that the overall shape of the spectra are very similar although the relative peak intensities can differ.

This makes porcine soft tissue a suitable model for human breast tissue during the first phases of our deep Raman experiments.

4.2 Sample thickness limits when using transmission Raman setup

In the case of using deep Raman spectroscopy as an adjunct to mammography, it would be ideal if the thicknesses to which it could be applied were at least as high as the thickness of the breast during mammography. During mammography the breast is compressed to reduce the radiation absorbed by the tissue and to improve the quality of the image taken by reducing for example the overlap of structures and improve image sharpness (Poulos et al., 2003). Since compression of the breast may be experienced as painful, it is important to push the penetration depth limits of the new screening techniques. However, when compressing the breast locally instead of compressing the whole of the breast lower thicknesses can be readily achieved.

Initial experiments concerning the sample thickness, and the effect this has on the Raman spectra measured, were performed on porcine soft tissue and freshly frozen human breast tissue. It was thought that freshly frozen breast tissue could be used as a model for fresh human breast tissue. Candefjord et al. (2009) tested the effect of snap freezing on porcine prostate tissue. They found several subtle changes when comparing the principal component scores, but these were not visible when comparing the mean spectra. However, in our initial experiments a striking difference in structural integrity was observed between freshly frozen and fresh breast tissue. The snap frozen tissue did not keep its shape and structure after defrosting and mounting of the tissue was therefore problematic. This is most likely due to the volume of the snap frozen specimens. In large specimens, the outer layers will freeze first after which the freezing rates are unpredictably slow due to insulation. When crystals start to expand the tissue inside the frozen shell, the whole specimen is damaged (Scouten and

Cunningham, 2012). Ice crystals will form in the interior of any piece of tissue over 10 mm from the cold source.

As expected, the amount of light coming through both the porcine and the freshly frozen samples decreases with the sample thickness (data not shown). However, it is not known how the transmission through the affected breast tissue is related to measurements on fresh human breast tissue. Therefore, the measurements on the freshly excised breast specimens with different thicknesses were analysed too.

The freshly excised breast specimens had a thickness ranging from 2 mm to 25 mm. In the whole range it was possible to measure a spectrum of the specimen in transmission mode with the accumulation time used (raw data shown in appendix E3) although the amount of signal decreases with increasing thickness, as does the fluorescence background shape.

In figure 4.2, the SNR is displayed for the range of thicknesses with the error bars indicating the standard deviation. In section 5.2 the SNR needed for correct estimation of the amount of carbonate substitution is evaluated which is 6.5 and thus relating to a maximum tissue thickness of 10 mm.

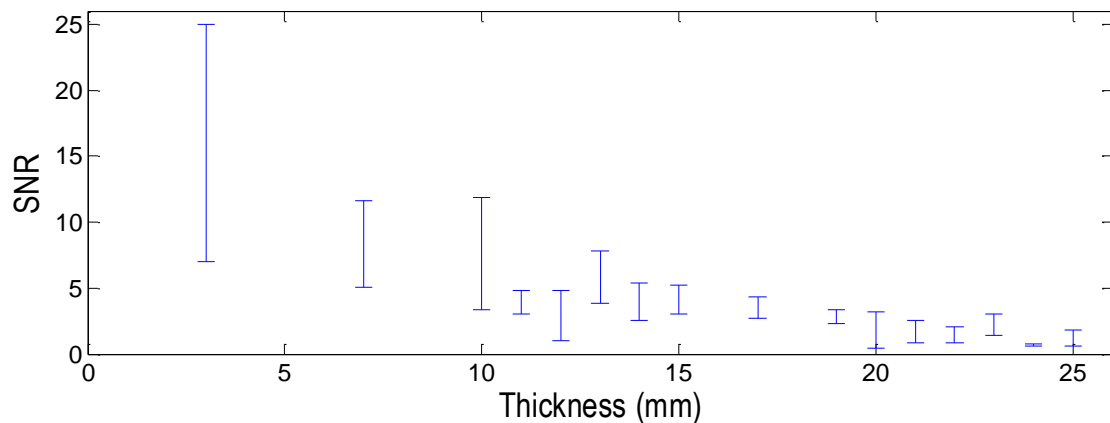


Figure 4.2: Plot of the SNR versus the thickness of the sample. Measurements were done during 3x60s with the cosmic removal function on. The error bars indicate the standard deviation.

For calcification vs. no calcification or type I vs. type II a lower SNR will be sufficient and thus a larger tissue thickness range could be used.

When plotting the log of the data, a linear trend is observed which indicates the decrease in signal is exponential. A similar link between the tissue thickness and the transmission Raman signal was observed in Monte Carlo simulations of Raman photons in breast performed by Matousek and Stone (2007).

The existing setup does not yet permit reaching 50 mm penetration depth – for this further optimisation is required (e.g. higher laser power, higher collecting power). A possible further improvement of detectable Raman intensity by more than two orders of magnitude was identified (Matousek and Stone, 2007).

4.2.1 SESORS

In the following exploratory study we also looked at the performance of our technique with SERS labels within tissue. Although this approach poses challenges stemming from the potential toxicity of nanoparticles it offers extremely high sensitivity providing high penetration depth and ability to detect low level bio-analytes. Here we used these nanoparticles only as a test target instead of calcifications to test the performance of our technique in thick tissue samples in an easy and reproducible way with our current Raman benchtop instrument. In an exploratory study, dye was injected in a breast model and measured. In figure 4.3, the spectra of nanoparticles x403 can be seen detected through both 20 and 47 mm thick samples. It should be noted that at the extended depth ~20 times more nanoparticles were used and a longer collection time.

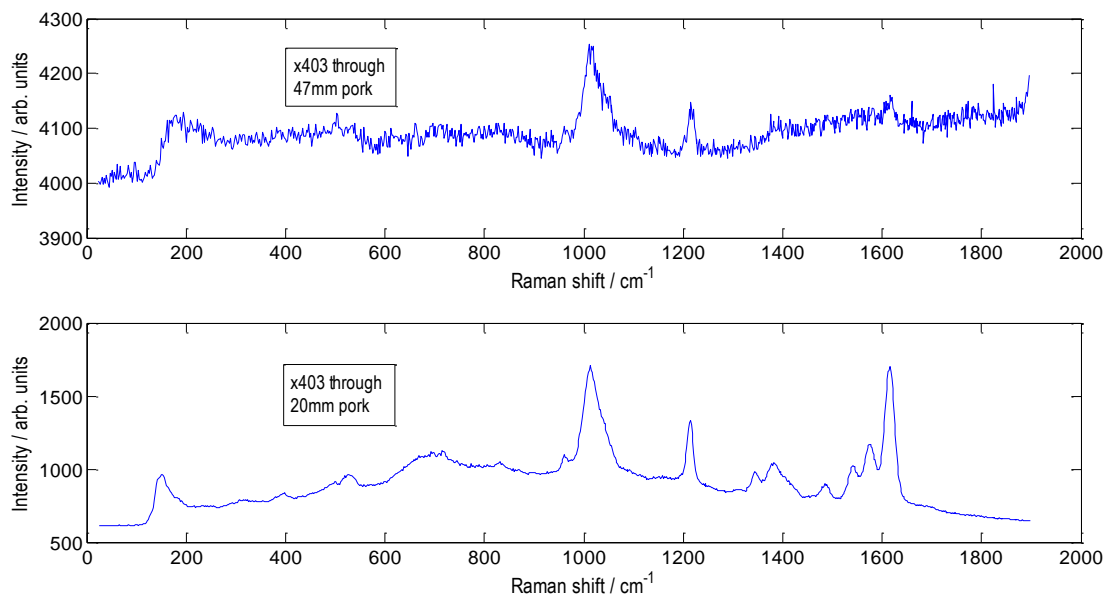


Figure 4.3: upper panel: x403 (3×10^{10} particles in $50 \mu\text{l}$) through 45-50 mm tissue; lower panel: x403 (1.8×10^9 particles in $3 \mu\text{l}$) through 20 mm tissue.

The spectrum measured through 47 mm tissue showed significant signal loss at higher wavenumbers (above 1250 cm^{-1}), which was not observed previously with tissue. It is suggested that at these wavelengths both water and myoglobin absorb significantly light passing through the tissue. The $1250\text{-}1600 \text{ cm}^{-1}$ region correspond to light of $925\text{-}957 \text{ nm}$ with the excitation wavelength used (830 nm). This covers the range where a strong lipid absorption band (930 nm) is located (Kukreti et al., 2008) and water absorption band (970 nm). The myoglobin may be specific to the porcine model used which has a high amount of striated muscle content. In contrast, breast tissue only has a small amount of smooth muscle near the nipple so contributions of myoglobin are unlikely in breast tissue.

4.3 Lateral spreading in transmission Raman measurements

The spectra obtained during transmission Raman spectroscopy give a biological fingerprint of the bulk sample. This is due to the random direction of the scattering in transmission Raman experiments. The thicker the sample, the more scattering events the photon undergoes before reaching the detector on the other side of the sample. In order to understand the spread of signal through

the thickness of the sample, measurements are performed on a porcine tissue breast model with a buried analyte which rule out inter patient variability fresh human breast tissue would have.

In figure 4.4, the intensity of the x403 SERS signal over the map is shown. Due to the fixed location of the input fibre, the sample has to be moved in order to collect signals from another area, which is done in translation steps of 2 mm. Each measurement, and therefore each pixel, gives information about the bulk tissue the photons travelled through. In panel A, measurements were performed on a specimen with 5 mm thickness and in panel B on a specimen with 20 mm thickness. In both specimens the same amount of dye was injected at roughly the same depth, which means the target has a similar size in both experiments.

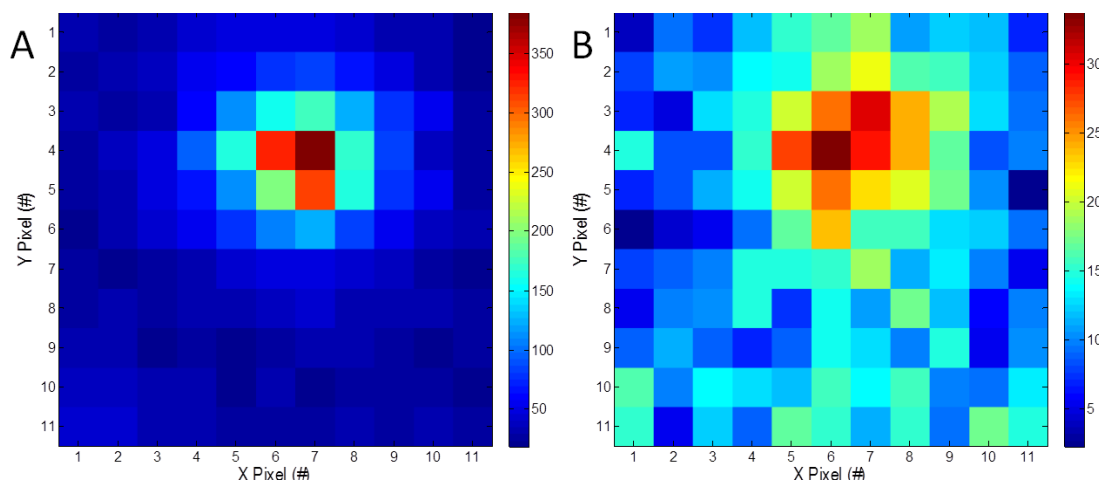


Figure 4.4: Mapping of porcine soft tissue breast models with 1 μ l x403 dye injected as an analyte. A) 5 mm sample thickness; B) 20 mm sample thickness.

When comparing the signal of the 5 and 20 mm thick specimen, a difference of ~ 10 times is observed in the intensity levels. This results in a decrease of the SNR of ~ 3 times. This is a smaller difference than would be expected based on the experiments on freshly excised human breast tissue shown in figure 4.2, but in those experiments it becomes clear that the SNR does not decrease linearly with increasing sample thickness. Furthermore, large standard deviations were obtained in samples with low thicknesses due to the limited amount of samples.

To study the spread of signal over both maps, 2D Gaussians were fitted to both datasets (figure 4.5). The original data points are indicated with green dots, and

Chapter 4

the fitted functions as surface plots. In case no lateral spreading of photons would occur, all of the x403 signal would be located in a small area depending on the size of the beam and the size of the analyte. The more lateral spreading occurs, the more pixels show traces of the x403 signal. As a result, the 2D Gaussian would have a larger full width half maximum (FWHM) when more lateral spreading occurs.

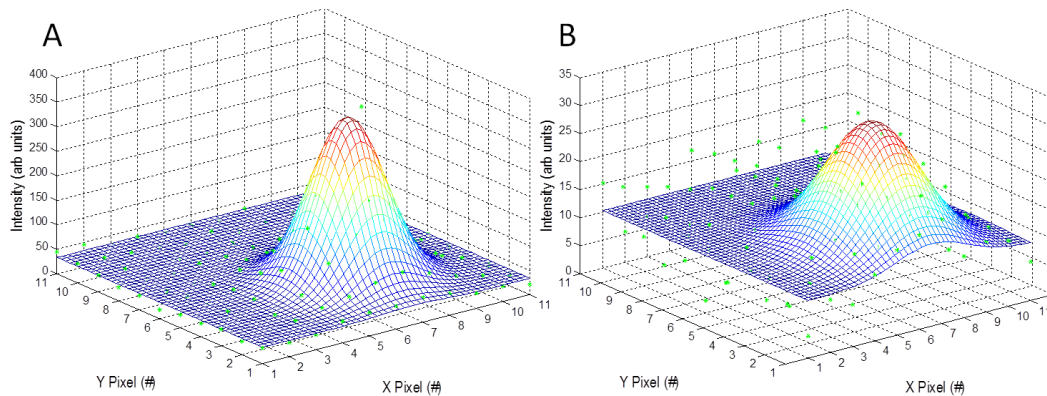


Figure 4.5: 2D Gaussian fitted to the intensity levels of x403 dye. A) 5 mm thick sample; B) 20 mm thick sample.

In a Gaussian function the FWHM is related to the sigma (σ) of the function.

$$FWHM = 2\sqrt{2 \ln 2} \sigma$$

Equation 4: FWHM of a Gaussian function.

The sigma was calculated for both 2D Gaussians and was 1.14 pixels for the 5 mm thick sample, and 1.62 pixels for the 20 mm thick sample. This would result in a FWHM of 5.4 and 7.6 mm, respectively.

In general, an increased sample thickness will result in lower signal intensities and more spread of the signal. This is beneficial for screening purposes, since larger areas can be interrogated during a measurement. However, for different clinical purposes, for example interrogating a designated cluster of microcalcifications or an attempt to measure the amount of carbonate substitution, it might be beneficial to compress the breast locally in order to decrease the sample thickness and lateral spreading and increase the signal levels.

4.4 The originating depth and spatial resolution of transmission Raman signal

In the previous sections, the effect of the sample thickness on the signal quality is explored. Other factors important in localising the analyte are for example its physical size, whether it is a strong Raman scatterer or not, and the actual location. In this section the effect of the originating depth (location of the analyte in the z-direction) is tested.

In a study by Everall et al (2010) it is shown that the resolution near either surface is improved compared to the bulk. When the analyte is on the surface the laser beam directly hits the object, so the beam size determines the resolution. On the collection surface the collection aperture limits the resolution since detected photons do not undergo significant migration anymore. In the experiment performed the analyte is almost at the same distance from the surface in both measurements, since the sample was rotated by 180° . X403 dye was injected in an 18 mm thick breast model and the sample is translated in 1 mm steps on the transmission Raman setup (figure 4.6).

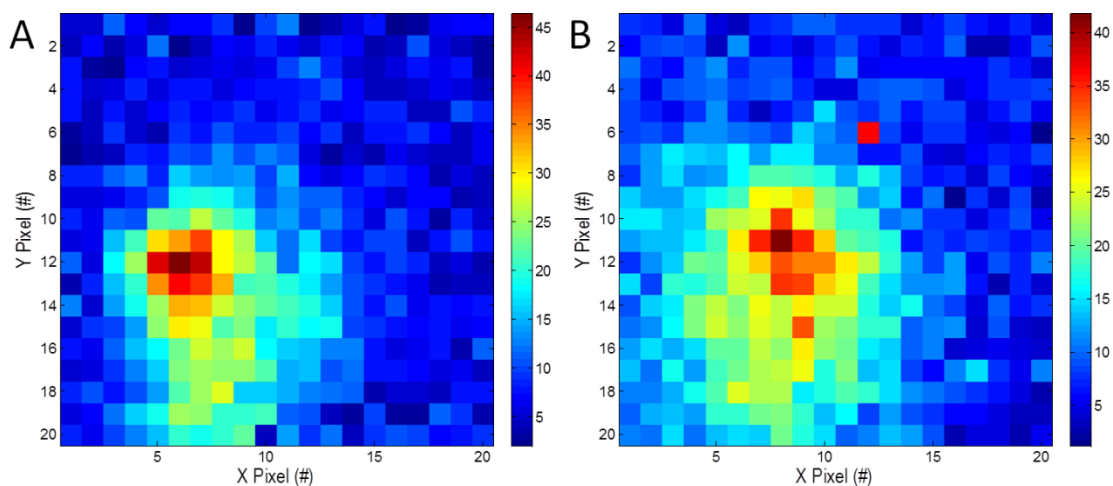


Figure 4.6: mapping of samples with same thickness but different injection depth analyte A) Analyte injected at the front of the 18 mm thick sample; B) Analyte injected at the back of the 18 mm thick sample.

Panel A of figure 4.6 shows the intensity of the x403 signal over the map. The sample was then rotated 180° so that the dye is no longer positioned at the front of the sample (where the beam comes in) but at the back of the sample where

the collection fibre is located. The intensity of the x403 signal over the map in this second alignment is depicted in panel B of figure 4.6.

A 2D Gaussian is fitted to both maps (figure 4.7). The original data points are indicated with green asterisks, and the fitted function is shown as a surface plot. The amplitude of the 2D Gaussian is slightly higher for the dye at the front of the sample (panel A) than for the dye at the back at the sample; 24.3 versus 27.6, respectively. A difference in signal spreading is observed in both figure 4.6 and 4.7. The 2D Gaussian has a sigma of 3.4 pixels for the dye at the front of the sample and 4.2 pixels for the dye at the sample. This results with a pixel size of 1 mm in a FWHM of 8.1 and 9.9 mm.

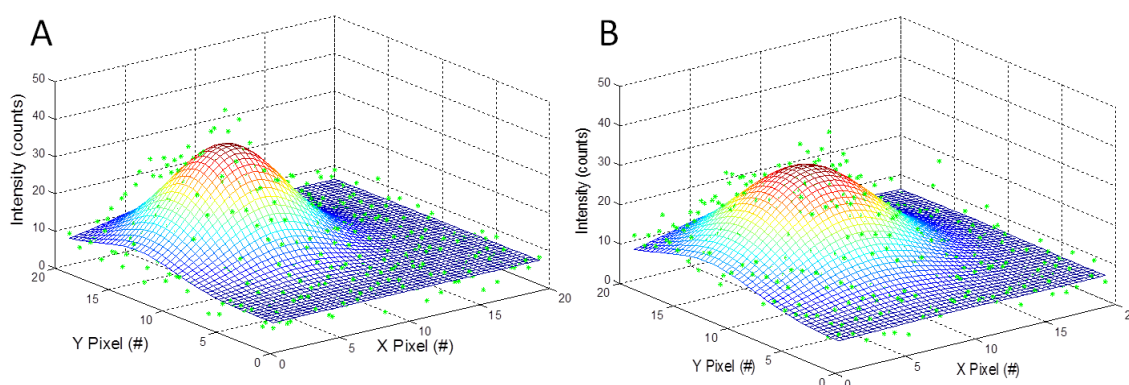


Figure 4.7: 2D Gaussian fitted to the intensity levels of the 1016 cm^{-1} band of x403 in 18 mm thick sample injected in front or back (baseline corrected).

In the transmission Raman measurements, signals are collected from all depths and there is no depth discrimination in the measurements. In the experiment described in this section, the size of the analyte was known, as was the thickness of the specimen. From a mapping experiment it could then be attempted to estimate the depth of origin of the analyte signal. However, from a single measurement the originating depth of the analyte signal cannot be calculated. Raman spectroscopy should thus be used as an adjunct to a traditional imaging technique such as mammography – if the depth information is required.

4.5 Measurements through skin

In order to use the deep Raman setup non-invasively, measurements through skin should be feasible. As a first step, measurements were performed through porcine soft tissue with attached skin.

In figure 4.8, measurements through a 15 mm porcine soft tissue sample with skin are shown. The intensity of the x403 over the translated sample is shown in panel A, and the 2D Gaussian fitted to these data points in panel B.

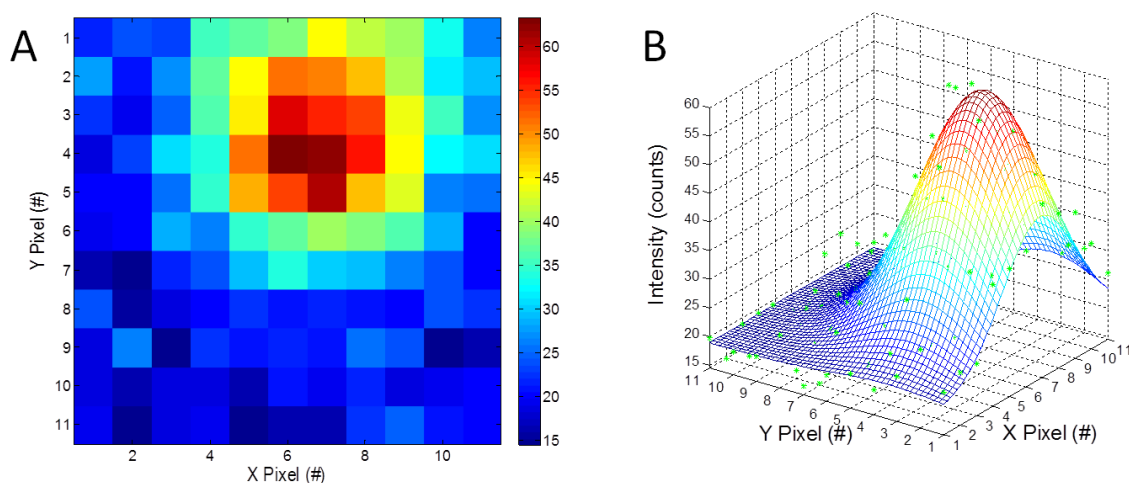


Figure 4.8: Intensity map of x403 dye in a porcine soft tissue sample of 15 mm thick including skin.

In the thickness experiments (4.3) expanding the depth from 5 to 20 mm led to a 10x signal decrease. The intensity through the 15 mm thick sample with skin is ~7 times lower compared to the 5 mm thick sample without skin in section 4.3, which is in the expected range. The fitted 2D Gaussian had a FWHM of 5.4 mm for the 5 mm thick sample, and 10.4 mm for the 15 mm thick sample including skin. The FWHM of the sample with skin was higher than that of the 20 mm thick sample, indicating that skin introduces more dispersion than tissue.

During the deep Raman theatre project (results found in Chapter 5), 41 specimens were measured of which four had skin attached. In figure 4.9, the Raman measurements on one of the fresh breast specimens with attached skin are shown. In the upper panel measurements through skin are shown and in the lower panel measurements through tissue on the same specimen.

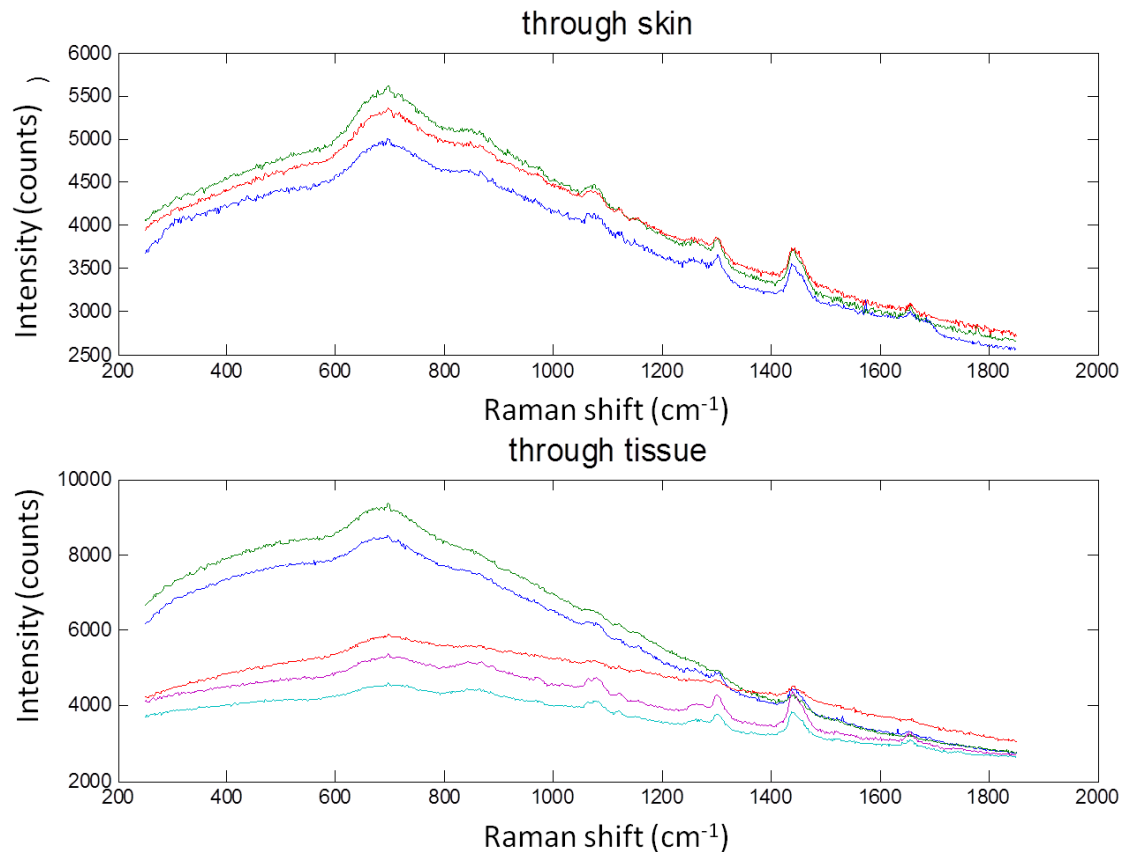


Figure 4.9: Measurements through skin and through tissue only on a fresh human breast specimen.

The sample thickness is equal for the area with and without skin and measurements could be obtained from both. However, the measurements through tissue clearly show a higher SNR than measurements through skin; 3.44, 4.77, 5.42, 5.75, and 7.24 compared to 2.98, 3.07, and 3.55. The SNR is calculated by taking the amplitude of the Gaussian fit to the band as the signal and divide this by the noise observed between 350 and 450 cm^{-1} .

In figure 4.10, measurements on a second breast specimen with attached skin are shown. In the upper panel, measurements through skin are shown, and in the lower panel measurements through tissue. Through both sets the characteristic Raman bands of breast tissue are shown although it should be noted that in the measurements without skin a higher SNR was obtained; 5.78, 6.20, and 6.31 for the measurements through skin and 4.50, 9.82, and 12.58 for the measurements through tissue only.

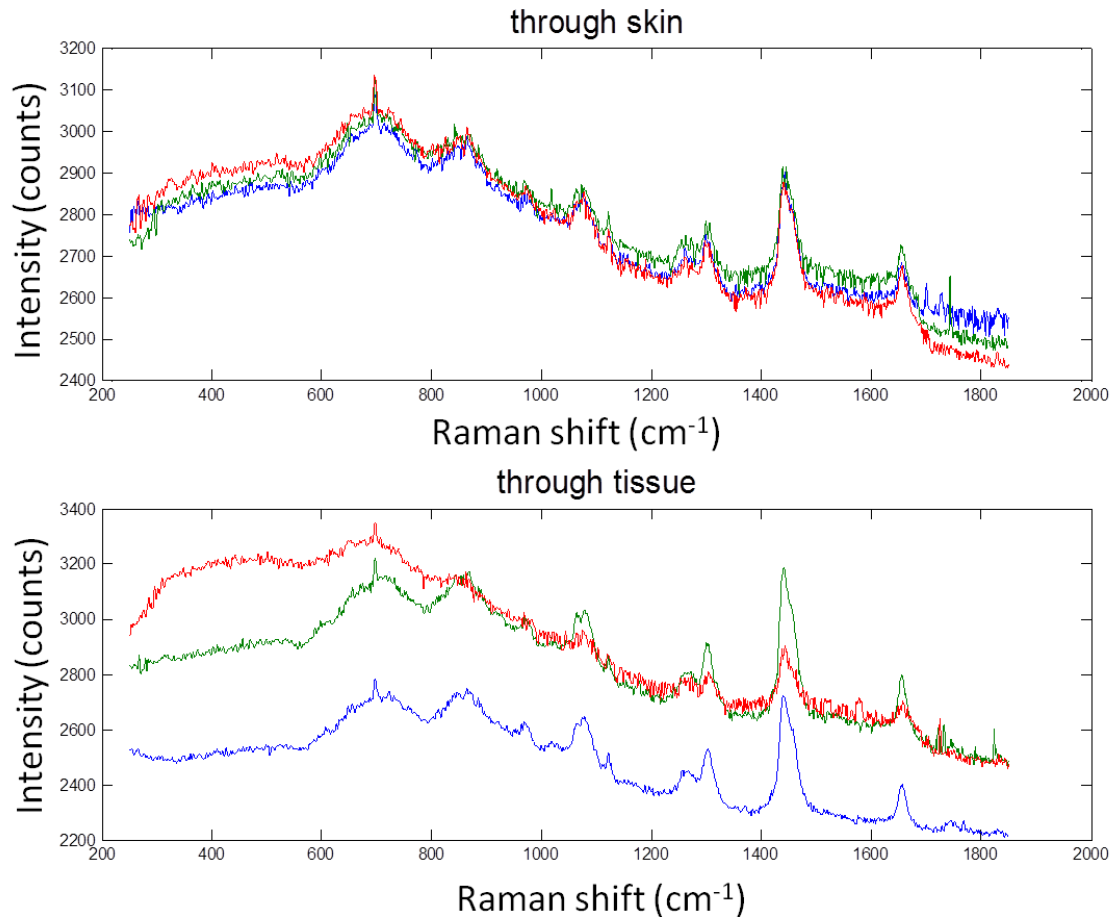


Figure 4.10: Measurements through skin (n=3) and through tissue only (n=3) on a fresh breast specimen.

Similar results were observed in the third specimen with skin attached. The two measurements through skin had a SNR of 3.9 and 4.0, while the measurements through tissue on the same sample had a SNR of 3.4, 6.3, 7.6, 8.8, and 9.7 (figure 4.11).

Chapter 4

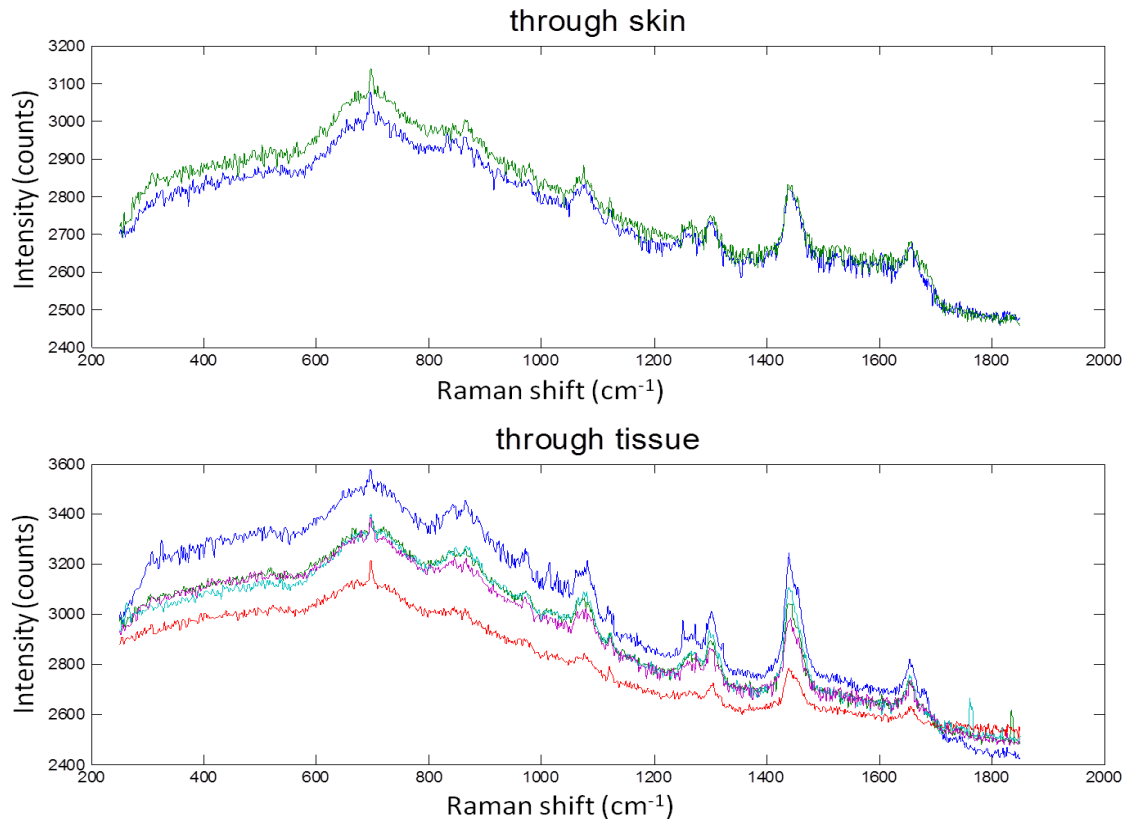


Figure 4.11: Measurements through skin (n=2) and through tissue only (n=4) on a fresh human breast specimen.

The last specimen had skin over the whole of the top and measurements comparing the signal with and without skin could not be performed.

5 Deep Raman spectroscopy on breast calcifications and tissue

In this chapter the use of the deep Raman system is tested on breast calcification standards and fresh human breast tissue. The feasibility of using a pseudo marker for the amount of carbonate substitution is tested with bare samples and samples buried in breast models. Furthermore, a proof of principle study is presented in which transmission Raman is applied on freshly excised human breast specimens.

5.1 Use of a pseudo marker to estimate the amount of carbonate substitution

The amount of CO_3 substitution in the lattice can be deduced from the relative intensities of the corresponding bands. Unfortunately, the CO_3 band at 1074 cm^{-1} is relatively weak and often obscured by photon shot-noise (predominantly from fluorescence) which makes it difficult to characterise, especially by non invasive means. Haka et al. (2002) found a linear relationship between the FWHM of the 960 cm^{-1} phosphate stretching mode and the calcium carbonate content. In dentin samples a shift was observed (Xu et al., 2009). If a shift or broadening of this peak was correlated to the carbonate concentration too it would make the development of a diagnostic tool substantially easier since this peak is much stronger than the features around 1042 and 1074 cm^{-1} . The goal of this study was to investigate if the 960 cm^{-1} band could be used as a pseudo marker for the amount of carbonate substitution.

5.1.1 Position of the 960 cm^{-1} band

Calcifications standards with different amounts of carbonate substitution were measured on the transmission Raman setup. A Gaussian band was fitted to the 960 cm^{-1} phosphate band of the apatite, as shown in figure 5.1. The interpolated data is shown in blue and the fitted Gaussian in red.

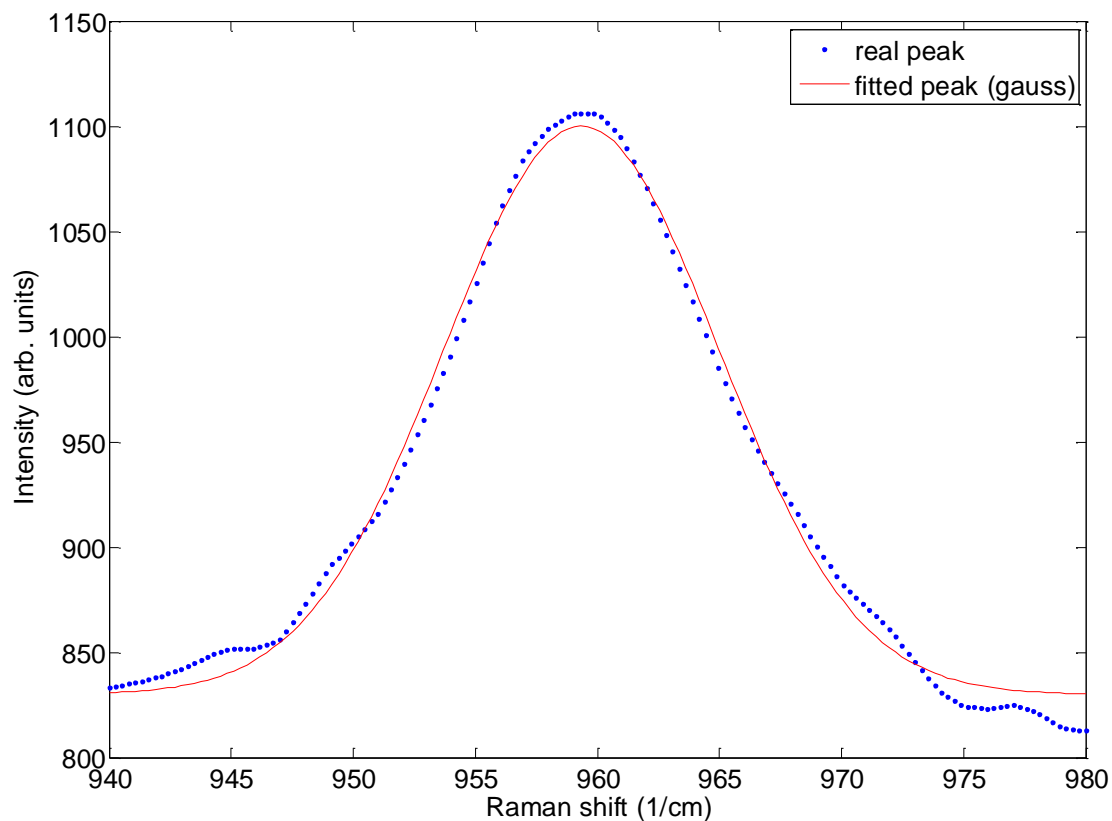


Figure 5.1: Gaussian fit on calcification standard with 2.3% carbonate substitution.

The width and position of the Gaussian fit was then examined for measurements ($n=5$) on each of the samples. The mean peak position for each of the bare standard samples ($n=5$) was plotted against the calcification substitution percentage (figure 5.2 in green).

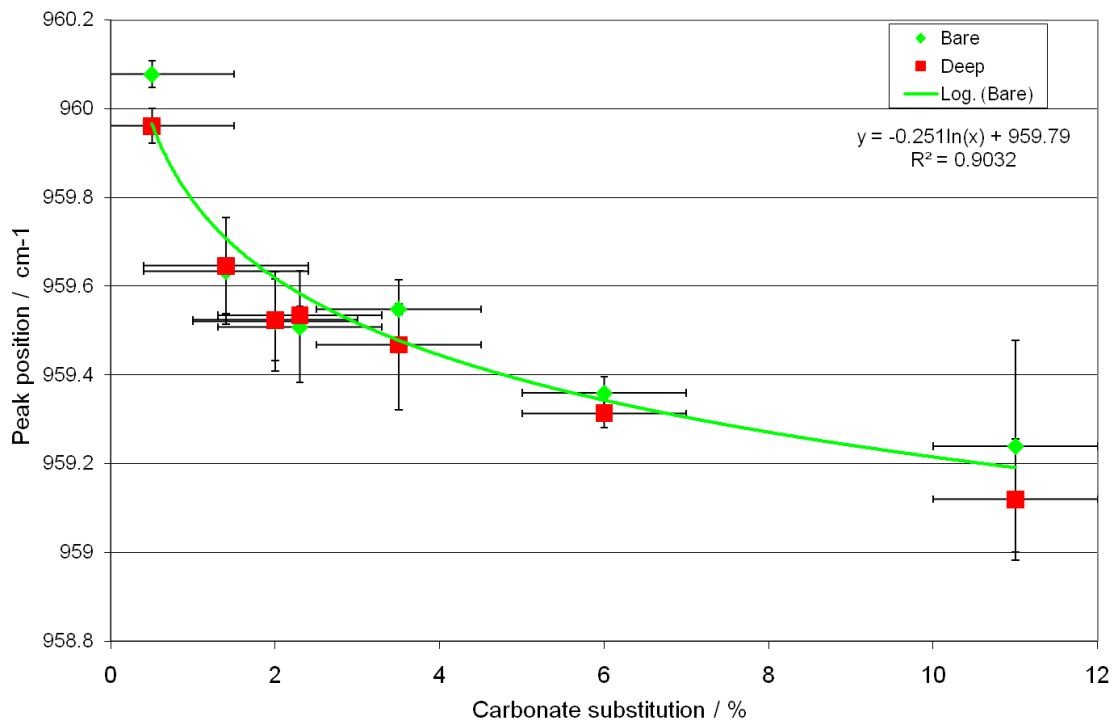


Figure 5.2: Relation of the carbonate substitution and the position of the 960 cm⁻¹ band.

A logarithmic function was fit to these points (Figure 5.2):

$$y = -0.251 \ln(x) + 959.79$$

Equation 5: Fit of the relationship between the carbonate concentration (x) of the calcification standard and the location of the 960 cm⁻¹ band (y).

The samples were buried in porcine soft tissue (tissue thickness = 3.6 mm, overall thickness 5.6 mm) and again a Gaussian was fitted to the data. The mean values for the buried calcifications (n=3) are depicted in the figure 5.2 in red. Equation 4 was used to provide a prediction for amount of carbonate substitution for the samples based on the peak positions of the 960 cm⁻¹ band. It can be seen that the buried calcification standards have peak positions within a standard deviation of each other (shown with error bars). The actual versus the predicted carbonate substitution was plotted in Figure 5.3. Table 5.1 shows the root-mean-square-error of these predictions.

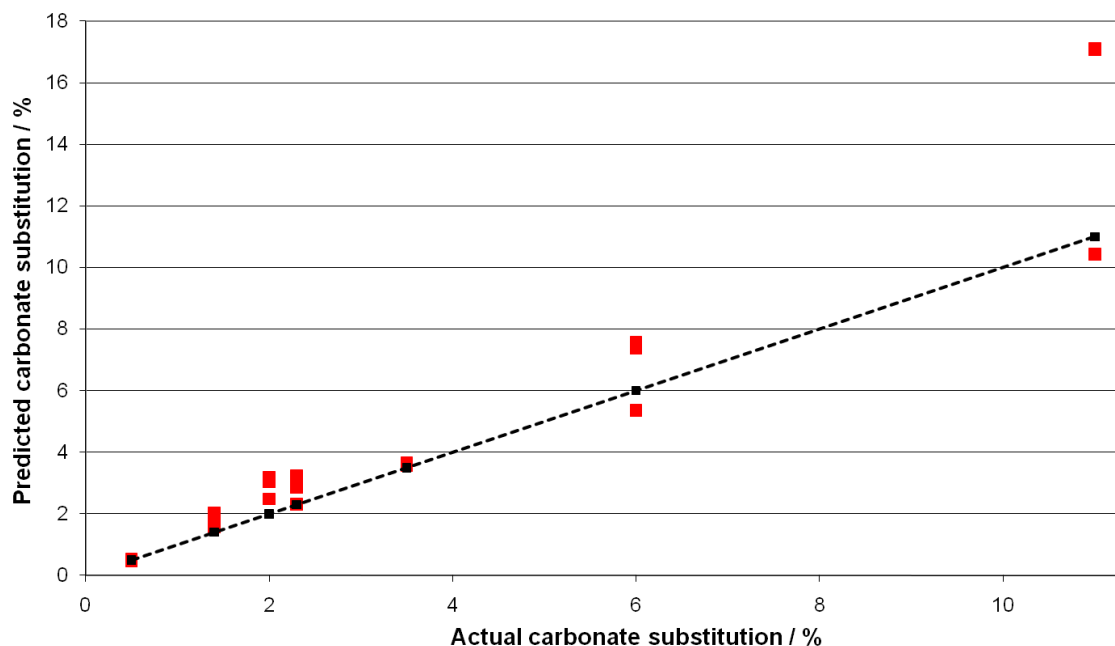


Figure 5.3: Actual versus predicted carbonate substitution based upon the position of the 960 cm^{-1} band.

Carbonate substitution according to supplier (quoted as $\pm 1\%$)	Mean predicted carbonate percentage through tissue (\pm std)	Root mean square error of prediction (% carbonate)
0.5%	0.51 ± 0.04	0.03
1.4%	1.79 ± 0.23	0.43
2.0%	2.91 ± 0.37	0.96
2.3%	2.80 ± 0.46	0.63
3.5%	3.61 ± 0.05	0.12
6.0%	6.77 ± 1.23	1.26
11.0%	14.88 ± 3.85	4.99

Table 5.1: Prediction of the percentage carbonate substitution based on the location of the peak.

There is some subtle variability in the position of the phosphate peak between measurements from different areas of the same sample. It is thought to be due to the heterogeneous nature of the apatite standards used. Also, a systematic difference in width between bare and buried samples can be observed which is believed to be caused by the SNR of the buried samples. When signal was acquired for a longer period of time these differences were not observed. The region of interest (clinically relevant area) is between 0.5% and 2.5% and is based on work of Baker (2010) which

indicated that calcifications corresponding to benign pathology have an average carbonate substitution around 2%. This percentage is lower for calcifications corresponding to *in situ* and invasive pathology; where the amount of carbonate substitution is ~1.7% and ~1.4% on average, respectively. The data of these three pathology groups show a spread from 0.5 to 2.5% carbonate substitution and in this clinically relevant area the relationship between the carbonate substitution and the band position of the phosphate band is semi-exponential.

Additional samples were kindly provided by Prof. Tecklenburg's group (Central Michigan University, Michigan, USA). The samples had a range of B-type carbonate substitution, and some which exhibited both A- and B-type substitution. Raman spectra measured on the Raman microscope system (Renishaw 1000 system, 60s accumulation time, n=5) are shown in figure 5.4. The phosphate band shifts to a higher wavenumber depending on the relative amount of A- and B-type substitution and not with the total amount of carbonate substitution. Therefore, the band position of the phosphate band can only be used if the relative amount of A- and B-type carbonate substitution are marker for disease and not to measure the total amount of carbonate substitution.

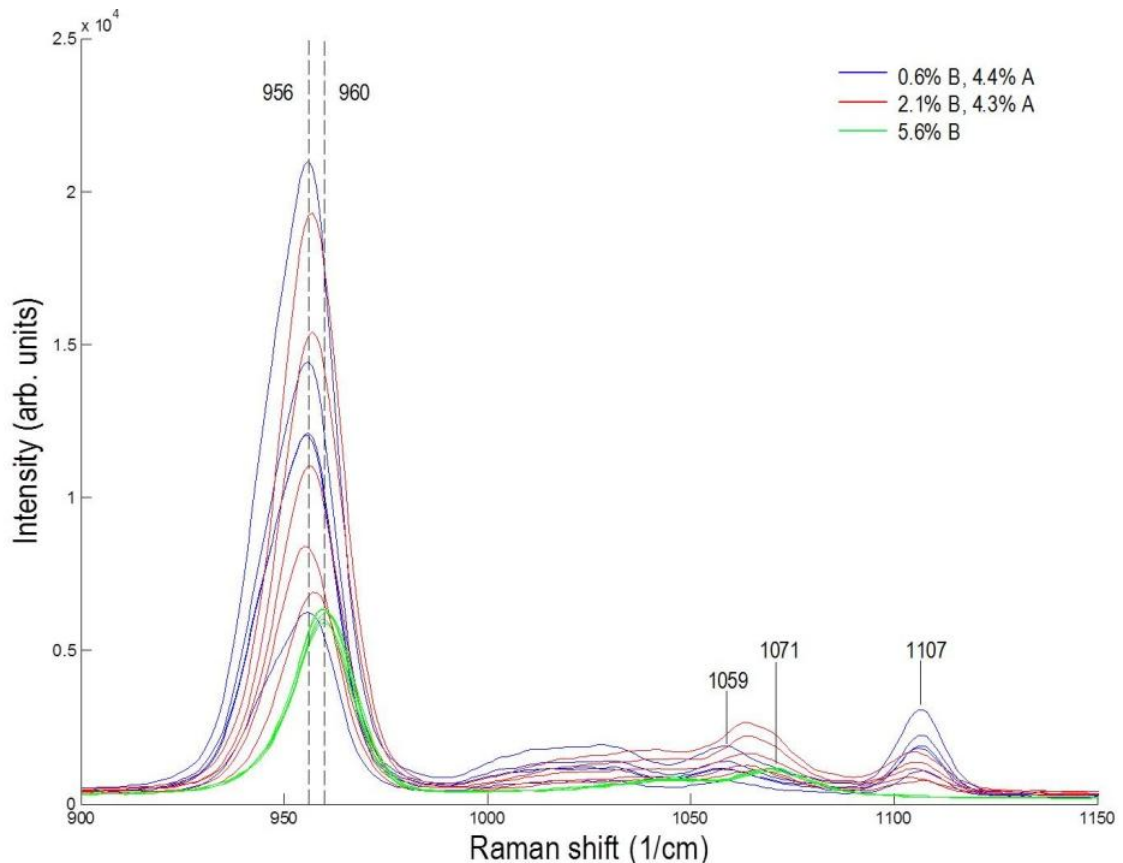


Figure 5.4: Band position of the phosphate band depends on the relative amount of A- and B-type carbonate substitution and not on the amount of carbonate substitution.

5.1.2 Width of the 960 cm⁻¹ band

The mean peak width for the fitted Gaussian of each of the bare standard samples ($n=5$) was plotted against the calcification substitution percentage in figure 5.5 in green. The width of the phosphate band increases with carbonate inclusion due to reduction of the crystallinity. Error bars show the uncertainty in the carbonate substitution value provided by the manufacturer (x axis) and the standard deviation of the replicate values of the spectral peak width (y axis).

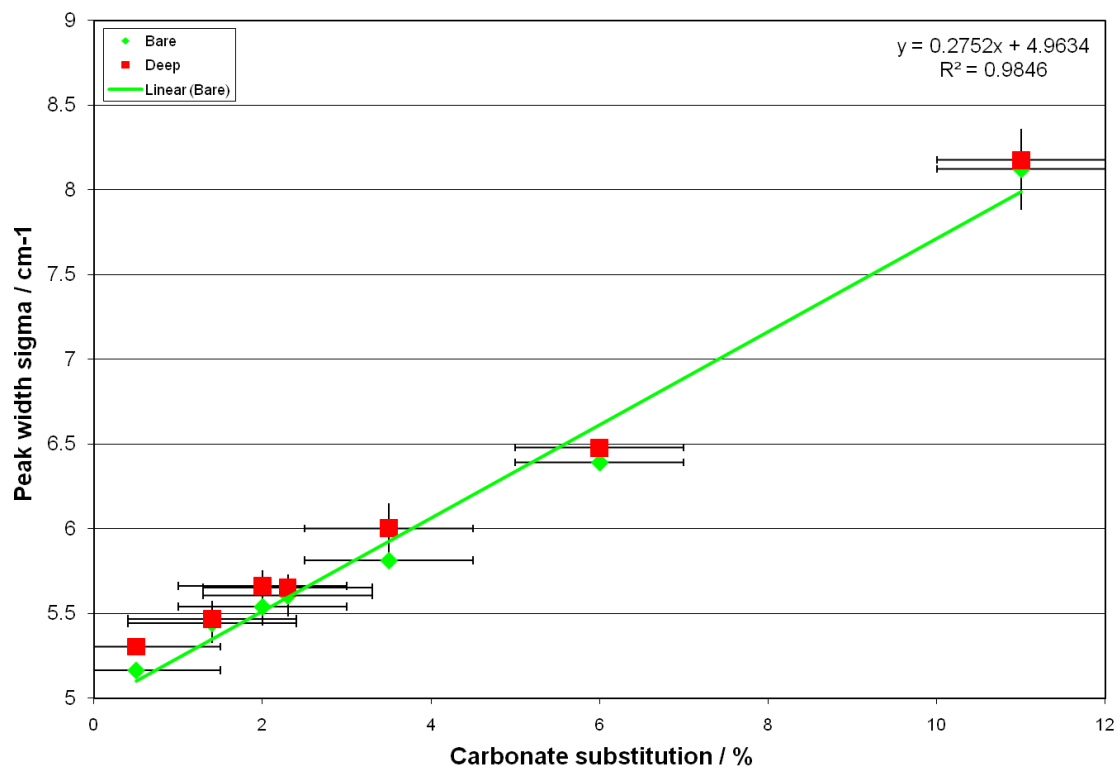


Figure 5.5: Peak with 960 cm^{-1} band versus carbonate substitution.

A linear function was fit to the width of the bare standards:

$$\sigma = 0.2752x + 4.9634$$

Equation 6: Fit of the relationship between the carbonate concentration (x) of the calcification standard and the width of the 960 cm^{-1} band (σ).

The mean values for the buried calcifications ($n=3$) are also depicted in red in figure 5.5. The buried calcification standards have peak widths within a standard deviation of each other (shown with error bars). Equation 5 was used to provide a prediction of the carbonate substitution percentage of the buried standards (tissue thickness = 3.6 mm, overall thickness 5.6 mm). Figure 5.6 shows the results plotted against actual concentration determined by the manufacturer with FTIR, the root-mean-square-error of the prediction is depicted in Table 5.2. Similar results were obtained for sample with an overall thickness of 16 mm (data not shown).

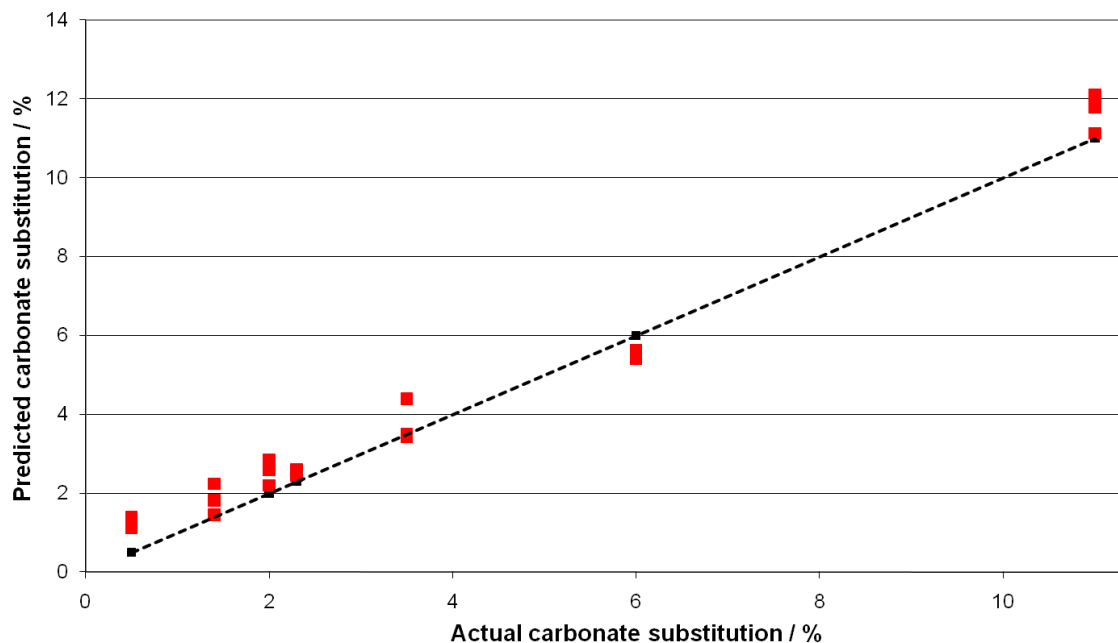


Figure 5.6: Predicted versus actual carbonate substitution of the buried material based on the width of the 960 cm^{-1} band.

Carbonate substitution according to supplier (quoted as $\pm 1\%$)	Mean predicted carbonate percentage through tissue (\pm std dev)	Root mean square error of prediction (% carbonate)
0.5%	1.22 \pm 0.14	0.75
1.4%	1.83 \pm 0.39	0.54
2.0%	2.55 \pm 0.33	0.61
2.3%	2.51 \pm 0.07	0.22
3.5%	3.78 \pm 0.53	0.52
6.0%	5.51 \pm 0.17	0.50
11.0%	11.68 \pm 0.50	0.79

Table 5.2: Prediction of the percentage carbonate substitution based on the width of the peak.

In a later stage of the project, apatite standards were available from Prof. Mary Tecklenburg. When comparing the new samples to the other batches (figure 5.7, samples Tecklenburg lab in blue, Clarkson Chromatography in red, and Rogers lab in green) it can be seen the same trend in the width of the Gaussian band is followed.

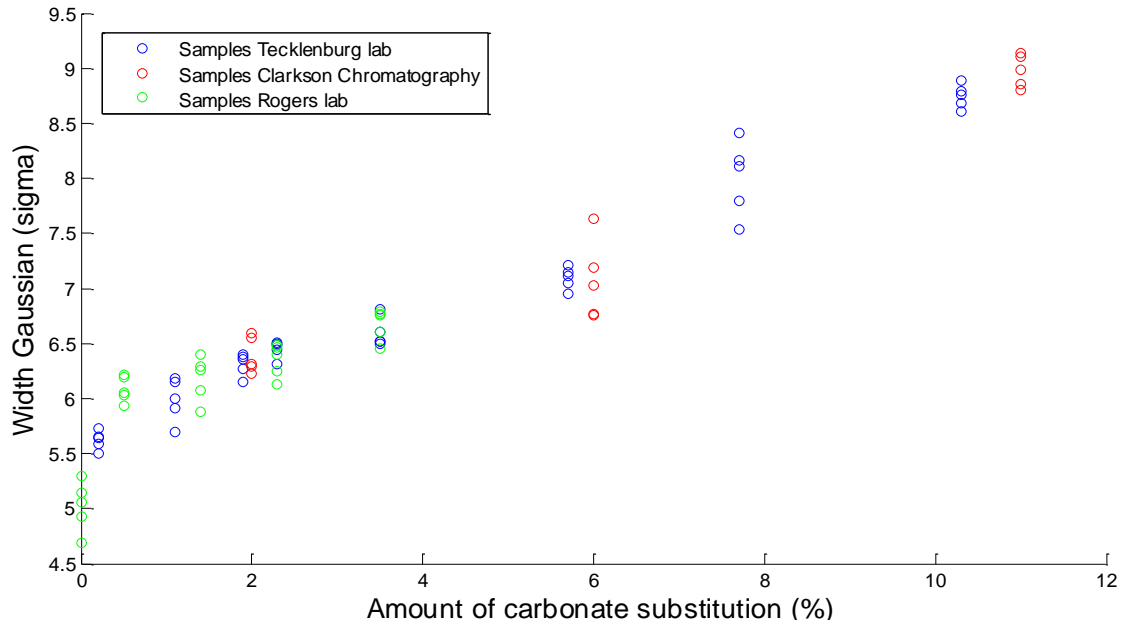


Figure 5.7: Gaussian fit on 960 cm^{-1} phosphate band on batches of apatites from different suppliers (Tecklenburg lab, Clarkson Chromatography, Rogers lab).

5.2 SNR limits for using the pseudo marker

In order to understand the limitations of this model, the signal to noise ratio is evaluated to understand what level of SNR is needed to predict a correct amount of carbonate substitution.

In figure 5.8, a measurement is shown in which a block of tissue with two buried calcification standards. When translating the specimen, apatite bands will appear and disappear when a calcification standard is measured.

The Gaussian fitting routine will try to fit a Gaussian to every single measurement. As can be seen in figure 5.8, this will not yield a valid answer in every case. For example, the measurement at 8mm does not show a peak in the spectrum to which a Gaussian can be fitted. A fit to this data will result to an answer with a high error bar.

Chapter 5

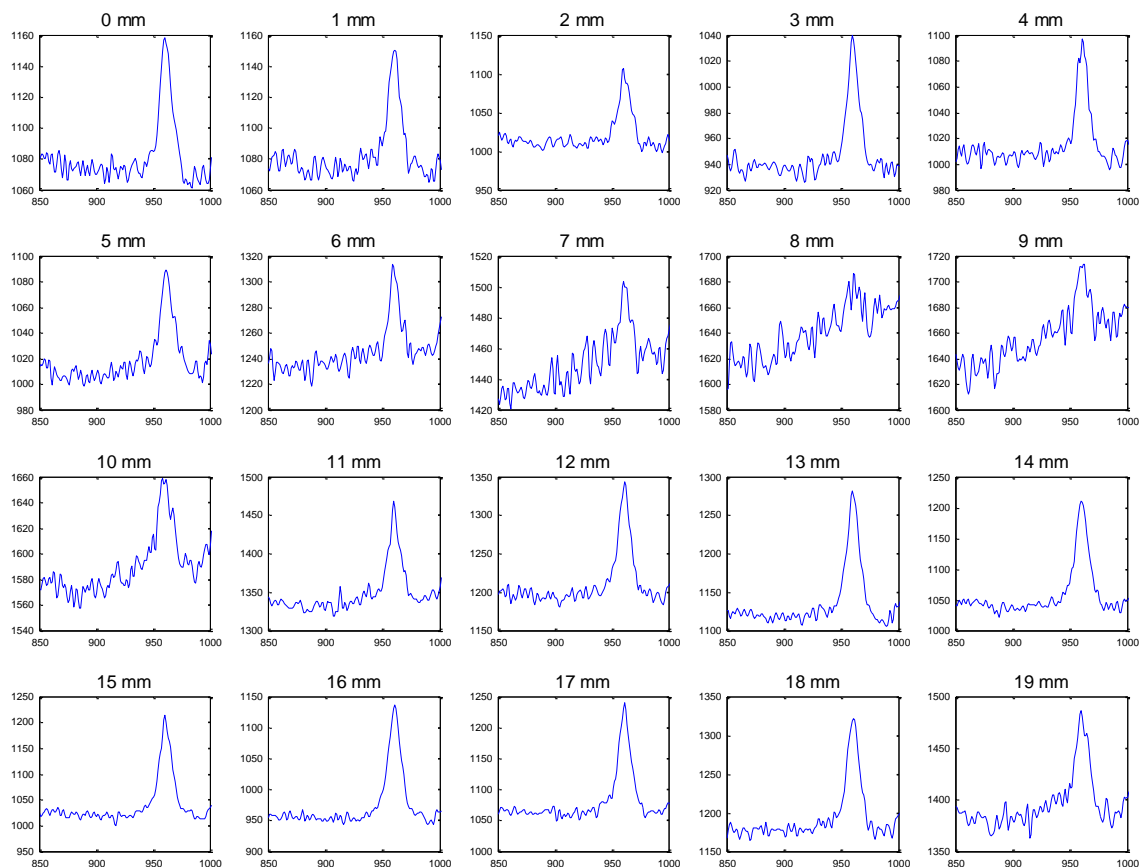


Figure 5.8: Spatial resolution experiment. The sample contains two calcification standards and is translated in steps of 1 mm (60 seconds accumulation time). Spectra of the 960 cm⁻¹ band (850-1000 cm⁻¹ region depicted) are shown for each step.

For every measurement the SNR was calculated and displayed against the grid position (Figure 5.9). By selecting data with a sufficient SNR, Gaussian fits will be a better representation of the spectrum and error bars will be smaller.

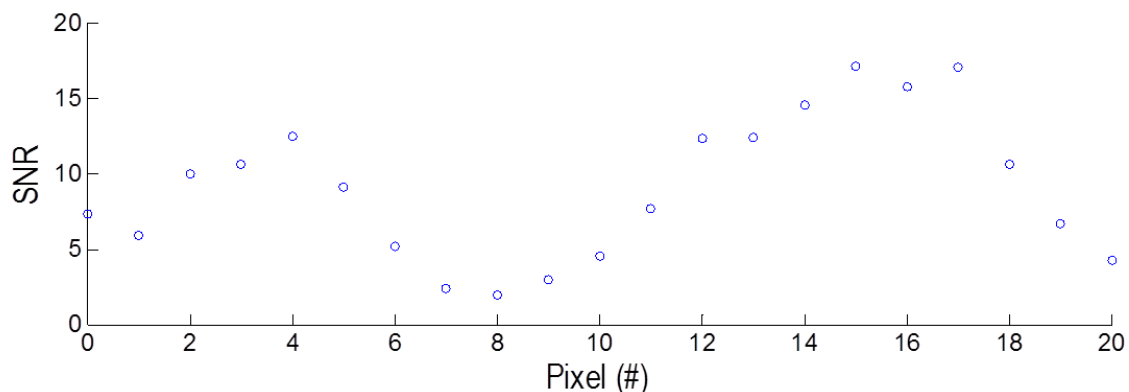


Figure 5.9: Mean SNR of measurements (n=5) versus the position.

The figure indicates that two regions of interest are passed (the maxima) and it can be seen that pixel 8, in which spectrum the 960 cm^{-1} band was not readily identified, shows a local minimum. The two maxima correspond to the cuvettes (high amount of apatite) and the minimum to the walls of the cuvettes and the area between them (low amount of apatite).

The carbonate substitution was evaluated based on the width of the 960 cm^{-1} band. Measurements of the bare standards were used to create a model. When the mean of steps 2-4, which have the highest SNR of the first feature, was evaluated a carbonate substitution of 1.4% was found, the same value was supplied by the manufacturer. The average of steps 14-17, the highest SNR for the second feature, indicated a carbonate substitution of 2.1%. The carbonate substitution quoted by the supplier was 2%.

To investigate the SNR limitation for using the pseudo marker calcifications standards were measured in front of a tissue block with a short accumulation time. By combining different spectra, as described in section 2.3.3.2, the SNR will increase. In table 5.3, the mean SNR is shown with the mean carbonate substitution and the predicted range in carbonate substitution for each amount of spectra averaged.

# of spectra	# of combinations	Predicted CO_3 range	CO_3 mean (std)	Mean SNR (std)
1	12	0-16.1%	6.5% (6.3)	3.43 (0.69)
2	66	0-15.6%	6.4 % (4.0)	4.20 (1.14)
3	220	0-14.4%	6.3% (3.1)	4.72 (1.16)
4	495	0.1-13.2%	6.3% (2.5)	5.15 (1.21)
5	792	0.7-12.2%	6.3% (2.1)	5.52 (1.28)
6	924	1.3-11.2%	6.3% (1.7)	5.83 (1.29)
7	792	2.0-10.2%	6.2% (1.5)	6.10 (1.30)
8	495	2.8-9.2%	6.2% (1.2)	6.32 (1.24)
9	220	3.7-8.5%	6.2% (1.0)	6.51 (1.14)
10	66	4.6-7.7%	6.2% (0.8)	6.66 (0.98)
11	12	5.4-7.1%	6.2% (0.5)	6.74 (0.67)
12	1	6.2%	6.2 %	6.81

Table 5.3: The predicted carbonate range, mean carbonate substitution and SNR for each combination of spectra.

Chapter 5

In general, the higher the SNR value the closer the value found for carbonate substitution is to the 6% quoted by the supplier. This is more readily displayed in figure 5.10, in which the calculate amount of carbonate substitution is plotted versus the SNR. The extreme values in carbonate substitution are found with the lowest SNR value and the highest SNR values indicate a carbonate substitution level closest to what the supplier quoted. The value quoted by the supplier is indicated by a red line and the range quoted by dotted red lines.

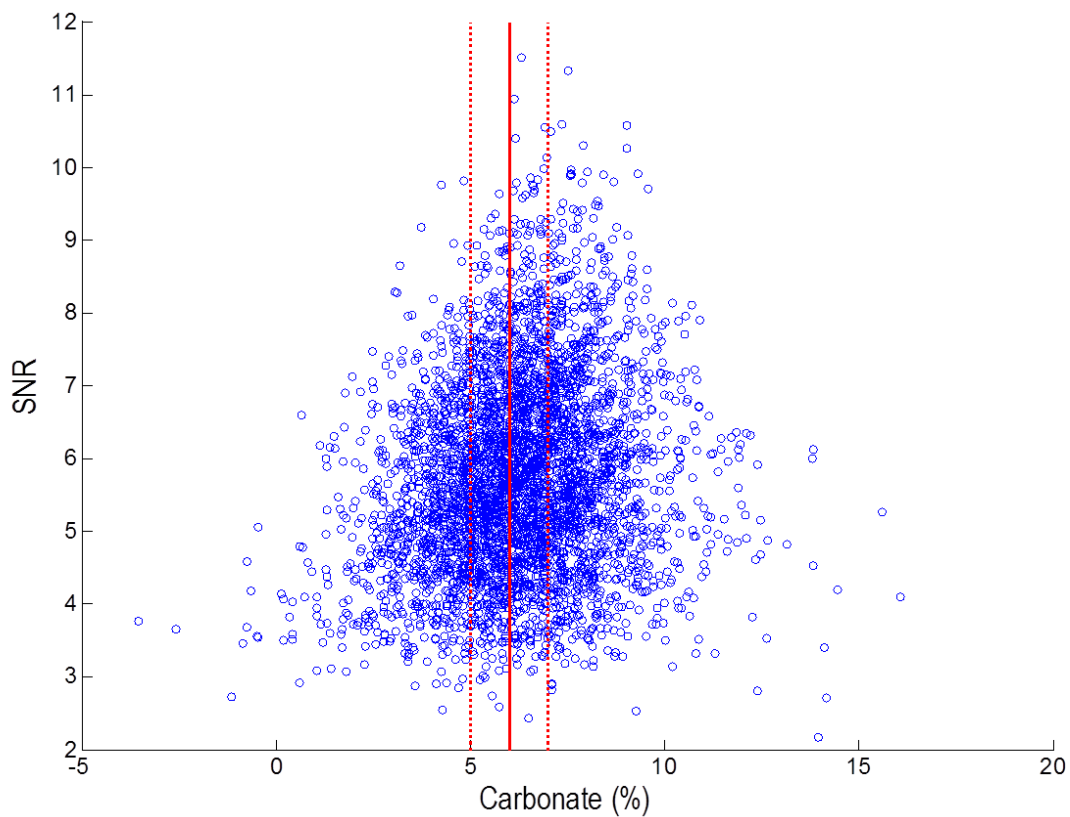


Figure 5.10: Predicted amount of carbonate substitution versus the SNR.

When nine measurements are averaged, the calculated carbonate substitution has a standard deviation equal to the range quoted by the supplier. Averaging nine measurements gives a SNR of 6.5.

5.3 Theatre project deep Raman spectroscopy on breast

As a proof of principle study for detection of calcifications in breast, breast tissue that was excised during (wire guided) local excisions was measured with the transmission Raman setup. X-ray images of the specimens (appendix E3) were used as a golden standard for the presence of calcifications.

Due to the nature of the samples, a range of different properties are observed such as thickness, and the presence of skin or blue dye within the sample group.

From all these measurements transmission spectra could still be measured. In figure 5.12, the mean spectra of the specimens with and without blue dye are plotted.

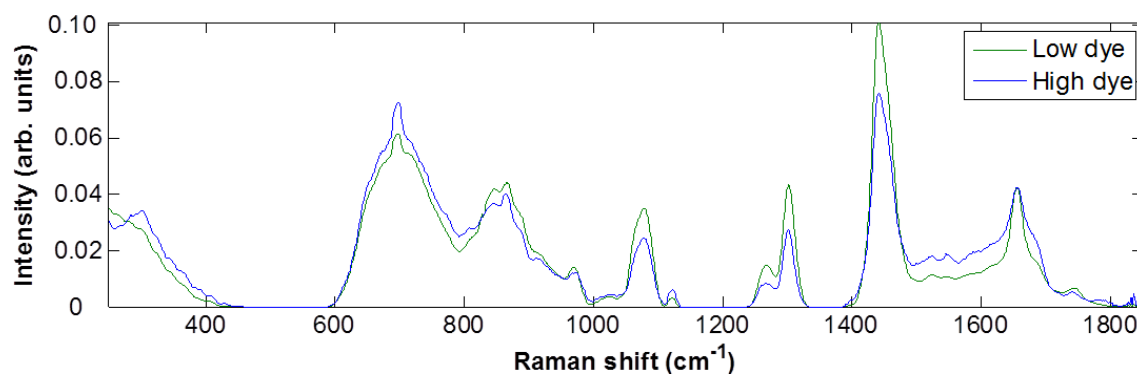


Figure 5.11: Mean spectra of specimens with (blue) and without blue dye (green). Both mean spectra show the same spectral features.

The mean spectra of both groups are shown in figure 5.13. No 960 cm⁻¹ band was detected in the calcification rich (red) spectrum which could be due to several limitations of the study.

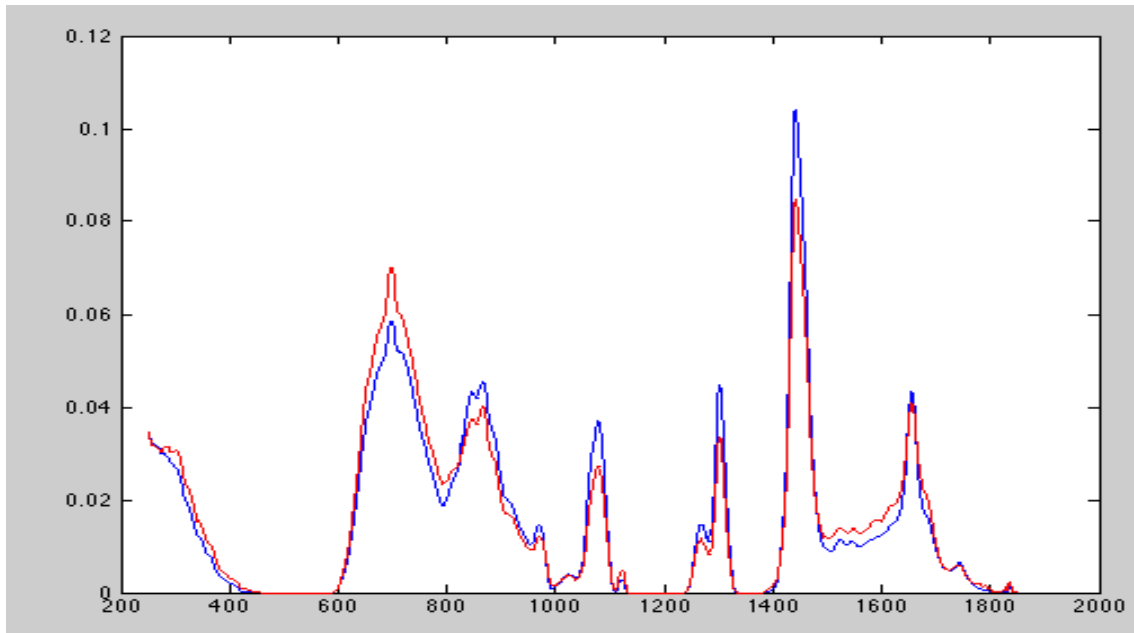


Figure 5.12: Mean spectra of calcification rich (red) and calcification poor (blue) specimens.

Due to the thickness of the samples, the intensity of the calcification bands will be limited. PCA was performed on the dataset in an attempt to pick up small variations between the calcification rich and calcification poor group. In figure 5.14 below, the loads of principal component one to twelve are displayed.

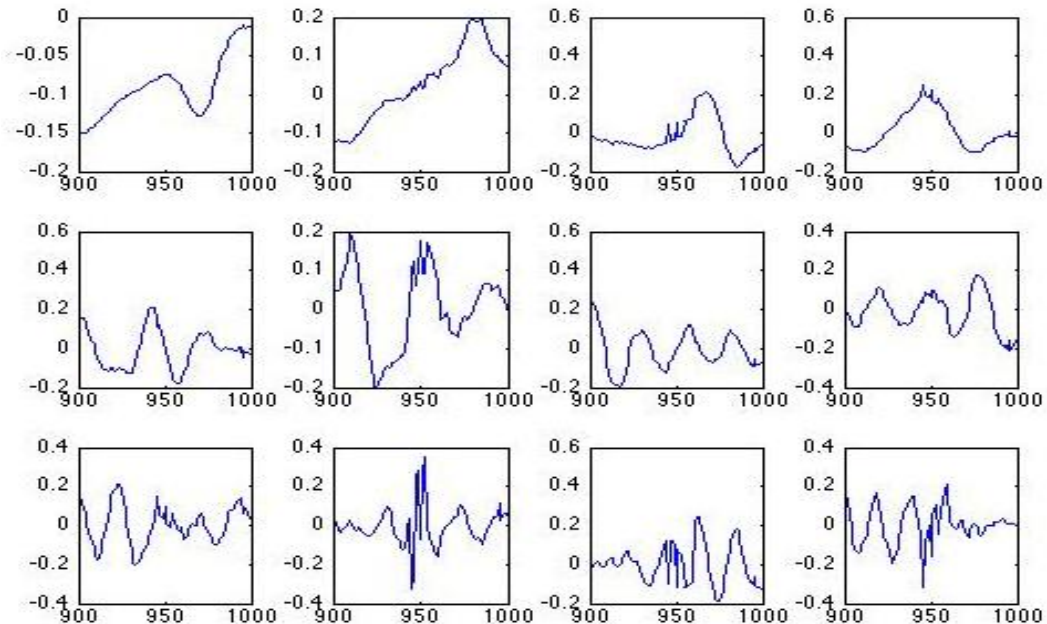


Figure 5.13: Loads of principal component one to twelve.

Chapter 5

The scores of each principal component are then plotted versus the next principal component for both specimens with (red) and without (blue) calcifications. A minimal separation was found when plotting principal component one versus principal component two.

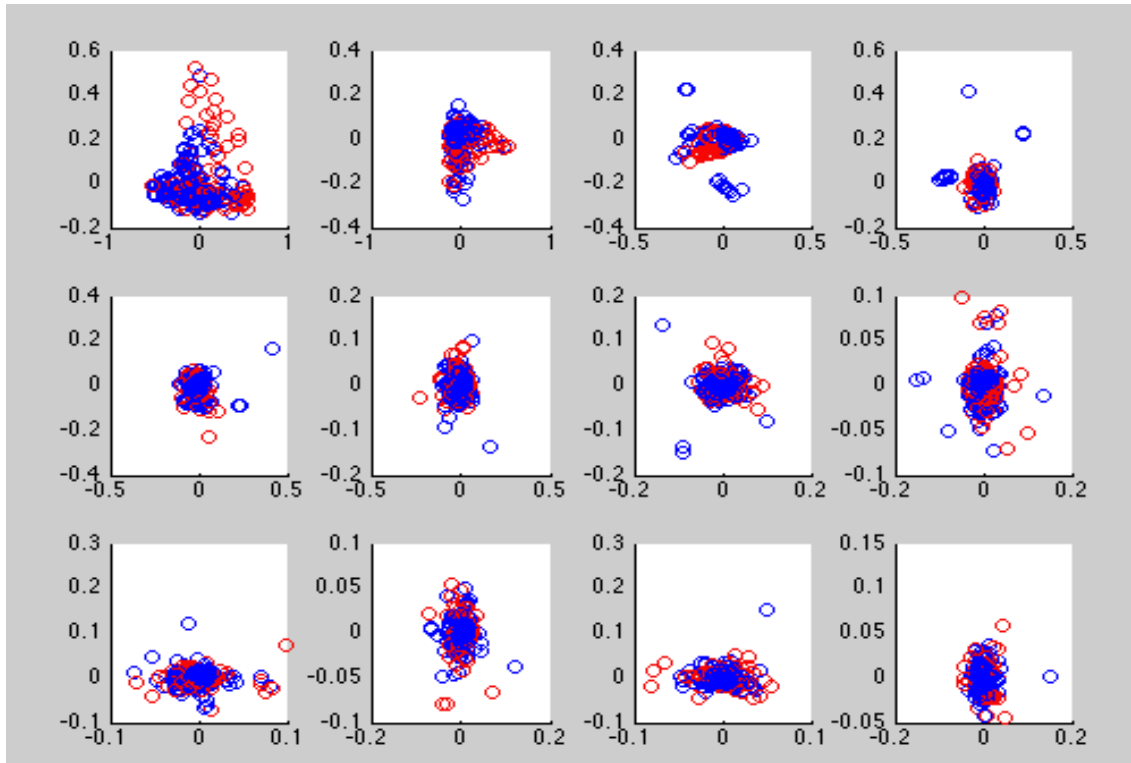


Figure 5.14: Principal component 1, 2, and PC scores of PC1 and PC2 of calcification rich (red) and calcification poor (blue) specimens.

It was then attempted to further improve the separation by increasing the amount of groups the data is split in to four: a group with no calcifications, a 'unknown' group in which it is unsure from the X-ray images whether or not the specimens do contain calcifications, a group in which calcifications are present, and a group in which the calcification density is high. Mean spectra of all four groups are displayed in figure 5.16 below.

Chapter 5

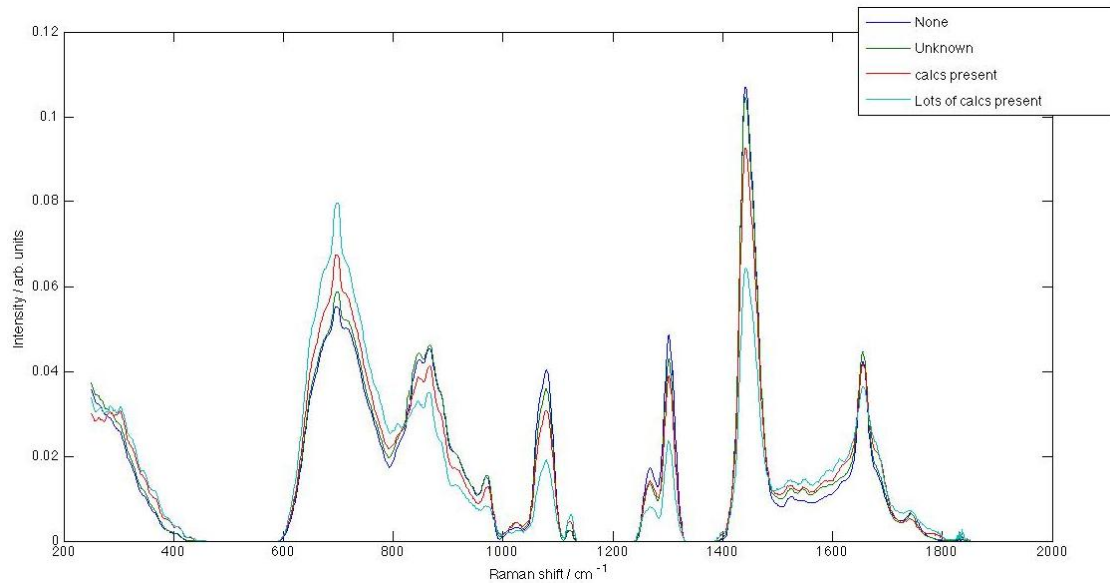


Figure 5.15: Mean spectra of specimens without calcifications (blue), specimens of which it is unsure whether they contain calcification (green), specimens with calcifications present (red) and specimens with a high amount of calcifications (cyan).

For each group (no calcifications in green, unknown in blue, calcifications in yellow and a high amount of calcifications in red) the scores for each PC were plotted versus the next PC. Examples are shown in figure 5.16 below.

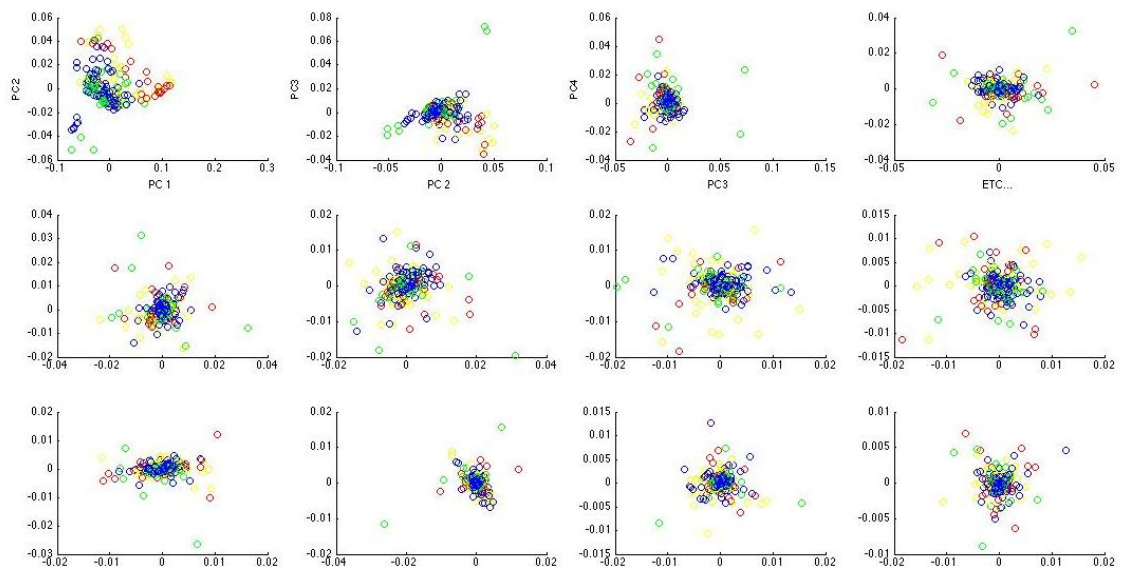


Figure 5.16: PC score versus the PC score for the next principal component for specimens without calcifications (green), unknown (blue), calcifications (yellow) and high amounts of calcifications (red).

The group without calcifications (in green) can be separated from the group with a high amount of calcification (in red) when plotting principal component 1 versus principal component 2 which is more readily displayed in figure 5.18.

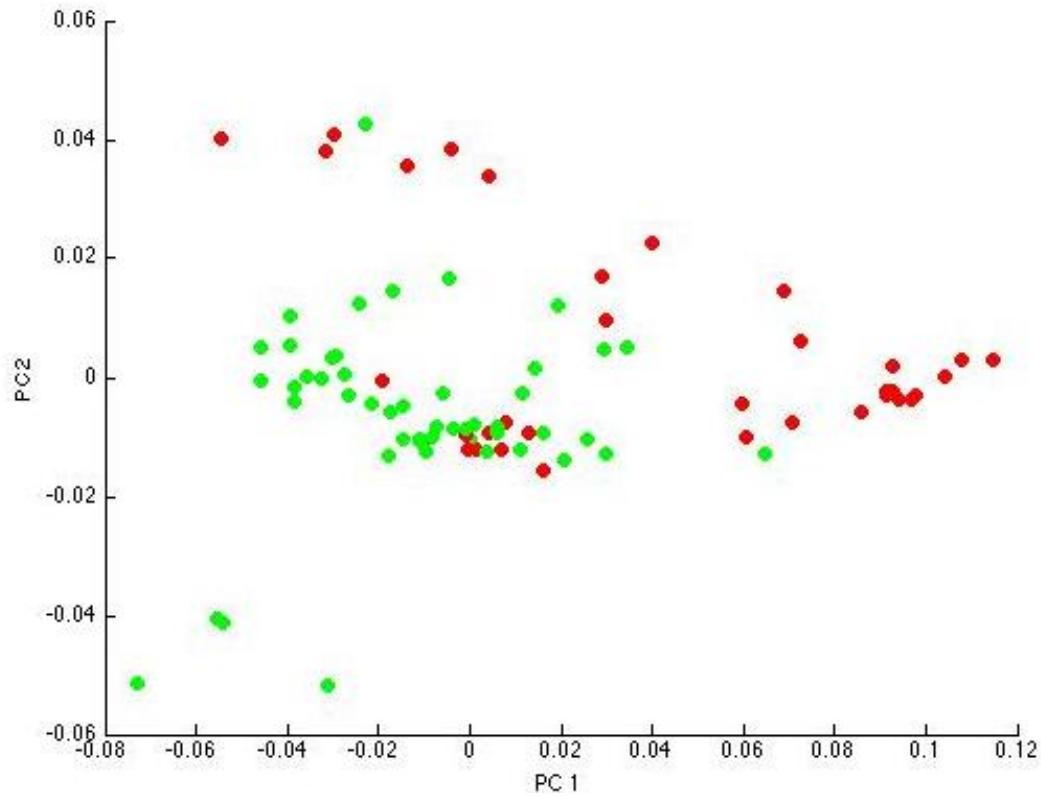


Figure 5.17: Plot of principal component 1 versus principal component 2 for specimens without calcifications (green) and specimens with a high amount of calcifications (red).

When feeding the PCA information into linear discriminant analysis (LDA) a linear combination of PCA features is used to discriminate both groups. The PCA-LDA result of the group without calcifications (displayed in green) and the group with a high amount of calcifications present (red) is shown in figure 5.19. Transmission Raman spectroscopy can pick up calcifications in the breast when measuring through a considerable amount of tissue (3-25 mm).

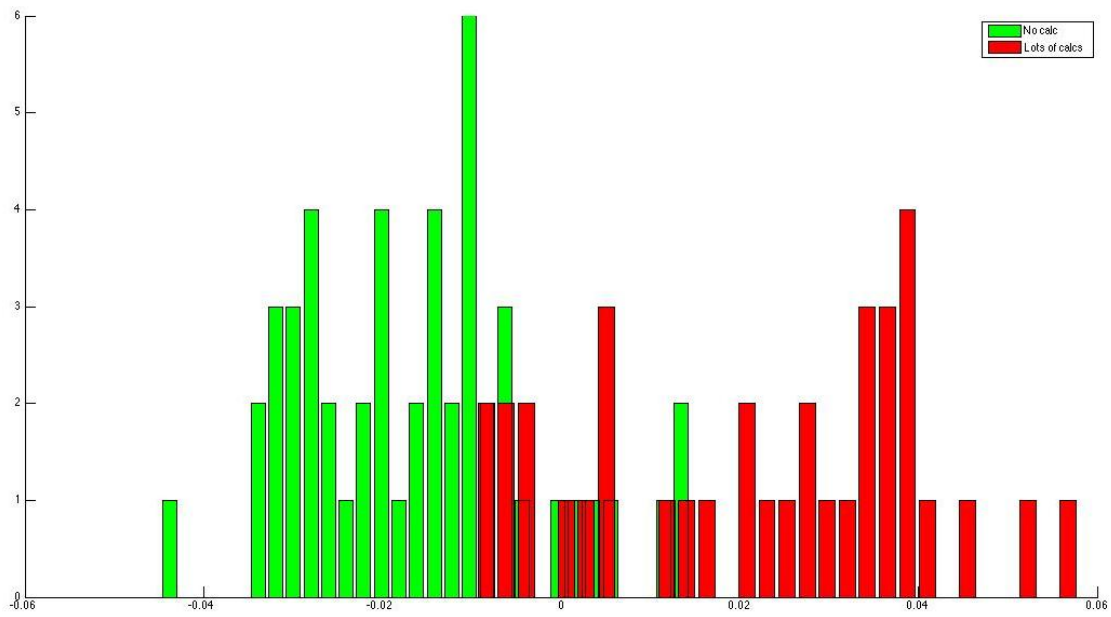


Figure 5.18: PCA LDA separation of specimens without calcifications (green) and specimens with a high amount of calcifications (red).

6 Discussion

6.1 Study of breast calcifications

6.1.1 Study of calcification standards

The FTIR and Raman measurements of the calcification standards were in agreement with existing literature. The position of the band in the 870 cm^{-1} - 880 cm^{-1} region is different for both types of carbonate inclusion, type A and B. Curve-fitting procedures are sometimes used on bands in this region to estimate the relative proportion of the carbonate species, but the accuracy of such a method can be questioned. According to Rey et al. (2007), these techniques have not been verified by other types of analyses. Fleet and Liu (2007) state that the 873 cm^{-1} , characteristic for B-type substitution, is not proportional to the content of B-type substituted carbonate in all apatites. In their study the samples were measured with both X-ray diffraction and FTIR. In all FTIR spectra the B-type substituted carbonate was dominant; while X-ray structures showed that in some samples the A-type substitution was more abundant than B-type substitution.

Transmission FTIR measurements of calcified materials are easily saturated which is not always obvious. ATR FTIR and Raman measurements do not show this saturation due to the limited thickness probed (ATR FTIR) and much weaker Raman effect (Raman measurements). When plotting the position and area under the curve of the phosphate band over a line scan across a calcification standard, a band shift is observed relating to the position on the calcification. This indicates the observed shift could be an artefact since the composition of the standard is expected to be similar over a grain of sample prepared in laboratory. Although band shifts were observed between different samples with similar levels but different types of carbonate substitution it is unsure whether this can be used to distinguish between samples with different types of carbonate substitution.

6.1.2 Comparison of spectroscopic techniques with staining

Most of the breast calcifications observed in the investigated samples were found in the ducts of the breast, although calcifications were distributed over the whole of the specimen in the invasive samples. In general, samples with invasive pathology contained most calcifications, followed by *in situ* and benign pathology (invasive > *in situ* > benign). However, making clinical decisions based on clustering (the amount of calcifications per unit area), or numbers of calcifications remains controversial. Park et al. (2000) indicated that the significance of clustering is lower than 50%, which means that clustering alone does not necessarily suggest malignancy.

In the benign samples FTIR imaging identified more calcification than both the AR and the VK staining. The finding of additional calcifications by FTIR analysis could be due to a higher sensitivity of the technique for calcifications that are forming or due to the small size of the calcifications which may result in them not being present in each of the slices of the samples. However, if differences between staining and FTIR were due to physical size of the calcifications resulting in the presence or absence in a certain slide, then it would be expected that also the reverse would be observed: i.e. positive staining by AR and/or VK and no spectroscopic sign of calcifications being present.

The location of AR and VK staining matched for the majority of the samples although AR stains a more extended area than VK and thus more readily visible. The area stained by VK matches the FTIR imaging and is thus thought to give a better indication of the size of the calcifications than AR staining. This size is important since it is thought to correlate to disease (Buchbinder et al., 2002). However, VK staining alone is not sufficient to identify and/or quantify bone like materials in cell cultures (Bonewald et al., 2003). It is proposed that techniques such as X-ray diffraction, electron microscopy or FTIR spectroscopy be applied. Furthermore it is suggested that in cases where there is no access to these techniques, both Alizarin Red and von Kossa staining should be used (Bonewald et al., 2003).

From the *in vitro* mineralisation time course study it becomes clear that the VK stain consistently lags the AR staining in the calcification formation process, which means that although calcium is present, hydroxyapatite has not crystallised. This means that caution should be exercised, when only employing one stain. For example, in many hospitals AR is used to show the presence of calcification in cartilage, whereas it is actually showing just the calcium distribution. Regions stained with AR appear to cover larger areas than the calcifications measured in this study and sometimes in early phases of calcification formation appear to stain when there are no calcifications apparent. When using stains, the use of at least two specific stains is therefore necessary. Raman and FTIR maps yield similar results so either one of these techniques would be sufficient to identify the presence of microcalcifications or to provide more detailed compositional information relating to the pathology, such as the amount of carbonate substitution. In pathology samples, FTIR will be preferable since the paraffin signal can be a problem when using Raman (Faoláin et al., 2005). However, *in vivo* measurements of breast calcification compositions will most likely require the use of Raman spectroscopy. Deep Raman developments show the most promise as an *in vivo* clinical tool for probing breast calcifications. Since the target for deep Raman measurements are mammographic calcifications, it should be noted that the resolution of histology for calcification detection is much higher than that of mammography. However, the spatial resolution of deep Raman spectroscopy is low and depends strongly on the thickness of the interrogated tissue.

6.1.3 Synchrotron FTIR imaging of breast calcifications

Previously, synchrotron FTIR measurements on breast calcifications were only described by Baker (2009) who included a study of three maps on frozen tissue in her PhD thesis. Baker observed a lower amide concentration in the calcification than in the surrounding tissue, which is under scribed by the studies presented in this thesis. This indicates that the features observed by

Baker et al. are genuinely caused by the chemical composition of the calcifications and rules out higher amide concentrations in the surrounding tissue and pixel crosstalk. In the benign specimens amide bands were not observed at all. An interesting finding presented here is that in the benign specimens bands were observed relating to A-type substitution and no bands related with B-type substitution, while both types were found in the samples with *in situ* pathology. This probably has to do with the formation and maturation processes of the calcifications and may be related to the tumour acidifying its surroundings. Carbonate is known to act as a buffer when the pH changes. The decreasing amount of carbonate substitution in the apatite lattice could then be explained by the carbonate being used to stabilise pH and the differences in substitution type by the preferential carbonate substitution (formation) or dissolving at that pH. The ratio of A- and B-type substitution should be further studied to find out if this feature can be used as a marker for disease.

In one of the specimens with invasive pathology a band was observed at 990 cm^{-1} . This band position is characteristic for whitlockite which can be observed *in vitro* together with apatite depending on the experimental variables and is observed in for example urinary calculi, prostatic deposits, cartilage and bone (Lagier and Baud, 2003) and might act as a seed for calcification. It would therefore be interesting to work backwards from the finding to the breast calcification environment. The amount of specimens and calcifications presented here is not enough for a quantitative study (although a qualitative study still fills a hole in literature), but the data obtained at the IRENI beamline will fill this gap.

6.1.4 ATR imaging of breast calcifications

During the ATR measurements a lower amount of amide was found in the calcification than in the surrounding tissue which is in agreement with the synchrotron measurements performed by Baker (2009). However, this could be

due to height differences caused by the slicing (the calcifications being higher than the surrounding tissue) which may cause a lack of tissue signal. The ATR FTIR measurements need more attention in order to understand the limitations and to understand which findings are genuinely caused by the chemical differences within the specimens and which by limitations of the system and specimens. The observed band shift between samples with different amounts of A- and B-type substitution could be due to the location of the measurements. When measuring at the middle of a grain calcification standard, a lower wave number position was found compared to measurements at the edge of a grain calcification standard. However, this is a really exciting proof of principle study for ATR FTIR measurements of breast calcifications. In other breast tissue ATR FTIR studies calcifications were not measured (Rehman et al., 2010; Walsh et al., 2012) and ATR FTIR might be an interesting technique to understand more of the environment of the calcifications and the formation and maturation processes.

6.1.5 Raman imaging of breast calcifications

In the past, Raman mapping on pathology samples has always been limited by the presence of paraffin. However, the paraffin removal protocol applied in this study was sufficient and no paraffin bands or fluorescence was observed. This gives way to more extensive studies. Raman mapping can be done in 1 μm steps with the Streamline software, which is similar to the ATR FTIR measurements performed and a huge improvement compared to the benchtop transmission FTIR system. Raman spectroscopy is less prone to artefacts observed with FTIR such as band shifts and therefore an interesting avenue to explore. An interesting study would be to measure maps over calcifications with a higher exposure time (thus improving the SNR) and evaluating the amount of carbonate over the calcifications and investigate if the amount of carbonate substitution is equally distributed over the calcifications or not.

6.2 Deep Raman system evaluation

6.2.1 Comparison porcine soft tissue and human mammary

During the system construction and evaluation, porcine soft tissue was used as a model for human mammary tissue. Porcine soft tissue is a valid model since the properties are similar, as is the Raman spectra of both types of tissue.

6.2.2 Sample thickness limits when using transmission Raman setup

During the theatre project 41 samples were measured on the transmission Raman setup which were compressed between 3 and 25 mm. The SNR decreases exponentially with increasing thickness. The calcification bands might not be visible when a low SNR is obtained and measurements with insufficient SNR could therefore give incorrect feedback on the composition of the specimens. Caution should be practised when basing judgements on measurements with a low SNR.

To achieve a SNR high enough to correctly assign the amount of carbonate substitution, a maximum thickness of 10 mm can be used with the current setup. The average thickness for compressed breast during the horizontal view is $54.1 \text{ mm} \pm 0.2 \text{ mm}$ and $56.8 \text{ mm} \pm 0.2 \text{ mm}$ for the oblique view (Robinson and Kotre, 2008). The SNR can be improved by employing a higher laser power and increasing the accumulation time of the measurements. In case the beam is defocused on the surface, the power is spread over a larger area and the laser power could be enhanced significantly without health risks. Furthermore, it should be noted that the breast can be compressed locally instead of the whole of the breast which would yield a lower sample thickness and thus higher SNR.

Deep Raman measurements were performed through a tissue block of 45-50 mm thickness by using a combination of SERS and SORS. The combination of

SERS and SORS opens up an interesting parallel avenue for probing organs with nanoparticles conjugated to specific antibodies to detect disease, ultimately, nanoparticles with different antibodies and reporter molecules (e.g. each disease is coded with a specific reporter molecule). Detection of several reporter molecules (the Raman label) simultaneously and separation of the signals makes it possible to indicate the origin of the signal; both in disease nature and its location. This capability would permit the use of the technique in a variety of medical fields such as cancer detection and the monitoring of treatments. In order to do this the target molecules needs to be known in order to tag the correct antibodies to the nanoparticles. To date, no studies have been performed on the excretion and toxicity of the nanoparticles used in this technique which can therefore not be used *in vivo*. It would however be possible to inject nanoparticles in excised tissue with tags to test for example the oestrogen and progesterone receptor status and HER2 expression. The whole of the specimen can be tested in this way instead of a few levels. Deep Raman techniques could in general be used to do an overall measurement of a specimen and used to warn a pathologist more levels of the specimen should be evaluated if one does not show abnormalities.

6.2.3 Lateral spreading in transmission Raman measurements

Due to lateral spreading of the photons, calcification signals will not only be measured right behind the calcification when aiming the beam right at the calcification, but also when the beam of the laser is placed slightly next to the calcification area. Lateral spreading might be utilised during interrogation of the breast by decreasing the amount of measurements in a grid and thus speeding up the procedure.

6.2.4 The originating depth and spatial resolution of transmission Raman signal

Transmission Raman spectroscopy does not make a distinction between signals originating from different depths. Other deep Raman techniques such as spatially offset Raman spectroscopy (SORS) do have this capability but have a more limited range of sample thicknesses for which they can be used. However, when using transmission Raman as an adjunct to mammography, the mammography will give spatial information whilst the transmission Raman measurements can be used for chemical information.

6.2.5 Measurements through skin

Measurements through skin were performed on human mammary tissue with attached skin. Although measurements through tissue and skin show a lower SNR than measurements through tissue only, it can be concluded that transmission Raman measurements can be done through skin. This is an important requirement for a non-invasive technique.

The measurements performed in this study are the first performed on mammary tissue with skin. In previous studies within the group (Baker et al., 2007; Matousek and Stone, 2007; Stone and Matousek, 2008; Stone et al., 2007) porcine soft tissue models were used and in other groups (Dingari et al., 2012; Saha et al., 2011) core biopsies without skin which also are much thinner than bulk tissue.

6.3 Deep Raman spectroscopy on breast calcifications and tissue

6.3.1 Use of a pseudo marker to estimate the amount of carbonate substitution

In this study, the use of the 960 cm^{-1} phosphate band as a pseudo marker for the amount of carbonate substitution was evaluated. The position of the band is not related to the amount of carbonate phosphate since this did not hold up when introducing new samples from different origin. The position is however related to the type of carbonate substitution. In contrast, the width of the phosphate band which is a marker for the amount of carbonate substitution. This 960 cm^{-1} phosphate band is the strongest in the apatite spectrum and not as easily obscured by shot noise as the other bands with which the carbonate content can be evaluated. Earlier studies (Haka et al., 2002) postulated a higher amount of carbonate within calcifications surrounded by tissue with benign pathology which was confirmed by Baker et al. (2010). This feature of the calcifications can now be exploited when measuring them through tissue. Measuring the amount of carbonate substitution through tissue gives way to a monitoring use of the deep Raman system. In certain cases monitoring would be preferable to invasive surgery, for example in older women where breast cancer may not advance in their lifetime. It might be interesting to study the type of carbonate substitution in a new study to investigate if there is a link with this feature and pathology grade. Another interesting possibility would be to study the calcifications change in time to shine light upon the formation and maturation process which is yet unknown.

6.3.2 SNR limits for using the pseudo marker

In this study it was evaluated that the measurement should have a SNR of 6.5 before applying the Gaussian fitting routine to correctly establish the amount of

carbonate substitution. This is an important study since a wrongly estimated amount of carbonate substitution, relating to the pathology of the surrounding tissue (Baker et al., 2010), might in the future lead to inappropriate judgements regarding treatment versus monitoring. It should be noted that for evaluation of the calcification type (i.e. type I or type II) a lower SNR could be used since the spectra are more distinct than type II calcifications with different amounts of carbonate substitution.

6.3.3 Theatre project deep Raman spectroscopy on breast

During the theatre studies, transmission Raman spectra were measured on fresh human breast tissue. Breast calcification signals could be picked up during these studies, which is an important step forward. Previous studies within the group were all based on porcine soft tissue models with mock up calcifications. Studies recently published by other groups (Dingari et al., 2012; Saha et al., 2011) were done on core biopsies and although they target natural human breast calcifications, lack the thickness component of the studies described in this writing. In order to move towards non-invasive screening techniques based around Raman spectroscopy, which would give chemical information in contrast to the commonly used mammography, measuring through several centimetres of human tissue and skin is of paramount importance. Hence, this study is the first in its kind to detect human breast calcifications within tissue. As stated before, this technique could be used as an adjunct to mammography before taking biopsies or to interrogate bulk specimens and in case abnormalities are detected this could be flagged up to the pathology department. More levels of the specimen should then be evaluated by the pathologist if one does not show abnormalities. Another application might be to use a deep Raman probe in the cavity left after a biopsy, to interrogate the margins.

7 Conclusion

7.1 Study of breast calcifications

Known calcification standards were studied with FTIR and Raman to understand the relationship between chemical differences and spectral differences. The observed spectral differences were in agreement with the literature. Vibrational spectroscopy was then compared to routine staining procedures. From the time series experiments it is evident calcium builds up before the apatite is formed. Calcification formation was detected by FTIR (both synchrotron and benchtop instruments) at the same formation stage as Raman mapping and in a similar size area. VK staining gives a better indication of the calcification size than AR staining. The staining experiments also indicated that most of the calcifications were located in the ducts of the breast and it is plausible that formation takes place there.

During the synchrotron experiments it transpired that amide is present in the centre of calcifications. Furthermore, a band shift was observed in the 1400-1500 cm^{-1} region, depending on the pathology grade, which is related to the type of carbonate substitution. It is therefore hypothesised that not only the amount of carbonate substitution can act as a marker for disease, but also the type of carbonate substitution within the breast calcifications.

Also, evidence for maturation was found in the shape and position of the phosphate band. In one of the calcifications a whitlockite core was observed which might act as a seed for the calcification.

Both ATR FTIR and Raman imaging are worth pursuing, since the phosphate bands are not as easily saturated and the spatial resolution much higher than that achieved with benchtop FTIR. Raman mapping seems more promising than ATR FTIR since larger areas could be interrogated, the specimen was not disrupted and information from higher wavenumbers could be obtained.

7.2 Deep Raman system evaluation

A deep Raman system was built which could be used in both SORS and transmission mode. Initial measurements were performed on porcine soft tissue to investigate the performance and limitations of the developed system. The amount of light coming through fresh human breast tissue decreases exponentially with thickness. An additional approach such as mammography should be used in parallel to complement the chemical information derived from deep Raman spectroscopy with spatial information. The presence of skin introduces an extra source of photon scattering which results in signal spread and diminishment. Although the SNR was lower for samples with skin than for samples without, satisfactory measurements could be performed on all specimens.

7.3 Deep Raman spectroscopy on breast calcifications and tissue

The performance of the 960 cm^{-1} phosphate band as a pseudo marker for the amount of carbonate substitution was tested. The width of the band changes linearly with increasing carbonate substitution. In contrast, the observed shift in position is not related to the amount but to the type of carbonate substitution. This band shift might be another marker for disease. Measurements were performed on calcification standards buried in both a porcine soft tissue model and human breast tissue. For an accurate estimation of carbonate substitution a SNR of at least 6.5 should be obtained.

Furthermore, a proof of principle study using 41 fresh human breast tissue specimens was presented. Measurements could also be performed on specimens with blue dye and/or attached skin. Specimens with many calcifications could be separated from specimens without any calcifications using a PCA-LDA model. This finding is an important step towards transmission

Raman spectroscopy as a non-invasive tool to probe the calcifications within the breast.

7.4 Recommendations for further work

The sample thickness used in the Diamond experiments resulted in saturation of the calcification bands in the FTIR spectra. Similar features were seen at the IRENI beamline, although the saturation problems were less significant. For future work, a lower sample thickness is suggested for Diamond experiments (< 3 micrometers). Originally, it was feared that slicing thinner sections would force out calcifications and therefore thicker sections were used. However, a pathology sample with a thickness of one micron was tested subsequently on the benchtop systems and it was observed that it still contained calcifications. It should be noted that the signals of the surrounding tissue will decrease significantly when doing transmission measurements on thinner samples.

Raman mapping showed great potential after removing the paraffin on the pathology samples. Part of the calcification patches were removed by applying the protocol so it would be useful to test the effect of different paraffin removal procedures. The protocol which removes the paraffin sufficiently and damages pathology samples the least should then be used to set up a Raman mapping study. In this thesis, only a proof of principle study is shown and in future studies it would be desirable to increase the sample numbers. Also it would be interesting to pay attention to the location of the carbonate inclusions in the calcifications since in the proof of principle study the amount of carbonate at the centre of the calcification was found to be higher than in the rest of the calcification.

The deep Raman study of fresh human specimens was limited by time and a more extensive study would be beneficial. To improve the detection of calcifications it is suggested that larger areas are interrogated using higher laser powers with defocused beam (maintaining the same power density).

Chapter 7

Furthermore it would be beneficial to have a direct access to X-ray images instead of receiving these afterwards because the time each sample can be taken out of the clinical pathway is limited and insufficient to map the entire sample. When X-ray images are taken when the specimens are already compressed the resolution of the image will increase and would it be easier to target specific locations during the deep Raman measurements. A translation system in the xy- plane would save time and it could also be used for additional measurements. Furthermore, it would be easier to position samples on a horizontal platform (i.e. laying them down and pointing the laser down through the sample) than mounting them upright as in our experiments. The sample holder can compress samples down to 10 mm and an extension of the range to lower thicknesses would be helpful for the sample study although not necessary for thicker samples such as whole breast.

REFERENCES

- Adibelli, Z.H., Oztekin, O., Gunhan-Bilgen, I., Postaci, H., Uslu, A., Ilhan, E., 2010. Imaging Characteristics of Male Breast Disease. *The Breast Journal* 16, 510–518.
- Antonakos, A., Liarakapis, E., Leventouri, T., 2007. Micro-Raman and FTIR studies of synthetic and natural apatites. *Biomaterials* 28, 3043–3054.
- Apfelbaum, F., Diab, H., Mayer, I., Featherstone, J.D.B., 1992. An FTIR study of carbonate in synthetic apatites. *Journal of Inorganic Biochemistry* 45, 277–282.
- Awonusi, A., Morris, M.D., Tecklenburg, M.M.J., 2007. Carbonate assignment and calibration in the Raman spectrum of apatite. *Calcif Tissue Int* 81, 46–52.
- Aydin, H.M., Hu, B., Sulé Suso, J., El Haj, A., Yang, Y., 2011. Study of tissue engineered bone nodules by Fourier transform infrared spectroscopy. *Analyst* 136, 775.
- Baker, R., Matousek, P., Ronayne, K.L., Parker, A.W., Rogers, K., Stone, N., 2007. Depth profiling of calcifications in breast tissue using picosecond Kerr-gated Raman spectroscopy. *Analyst* 132, 48–53.
- Baker, R., Rogers, K.D., Shepherd, N., Stone, N., 2010. New relationships between breast microcalcifications and cancer. *Br J Cancer* 103, 1034–1039.
- Baker, R.N., 2009. Spectroscopic Analysis Of Breast Tissue Microcalcifications. Cranfield University.
- Bellahcène, A., Castronovo, V., 1995. Increased expression of osteonectin and osteopontin, two bone matrix proteins, in human breast cancer. *Am J Pathol* 146, 95–100.
- Bellahcène, A., Castronovo, V., 1997. Expression of bone matrix proteins in human breast cancer: potential roles in microcalcification formation and in the genesis of bone metastases. *Bull Cancer* 84, 17–24.
- Blamey, R.W., 2000. ABC of breast diseases: Screening for breast cancer. *BMJ* 321, 689–693.
- Boczar, M., Wojcik, M.J., Szczeponek, K., Jamroz, D., Zieba, A., Kawalek, B., 2003. Theoretical modeling of infrared spectra of aspirin and its deuterated derivative. *Chemical Physics* 286, 63–79.
- Bonewald, L.F., Harris, S.E., Rosser, J., Dallas, M.R., Dallas, S.L., Camacho, N.P., Boyan, B., Boskey, A., 2003. Von Kossa Staining Alone Is Not Sufficient to Confirm that Mineralization In Vitro Represents Bone Formation. *Calcif Tissue Int* 72, 537–547.
- Bonucci, E., 2007. Biological calcification: normal and pathological processes in the early stages. Springer.
- Boskey, A.L., Mendelsohn, R., 2005. Infrared spectroscopic characterization of mineralized tissues. *Vibrational Spectroscopy* 38, 107–114.
- Boyd, N.F., Guo, H., Martin, L.J., Sun, L., Stone, J., Fishell, E., Jong, R.A., Hislop, G., Chiarelli, A., Minkin, S., Yaffe, M.J., 2007. Mammographic

References

- Density and the Risk and Detection of Breast Cancer. *New England Journal of Medicine* 356, 227–236.
- Buchbinder, S.S., Leichter, I.S., Lederman, R.B., Novak, B., Bamberger, P.N., Coopersmith, H., Fields, S.I., 2002. Can the Size of Microcalcifications Predict Malignancy of Clusters at Mammography? *Academic Radiology* 9, 18–25.
- Cancer Research UK, 2012a. CancerStats Incidence 2009 - UK.
- Cancer Research UK, 2012b.
www.cancerresearchuk.org/cancerstats/incidence/commoncancers.
Cancer incidence for common cancers, accessed 19 July 2012.
- Cassidy, J., Bissett, D., Spence OBE, R.A.J., Payne, M. (Eds.), 2006. *Oxford Handbook of Oncology*, second edition. ed. Oxford University Press.
- Cheng, H.D., Cai, X., Chen, X., Hu, L., Lou, X., 2003. Computer-aided detection and classification of microcalcifications in mammograms: a survey. *Pattern Recognition* 36, 2967–2991.
- Chiou, H.-J., Hung, S.-C., Lin, S.-Y., Wei, Y.-S., Li, M.-J., 2010. Correlations among mineral components, progressive calcification process and clinical symptoms of calcific tendonitis. *Rheumatology* 49, 548–555.
- Clark, R.J.H., 2002. Pigment identification by spectroscopic means: an arts/science interface. *Comptes Rendus Chimie* 5, 7–20.
- Cox, R., 2011. Cellular and molecular basis of mammary microcalcifications (PhD). Royal College of Surgeons in Ireland, Dublin.
- Cox, R.F., Hernandez-Santana, A., Ramdass, S., McMahon, G., Harmey, J.H., Morgan, M.P., 2012. Microcalcifications in breast cancer: novel insights into the molecular mechanism and functional consequence of mammary mineralisation. *Br J Cancer* 106, 525–537.
- Dekker, R.J., De Bruijn, J.D., Stigter, M., Barrere, F., Layrolle, P., Van Blitterswijk, C.A., 2005. Bone tissue engineering on amorphous carbonated apatite and crystalline octacalcium phosphate-coated titanium discs. *Biomaterials* 26, 5231–5239.
- Dessombz, A., Bazin, D., Dumas, P., Sandt, C., Sule-Suso, J., Daudon, M., 2011. Shedding Light on the Chemical Diversity of Ectopic Calcifications in Kidney Tissues: Diagnostic and Research Aspects. *PLoS ONE* 6, e28007.
- Dey, P., Bundred, N., Gibbs, A., Hopwood, P., Baildam, A., Boggis, C., James, M., Knox, F., Leidecker, V., Woodman, C., 2002. Costs and benefits of a one stop clinic compared with a dedicated breast clinic: randomised controlled trial. *BMJ* 324, 507.
- Dingari, N.C., Barman, I., Saha, A., McGee, S., Galindo, L.H., Liu, W., Plecha, D., Klein, N., Dasari, R.R., Fitzmaurice, M., 2012. Development and comparative assessment of Raman spectroscopic classification algorithms for lesion discrimination in stereotactic breast biopsies with microcalcifications. *Journal of Biophotonics* n/a–n/a.
- Duffy, S.W., Tabar, L., Olsen, A.H., Vitak, B., Allgood, P.C., Chen, T.H.H., Yen, A.M.F., Smith, R.A., 2010. Absolute numbers of lives saved and overdiagnosis in breast cancer screening, from a randomized trial and

References

- from the Breast Screening Programme in England. *J Med Screen* 17, 25–30.
- Eckel, R., Huo, H., Guan, H.-W., Hu, X., Che, X., Huang, W.-D., 2001. Characteristic infrared spectroscopic patterns in the protein bands of human breast cancer tissue. *Vibrational Spectroscopy* 27, 165–173.
- Elmore, J.G., Armstrong, K., Lehman, C.D., Fletcher, S.W., 2005. Screening for breast cancer. *JAMA* 293, 1245–1256.
- Elston, C. w., Ellis, I. o., 1991. pathological prognostic factors in breast cancer. I. The value of histological grade in breast cancer: experience from a large study with long-term follow-up. *Histopathology* 19, 403–410.
- Estepa, L., Daudon, M., 1997. Contribution of Fourier transform infrared spectroscopy to the identification of urinary stones and kidney crystal deposits. *Biospectroscopy* 3, 347–369.
- Evans, A., 2003. The diagnosis and management of pre-invasive breast disease: Radiological diagnosis. *Breast Cancer Res* 5, 1–4.
- Evans, A., Pinder, S., Wilson, R. (Eds.), 2002. Breast calcification: A diagnostic manual. Greenwich Medical Media.
- Evans, A.J., Wilson, A.R.M., Burrell, H.C., Ellis, I.O., Pinder, S.E., 1999. Mammographic features of ductal carcinoma in situ (DCIS) present on previous mammography. *Clinical Radiology* 54, 644–646.
- Everall, N., Matousek, P., MacLeod, N., Ronayne, K.L., Clark, I.P., 2010. Temporal and Spatial Resolution in Transmission Raman Spectroscopy. *Applied Spectroscopy* 64, 52–60.
- Faibish, D., Gomes, A., Boivin, G., Binderman, I., Boskey, A., 2005. Infrared imaging of calcified tissue in bone biopsies from adults with osteomalacia. *Bone* 36, 6–12.
- Fandos-Morera, A., Prats-Estève, M., Tura-Soteras, J.M., Traveria-Cros, A., 1988. Breast tumors: composition of microcalcifications. *Radiology* 169, 325–327.
- Faoláin, E.Ó., Hunter, M.B., Byrne, J.M., Kelehan, P., Lambkin, H.A., Byrne, H.J., Lyng, F.M., 2005. Raman Spectroscopic Evaluation of Efficacy of Current Paraffin Wax Section Dewaxing Agents. *Journal of Histochemistry & Cytochemistry* 53, 121–129.
- Fleet, M.E., 2009. Infrared spectra of carbonate apatites: ν_2 -Region bands. *Biomaterials* 30, 1473–1481.
- Fleet, M.E., Liu, X., 2007. Coupled substitution of type A and B carbonate in sodium-bearing apatite. *Biomaterials* 28, 916–926.
- Fleisch, H., 1998. Bisphosphonates: Mechanisms of Action. *Endocrine Reviews* 19, 80–100.
- Fleischmann, M., Hendra, P.J., McQuillan, A.J., 1974. Raman spectra of pyridine adsorbed at a silver electrode. *Chemical Physics Letters* 26, 163–166.
- Fondrinier, E., Lorimier, G., Guerin-Boblet, V., Bertrand, A.-F., Mayras, C., Dauver, N., 2002. Breast Microcalcifications: Multivariate Analysis of Radiologic and Clinical Factors for Carcinoma. *World Journal of Surgery* 26, 290–296.

References

- Foschini, M.P., Fornelli, A., Peterse, J.L., Mignani, S., Eusebi, V., 1996. Microcalcifications in ductal carcinoma in situ of the breast: histochemical and immunohistochemical study. *Hum Pathol* 27, 178–183.
- Frank, C.J., McCreery, R.L., Redd, D.C.B., 1995. Raman Spectroscopy of Normal and Diseased Human Breast Tissues. *Analytical Chemistry* 67, 777–783.
- Frank, C.J., Redd, D.C.B., Gansler, T.S., McCreery, R.L., 1994. Characterization of human breast biopsy specimens with near-IR Raman spectroscopy. *Analytical Chemistry* 66, 319–326.
- Frappart, L., Boudeulle, M., Boumendil, J., Lin, H.C., Martinon, I., Palayer, C., Mallet-Guy, Y., Raudrant, D., Bremond, A., Rochet, Y., Feroldi, J., 1984. Structure and composition of microcalcifications in benign and malignant lesions of the breast: Study by light microscopy, transmission and scanning electron microscopy, microprobe analysis, and X-ray diffraction. *Human Pathology* 15, 880–889.
- Frappart, L., Remy, I., Lin, H.C., Bremond, A., Raudrant, D., Grousseau, B., Vauzelle, J.L., 1986. Different types of microcalcifications observed in breast pathology. Correlations with histopathological diagnosis and radiological examination of operative specimens. *Virchows Arch A Pathol Anat Histopathol* 410, 179–187.
- Furedi, H., Walton, A.G., 1968. Transmission and Attenuated Total Reflection (ATR) Infrared Spectra of Bone and Collagen. *Appl. Spectrosc.* 22, 23–26.
- Gadaleta, S.J., Gericke, A., Boskey, A.L., Mendelsohn, R., 1996a. Two-dimensional infrared correlation spectroscopy of synthetic and biological apatites. *Biospectroscopy* 2, 353–364.
- Gadaleta, S.J., Paschalis, E.P., Betts, F., Mendelsohn, R., Boskey, A.L., 1996b. Fourier transform infrared spectroscopy of the solution-mediated conversion of amorphous calcium phosphate to hydroxyapatite: New correlations between X-ray diffraction and infrared data. *Calcif Tissue Int* 58, 9–16.
- Galkin, B.M., Muir, H.D., Feig, S.A., Soriano, R.Z., Frasca, P., 1983. Photomicrographs of breast calcifications. *Radiographics* 3, 450–477.
- Griffiths, P., De Haseth, J.A., 2007. *Fourier Transform Infrared Spectrometry*. John Wiley & Sons.
- Guinebretiere, J.M., Menet, E., Tardivon, A., Cherel, P., Vanel, D., 2005. Normal and pathological breast, the histological basis. *Eur J Radiol* 54, 6–14.
- Gulley-Stahl, H.J., Haas, J.A., Schmidt, K.A., Evan, A.P., Sommer, A.J., 2009. Attenuated Total Internal Reflection Fourier Transform Infrared Spectroscopy: A Quantitative Approach for Kidney Stone Analysis. *Appl. Spectrosc.* 63, 759–766.
- Gulsun, M., Demirkazik, F., Ariyurek, M., 2003. Evaluation of breast microcalcifications according to breast imaging reporting and data system criteria and Le Gal's classification. *European Journal of Radiology* 47, 227–231.

References

- Haka, A.S., Shafer-Peltier, K.E., Fitzmaurice, M., Crowe, J., Dasari, R.R., Feld, M.S., 2002. Identifying microcalcifications in benign and malignant breast lesions by probing differences in their chemical composition using Raman spectroscopy. *Cancer Res* 62, 5375–5380.
- Haka, A.S., Shafer-Peltier, K.E., Fitzmaurice, M., Crowe, J., Dasari, R.R., Feld, M.S., 2005. Diagnosing breast cancer by using Raman spectroscopy. *Proceedings of the National Academy of Sciences of the United States of America* 102, 12371–12376.
- Haka, A.S., Volynskaya, Z., Gardecki, J.A., Nazemi, J., Lyons, J., Hicks, D., Fitzmaurice, M., Dasari, R.R., Crowe, J.P., Feld, M.S., 2006. In vivo margin assessment during partial mastectomy breast surgery using Raman spectroscopy. *Cancer Res* 66, 3317–3322.
- Haka, A.S., Volynskaya, Z., Gardecki, J.A., Nazemi, J., Shenk, R., Wang, N., Dasari, R.R., Fitzmaurice, M., Feld, M.S., 2009. Diagnosing breast cancer using Raman spectroscopy: prospective analysis. *J Biomed Opt* 14, 054023.
- Hirschmugl, C.J., Gough, K.M., 2012. Fourier Transform Infrared Spectrochemical Imaging: Review of Design and Applications with a Focal Plane Array and Multiple Beam Synchrotron Radiation Source. *Applied Spectroscopy* 66, 475–492.
- Horsnell, J., 2012. The use of Raman spectroscopy for the intra-operative assesment of axillary lymph nodes in breast cancer. Cranfield University.
- James, J.J., Evans, A.J., Pinder, S.E., Macmillan, R.D., Wilson, A.R.M., Ellis, I.O., 2003. Is the Presence of Mammographic Comedo Calcification Really a Prognostic Factor for Small Screen-detected Invasive Breast Cancers? *Clinical Radiology* 58, 54–62.
- Johnson, J.M., Dalton, R.R., Wester, S.M., Landercasper, J., Lambert, P.J., 1999. Histological correlation of microcalcifications in breast biopsy specimens. *Arch Surg* 134, 712–5; discussion 715–6.
- Kalager, M., Adami, H.-O., Bretthauer, M., Tamimi, R.M., 2012. Overdiagnosis of Invasive Breast Cancer Due to Mammography Screening: Results From the Norwegian Screening Program. *Ann Intern Med* 156, 491–499.
- Kazarian, S.G., Chan, K.L.A., 2006. Applications of ATR-FTIR spectroscopic imaging to biomedical samples. *Biochimica et Biophysica Acta (BBA) - Biomembranes* 1758, 858–867.
- Keller, M.D., Majumder, S.K., Mahadevan-Jansen, A., 2009. Spatially offset Raman spectroscopy of layered soft tissues. *Opt Lett* 34, 926–928.
- Keller, M.D., Vargis, E., De Matos Granja, N., Wilson, R.H., Mycek, M.-A., Kelley, M.C., Mahadevan-Jansen, A., 2011. Development of a spatially offset Raman spectroscopy probe for breast tumor surgical margin evaluation. *Journal of Biomedical Optics* 16, 077006–077006–8.
- Kerssens, M.M., Matousek, P., Rogers, K., Stone, N., 2010. Towards a safe non-invasive method for evaluating the carbonate substitution levels of hydroxyapatite (HAP) in micro-calcifications found in breast tissue. *Analyst* 135, 3156–3161.
- Kontoyannis, C.G., Bouropoulos, N.C., Koutsoukos, P.G., 1997. Use of Raman Spectroscopy for the Quantitative Analysis of Calcium Oxalate Hydrates:

References

- Application for the Analysis of Urinary Stones. *Appl. Spectrosc.* 51, 64–67.
- Kopans, D.B., 2007. Breast imaging. Lippincott Williams & Wilkins.
- Kriege, M., Brekelmans, C.T.M., Boetes, C., Besnard, P.E., Zonderland, H.M., Obdeijn, I.M., Manoliu, R.A., Kok, T., Peterse, H., Tilanus-Linthorst, M.M.A., Muller, S.H., Meijer, S., Oosterwijk, J.C., Beex, L.V.A.M., Tollenaar, R.A.E.M., Koning, H.J. de, Rutgers, E.J.T., Klijn, J.G.M., 2004. Efficacy of MRI and mammography for breast-cancer screening in women with a familial or genetic predisposition. *N Eng J Med* 351, 427–437.
- Kuhl, C.K., Schrading, S., Leutner, C.C., Morakkabati-Spitz, N., Wardelmann, E., Fimmers, R., Kuhn, W., Schild, H.H., 2005. Mammography, breast ultrasound, and magnetic resonance imaging for surveillance of women at high familial risk for breast cancer. *J Clin Oncol* 23, 8469–8476.
- Kukreti, S., Cerussi, A., Tromberg, B., Gratton, E., 2008. Intrinsic near-infrared spectroscopic markers of breast tumors. *Dis. Markers* 25, 281–290.
- Kumar, G.L., Kiernan, J.A. (Eds.), 2010. Special stains and H&E, Second edition. ed. Dako North America, Carpinteria, California.
- Lagier, R., Baud, C.-A., 2003. Magnesium Whitlockite, a Calcium Phosphate Crystal of Special Interest in Pathology. *Pathology - Research and Practice* 199, 329–335.
- Lee, A.H.S., Ellis, I.O., 2008. The Nottingham Prognostic Index for Invasive Carcinoma of the Breast. *Pathol. Oncol. Res.* 14, 113–115.
- Leroy, G., Penel, G., Leroy, N., Bres, E., 2002. Human Tooth Enamel: A Raman Polarized Approach. *Appl. Spectrosc.* 56, 1030–1034.
- Liberman, L., Abramson, A.F., Squires, F.B., Glassman, J.R., Morris, E.A., Dershaw, D.D., 1998a. The breast imaging reporting and data system: positive predictive value of mammographic features and final assessment categories. *AJR Am J Roentgenol* 171, 35–40.
- Liberman, L., Evans, W.P., Dershaw, D.D., Hann, L.E., Deutch, B.M., Abramson, A.F., Rosen, P.P., 1994. Radiography of microcalcifications in stereotaxic mammary core biopsy specimens. *Radiology* 190, 223–225.
- Liberman, L., Gougoutas, C.A., Zakowski, M.F., LaTrenta, L.R., Abramson, A.F., Morris, E.A., Dershaw, D.D., 2001. Calcifications highly suggestive of malignancy: comparison of breast biopsy methods. *Am J Roentgenol* 177, 165–172.
- Liberman, L., Smolkin, J.H., Dershaw, D.D., Morris, E.A., Abramson, A.F., Rosen, P.P., 1998b. Calcification retrieval at stereotactic, 11-gauge, directional, vacuum-assisted breast biopsy. *Radiology* 208, 251–260.
- Lin, X.-M., Cui, Y., Xu, Y.-H., Ren, B., Tian, Z.-Q., 2009. Surface-enhanced Raman spectroscopy: substrate-related issues. *Analytical and Bioanalytical Chemistry* 394, 1729–1745.
- Margolin, F.R., Kaufman, L., Jacobs, R.P., Denny, S.R., Schrupf, J.D., 2004. Stereotactic Core Breast Biopsy of Malignant Calcifications: Diagnostic Yield of Cores with and Cores without Calcifications on Specimen Radiographs¹. *Radiology* 233, 251–254.

References

- Matousek, P., 2007. Deep non-invasive Raman spectroscopy of living tissue and powders. *Chem Soc Rev* 36, 1292–1304.
- Matousek, P., Everall, N., Littlejohn, D., Nordon, A., Bloomfield, M., 2011. Dependence of Signal on Depth in Transmission Raman Spectroscopy. *Appl. Spectrosc.* 65, 724–733.
- Matousek, P., Stone, N., 2007. Prospects for the diagnosis of breast cancer by noninvasive probing of calcifications using transmission Raman spectroscopy. *J Biomed Opt* 12, 024008–1–024008–8.
- Matousek, P., Stone, N., 2009. Emerging concepts in deep Raman spectroscopy of biological tissue. *Analyst* 134, 1058–1066.
- Maurice-Esteva, L., Levillain, P., Lacour, B., Daudon, M., 2000. Advantage of zero-crossing-point first-derivative spectrophotometry for the quantification of calcium oxalate crystalline phases by infrared spectrophotometry. *Clinica Chimica Acta* 298, 1–11.
- McNay, G., Eustace, D., Smith, W.E., Faulds, K., Graham, D., 2011. Surface-Enhanced Raman Scattering (SERS) and Surface-Enhanced Resonance Raman Scattering (SERRS): A Review of Applications. *Applied Spectroscopy* 65, 825–837.
- McPherson, K., 2000. ABC of breast diseases: Breast cancer---epidemiology, risk factors, and genetics. *BMJ* 321, 624–628.
- Miller, L.M., Smith, R.J., 2005. Synchrotrons versus globars, point-detectors versus focal plane arrays: Selecting the best source and detector for specific infrared microspectroscopy and imaging applications. *Vibrational Spectroscopy* 38, 237–240.
- Miller, L.M., Vairavamurthy, V., Chance, M.R., Mendelsohn, R., Paschalis, E.P., Betts, F., Boskey, A.L., 2001. In situ analysis of mineral content and crystallinity in bone using infrared micro-spectroscopy of the ν_4 PO₄-vibration. *Biochimica et Biophysica Acta (BBA) - General Subjects* 1527, 11–19.
- Mohlenhoff, B., Romeo, M., Diem, M., Wood, B.R., 2005. Mie-Type Scattering and Non-Beer-Lambert Absorption Behavior of Human Cells in Infrared Microspectroscopy. *Biophys J* 88, 3635–3640.
- Moreira, L.M., Silveira Jr., L., Santos, F.V., Lyon, J.P., Rocha, R., Zângaro, R.A., Villaverde, A.B., Pacheco, M.T.T., 2008. Raman spectroscopy: A powerful technique for biochemical analysis and diagnosis. *Spectroscopy* 22, 1–19.
- Morgan, M.P., Cooke, M.M., Christopherson, P.A., Westfall, P.R., McCarthy, G.M., 2001. Calcium hydroxyapatite promotes mitogenesis and matrix metalloproteinase expression in human breast cancer cell lines. *Mol Carcinog* 32, 111–117.
- Morgan, M.P., Cooke, M.M., McCarthy, G.M., 2005. Microcalcifications associated with breast cancer: an epiphenomenon or biologically significant feature of selected tumors? *Journal of Mammary Gland Biology and Neoplasia* 10, 181–187.
- Mun, H.S., Shin, H.J., Kim, H.H., Cha, J.H., Kim, H., 2013. Screening-detected calcified and non-calcified ductal carcinoma in situ: Differences in the imaging and histopathological features. *Clinical Radiology* 68, e27–e35.

References

- Nasse, M.J., Walsh, M.J., Mattson, E.C., Reininger, R., Kajdacsy-Balla, A., Macias, V., Bhargava, R., Hirschmugl, C.J., 2011. High-resolution Fourier-transform infrared chemical imaging with multiple synchrotron beams. *Nat Meth* 8, 413–416.
- Nguyen, C.V., Albarracin, C.T., Whitman, G.J., Lopez, A., Sneige, N., 2010. Atypical Ductal Hyperplasia in Directional Vacuum-Assisted Biopsy of Breast Microcalcifications: Considerations for Surgical Excision. *Annals of Surgical Oncology* 18, 752–761.
- Nishino, M., Yamashita, S., Aoba, T., Okazaki, M., Moriwaki, Y., 1981. The Laser-Raman Spectroscopic Studies on Human Enamel and Precipitated Carbonate-containing Apatites. *Journal of Dental Research* 60, 751 – 755.
- Nover, A.B., Jagtap, S., Anjum, W., Yegingil, H., Shih, W.Y., Shih, W.-H., Brooks, A.D., 2009. Modern breast cancer detection: a technological review. *International Journal of Biomedical Imaging* 2009, 902326.
- Orel, S.G., Schnall, M.D., 2001. MR imaging of the breast for the detection, diagnosis, and staging of breast cancer. *Radiology* 220, 13–30.
- Pampena, D.A., Robertson, K.A., Litvinova, O., Lajoie, G., Goldberg, H.A., Hunter, G.K., 2004. Inhibition of hydroxyapatite formation by osteopontin phosphopeptides. *Biochem J* 378, 1083–1087.
- Parham, D.M., Anderson, N., Buley, I., Pinder, S.E., Robertson, A.J., Wells, C., Alexander, J., Hussein, K.A., Kissen, L., Lesna, M., McCutcheon, J., Nicholas, D.S., Rasbridge, S.A., D'Sousa, L., Van der Horst, C., Haider, S., Hickling, M., 2010. Experts and performance in histopathology—A study in breast pathology. *Pathology - Research and Practice* 206, 749–752.
- Park, J.M., Choi, H.K., Bae, S.-J., Lee, M.-S., Ahn, S.-H., Gong, G., 2000. Clustering of Breast Microcalcifications: Revisited. *Clinical Radiology* 55, 114–118.
- Patnick, J. (Ed.), 2011. *NHS Breast Screening Programme 2011 Annual Review*.
- Penel, G., Delfosse, C., Descamps, M., Leroy, G., 2005. Composition of bone and apatitic biomaterials as revealed by intravital Raman microspectroscopy. *Bone* 36, 893–901.
- Penel, G., Leroy, G., Rey, C., Bres, E., 1998. MicroRaman Spectral Study of the PO₄ and CO₃ Vibrational Modes in Synthetic and Biological Apatites. *Calcif Tissue Int* 63, 475–481.
- Penel, G., Leroy, G., Rey, C., Sombret, B., Huvenne, J.P., Bres, E., 1997. Infrared and Raman microspectrometry study of fluor-fluor-hydroxy and hydroxy-apatite powders. *Journal of Materials Science: Materials in Medicine* 8, 271–276.
- Peroos, S., Du, Z., De Leeuw, N.H., 2006. A computer modelling study of the uptake, structure and distribution of carbonate defects in hydroxy-apatite. *Biomaterials* 27, 2150–2161.
- Popli, M., 2002. Pictorial essay : Breast calcification. *Indian J Radiol Imaging* 12, 33–36.

References

- Proia, A.D., Brinn, N.T., 1985. Identification of calcium oxalate crystals using alizarin red S stain. *Arch. Pathol. Lab. Med.* 109, 186–189.
- Puchtler, H., Meloan, S.N., Terry, M.S., 1969. On the History and Mechanism of Alizarin and Alizarin Red S Stains for Calcium. *J Histochem Cytochem* 17, 110–124.
- Purdie, C.A., McLean, D., 2009. Benign microcalcification and its differential diagnosis in breast screening. *Diagnostic Histopathology* 15, 382–394.
- Rakha, E.A., El-Sayed, M.E., Lee, A.H.S., Elston, C.W., Grainge, M.J., Hodi, Z., Blamey, R.W., Ellis, I.O., 2008. Prognostic Significance of Nottingham Histologic Grade in Invasive Breast Carcinoma. *JCO* 26, 3153–3158.
- Raman, C.V., Krishnan, K.S., 1928. A new type of secondary radiation. *Nature* 121, 501–502.
- Rankov, V., 2005. An Algorithm for image stitching and blending. *SPIE*, pp. 190–199.
- Rehman, I., Bonfield, W., 1997. Characterization of hydroxyapatite and carbonated apatite by photo acoustic FTIR spectroscopy. *Journal of Materials Science: Materials in Medicine* 8, 1–4.
- Rehman, S., Movasaghi, Z., Darr, J.A., Rehman, I.U., 2010. Fourier Transform Infrared Spectroscopic Analysis of Breast Cancer Tissues; Identifying Differences between Normal Breast, Invasive Ductal Carcinoma, and Ductal Carcinoma In Situ of the Breast. *Applied Spectroscopy Reviews* 45, 355.
- Ren, B., Liu, G.-K., Lian, X.-B., Yang, Z.-L., Tian, Z.-Q., 2007. Raman spectroscopy on transition metals. *Analytical and Bioanalytical Chemistry* 388, 29–45.
- Rey, C., Combes, C., Drouet, C., Lebugle, A., Sfihi, H., Barroug, A., 2007. Nanocrystalline apatites in biological systems: characterisation, structure and properties. *Mat.-wiss. u. Werkstofftech.* 38, 996–1002.
- Rey, C., Renugopalakrishnan, V., Collins, B., Glimcher, M., 1991a. Fourier transform infrared spectroscopic study of the carbonate ions in bone mineral during aging. *Calcified Tissue International* 49, 251–258.
- Rey, C., Shimizu, M., Collins, B., Glimcher, M.J., 1991b. Resolution-enhanced fourier transform infrared spectroscopy study of the environment of phosphate ion in the early deposits of a solid phase of calcium phosphate in bone and enamel and their evolution with age: 2. Investigations in the $3 PO_4$ domain. *Calcif Tissue Int* 49, 383–388.
- Robinson, M., Kotre, C.J., 2008. Trends in Compressed Breast Thickness and Radiation Dose in Breast Screening Mammography. *Br J Radiol* 81, 214–218.
- Saha, A., Barman, I., Dingari, N.C., McGee, S., Volynskaya, Z., Galindo, L.H., Liu, W., Plecha, D., Klein, N., Dasari, R.R., Fitzmaurice, M., 2011. Raman spectroscopy: a real-time tool for identifying microcalcifications during stereotactic breast core needle biopsies. *Biomedical Optics Express* 2, 2792.
- Sainsbury, J.R.C., 2000. ABC of breast diseases: Breast cancer. *BMJ* 321, 745–750.

References

- Scouten, C.W., Cunningham, M., 2012. Freezing Biological Samples. www.leica-microsystems.com white paper.
- Seregin, V.V., Coffey, J.L., 2006. Bias-assisted in vitro calcification of calcium disilicide growth layers on spark-processed silicon. *Biomaterials* 27, 3726–3737.
- Shafer-Peltier, K.E., Haka, A.S., Fitzmaurice, M., Crowe, J., Myles, J., Dasari, R.R., Feld, M.S., 2002. Raman microspectroscopic model of human breast tissue: implications for breast cancer diagnosis in vivo. *Journal of Raman Spectroscopy* 33, 552–563.
- Shimoda, S., Aoba, T., Moreno, E. c., Miake, Y., 1990. Effect of Solution Composition on Morphological and Structural Features of Carbonated Calcium Apatites. *Journal of Dental Research* 69, 1731–1740.
- Shoji, K., 1993. [Alizarin red S staining of calcium compound crystals in synovial fluid]. *Nippon Seikeigeka Gakkai Zasshi* 67, 201–210.
- Sickles, E.A., 1982. Mammographic detectability of breast microcalcifications. *American Journal of Roentgenology* 139, 913–918.
- Singh, N., Theaker, J.M., 1999. Calcium oxalate crystals (Weddellite) within the secretions of ductal carcinoma in situ—a rare phenomenon. *Journal of Clinical Pathology* 52, 145–146.
- Ślósarczyk, A., Paluszkiwicz, C., Gawlicki, M., Paszkiewicz, Z., 1997. The FTIR spectroscopy and QXRD studies of calcium phosphate based materials produced from the powder precursors with different CaP ratios. *Ceramics International* 23, 297–304.
- Smekal, A., 1923. Zur Quantentheorie der Dispersion. *Naturwissenschaften* 11, 873–875.
- Stolik, S., Delgado, J.A., Pérez, A., Anasagasti, L., 2000. Measurement of the penetration depths of red and near infrared light in human “ex vivo” tissues. *Journal of Photochemistry and Photobiology B: Biology* 57, 90–93.
- Stomper, P.C., Geradts, J., Edge, S.B., Levine, E.G., 2003. Mammographic Predictors of the Presence and Size of Invasive Carcinomas Associated With Malignant Microcalcification Lesions Without a Mass. *AJR* 181.
- Stone, N., Baker, R., Rogers, K., Parker, A.W., Matousek, P., 2007. Subsurface probing of calcifications with spatially offset Raman spectroscopy (SORS): future possibilities for the diagnosis of breast cancer. *Analyst* 132, 899–905.
- Stone, N., Faulds, K., Graham, D., Matousek, P., 2010. Prospects of Deep Raman Spectroscopy for Noninvasive Detection of Conjugated Surface Enhanced Resonance Raman Scattering Nanoparticles Buried within 25 mm of Mammalian Tissue. *Analytical Chemistry* 82, 3969–3973.
- Stone, N., Kerssens, M., Lloyd, G.R., Faulds, K., Graham, D., Matousek, P., 2011. Surface enhanced spatially offset Raman spectroscopic (SESORS) imaging – the next dimension. *Chem. Sci.* 2, 776–780.
- Stone, N., Matousek, P., 2008. Advanced transmission Raman spectroscopy: a promising tool for breast disease diagnosis. *Cancer Research* 68, 4424–4430.

References

- Tabar, L., Tony Chen, H., Amy Yen, M.F., Tot, T., Tung, T., Chen, L., Chiu, Y., Duffy, S.W., Smith, R.A., 2004. Mammographic tumor features can predict long-term outcomes reliably in women with 1–14-mm invasive breast carcinoma. *Cancer* 101, 1745–1759.
- Terkeltaub, R.A., 2001. Inorganic pyrophosphate generation and disposition in pathophysiology. *Am J Physiol Cell Physiol* 281, C1–11.
- Tfayli, A., Gobinet, C., Vrabie, V., Huez, R., Manfait, M., Piot, O., 2009. Digital Dewaxing of Raman Signals: Discrimination Between Nevi and Melanoma Spectra Obtained from Paraffin-Embedded Skin Biopsies. *Applied Spectroscopy* 63, 564–570.
- Thouverey, C., Bechhoff, G., Pikula, S., Buchet, R., 2009. Inorganic pyrophosphate as a regulator of hydroxyapatite or calcium pyrophosphate dihydrate mineral deposition by matrix vesicles. *Osteoarthritis and Cartilage* 17, 64–72.
- Tse, G.M., Tan, P.-H., Cheung, H.S., Chu, W.C.W., Lam, W.W.M., 2007. Intermediate to highly suspicious calcification in breast lesions: a radio-pathologic correlation. *Breast Cancer Res Treat* 110, 1–7.
- Vardaxis, N.J., Brans, T.A., Boon, M.E., Kreis, R.W., Marres, L.M., 1997. Confocal laser scanning microscopy of porcine skin: implications for human wound healing studies. *J Anat* 190, 601–611.
- Vestergaard, P., Fischer, L., Mele, M., Mosekilde, L., Christiansen, P., 2011. Use of Bisphosphonates and Risk of Breast Cancer. *Calcified Tissue International* 88, 255–262.
- Vesty, S., 2013. Private communication.
- Volmer, M., Bolck, A., Wolthers, B., De Ruiter, A., Doornbos, D., Van der Slik, W., 1993. Partial least-squares regression for routine analysis of urinary calculus composition with Fourier transform infrared analysis. *Clin Chem* 39, 948–954.
- Walsh, M.J., Kajdacsy-Balla, A., Holton, S.E., Bhargava, R., 2012. Attenuated total reflectance Fourier-transform infrared spectroscopic imaging for breast histopathology. *Vibrational Spectroscopy* 60, 23–28.
- Weaver, D.L., Rosenberg, R.D., Barlow, W.E., Ichikawa, L., Carney, P.A., Kerlikowske, K., Buist, D.S.M., Geller, B.M., Key, C.R., Maygarden, S.J., Ballard-Barbash, R., 2006. Pathologic findings from the Breast Cancer Surveillance Consortium. *Cancer* 106, 732–742.
- Wilson, E.V., Bushiri, M.J., Vaidyan, V.K., 2010. Characterization and FTIR spectral studies of human urinary stones from Southern India. *Spectrochimica Acta Part A: Molecular and Biomolecular Spectroscopy* 77, 442–445.
- Wopenka, B., Pasteris, J.D., 2005. A mineralogical perspective on the apatite in bone. *Materials Science and Engineering: C* 25, 131–143.
- Xie, H., Stevenson, R., Stone, N., Hernandez-Santana, A., Faulds, K., Graham, D., 2012. Tracking Bisphosphonates through a 20 mm Thick Porcine Tissue by Using Surface-Enhanced Spatially Offset Raman Spectroscopy. *Angewandte Chemie International Edition* n/a–n/a.

References

- Xu, C., Karan, K., Yao, X., Wang, Y., 2009. Molecular structural analysis of noncarious cervical sclerotic dentin using Raman spectroscopy. *Journal of Raman Spectroscopy* 40, 1780–1785.
- Zonderland, H.M., Coerkamp, E.G., Hermans, J., Vijver, M.J. van de, Voorthuisen, A.E. van, 1999. Diagnosis of breast cancer: contribution of US as an adjunct to mammography. *Radiology* 213, 413–422.

APPENDICES

Appendix A FTIR band assignments calcified materials (750-4000 cm⁻¹)

Band (cm ⁻¹)	Band assignment	Tissue/ material	Reference
770		Urates	(Estepa and Daudon, 1997)
780	Water	COM and COD	(Maurice-Estepa et al., 2000)
852	HPO ₄ ²⁻	Octacalcium phosphate	(Dekker et al., 2005)
856	CO ₃	HAP	(Antonakos et al., 2007)
866	CO ₃	Labile carbonated apatite	(Fleet, 2009), (Rey et al., 2007)
866	HPO ₄ ²⁻	Carbonated apatite	(Apfelbaum et al., 1992)
871	CO ₃	Type B carbonated apatite	(Fleet, 2009)
873	CO ₃	Type B carbonated apatite	(Rey et al., 2007)
875	CO ₃ (B)	Carbonated apatite	(Apfelbaum et al., 1992)
877	CO ₃	HAP	(Rehman and Bonfield, 1997)
878	CO ₃	Type A carbonated apatite	(Fleet, 2009)
878	CO ₃ (A)	Carbonated apatite	(Apfelbaum et al., 1992)
880	CO ₃	Type A carbonated apatite	(Rey et al., 2007)
906	HPO ₄ ²⁻	Octacalcium phosphate	(Dekker et al., 2005)
912		COD	(Maurice-Estepa et al., 2000)
947	TCP*	Biphasic calcium phosphate	(Victor and Kumar, 2007)
948		COM	(Maurice-Estepa et al., 2000)
948	CO ₃	Type A carbonated apatite	(Antonakos et al., 2007)
961	PO ₄	Carbonated apatite	(Rehman and Bonfield, 1997)
962	PO ₄	HAP	(Antonakos et al., 2007)

Appendix A

986	TCP*	Biphasic calcium phosphate	(Victor and Kumar, 2007)
987		Brushite	(Rey et al., 1991b)
1000		Urates	(Estepa and Daudon, 1997)
1004	Sodium hydrogen monohydrate	Calcification in kidney tissue	(Dessombz et al., 2011)
1004		Brushite	(Rey et al., 1991b)
1006		Type B carbonated apatite	(Rey et al., 1991b)
1015		AB carbonated apatite	(Antonakos et al., 2007)
1018	PO ₄	Poorly crystalline non-stoichiometric apatites	(Chiou et al., 2010)
1023		Type B carbonated apatite	(Rey et al., 1991b)
1023	PO	Octacalcium phosphate	(Dekker et al., 2005)
1025	Whitlockite	Calcification in kidney tissue	(Dessombz et al., 2011)
1028	PO ₄	Resting phase	(Chiou et al., 2010)
1029	PO ₄	Type B carbonated apatite	(Antonakos et al., 2007)
1029	PO ₄	HAP	(Antonakos et al., 2007)
1031	PO ₄	Matured crystalline stoichiometric apatite, resorptive phase	(Chiou et al., 2010)
1041	PO ₄	Carbonated apatite	(Rehman and Bonfield, 1997)
1042	PO ₄	HAP	(Rehman and Bonfield, 1997)
1044		Type B carbonated apatite	(Rey et al., 1991b)
1045		AB carbonated apatite	(Antonakos et al., 2007)
1058		Brushite	(Rey et al., 1991b)
1060	PO ₄	Type B carbonated apatite	(Antonakos et al., 2007)
1065	PO ₄	Brushite	(Estepa and Daudon, 1997)
1070	PO	Octacalcium phosphate	(Dekker et al., 2005)
1072		Type B carbonated apatite	(Rey et al., 1991b)
1079		Brushite	(Rey et al., 1991b)

Appendix A

1080	Whitlockite	Calcification in kidney tissue	(Dessombz et al., 2011)
1091	PO ₄	HAP	(Rehman and Bonfield, 1997)
1092	PO ₄	AB carbonated apatite	(Antonakos et al., 2007)
1100	PO	Octacalcium phosphate	(Dekker et al., 2005)
1102	Amorphous silica	Calcification in kidney tissue	(Dessombz et al., 2011)
1104		Type B carbonated apatite	(Rey et al., 1991b)
1108		Brushite	(Rey et al., 1991b)
1110		Newly precipitated apatite	(Rey et al., 1991b)
1119	Octacalcium and carbatite	Calcification in kidney tissue	(Dessombz et al., 2011)
1122	TCP*	Biphasic calcium phosphate	(Victor and Kumar, 2007)
1124		Brushite	(Rey et al., 1991b)
1125		Newly precipitated apatite	(Rey et al., 1991b)
1133		Brushite	(Rey et al., 1991b)
1135	PO ₄	Brushite	(Estepa and Daudon, 1997)
1140		Urates	(Estepa and Daudon, 1997)
1145	Acid phosphate	Bone	(Miller et al., 2001)
1225-1235	Amide III, β -sheet structure	Tissue	(Socrates, 2001)
1240-1255	Amide III, random chain	Tissue	(Socrates, 2001)
1270-1300	Amide III, α -helix	Tissue	(Socrates, 2001)
1316	CC stretch	Urinary stone	(Wilson et al., 2010)
1316	CO stretch	COM	(Maurice-Estepa et al., 2000)
1324	CO stretch	COD	(Maurice-Estepa et al., 2000)
1321	CO ₃	Carbonated apatite	(Rehman and Bonfield, 1997)
1324		COM	(Maurice-Estepa et al., 2000)

Appendix A

1345		Ammonium hydrogen urate	(Estepa and Daudon, 1997)
1410	CO ₃	Type B carbonated apatite	(Fleet, 2009)
1417	CO ₃	Carbonated apatite and HAP	(Rehman and Bonfield, 1997)
1420	CO ₃ (B)	Carbonated apatite	(Apfelbaum et al., 1992)
1420	CO ₃	A+B carbonated apatite	(Apfelbaum et al., 1992)
1427		Type B carbonated apatite	(Antonakos et al., 2007)
1435		Struvite	(Estepa and Daudon, 1997)
1444		Type A carbonated apatite	(Antonakos et al., 2007)
1450		Type A carbonated apatite	(Fleet, 2009)
1450		Type B carbonated apatite	(Antonakos et al., 2007)
1454	CO ₃	Carbonated apatite and HAP	(Rehman and Bonfield, 1997)
1455		Type B carbonated apatite	(Fleet, 2009)
1460	CO ₃ (B)	Carbonated apatite	(Apfelbaum et al., 1992)
1460	CO ₃ (A)	Carbonated apatite	(Apfelbaum et al., 1992)
1460	CO ₃	A+B carbonated apatite	(Apfelbaum et al., 1992)
1472	CO ₃	Type B carbonated apatite	(Antonakos et al., 2007)
1495		Type A carbonated apatite	(Antonakos et al., 2007)
1520-1525	Amide II (extended chain)	Proteins and peptides	(Socrates, 2001)
1525 (sh)		Type A carbonated apatite	(Antonakos et al., 2007)
1540-1550	Amide II (folded)	Proteins and peptides	(Socrates, 2001)
1545 (sh)		Type A carbonated apatite	(Fleet, 2009)
1550	CO ₃ (A)	Carbonated apatite	(Apfelbaum et al., 1992)
1550	CO ₃	A+B carbonated apatite	(Apfelbaum et al., 1992)
1620	CO stretch	COM	(Maurice-Estepa et al., 2000)
1620	δ OH	Urinary stone	(Wilson et al., 2010)

Appendix A

1640	CO stretch	COD	(Maurice-Esteba et al., 2000)
1645-1655	Amide I, α -helix	Tissue	(Socrates, 2001)
1648	CO ₃	HAP	(Rehman and Bonfield, 1997)
1649		Brushite	(Esteba and Daudon, 1997)
1650	CO ₃	Carbonated apatite	(Rehman and Bonfield, 1997)
1660-1670	Amide I, random chain	Tissue	(Socrates, 2001)
1665-1675	Amide I, β -sheet structure	Tissue	(Socrates, 2001)
2345 (sh)	OH + NH ₄ ⁺	Struvite	(Esteba and Daudon, 1997)
3485	water	COM and COD	(Maurice-Esteba et al., 2000)
3570	OH	HAP	(Rehman and Bonfield, 1997)
3571	OH	Carbonated apatite	(Rehman and Bonfield, 1997)
3600	OH	Sodium hydrogen urate	(Esteba and Daudon, 1997)
3600	Sodium hydrogen urate monohydrate	Calcification in kidney tissue	(Dessombz et al., 2011)

Appendix B Raman band assignments calcified materials (400 – 2000 cm⁻¹)

Band (cm ⁻¹)	Band assignment	Tissue/ material	Reference
427	PO ₄	Enamel	(Nishino et al., 1981)
430	PO ₄	Bone	(Penel et al., 2005)
432	PO ₄	Type B carbonated apatite	(Penel et al., 1998)
432	PO ₄	Dentine and bone	(Penel et al., 1998)
433	PO ₄	HAP	(Penel et al., 1998)
433	PO ₄	Enamel	(Penel et al., 1998)
440	PO ₄	Type A carbonated apatite	(Penel et al., 1998)
442	PO ₄	Enamel	(Nishino et al., 1981)
445	PO ₄	Type B carbonated apatite	(Penel et al., 1998)
448	PO ₄	HAP	(Penel et al., 1998)
450	PO ₄	Dentine and enamel	(Penel et al., 1998)
450	PO ₄	Bone	(Penel et al., 2005)
452	PO ₄	Bone	(Penel et al., 1998)
502	OCO bend	COM	(Kontoyannis et al., 1997)
508	OCO bend	COD	(Kontoyannis et al., 1997)
572	PO ₄	Enamel	(Nishino et al., 1981)
579	PO ₄	Type A carbonated apatite	(Penel et al., 1998)
579	PO ₄	Type B carbonated apatite	(Penel et al., 1998)
579	PO ₄	Enamel	(Penel et al., 1998)
580	PO ₄	HAP	(Penel et al., 1998)
580	PO ₄	Dentine	(Penel et al., 1998)
584	PO ₄	Bone	(Penel et al., 1998)
587	PO ₄	Bone	(Penel et al., 2005)
588	PO ₄	Enamel	(Nishino et al., 1981)
589	PO ₄	Type A carbonated apatite	(Penel et al., 1998)
590	PO ₄	Type B carbonated apatite	(Penel et al., 1998)

Appendix B

590	PO ₄	Dentine and bone	(Penel et al., 1998)
591	PO ₄	HAP	(Penel et al., 1998)
604	PO ₄	Bone	(Penel et al., 2005)
605	PO ₄	Enamel	(Nishino et al., 1981)
607	PO ₄	HAP	(Penel et al., 1998)
608	PO ₄	Type A carbonated apatite	(Penel et al., 1998)
608	PO ₄	Enamel	(Penel et al., 1998)
609	PO ₄	Type B carbonated apatite	(Penel et al., 1998)
610	PO ₄	Dentine	(Penel et al., 1998)
611	PO ₄	Bone	(Penel et al., 1998)
614	PO ₄	HAP	(Penel et al., 1998)
630		Type A carbonated apatite	(Penel et al., 1998)
665	C-S	Bone	(Penel et al., 2005)
675	CO ₃	Type A carbonated apatite	(Penel et al., 1998)
686	CO ₃	Enamel	(Nishino et al., 1981)
708	CO ₃	Enamel	(Nishino et al., 1981)
720		Bone	(Penel et al., 2005)
727	CH	Breast tissue	(Frank et al., 1994)
750	CO ₃	Enamel	(Nishino et al., 1981)
756	CO ₃ (B)	Bone	(Penel et al., 2005)
765	CO ₃	Type A carbonated apatite	(Penel et al., 1998)
782	C-C-O	Bone	(Penel et al., 2005)
813	C-C, C-O-C	Bone	(Penel et al., 2005)
849		Breast tissue	(Frank et al., 1994)
853	C-C-H (aromatic)	Bone	(Penel et al., 2005)
870		Breast tissue	(Frank et al., 1994)
873	P-OH stretch	Dentine and bone	(Penel et al., 1998)
874	CC (amino acids)	Bone	(Penel et al., 2005)
890		Breast tissue	(Frank et al., 1994)
892		Bone	(Penel et al., 2005)
896	CC stretch	COM	(Kontoyannis et al., 1997)
912	CC stretch	COD	(Kontoyannis et al., 1997)
920		Dentine	(Penel et al., 1998)

Appendix B

920	P-OH	Bone	(Penel et al., 2005)
924		Bone	(Penel et al., 1998)
947	PO ₄	Type A carbonated apatite	(Penel et al., 1998)
956	PO ₄	Enamel	(Nishino et al., 1981)
957	PO ₄	Type A carbonated apatite	(Penel et al., 1998)
959	PO ₄	Enamel and dentine	(Penel et al., 1998)
960	PO ₄	Type B carbonated apatite	(Penel et al., 1998)
961	PO ₄	Bone	(Penel et al., 1998)
964	PO ₄	HAP	(Penel et al., 1998)
972	=CH	Breast tissue	(Frank et al., 1994)
1002	HPO ₄ ²⁻	Enamel	(Penel et al., 1998)
1003	HPO ₄ ²⁻	Dentine	(Penel et al., 1998)
1003	HPO ₄ ²⁻ , Phe	Bone	(Penel et al., 2005)
1005	HPO ₄ ²⁻	Bone	(Penel et al., 1998)
1018	PO ₄	Type A carbonated apatite	(Penel et al., 1998)
1021	CO ₃ , PO ₄	Enamel	(Nishino et al., 1981)
1026	PO ₄	Enamel	(Penel et al., 1998)
1029	PO ₄	HAP	(Penel et al., 1998)
1030	PO ₄	Type B carbonated apatite	(Penel et al., 1998)
1031	PO ₄	Type A carbonated apatite	(Penel et al., 1998)
1031	PO ₄	Dentine	(Penel et al., 1998)
1032	PO ₄	Bone	(Penel et al., 1998)
1034	PO ₄	HAP	(Penel et al., 1998)
1035	PO ₄	Bone	(Penel et al., 2005)
1040	CO ₃ , PO ₄	Enamel	(Nishino et al., 1981)
1041	PO ₄	HAP	(Penel et al., 1998)
1043	PO ₄	Enamel	(Penel et al., 1998)
1044	PO ₄	Bone	(Penel et al., 1998)
1045	PO ₄	Type B carbonated apatite	(Penel et al., 1998)
1046	PO ₄	Dentine	(Penel et al., 1998)
1048	PO ₄	HAP	(Penel et al., 1998)
1057	PO ₄	HAP	(Penel et al., 1998)
1059	PO ₄	Type A carbonated apatite	(Penel et al., 1998)

Appendix B

1064	PO ₄	HAP	(Penel et al., 1998)
1066	CO ₃ , PO ₄	Enamel	(Nishino et al., 1981)
1066	C-C stretch	Breast tissue	(Frank et al., 1994)
1069	PO ₄	Dentine	(Penel et al., 1998)
1069	CO ₃ (B)	Dentine	(Penel et al., 1998)
1070	CO ₃	Type B carbonated apatite	(Penel et al., 1998)
1071	PO ₄	Enamel and bone	(Penel et al., 1998)
1071	CO ₃ (B)	Enamel and bone	(Penel et al., 1998)
1073	PO ₄ , CO ₃ (B)	Bone	(Penel et al., 2005)
1077	PO ₄	HAP	(Penel et al., 1998)
1079	C-C stretch	Breast tissue	(Frank et al., 1994)
1100		Enamel	(Nishino et al., 1981)
1102	CO ₃ (A)	Dentine	(Penel et al., 1998)
1103	CO ₃ (A)	Enamel and bone	(Penel et al., 1998)
1107	CO ₃	Type A carbonated apatite	(Penel et al., 1998)
1119	C-C stretch	Breast tissue	(Frank et al., 1994)
1176	COC, Tyr, Phe,	Bone	(Penel et al., 2005)
1204	Tyr	Bone	(Penel et al., 2005)
1242	Amide III	Bone	(Penel et al., 2005)
1243	Amide III	Bone	(Penel et al., 1998)
1245	Amide III	Dentine	(Penel et al., 1998)
1260		Dentine	(Penel et al., 1998)
1262		Bone	(Penel et al., 1998)
1265	=CH	Breast tissue	(Frank et al., 1994)
1303	CH ₂	Breast tissue	(Frank et al., 1994)
1340	Amide III	Bone	(Penel et al., 2005)
1398	Heme	Bone	(Penel et al., 2005)
1439	CH ₂	Breast tissue	(Frank et al., 1994)
1449		Bone	(Penel et al., 1998)
1450	CH ₂ /CH ₃	Bone	(Penel et al., 2005)
1450		Dentine	(Penel et al., 1998)
1455	CH ₂	Breast tissue	(Frank et al., 1994)
1462	CO stretch	COD	(Kontoyannis et al., 1997)
1477	CO stretch	COM	(Kontoyannis et al., 1997)
1489	CO stretch	COD	(Kontoyannis et al., 1997)

Appendix B

1585	CCH aromatic ring	Bone	(Penel et al., 2005)
1629	CO stretch	COM	(Kontoyannis et al., 1997)
1632	CO stretch	COD	(Kontoyannis et al., 1997)
1654	C=C stretch	Breast tissue	(Frank et al., 1994)
1660	Amide I	Dentine	(Penel et al., 1998)
1662	Amide I	Bone	(Penel et al., 1998)
1743	C=O stretch	Breast tissue	(Frank et al., 1994)

Appendix C Additional images FTIR imaging compared to staining

C.1 Benign specimens

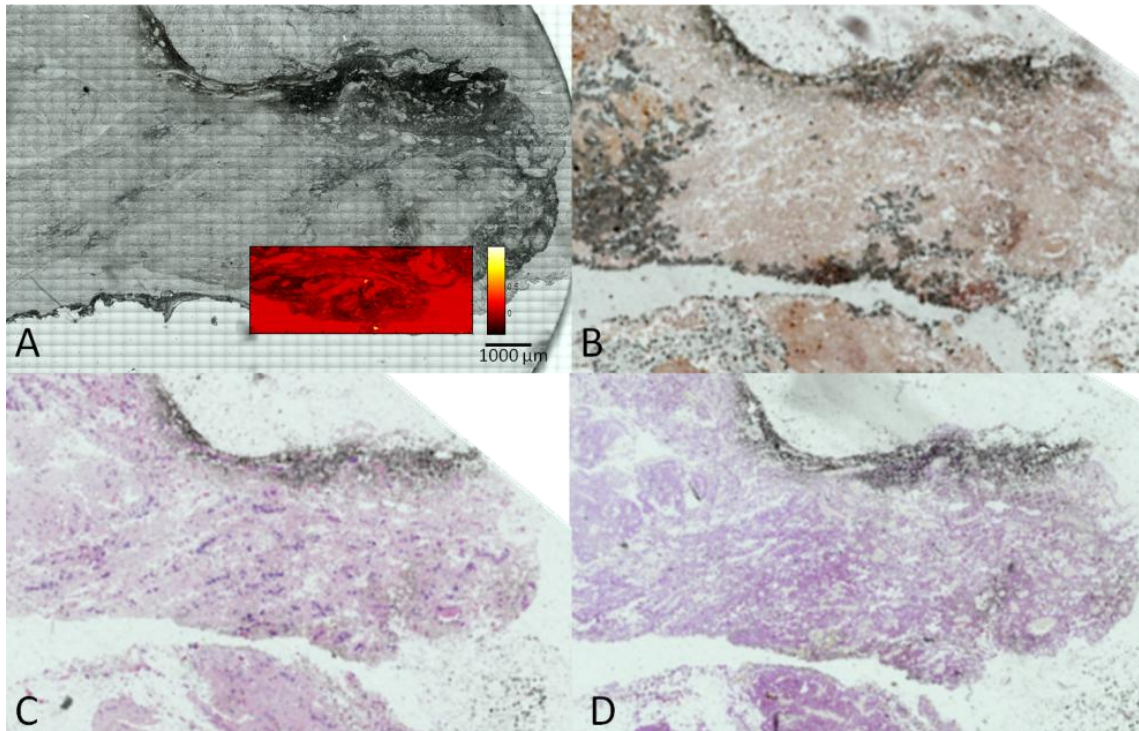


Figure C-1: A) White light image of benign sample with overlaid the intensity fit of the hydroxyapatite; B) Alizarin Red staining of adjacent slide; C) H&E staining of adjacent slide; D) von Kossa staining of adjacent slide.

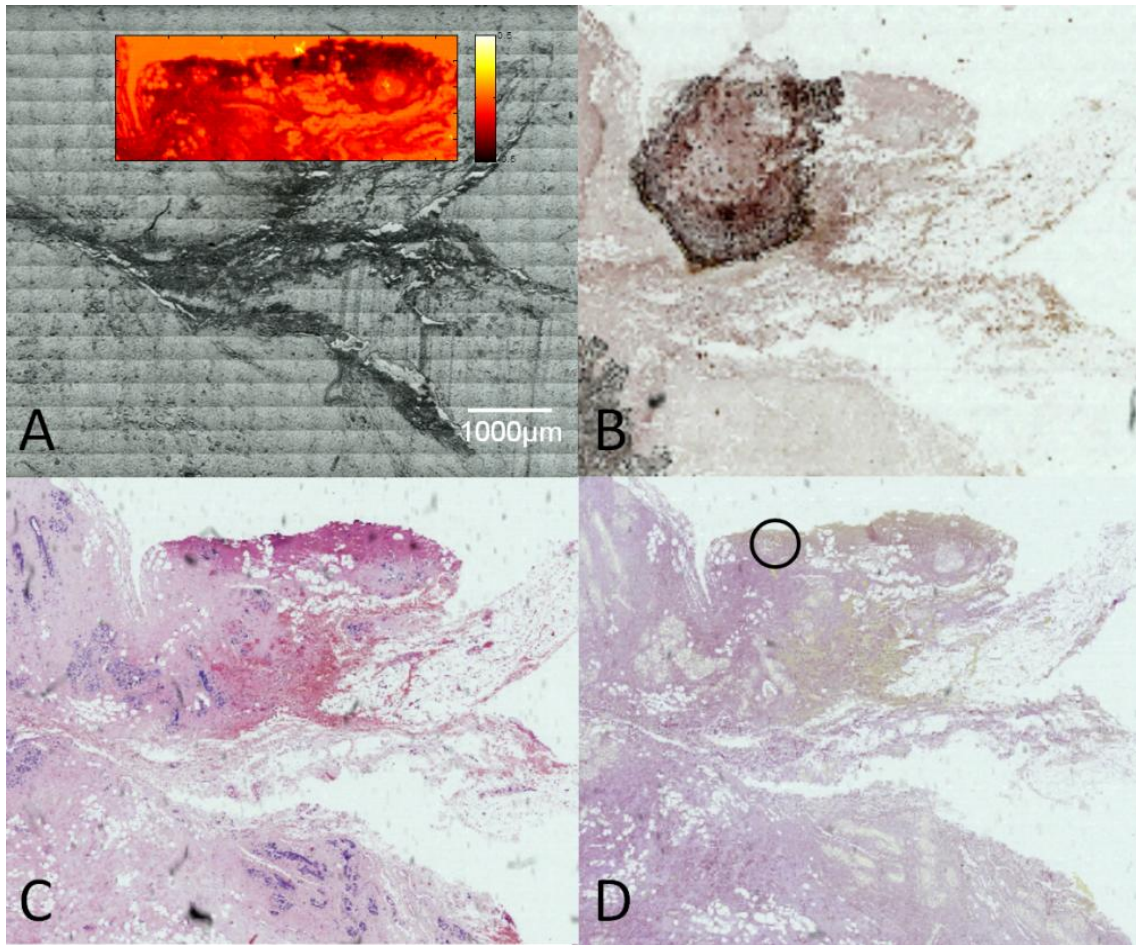


Figure C-2: A) White light image of benign sample with overlaid intensity of apatite fit; B) Alizarin Red staining adjacent slide; C) H&E staining adjacent slide; D) von Kossa staining adjacent slide, calcification highlighted by circle.

C.2 *In situ* specimens

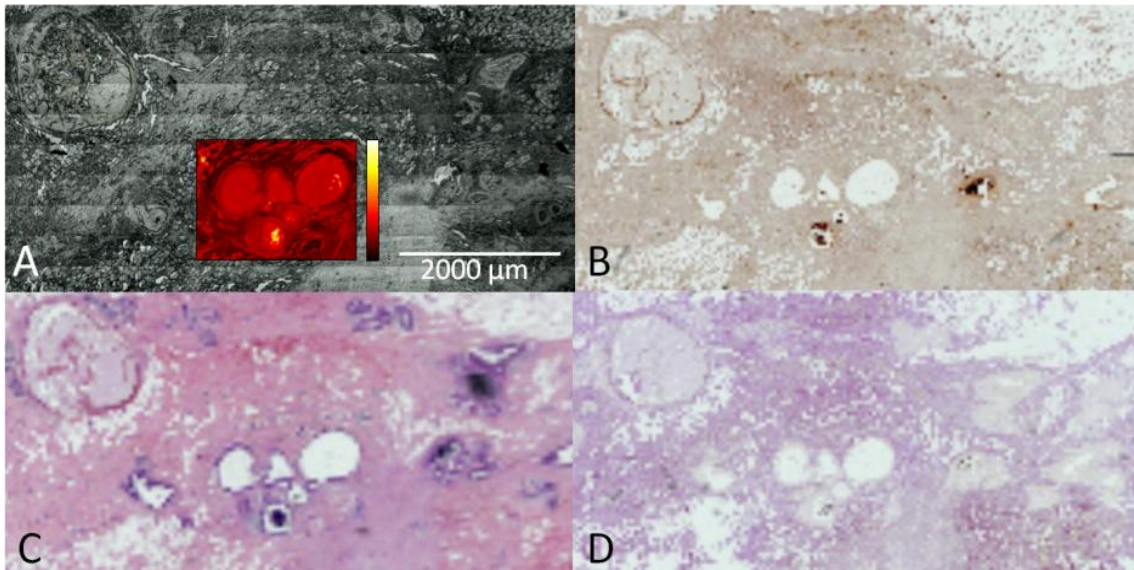


Figure C-3: A) Sample with *in situ* pathology; A) White light image with overlaid apatite fit; B) Alizarin Red stain on adjacent slide; C) H&E stain on adjacent slide; D) von Kossa staining adjacent slide.

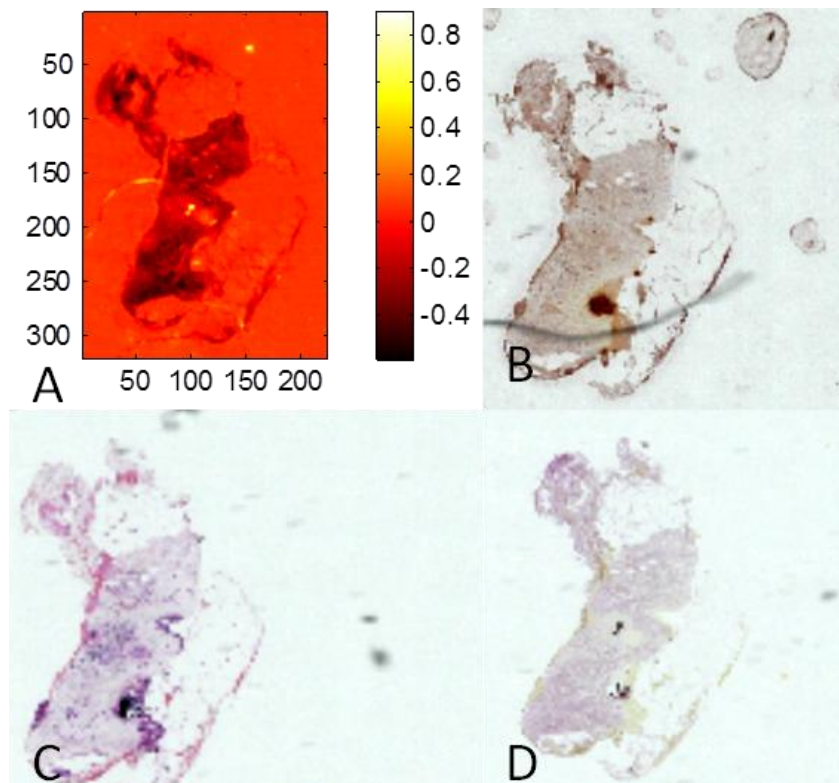


Figure C-4: A) Sample with *in situ* pathology; A) Apatite fit, each pixel is 6.25 μm; B) Alizarin Red staining on adjacent slide; C) H&E staining on adjacent slide; D) Von Kossa staining on adjacent slide.

C.3 Invasive specimens

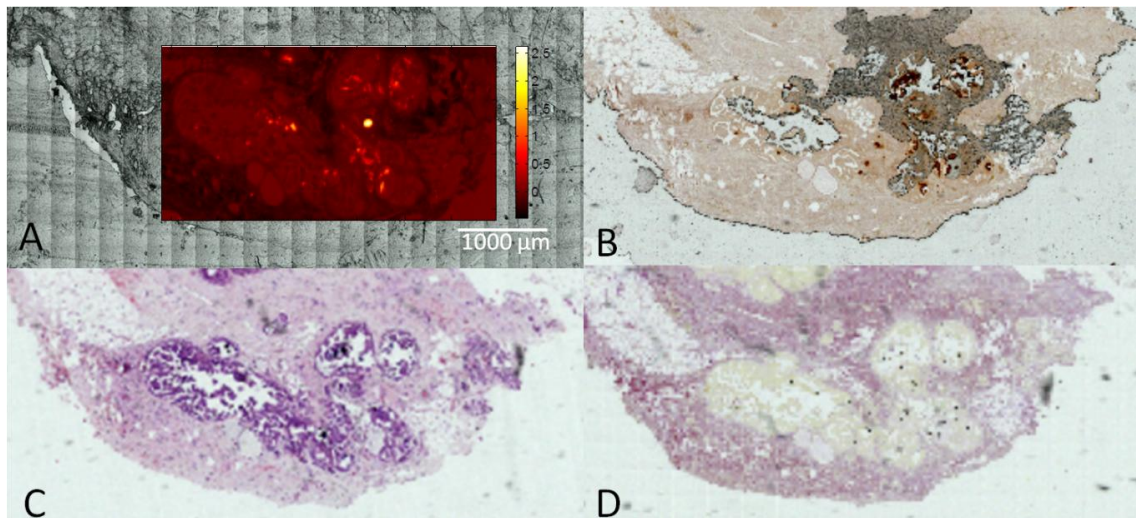


Figure C-5: A) White light image with biochemical fit apatite overlaid; B) Alizarin Red staining on adjacent slide; C) H&E staining on adjacent slice; D) von Kossa staining (counterstain van Gieson) on adjacent slide.

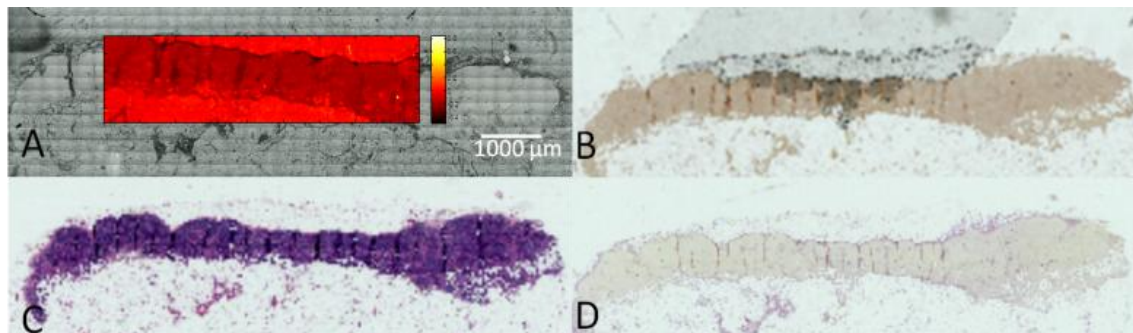


Figure C-6: A) White light image with overlaid the apatite fit; B) Alizarin Red stain on adjacent slide; C) H&E staining on adjacent slide; D) Von Kossa staining on adjacent slide with van Gieson as counterstain.

Appendix C

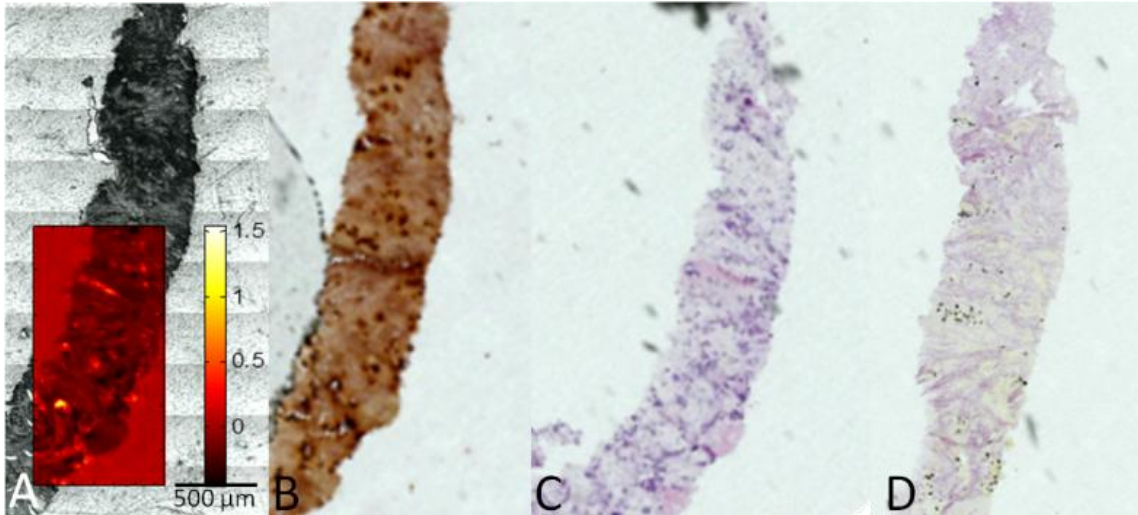


Figure C-7: A) White light image with overlaid the apatite fit; B) Alizarin Red staining on adjacent slide; C) H&E staining adjacent slide; D) Von Kossa staining adjacent slide with counterstain van Gieson.

Appendix D Paraffin removal

In order to perform Raman imaging on tissue sections from blocks in storage, the paraffin has to be removed as it generates excessive interfering fluorescence. In this section the chemical removal of paraffin with paraffin oil and hexane is evaluated by FTIR measurements before and after applying the de-paraffin protocol described in section 2.1.4.

Pathology samples are normally stored in paraffin blocks. When these are sectioned and measured a paraffin signal will be present in addition to the signal of the specimen itself. In FTIR spectroscopy the paraffin signal contains of one strong band $\sim 1472\text{ cm}^{-1}$ and a weaker band $\sim 1463\text{ cm}^{-1}$. This obscures some of the carbonate bands of the apatite, but measurements are still valuable. The Raman spectrum of paraffin is however more disruptive. In figure D-1 the Raman spectrum of paraffin is shown. Also, the paraffin induces a strong fluorescence background on the Raman measurements.

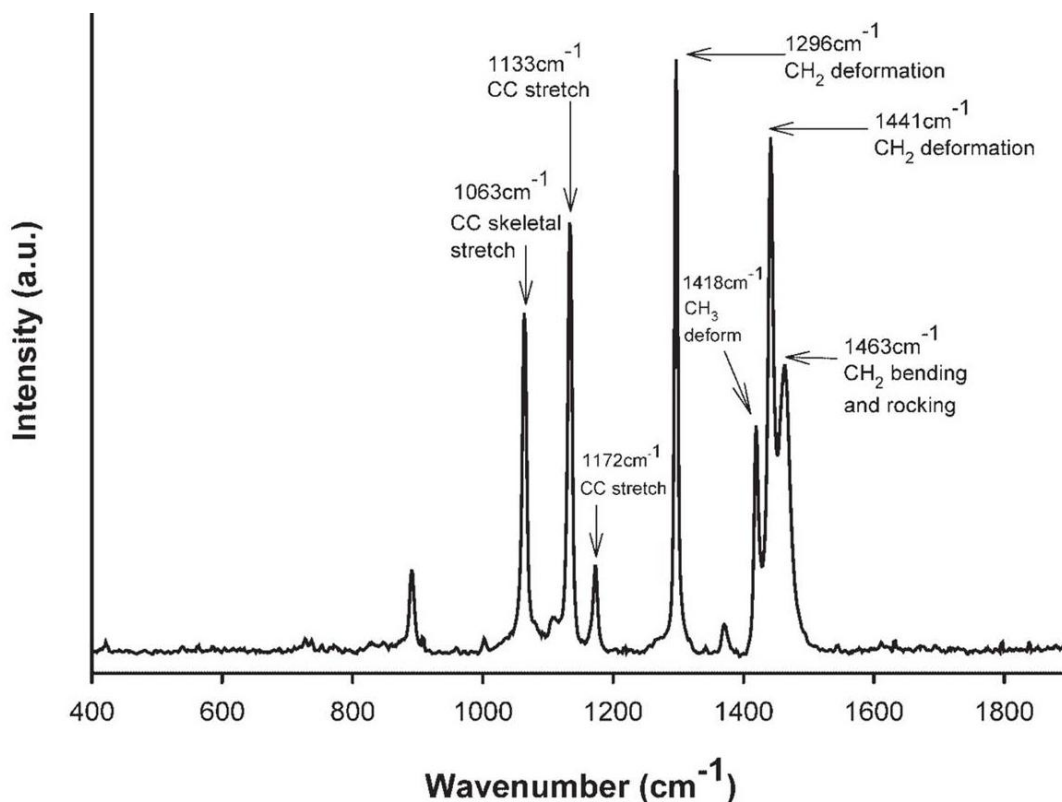


Figure D-1: Raman spectrum of paraffin wax (Faoláin et al., 2005).

Appendix D

Paraffin can be removed by chemical treatments, such as xylene or hexane dewaxing, or commercial products such as histoclear and trilogy (Faoláin et al., 2005). Another possibility is 'digital dewaxing' in which paraffin signals are removed during the data analysis (Tfayli et al., 2009). Faoláin et al (2005) report that from all chemical removal protocols tested, hexane removes most of the paraffin. Therefore, it was decided to use a hexane based protocol to remove paraffin of a pathology sample for a proof of concept Raman mapping study.

In figure D-2, a sample is shown before applying the protocol. In panel A, the white light image is shown with in red the area (2000x300 μm) measured with FTIR. In panel B, the biochemical fit of apatite is shown with three distinct areas of calcifications which are visible in the white light image (panel A) as dark patches. The same fit is shown in panel C with a threshold of 1 applied. The spectra corresponding to the white pixels in panel C are shown in panel D. The spectra show the characteristic phosphate band ($\sim 1030\text{ cm}^{-1}$), amide bands in the $1500\text{-}1700\text{ cm}^{-1}$, and paraffin bands.

Appendix D

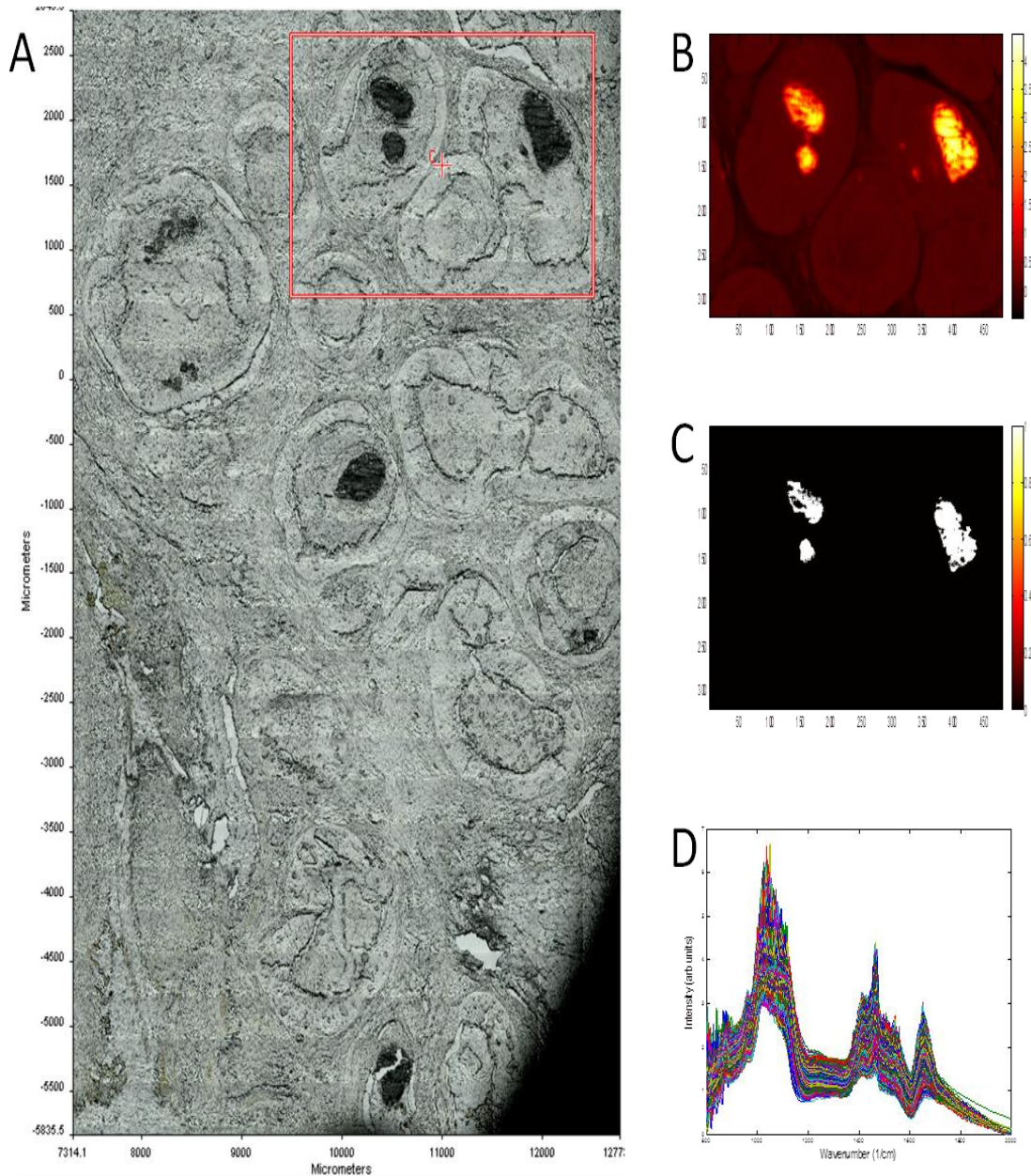


Figure D-2: Sample before de-paraffin protocol A) White light image; B) Biochemical fit for apatite on area highlighted in panel A; C) Biochemical fit for apatite with threshold 2; D) Spectra correlated to white pixels in panel C.

After applying the de-paraffin protocol the structure of the tissue changes dramatically, which can be seen in the white light image shown in panel A of figure D-3. The calcifications previously visible as darker patches are less distinctive after the protocol has been applied. In panel B and C the biochemical fit for apatite is shown for the same region as the data shown in figure D-2. In panel C, a threshold on 1 is applied. The spectra corresponding to the white pixels in panel C are displayed in panel D.

Appendix D

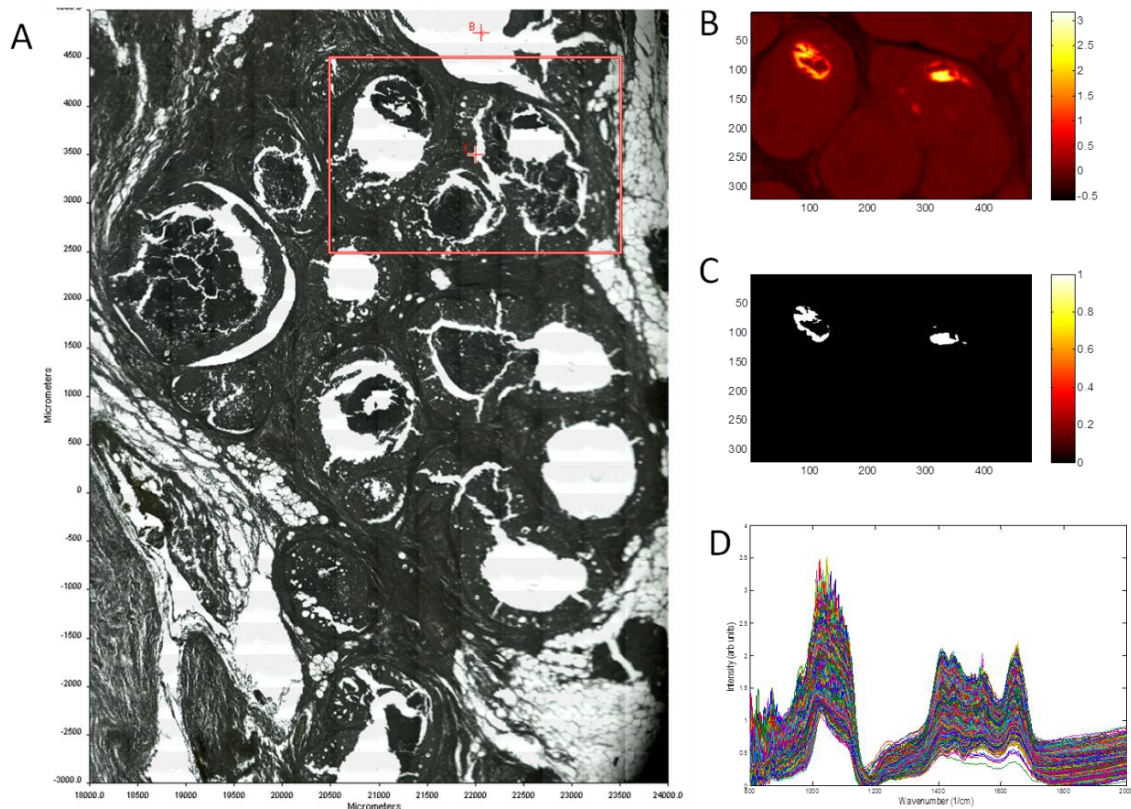


Figure D-3: Sample after de-paraffin protocol A) White light image; B) Biochemical fit for apatite on area highlighted in panel A; C) Biochemical fit for apatite with threshold 2; D) Spectra correlated to white pixels in panel C

Compared to the measurement done before applying the de-paraffin protocol, less and smaller areas of calcification were found. In panel D, less of the characteristic paraffin bands can be seen, which is more readily displayed in figure D-4, in which the mean spectrum of the spectra shown in panel D of both figure D-2 and D-3 are displayed.

Characteristic paraffin bands in FTIR are found ~ 1378 , 1463 , and 1472 cm^{-1} . In figure D-4, these positions are highlighted by dotted lines. After the de-paraffin protocol (depicted in green) these bands disappear and the 1450 cm^{-1} band characteristic for carbonate become visible.

Appendix D

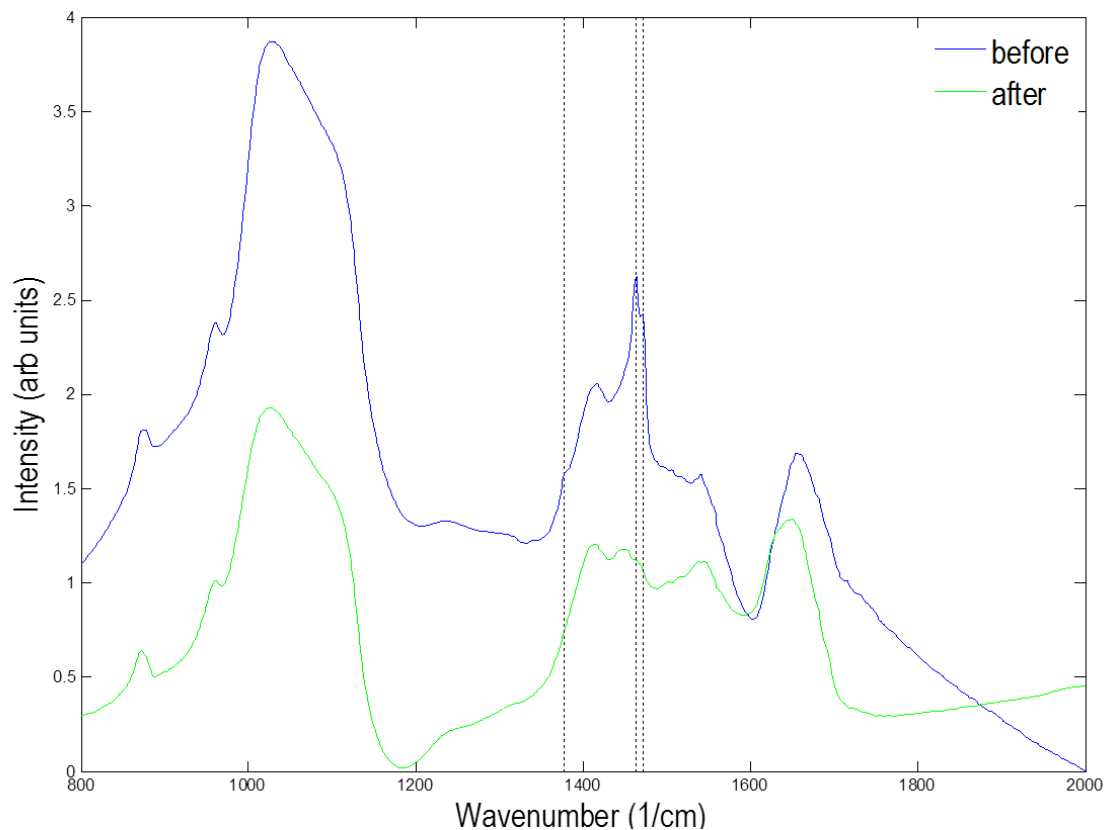


Figure D-4: Mean spectra of the spectra showed in panel D of figure 4.23 and 4.24 (relating to white pixels in panels C). Locations of the characteristic paraffin bands are highlighted with dotted lines.

In figure D-5, the chemical fit for paraffin is showed for both FTIR measurements. While paraffin is abundant before applying the de-paraffin protocol, the chemical fit scores close to zero in the map measured after the de-paraffin protocol.

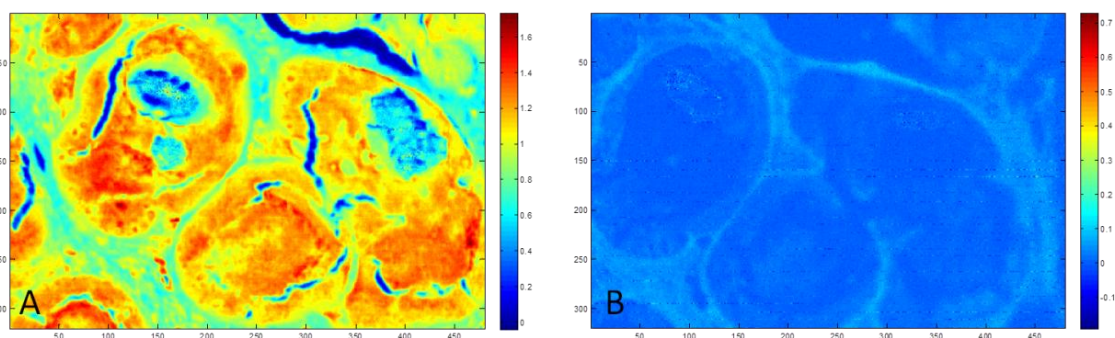



Figure D-5: Chemical fit of paraffin in panel A) Before de-paraffin protocol; B) After de-paraffin protocol

Appendix E Deep Raman on theatre samples

E.1 Consent form

Gloucestershire Hospitals 
NHS Trust
Biophotonics Research Group
Gloucestershire Royal Hospital
Great Western Road
Gloucester, GL1 3NN
08454 225470
08454 225485
c.kendall@medical-research-centre.com

CONFIDENTIAL

CONSENT FORM
Version 2.0 April 2008
Applications of Raman spectroscopy in Breast cancer
DONATION OF TISSUE SAMPLES TO ADVANCE THE DIAGNOSIS OF
BREAST CANCER USING OPTICAL AND MOLECULAR BIOLOGY
TECHNIQUES

Lead Researchers: Dr C Kendall, Dr N Stone.

Please initial each box

1. I confirm that I have read and understand the patient information leaflet dated April 2008 (version 2.0), for the above study and have had the opportunity to ask questions.
2. I request that any tissue samples taken during the course of my surgical procedure at Gloucestershire Hospitals NHS Trust may be made available for additional research tests as part of the above study.
3. I understand that my participation is voluntary and that I am free to ~~withdraw~~ withdraw at any time without giving any reason, without my medical care or legal rights being affected. In the event that I wish to withdraw from this study, data collection will cease immediately and I can request that all data collected is confidentially destroyed.
4. I understand that sections of any of my medical notes may be looked at by the researchers or by regulatory authorities where it is relevant to my taking part in research. I give permission for these individuals to have access to my records.
5. I agree to take part in the above study.


..... Name of Patient Date Signature
..... Name of person taking consent (if different from researcher) Date Signature
..... Name of Researcher Date Signature

Chair:
Prof. Clair Chibvers DSc

Chief Executive:
Dr Frank Haxworth PhD, MBA

Figure E 1: Consent form used in the deep Raman study.

E.2 Patient information leaflet

Gloucestershire Hospitals 
NHS Foundation Trust

PATIENT INFORMATION LEAFLET
Version 2.0 April 2008

Applications of Raman spectroscopy in Breast cancer
Lead Researchers: Dr C Kendall, Dr N Stone.

You are invited to take part in a research study being carried out at Gloucestershire Hospitals NHS Trust. Before you decide whether you would like to participate it is important for you to understand why the research is being done, and what it will involve. Please take time to read the following information carefully and discuss it with others if you wish. Please ask us if there is anything unclear or if you would like further information. Please take time to decide whether or not you wish to take part. Thank you for reading this information.

Background
A team at Gloucestershire Hospitals NHS Trust together with scientists at Cranfield University are working to improve clinical management of breast cancer. Using advanced techniques of tissue identification we hope to identify abnormal tissue during surgery more accurately and more quickly. This could result in a shorter duration of surgery and possibly a decreased likelihood of further surgery for people with breast cancers in the future. Before safe and effective use with patients, it is necessary to assess these techniques on human tissue in the laboratory.

Do I need to take part?
NO. IT IS ENTIRELY VOLUNTARY. You can refuse to provide a sample at any time and you do not need to give reasons and your future treatment will not be affected.

If you do decide to take part you will be given this information sheet to keep and be asked to sign a consent form. If you decide to take part you are still free to withdraw at any time and without giving a reason. A decision to withdraw at any time, or a decision not to take part, will not affect the standard of care you receive.


What will happen to me if I take part?
Your surgical team has explained that you need an operation or biopsy as a part of your treatment. Specialist staff within the hospital will examine this tissue and your care will be guided by what they find. If you are willing to allow us, we can use a small number of additional samples to help us develop new diagnostic tests. No additional procedures will be undertaken as a result of your consent. In addition there is no need for any lifestyle restrictions to participate in this study. This request does not mean that your diagnosis is unsure.

Chair:
Prof Clair Chilvers DSc.
Raman spectroscopy in Breast cancer

Chief Executive:
Dr Frank Hargrett, PhD, MBA.
PILv2.0 April 2008

1 of 2

Figure E 2: Patient information leaflet used in the deep Raman study (page 1).

Gloucestershire Hospitals 
NHS Foundation Trust

Will these additional tests change my diagnosis?
No. All the usual tests would be performed to provide your surgical team with information to plan any further treatment. The additional tests would not affect your treatment or change your diagnosis.

Will these additional tests change the care offered to me?
Further treatment or procedures offered to you will not be changed by these tests. Your care will not be altered by your decision to allow us to use your tissue or not.

What are the possible disadvantages and risks of taking part?
No additional procedures to your routine care will be undertaken as part of this study, therefore there are no associated additional risks.

What are the possible benefits of taking part?
If you decide to participate, you are unlikely to benefit directly from this study. However if this study is successful, this study might help us to treat future patients more effectively.

Will my taking part in this study be kept confidential?
All information that is collected about you during the course of the research will be kept strictly confidential. If you consent to taking part in this study you will give permission for the researchers from the Biophotonics Research Group to have access to your medical notes, where it is relevant to your taking part in research.

What will happen to the results of the research study?
We hope that the results will be published in scientific and medical journals. You will not be identified in any way in such a publication.

Who has reviewed the study?
The Gloucestershire Local Research Ethics Committee has reviewed the study.

Consumers for Ethics in Research (CERES) publish a leaflet entitled 'Medical Research and You'. This leaflet gives more information on medical research. A copy can be obtained from
[CERES, PO Box 1365, London N16 0BW.](mailto:CERES.PO.Box.1365.London.N16.0BW)

Thank you for your help and co-operation. If you have any questions please contact one of the following researchers:
Dr Nick Stone, Tel. No: 08454 225486

2 of 2

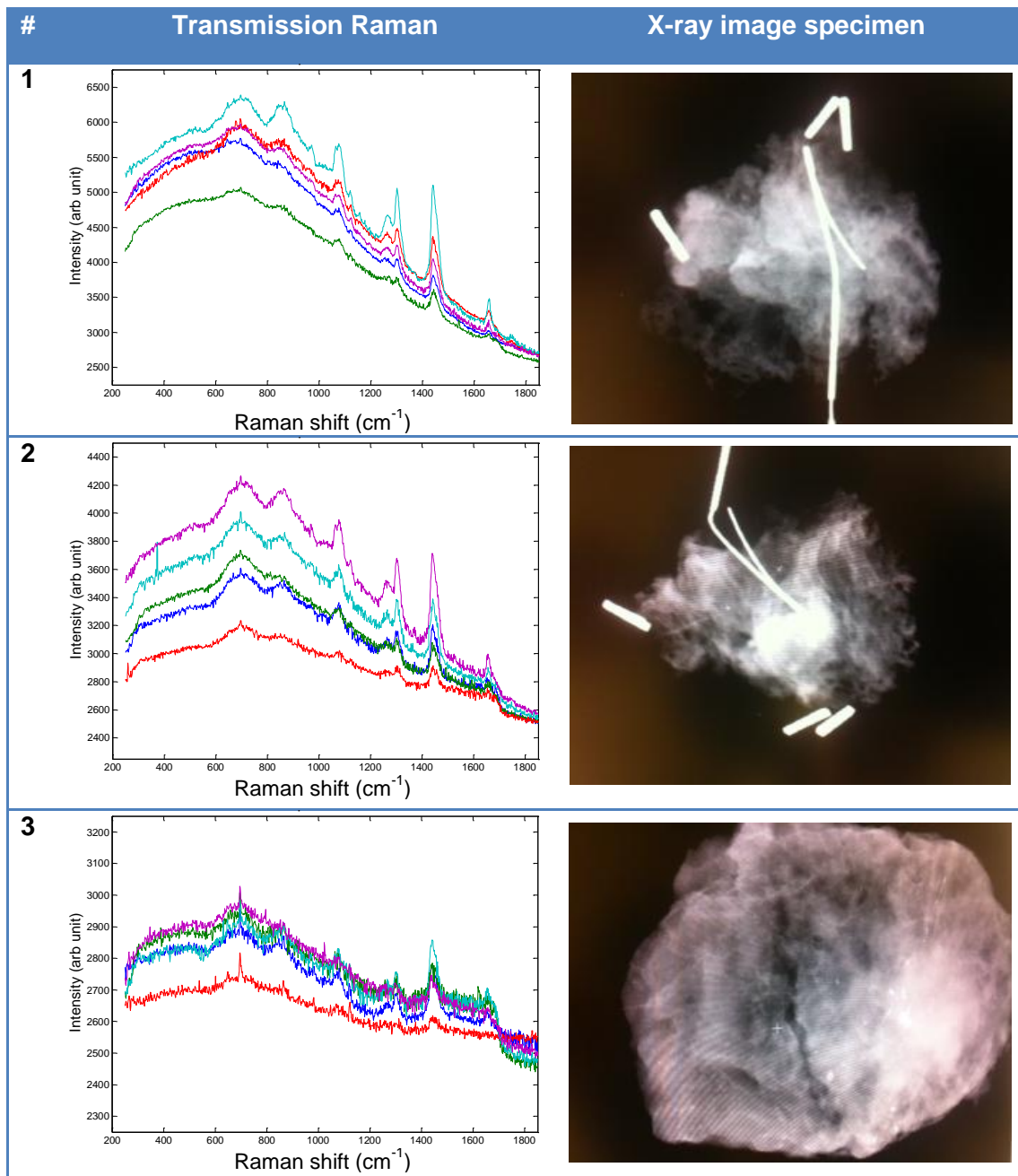
Chair:
Prof Clair Chilvers DSc.
Raman spectroscopy in Breast cancer

Chief Executive:
Dr Frank Hayward PhD, MBA.
PILv2.0 April 2008

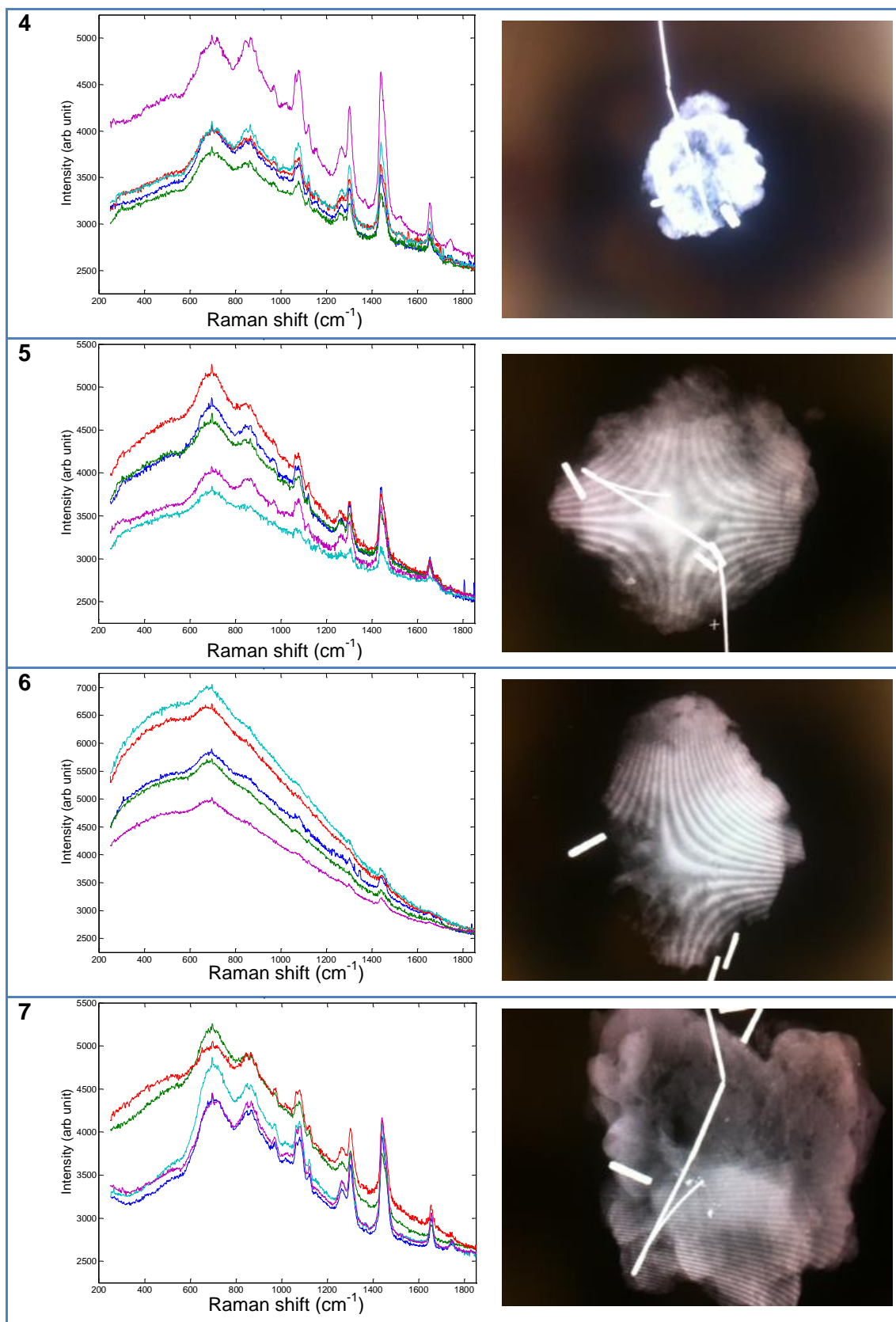
Figure E 3: Patient information leaflet used in the deep Raman study (page 2).

E.3 Raw deep Raman data and X-ray images of the specimens

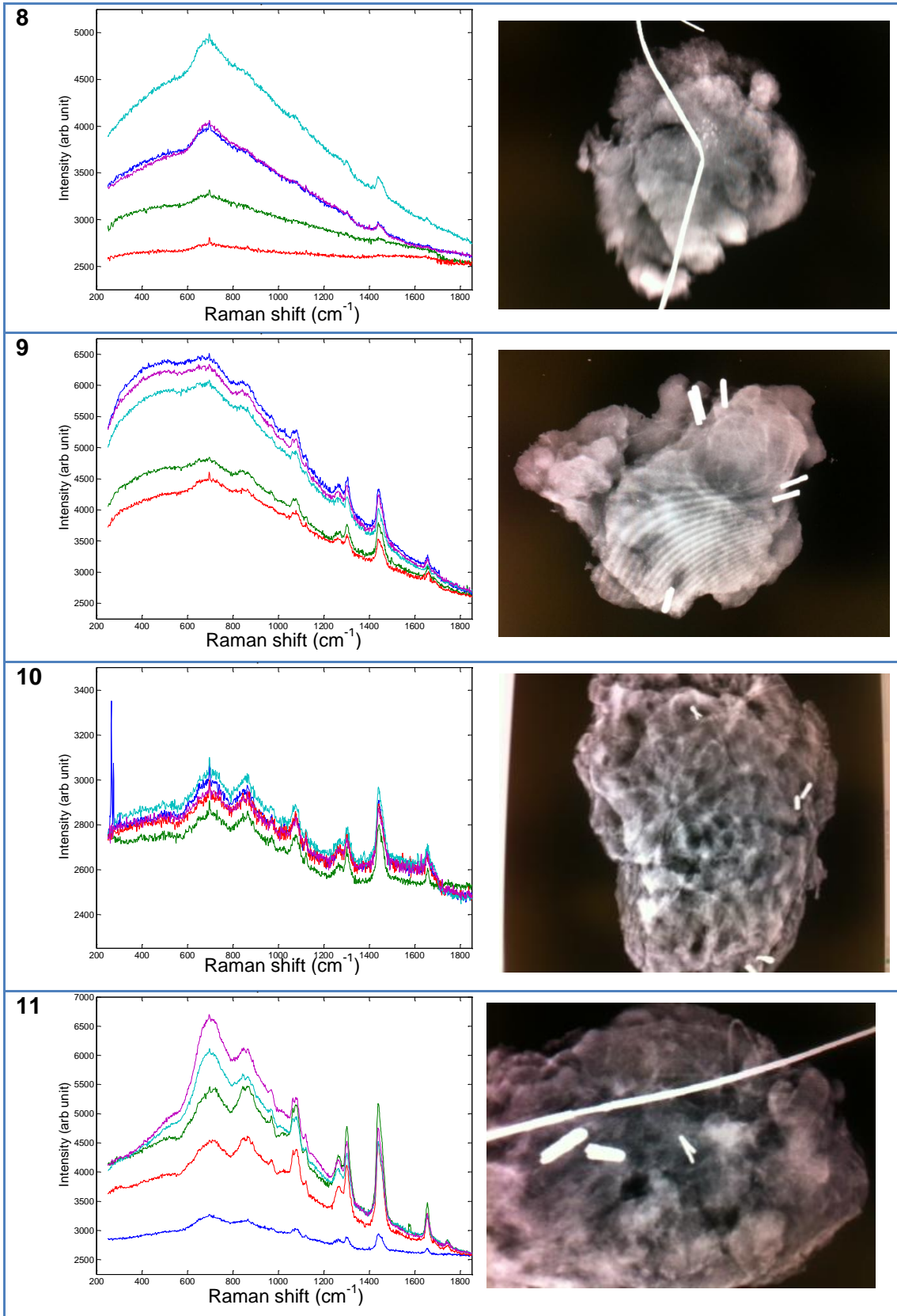
An overview of the deep Raman measurements on the theatre specimens is shown and compared to the X-ray images obtained in theatre. Deep Raman measurements were done in transmission mode, 3x60s, with the cosmic ray removal function on. On each specimen five measurements were performed on different locations.



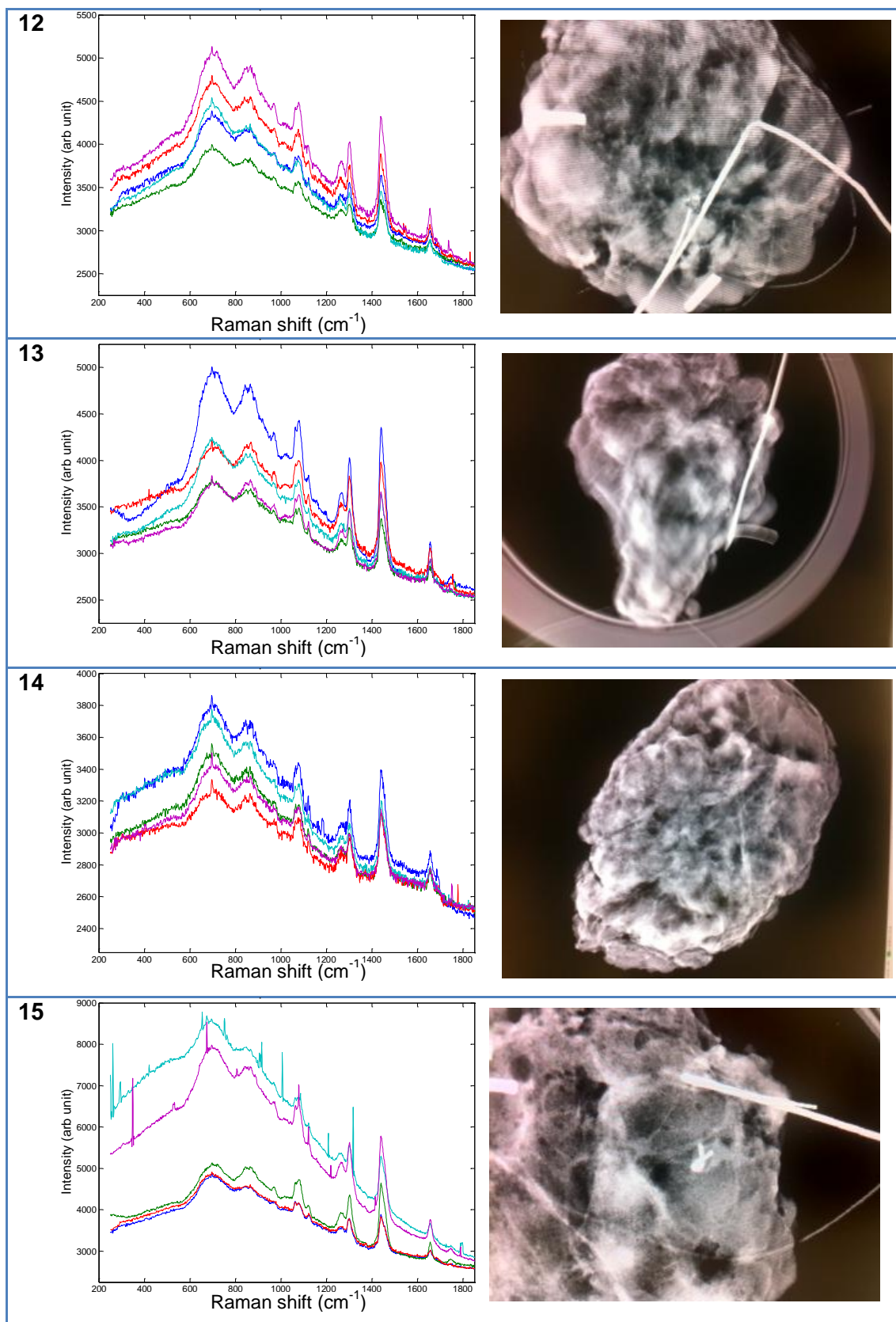
Appendix E



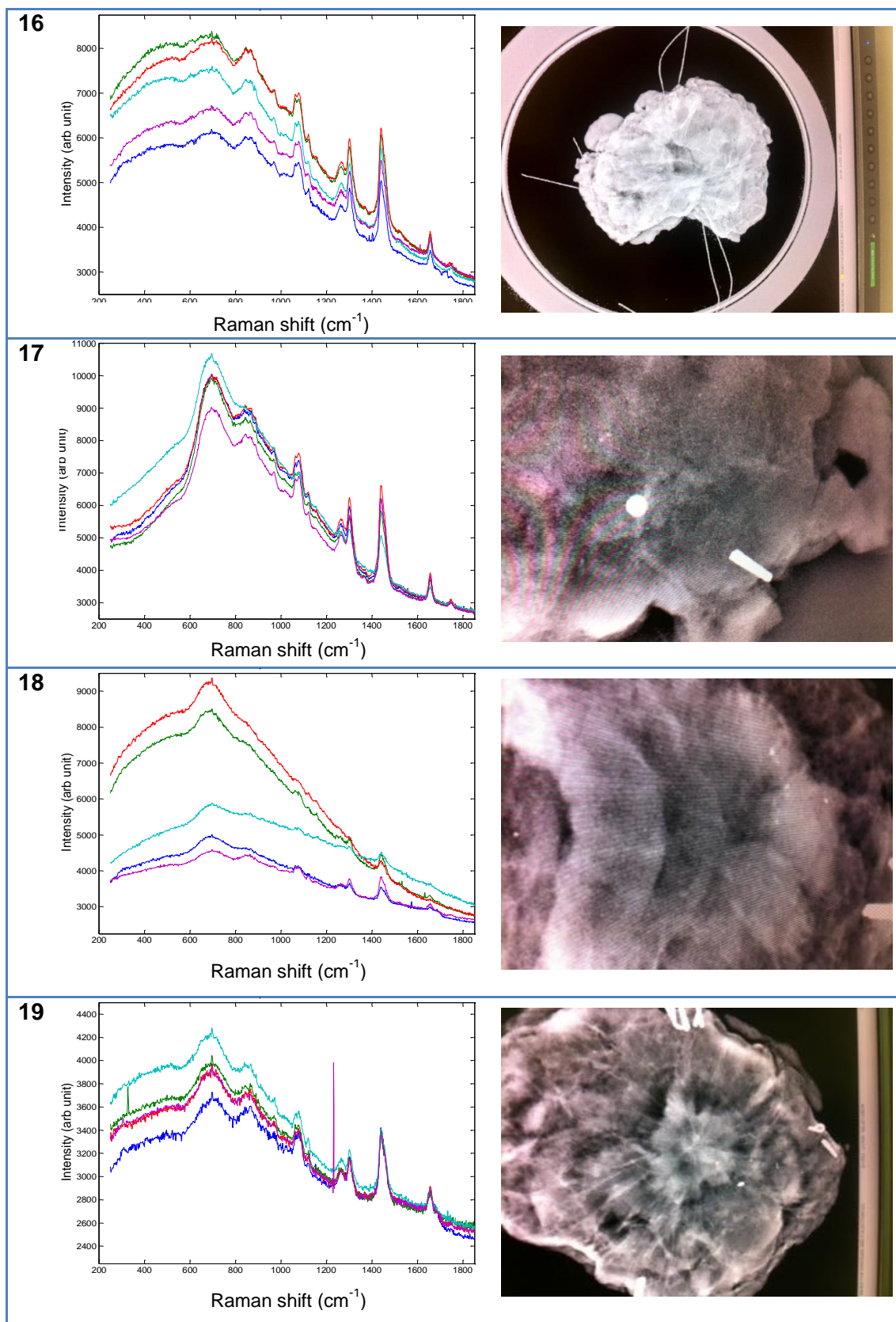
Appendix E



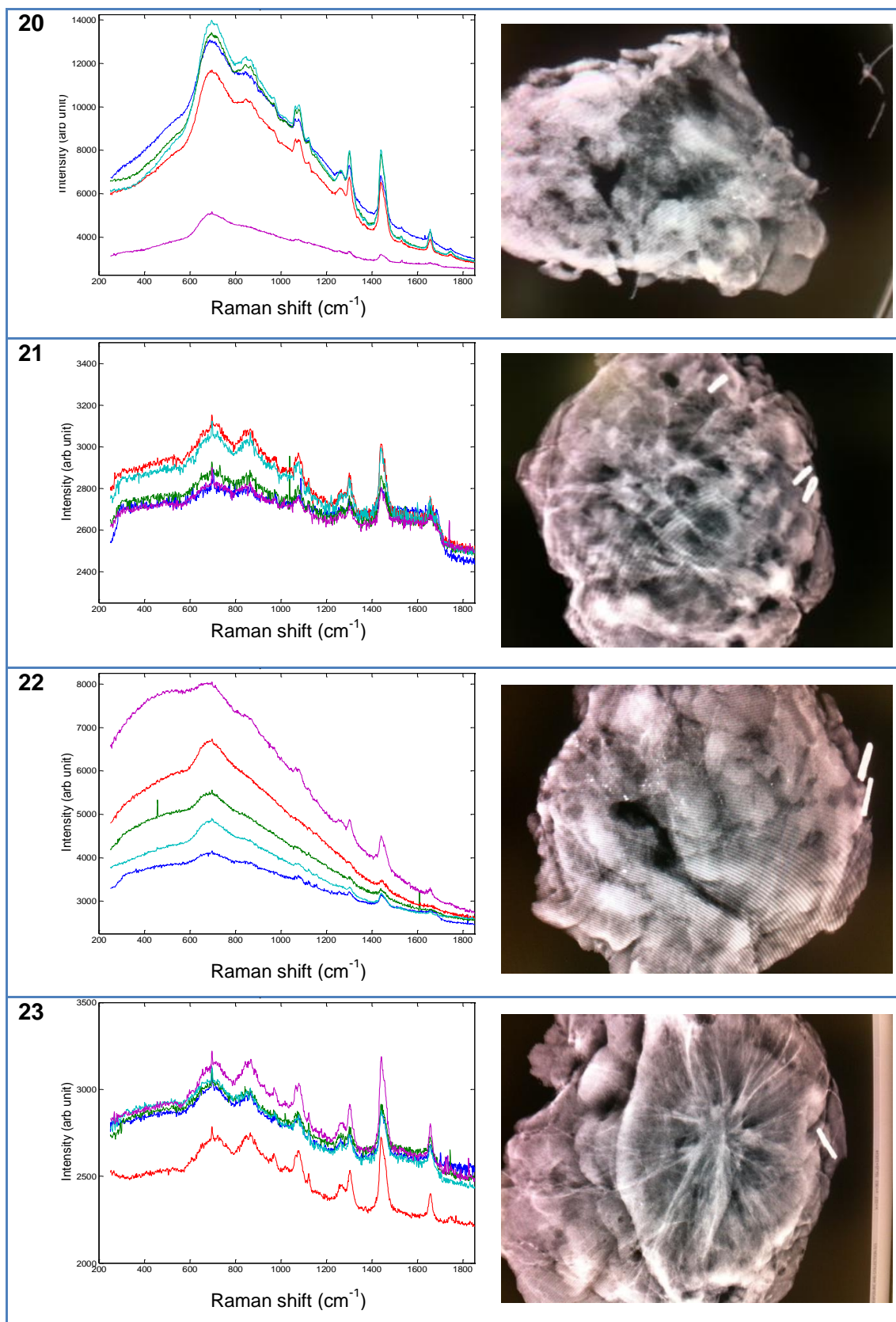
Appendix E



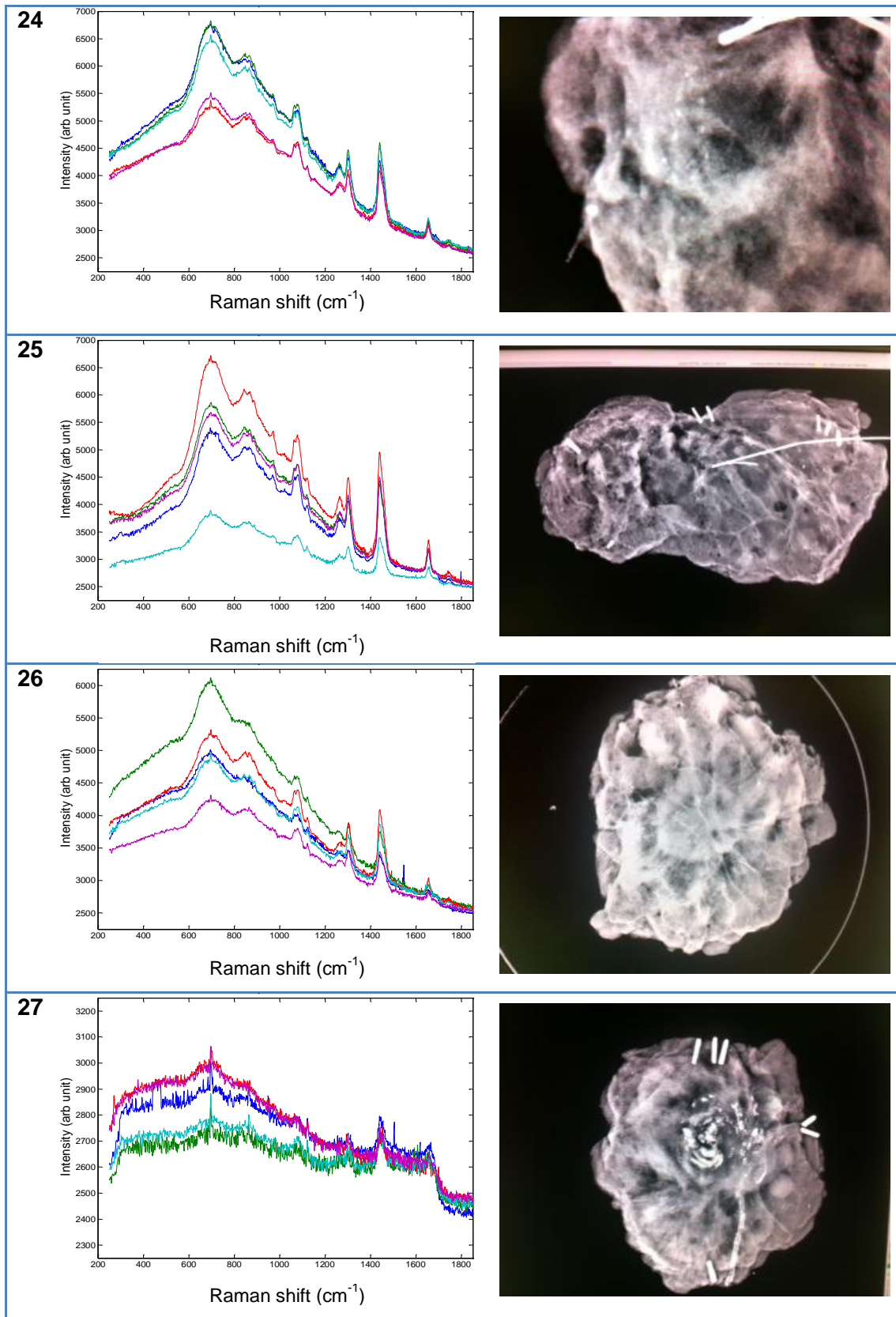
Appendix E



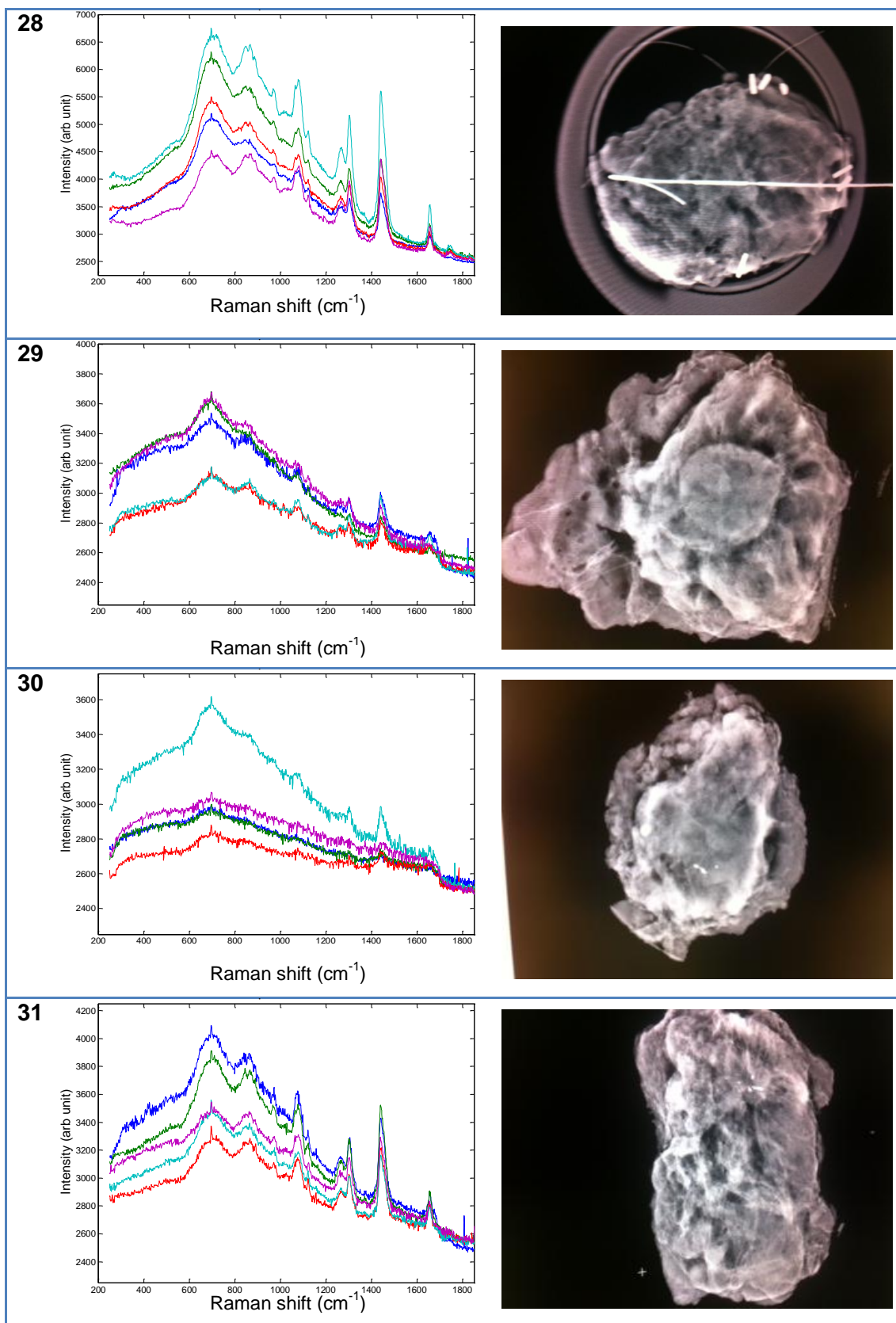
Appendix E



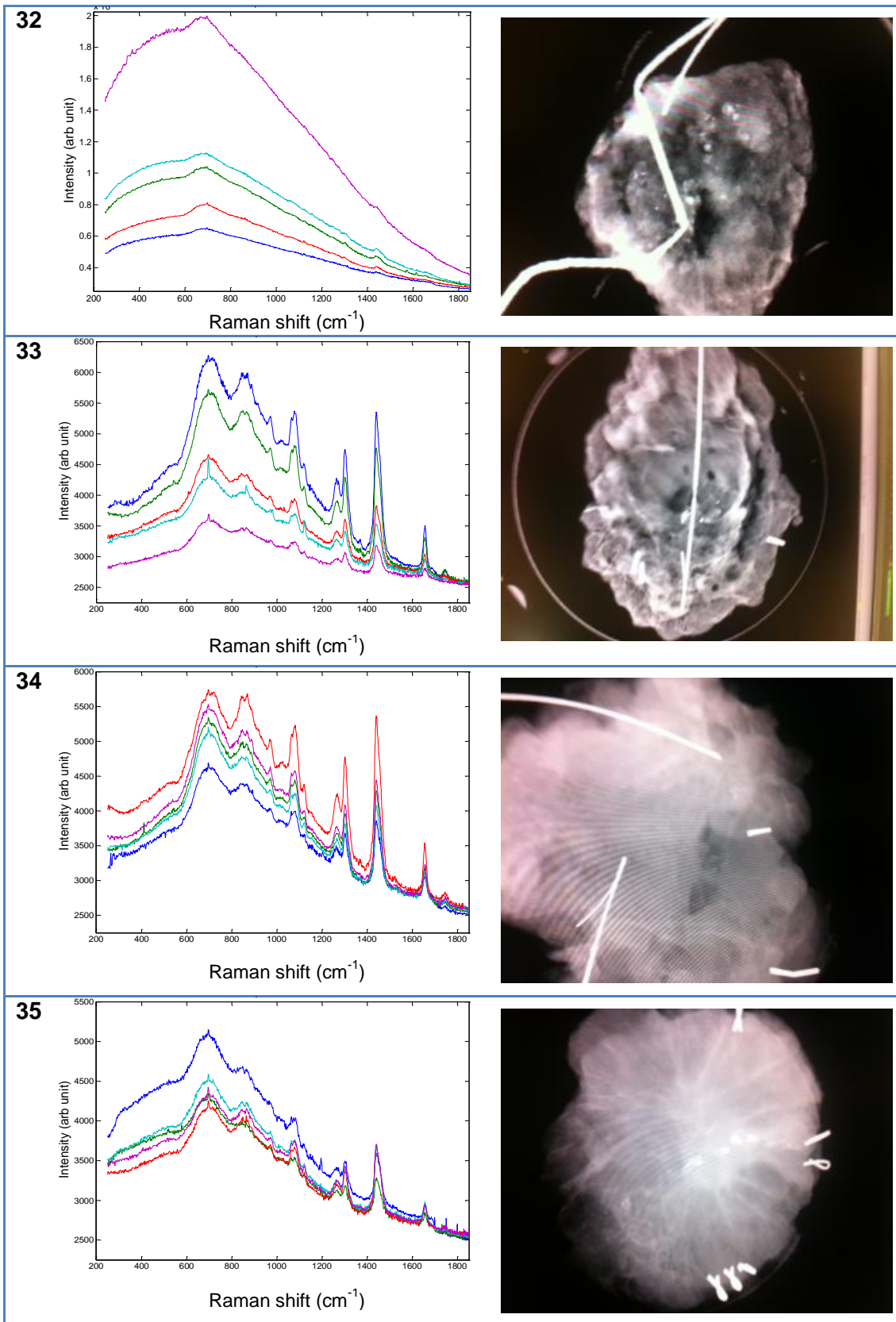
Appendix E



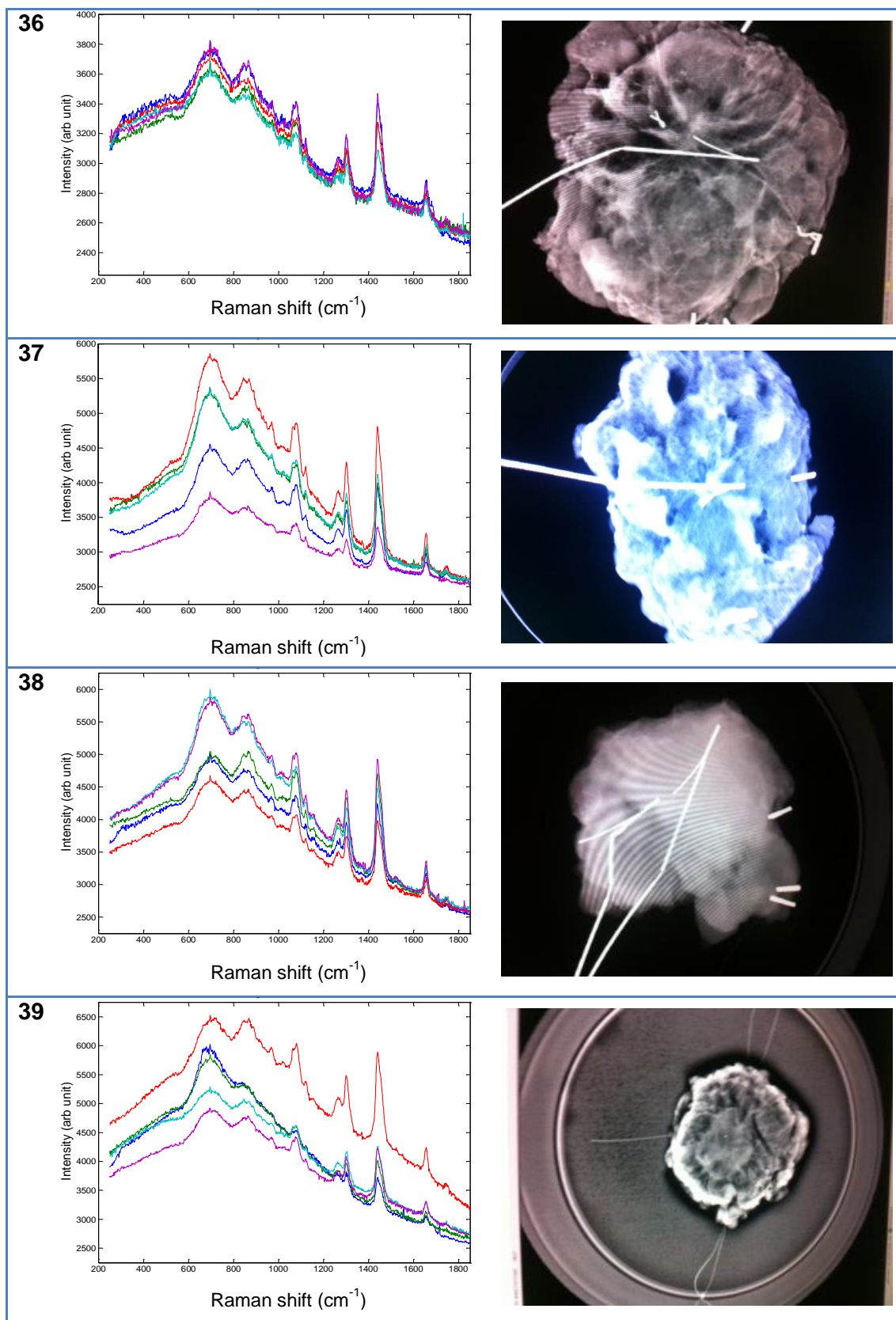
Appendix E



Appendix E



Appendix E



Appendix E

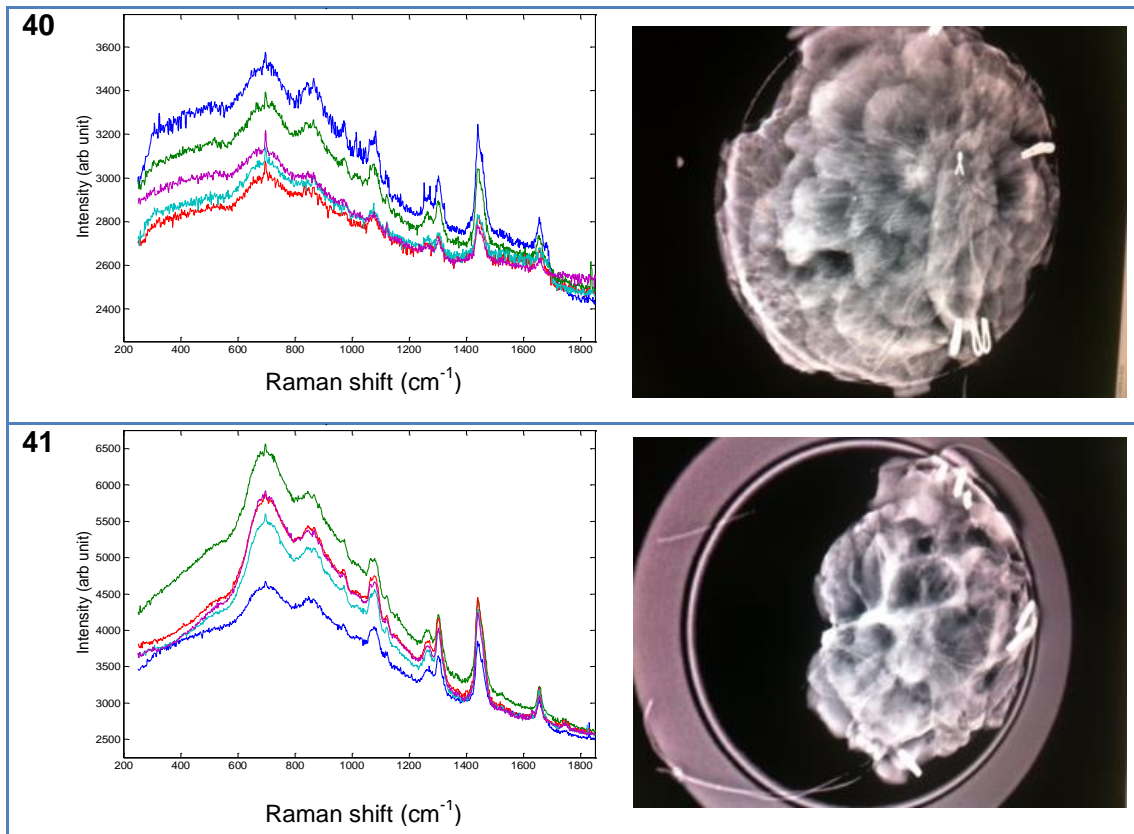


Table E 1: Raw deep Raman data and X-ray images of fresh human breast specimens used in the study.

Appendix F Scientific output

F.1 Publications

F.1.1 Peer reviewed journals

- Nicholas Stone, Marleen Kerssens, Gavin Rhys Lloyd, Karen Faulds, Duncan Graham, and Pavel Matousek, 2011. Surface enhanced spatially offset Raman spectroscopic (SESORS) imaging- the next dimension. **Chemical Science**, 2, pp.776-780. DOI: 10.1039/c0sc00570c ¹
- Marleen M. Kerssens, Pavel Matousek, Keith Rogers, and Nicholas Stone. 2010. Towards a safe non-invasive method for evaluating the carbonate substitution levels of hydroxyapatite (HAP) in micro-calcifications found in breast tissue. **Analyst**, 135, pp. 6156-6161. DOI: 10.1039/C0an00565g

F.1.2 Other

- M. Kerssens, R. Fullerton, P. Matousek, K. Rogers, N. Stone, 2011. Detecting breast cancer by probing micro calcifications with deep-Raman. **Lasers in Medical Science**, 26, pp. 721 (published abstract). DOI: 10.1007/s10103-011-0967-1
- Marleen M. Kerssens, Rachel F. Cox, Pavel Matousek, Keith D. Rogers, Maria P. Morgan and Nicholas Stone. New methodologies for identification of breast calcifications. **Breast cancer research**, (submitted)
- Marleen M. Kerssens, Pavel Matousek, Nick Stone. Detecting breast microcalcifications in theatre: transmission Raman spectroscopy

¹ This paper was accompanied by a press release: 'Raman imaging gives new hope for cancer diagnosis', **RSC website**, February 10, 2011

measurements on freshly excised surgical breast specimens. (in preparation)

- Marleen M. Kerssens, Robert Scott, Pavel Matousek, Keith D. Rogers, Nick Stone. FTIR synchrotron studies on human breast calcifications. (in preparation)
- Marleen M. Kerssens, Alina B. Zoladek, Pavel Matousek, Keith D. Rogers, Sergei Kazarian, Nick Stone. ATR FTIR studies on human breast calcifications, a proof of principle. (in preparation)

F.2 Conference contributions (oral presentations)

- ‘Transmission Raman spectroscopy on freshly excised breast pathology specimens’, **SciX 2012**, Kansas City, Missouri, USA, September 30 – October 5
- ‘High resolution imaging of breast calcification’, **SciX 2012**, Kansas City, Missouri, USA, September 30 – October 5
- ‘Study of calcification formation and disease diagnostics utilising advanced vibrational spectroscopy’, **Cranfield Health Postgraduate Conference**, September 19 2012
- ‘Non invasive breast cancer detection using Raman spectroscopy’, **RCaH (Research Complex at Harwell) PhD Symposium Day**, September 7 2012
- ‘Exploring deep Raman spectroscopy for real-time non-invasive diagnosis of breast cancer’, **Lasers for Science Facility User Meeting**, Abingdon, April 24-26 2012
- ‘Spectroscopic evaluation of breast calcifications’, **Translational Medicine Day**, Cranfield University, March 29 2012

- 'Towards in vivo application of Deep-Raman to detect breast cancer: capability vs. clinical requirements', **FACSS 2011**, Reno, Nevada, USA, October 2-7 (invited)
- 'Detecting breast cancer by probing micro calcifications with Deep-Raman', **British Medical Laser Association (BMLA) Annual Conference**, Woburn, April 19-20 2011
- 'Detecting breast cancer by probing microcalcifications', **Translational Medicine day**, Cranfield University, March 4 2011
- 'Non invasive pathology the 'Raman style': detecting breast cancer by probing micro calcifications', **FACSS 2010**, Raleigh, North Carolina, USA October 17 – 21

F.3 Conference contributions (poster presentations)

- 'Transmission Raman spectroscopy on freshly excised breast pathology specimens', **SciX 2012**, Kansas City, Missouri, USA, September 30 – October 5
- 'Comparison of breast calcification staining versus FTIR and Raman spectroscopy', **ICORS**, Bangalore, India, August 12-17 2012 (presented by Prof Nick Stone)
- 'The use of deep Raman spectroscopy in the NHS breast screening programme', **SET for Britain 2012**, London, March 12 and **RCaH PhD Symposium Day** September 7 2012²
- 'Elucidating the relationship between breast calcifications and breast disease', **FACSS 2011**, Reno, Nevada, USA, October 2-7 (poster prize) and **Cranfield postgraduate conference** September 23

² This poster was accompanied by a press release: 'Taking science to parliament', **Outline** (staff newsletter GRH), March 2012, pp 20.

Appendix F

- ‘Non-invasive pathology with Raman spectroscopy: a potential technique for biopsy reduction in the breast screening programme’, **Infrared and Raman discussion group meeting Christmas 2010**, London, December 16
- ‘Shining light on pathology: Towards a simple non-invasive method for evaluating the carbonate substitution levels of HAP’, **SPEC 2010**, Manchester, June 26-July 1
- ‘Breast screening with Raman spectroscopy’, **Public engagement symposium**, Rutherford Appleton Laboratory, May 19 2010

F.4 Prizes and awards

- Coblenz Society Student Award, 2012³
- FACSS Student Poster Prize (3rd place), 2011
- British Medical Laser Association Educational Award, 2011
- Science and Technology Facility Council Science in society small award, 2010 (£4k)
- Finalist Biotechnology YES (Young Entrepreneur Scheme) 2009
- Smith Nephew prize ‘Best medical technology’ Biotechnology YES (Young entrepreneur Scheme) 2009

F.5 Public Engagement

- Cheltenham Science Festival 2012 Optical Diagnostics session
- Rainbow project, Chestnuts day nursery, May 2012
- SET for Britain, 2012

³ This award was accompanied by a press release: ‘International prize for ‘no needles’ breast cancer diagnosis technique’, www.stfc.ac.uk, October 1, 2012.

Appendix F

- Cheltenham Science Festival 2011 Optical Diagnostics session⁴
- Volunteer Cheltenham Science Festival 2010

⁴ This was publicised in the following article: 'Hands-on in Cheltenham', *Fascination* (STFC newsletter), issue 7, pp. 6-7, August 2011

Cite this: *Chem. Sci.*, 2011, **2**, 776

www.rsc.org/chemicalscience

EDGE ARTICLE

Surface enhanced spatially offset Raman spectroscopic (SESORS) imaging – the next dimension

Nicholas Stone,^{*a} Marleen Kerssens,^a Gavin Rhys Lloyd,^a Karen Faulds,^b Duncan Graham^b and Pavel Matousek^c

Received 11th November 2010, Accepted 13th December 2010

DOI: 10.1039/c0sc00570c

SESORS - Surface enhanced spatially offset Raman spectroscopy-imaging is explored for the first time in this study. Multiplexed surface enhanced Raman scattering (SERS) signals have been recovered non-invasively from a depth of 20 mm in tissues for the first time and reconstructed to produce a false colour image. Four unique 'flavours' of SERS nanoparticles (NPs) were injected into a 20 × 50 × 50 mm porcine tissue block at the corners of a 10 mm square. A transmission Raman data cube was acquired over an 11 × 11 pixel grid made up of 2 mm steps. The signals were reconstructed using the unique peak intensities of each of the nanoparticles. A false colour image of the relative signal levels was produced, demonstrating the capability of multiplexed imaging of SERS nanoparticles using deep Raman spectroscopy. A secondary but no less significant achievement was to demonstrate that Raman signals from SERS nanoparticles can be recovered non-invasively from samples of the order of 45–50 mm thick. This is a significant step forward in the ability to detect and identify vibrational fingerprints within tissue and offers the opportunity to adapt these particles and this approach into a clinical setting for disease diagnosis.

Introduction

Numerous advances in deep Raman techniques have led to the possibility of combining both surface enhanced Raman scattering (SERS) and deep Raman techniques together.^{1–3} The combination of SERS and spatially offset Raman spectroscopy (SORS) techniques, referred to as SESORS, opens the way for sampling a number of disease conditions in the same organ at the same time, thus potentially leading to a new methodology for enhanced personalised treatment plans to be developed in real-time. Here we explore the possibility of using this method to provide multiplexed imaging for the first time at depths of greater than 20 mm in tissues.

SERS can provide molecularly specific enhancement of Raman signals,^{4,5} when the target molecule and a roughened (nanometre scale) noble metal surface are brought in close proximity to one another. Enhancement factors on the order of 10⁹ are possible and single molecule detection has been reported.^{6,7} A lack of

reproducibility of signals has limited uptake in a clinical environment. However, recent developments of novel substrates, such as encapsulated nanoparticles⁸ and photonic crystals^{9,10} show great promise in overcoming these difficulties.

Further developments have included the use of surface enhanced resonance Raman scattering (SERRS), a resonance SERS technique pioneered by Stacy and Van Duyne¹¹ and developed for use as a clinical tool by Graham *et al.*,¹² which is able to provide equivalent detection limits to fluorescence labelled dyes.¹³ It has become routine to tag SERS nanoparticles (NPs) with antibodies for molecules of interest and numerous groups are exploring the clinical application of this approach. In the cancer environment, tagged nanoparticles enhancing specific signals from malignant markers, are either being used *in vivo*^{14–16} or as molecular specific stains for histopathology,^{17–19} with the possibility of numerous multiplexed SERS/SERRS stains providing hyperspectral images of the locations of molecules of interest from the same spectral acquisition and tissue slice.²⁰

Until very recently it was only considered possible to measure signals from these NPs at maximum depths of around 5 mm.¹⁵ The majority of the work performed to date has explored SERS use *ex vivo* with the recent advances into *in vivo* animal based studies. However, these have generally been measuring SERS nanoparticles injected or accumulating at the surface of the animal.^{14–16}

An *in vivo* study demonstrating the use of multiplexed tags within a mouse model was able to demonstrate the detection of

^aBiophotonics Research Unit, Gloucestershire Hospitals NHS Foundation Trust, Great Western Road, Gloucester, GL1 3NN, UK. E-mail: n.stone@medical-research-centre.com; Fax: +44 8454 225485; Tel: +44 8454 225486

^bCentre for Molecular Nanometrology, WestCHEM, Department of Pure and Applied Chemistry, University of Strathclyde, 295 Cathedral Street, Glasgow, G1 1XL, UK

^cCentral Laser Facility, Research Complex at Harwell, Science and Technology Facilities Council, Rutherford Appleton Laboratory, Didcot, Oxfordshire, OX11 0QX, UK

1.6×10^7 nanoparticles subcutaneously and 3.1×10^7 nanoparticles following intravenous injection.¹⁵ Furthermore this study demonstrated the maximum penetration depth achieved to date with SERS and traditional Raman microscopy was of the order of 5.5 mm with a bolus of 1.6×10^{11} nanoparticles.

Rather than rely upon confocal techniques able to probe depths of up to around 200 μm in turbid media with conventional non-SERS samples, deep Raman techniques have been able to distinguish chemical composition of samples through around 2.5 cm thick or 100 times deeper.²¹ The limits have theoretically been extrapolated to 4–5 cm of tissue thickness with proposed optimisation of instrumentation.²² This rapidly expanding field is leading towards many novel potential applications for *in vivo* medical diagnostics from probing bone composition through the skin to disease specific breast calcifications and soft tissue lesions for cancer diagnostics.^{23–27} A further possibility includes *in vivo* monitoring of drug delivery and identification of the location of the drug interactions.

Our recent paper introducing the concept of SESORS, reached a key milestone in deep Raman spectroscopy by demonstrating the possibility of probing signals from SERS nanoparticles buried, or injected into tissues from depths significantly deeper (25 mm) than that previously achieved in epi-Raman approaches.²⁸ In this work we used transmission Raman spectroscopy to demonstrate the concept of deep Raman spectroscopy. This method can be considered a special form of spatially offset Raman spectroscopy (SORS) where the collection and laser delivery areas are displaced to the extreme, *i.e.* being on the opposite sides of the sample. In this study it was possible to detect 1.1×10^9 NPs through 25 mm of porcine tissue. This was achieved at a depth of around five times that achieved by Keren *et al.*¹⁵ and around 100 times less SERS NPs.

A recent paper by Van Duyn's group²⁹ expands on the proposed SESORS approach by exploring the potential of sensing glucose concentration subcutaneously in tissue fluid. They use a similar configuration to the one that we have described for signal collection coupled to an implanted silver film over a nanosphere substrate. They found that it was possible to achieve mean absolute relative difference values for calibration of 16.6% and validation 34.6%. Higher error RMSEC of 58.11 mg dL^{-1} (3.23 mM) and RMSEP of 96.35 mg dL^{-1} (5.35 mM) was seen than in previous *in vivo* results by the same group. This is not unexpected considering the added optical dispersion of the skin and the displacement of the sensor during the experiment.

In this paper, we take a significant step by adding not only the capability to probe nanoparticles at depth in tissues, but to image multiple 'flavours' in the same sample. This demonstrates the potential for multiplexed sensing capability to distinguish both spatially and spectrally between several different nanoparticles.

The postulated depth limit for recovery of signals with transmission Raman (as outlined in previous publications) was around 4–5 cm.²² An additional experiment described here has explored the maximum depth in tissues through which a recognisable signal from the SERS NPs could be obtained at a depth of around 5 cm.

Encapsulated SERS active nanoparticles produced by Cabot (formerly Oxonica) (Boston, Massachusetts) were used in this study.⁸ In contrast to our previous study, these SERS active nanoparticles consisted of gold particles coated with Raman

reporters which were optimised for use with 785 or 830 nm excitation and were encapsulated in a silica shell. One of the benefits of the use of encapsulated SERS nanoparticles is that the signals are obtained only from the reporter molecule, rather than for the target molecule of interest. This allows us to demonstrate the performance of the technology using NPs which would produce the same signals when conjugated directly with molecules of diagnostic interest. They could be labelled for numerous targets, such as PSA, p53 proteins, DNA-fragments and cell specific proteins. This reveals the prospects for numerous clinical applications such as early cancer detection and staging, meta-static detection, treatment monitoring and chemo-sensitivity, provided that the disease specific target molecule is known.³⁰

Results and discussions

Nanoparticle signals from four distinct flavours were identified using the peak intensities unique (within this set) to each of the four nanoparticles flavours. These were 1385, 1300, 928, and 1645 cm^{-1} for the Cabot NPs flavours 403, 421, 422, 440 respectively (see experimental section for SERS reporter identities). Fig. 1 shows spectra measured from the NP suspensions air dried and measured at 830 nm on a calcium fluoride slide.

Injecting the four flavours into a large porcine tissue block ($20 \times 50 \times 50$ mm) enabled the spatial distribution of the spectral signals to be measured and visualised. The signal level for each pixel using the distinct NP identity peaks relative to the quiet spectral region intensity at 800 cm^{-1} was calculated. This produced a four-layered matrix, where each layer corresponded to the relative signal from each NP flavour. False colour map images of the relative signal levels were constructed. Fig. 2 shows the distribution of the signals from each individual nanoparticle flavour (right) and a combined image with all flavours displayed together. This clearly demonstrates the capability of multiplexed imaging of SERS nanoparticles using SESORS.

The images shown were reconstructed from peak intensities of the most distinct SERS bands from each NP flavour. Other multivariate approaches were also explored, such as principal component analysis and least squares fitting of the pure spectra to the SESORS spectra, but produced similar results (not shown). If more flavours of NPs were used, it is expected that these approaches may become more important.

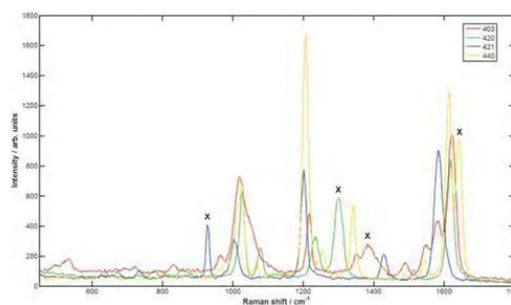


Fig. 1 Spectra at 830 nm of Cabot NPs. Red is x403, green is x420, blue is x421, yellow is x440. The Xs signify the identity peaks used to measure the NP flavour signal in the SESORS spectrum.

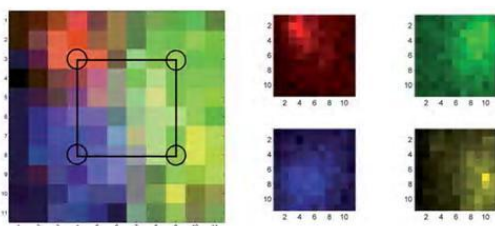


Fig. 2 False colour images of the SERS NP signals, measured in a 11×11 grid, pixel size 2 mm. Left image shows all signals plotted together (with pixel colour mix showing combined signals) with the approximate injection points marked, right image shows each 'flavour' separately. Red is x403, green is x420, blue is x421, yellow is x440.

It should be noted that the maximum injected volume was 13 μL for each flavour which is equivalent to around a 2 mm diameter droplet, the same as a single pixel in the image. Each droplet contained a maximum of 1.8×10^9 NPs. It is clear from the images in Fig. 2, that the diffuse scattering of the Raman photons produced by the NPs has the effect of increasing the apparent spot sizes, *i.e.* the spot areas that the signals are collected from at the surface of the tissue, when measured through the tissue. The lateral spatial resolution in transmission Raman spectroscopy deteriorates linearly with sample thickness and could be typically expected to be approximately equal to a half of the sample thickness.^{31,32} To investigate this a Gaussian peak shape was fitted to each of the NP layers used to generate the pseudo-colour image. This was achieved using a simplex search method to minimise the residual error between the fitted peak and the raw data using five peak parameters: the intensity of the maximum, the position of the maximum (both x and y coordinates), the width (σ) and an offset. The full width at half maximum (FWHM) was then calculated from σ as follows: $FWHM = 2\sqrt{2\ln 2}\sigma$ using a standard Gaussian function.³³ The FWHM for NPs 403, 421, 422, 440 were calculated to be 7.6, 13.6, 12 and 18 mm respectively. Although these values are subject to various sources of error, such as assuming that a Gaussian is a suitable shape to fit the data, they are within the expected range for this experiment. Other potential errors may come from accidental variation of the depth of injection and diffusion of the NPs across natural voids in heterogeneous tissue. Further to the deterioration in localisation of the source scatters with sample thickness, there is significant signal mixing in deeper tissues due to the high turbidity of tissues at NIR wavelengths. However, by using the approach outlined it was a trivial process to separate the spectral signals of the SERS NPs.

The particle numbers used in both this and our previous SESORS study²⁸ were very similar, although the signal to noise achieved with these NPs was significantly greater. Raman spectra measured in transmission mode for particles injected into around 20 mm and 47 (45–50) mm thick blocks are shown in Fig. 3. It can be seen from the raw spectra that SERS signals can be identified clearly at both thicknesses, although the 47 mm specimen required more particles (around 20 times more) and a longer collection time (5×60 s) to achieve this effect. Signals recovered show an order of magnitude increase in depth with an order of magnitude less NPs than shown in previous state-of-the-art results.¹⁵

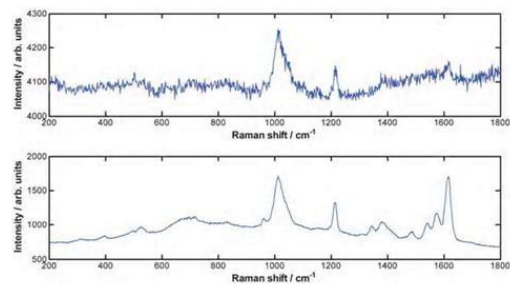


Fig. 3 Raw spectra of NP flavour x403 with 3×10^{10} particles in 50 μL for 47 mm (range 45–50 mm) $\times 50 \times 50$ mm tissue block (top frame) and 1.8×10^9 particles in 3 μL for 20 mm thick $\times 50 \times 50$ mm tissue block (bottom frame).

One feature of the results to note is that the SESORS spectra measured through 47 mm of tissue show significant signal loss, particularly above 1250 cm^{-1} , which we had not previously observed with tissue. We propose the following mechanism; at these wavelengths both water and myoglobin contribute to the absorption. The 1250 to 1600 cm^{-1} Stokes-shifted range with an 830 nm excitation equates to around 925 to 957 nm, which covers the range where a strong lipid absorption band ($\sim 930 \text{ nm}$)³⁴ and water absorption band (max $\sim 970 \text{ nm}$) are located.³⁵ In addition a more subtle contribution also comes from a rising absorption in this wavelength region from myoglobin.³⁶

Experimental

Apparatus

The deep Raman system utilised for this study was constructed at Gloucestershire Royal Hospital using the same configuration as outlined in previous papers.^{27,22} This includes an Innovative Photonics Solutions 830 nm laser as the source which was filtered with two 830 nm laser line filters (Thorlabs), leaving a collimated spot of 4 mm diameter and 219 mW at the sample surface.

The transmitted Raman light was collected using a standard 50 mm diameter fused silica lens with a focal length of 60 mm. The scattered light was collimated and passed through a 50 mm diameter holographic notch filter (830 nm, Kaiser Optical Systems, Inc.) to suppress the elastically scattered component of light. The second lens, identical to the first, was then used to image, with magnification 1 : 1, the sample interaction zone onto the front face of a fibre bundle. The laser incident spot was positioned in such a way so that it coincided with the centre of the fibre probe axis projected through the imaging system on the sample.

The fibre bundle collecting the Raman light consisted of 22 active fibres made of silica with a core diameter of 220 μm , a doped silica cladding diameter of 240 μm and a polyimide coating of 265 μm diameter. The fibre numerical aperture was 0.37. The bundle was custom made by CeramOptec Industries, Inc. The Raman scattered light was propagated through the fibre bundle of length ~ 2 m to the end with the fibres mounted in a linear array, which was oriented vertically and placed in the input image plane of a Kaiser Optical Technologies Holospec 1.8i NIR spectrograph. Raman spectra were collected using

a NIR back-illuminated deep-depletion TE cooled ($-80\text{ }^{\circ}\text{C}$) CCD camera (Andor Technology, DU420A-BR-DD, 1024×256 pixels) by binning the entire chip vertically.

Samples

Tissue preparation involved collection of fresh porcine samples from the local abattoir and dissecting them to the required dimensions. Muscle tissue was chosen to represent dense human tissues as discussed elsewhere.²² A demonstration of signal obtained through increasing depth was achieved by cutting samples from pork muscle to thicknesses of around 20 and 50 mm (other dimensions 50×50 mm) and mounted in the experimental apparatus. All dimensions were measured approximately using a basic ruler at a number of points and mean thicknesses were calculated.

SESORS multiplexing

Four flavours of NPs (Cabot x403 (5-(4-pyridyl)-1,3,4-oxadiazole-2-thiol - POT), x420 (4,4'-dipyridyl - DIPY), x421 (d8-4,4'-dipyridyl - d8DIPY) and x440 (Trans-1,2-Bis(4-pyridyl)-ethylene - BPE) were used in this multiplexing experiment. Their construction is described in detail elsewhere;⁸ briefly, they include a gold core of around 100 nm diameter surrounded by a reporter molecule, the whole encapsulated in a thin silica layer. The particles were delivered suspended in water.

The suspension was shaken for one minute prior to pipetting the required volume into a syringe for injection into the tissue. Both $3\text{ }\mu\text{L}$ of NP stock solution plus $10\text{ }\mu\text{L}$ pestanal water (Sigma) (1.8×10^9 NPs) were pipetted into a 10 mL syringe with a 21G needle of inner diameter 0.51 mm (other needles of finer bore were initially tested and they were found to prevent the majority of the NPs from passing through). Each NP suspension was injected into points at the corners of a 10 mm square, to approximately 50% of the depth of the tissue. It was not possible to be certain that some NPs did not remain in the syringe so the number of NPs pipetted into the syringe prior to injection should be taken as a maximum value. Fig. 4 shows the template grid used. The tissue block (and the NP grid square) was then centered in the sample compartment. The template was then removed, prior to taking SESORS measurements.

Translational x-y stages with a range of 20 mm were used to translate the sample in steps of 2 mm to construct an image of 11×11 pixels. Time of collection was 10 s at each point. Fig. 4 also shows the tissue mounting, laser fibre ($400\text{ }\mu\text{m}$ core), 2 laser line filters and the laser spot and laser back-scattering at the surface of the tissue, which was mounted in a hollow anodised metal bracket.

Extended depth SESORS measurements

For this experiment a single SERS NP flavour (x403) was selected and a large number of particles (3×10^{10}) were injected into the approximate centre of a porcine muscle tissue block of 45–50 mm (mean 47 mm) thick by 50×50 mm. Fig. 5 shows the side projection of the 47 mm tissue block in the experimental position, the illumination provided on one side and the collection at the other side of the tissue block. The signal was measured in 5×60 s and compared with that achieved using the imaging block (20 mm thick) with 1.8×10^9 particles.

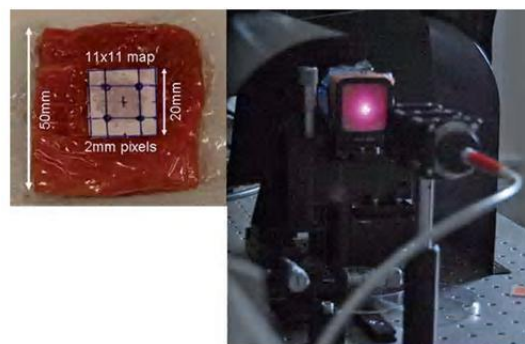


Fig. 4 Left: $20 \times 50 \times 50$ mm porcine block with grid used to align injection points for NPs. The image grid was acquired over the 20×20 mm square shown by the template (removed for measurements). Right tissue mounting, laser fibre ($400\text{ }\mu\text{m}$ core), 2 laser line filters and the laser spot and scattering on the surface of the tissue mounted in the hollow anodised metal bracket.



Fig. 5 $47(45\text{--}50) \times 50 \times 50$ mm tissue block used for the extended depth SESORS experiment.

Conclusions

Multiplexed SERS signals have been recovered from 20 mm in tissues for the first time and reconstructed to produce a false colour image. The signals were reconstructed using the unique peak intensities of each of the nanoparticle flavours. A false colour map image of the relative signal levels was constructed, demonstrating the capability of multiplexed SESORS imaging of SERS nanoparticles using transmission Raman spectroscopy. A secondary but no less significant achievement was to demonstrate that Raman signals from SERS nanoparticles can be recovered from samples of the order of 50 mm thick. This is double that achieved in the first demonstration of this method (although with around 20–30 times as many particles).

The prospects for SESORS as a medical tool are significant. There are numerous applications where this approach would have a major impact on rapid specific diagnosis, patient specific

treatment selection and treatment monitoring. However, in addition to further developments in disease specific SERS particles and read out methodologies; the greatest hurdle will be the issue of introducing nanoparticles into the body without yet a full understanding of their excretion mechanism or long term accumulation sites and whether this is likely to have any detrimental effects.

Acknowledgements

The authors would like to acknowledge the support of Michael Natan and Cabot in providing the NPs used in this study.

Nick Stone holds a Senior Research Fellowship (Career Scientist) from the National Institute of Health Research. Marleen Kerssens is jointly funded by Gloucestershire Hospitals NHS Foundation Trust and the Science and Technology Facilities Council Biomedical Network (4161234). Duncan Graham and Karen Faulds acknowledge the awards of a Science and Innovation and Platform Grant from the EPSRC to support this work.

References

- 1 P. Matousek, I. P. Clark, E. R. C. Draper, M. D. Morris, A. E. Goodship, N. Everall, M. Towrie, W. F. Finney and A. W. Parker, *Appl. Spectrosc.*, 2005, **59**, 393–400.
- 2 P. Matousek, M. D. Morris, N. Everall, I. P. Clark, M. Towrie, E. Draper, A. Goodship and A. W. Parker, *Appl. Spectrosc.*, 2005, **59**, 1485–1492.
- 3 N. A. Macleod and P. Matousek, *Appl. Spectrosc.*, 2008, **62**, 291A–304A.
- 4 M. Fleischmann, P. J. Hendra and A. J. McQuillan, *Chem. Phys. Lett.*, 1974, **26**, 163–166.
- 5 D. L. Jeanmaire and R. P. Van Duyne, *J. Electroanal. Chem.*, 1977, **84**, 1–20.
- 6 K. Kneipp *et al.*, *Phys. Rev. Lett.*, 1997, **78**, 1667.
- 7 J. A. Dieringer, K. L. Wustholz, D. J. Masiello, J. P. Camden, S. L. Kleinman, G. C. Schatz and R. P. Van Duyne, *J. Am. Chem. Soc.*, 2009, **131**, 849–854.
- 8 W. E. Doering, M. E. Piotti, M. J. Natan and R. G. Freeman, *Adv. Mater.*, 2007, **19**, 3100–3108.
- 9 S. Cintra *et al.*, *Faraday Discuss.*, 2006, **132**, 191–199.
- 10 S. Mahajan *et al.*, *Phys. Chem. Chem. Phys.*, 2007, **9**, 104–109.
- 11 A. A. Stacy and R. P. Van Duyne, *Chem. Phys. Lett.*, 1983, **102**, 365–370.
- 12 D. Graham, W. E. Smith, A. M. T. Linacre, C. H. Munro, N. D. Watson and P. C. White, *Anal. Chem.*, 1997, **69**, 4703–4707.
- 13 G. Sabatte, R. Keir, M. Lawlor, M. Black, D. Graham and W. E. Smith, *Anal. Chem.*, 2008, **80**, 2351–2356.
- 14 A. Pal, N. R. Isola, J. P. Alarie, D. L. Stokes and T. Vo-Dinh, *Faraday Discuss.*, 2006, **132**, 293–301.
- 15 S. Keren, C. Zavaleta, Z. Cheng, A. de la Zerda, O. Gheysens and S. S. Gambhir, *Proc. Natl. Acad. Sci. U. S. A.*, 2008, **105**, 5844–5849.
- 16 X. M. Qian *et al.*, *Nat. Biotechnol.*, 2008, **26**, 83–90.
- 17 L. Sun *et al.*, *Nano Lett.*, 2007, **7**, 351–356.
- 18 B. Lutz *et al.*, *J. Histochem. Cytochem.*, 2008, **56**, 371–379.
- 19 Y. N. Liu, Z. O. Zou, Y. O. Liu, X. X. Xu, G. Yu and C. Z. Zhang, *Spectroscopy and Spectral Analysis*, 2007, **27**, 2045–2048.
- 20 K. Faulds, R. Jarvis, W. E. Smith, D. Graham and R. Goodacre, *Analyst*, 2008, **133**, 1505–1512.
- 21 P. Matousek and N. Stone, *Analyst*, 2009, **134**, 1058.
- 22 N. Stone and P. Matousek, *Cancer Res.*, 2008, **68**, 4424–4430.
- 23 M. V. Schulmerich, *Proceedings of SPIE*, 2006, **6093**, 60930O.
- 24 M. V. Schulmerich, K. A. Dooley, M. D. Morris, T. M. Vanasse and S. A. Goldstein, *J. Biomed. Opt.*, 2006, **11**, 060502.
- 25 P. Matousek *et al.*, *Appl. Spectrosc.*, 2006, **60**, 758.
- 26 M. V. Schulmerich, *J. Biomed. Opt.*, 2008, **13**, 020506.
- 27 P. Matousek and N. Stone, *J. Biomed. Opt.*, 2007, **12**, 024008.
- 28 N. Stone, K. Faulds, D. Graham and P. Matousek, *Anal. Chem.*, 2010, **82**, 3969–3973.
- 29 J. M. Yuen, N. C. Shah, J. T. Walsh, Jr., M. R. Glucksberg and R. P. Van Duyne, *Anal. Chem.*, 2010, **82**, 8382–8385.
- 30 C. G. Rao *et al.*, *Int. J. Oncol.*, 2005, **27**, 49–57.
- 31 N. Everall, P. Matousek, N. Macleod, K. L. Ronayne and I. P. Clark, *Appl. Spectrosc.*, 2010, **64**, 52–60.
- 32 N. Everall, I. Priestnall, P. Dallin, J. Andrews, I. Lewis, K. Davis, H. Owen and M. W. George, *Appl. Spectrosc.*, 2010, **64**, 476–484.
- 33 Eric W. Weisstein, “Gaussian Function”. From MathWorld—A Wolfram Web Resource. <http://mathworld.wolfram.com/GaussianFunction.html>.
- 34 S. Kukreti, A. Cerussi, B. Tromberg and E. Gratton, *Dis Markers.*, 2008, **25**, 281–290.
- 35 S. J. Matcher, M. Cope and D. T. Delpy, *Phys. Med. Biol.*, 1994, **39**, 177.
- 36 J. J. Xia, E. P. Berg, J. W. Lee and Yao, *Meat Sci.*, 2007, **75**, 78–83.

Towards a safe non-invasive method for evaluating the carbonate substitution levels of hydroxyapatite (HAP) in micro-calcifications found in breast tissue†

Marleen M. Kerssens,^{ab} Pavel Matousek,^c Keith Rogers^b and Nicholas Stone^{*,a}

Received 23rd July 2010, Accepted 22nd September 2010

DOI: 10.1039/c0an00565g

A new diagnostic concept based on deep Raman spectroscopy is proposed permitting the non-invasive determination of the level of carbonate substitution in type II calcifications (HAP). The carbonate substitution has shown to be directly associated with the pathology of the surrounding breast tissue and different pathology groups can therefore be separated using specific features in the Raman spectra of the calcifications. This study explores the principle of distinguishing between type II calcifications, found in proliferating lesions, by using the strongest Raman peak from calcium hydroxyapatites (the phosphate peak at 960 cm⁻¹) to act as a surrogate marker for carbonate substitution levels. It is believed that carbonate ion substitution leads to a perturbation of the hydroxyapatite lattice which in turn affects the phosphate vibrational modes. By studying calcifications, with known carbonate content, buried in porcine tissue it has been possible to evaluate the feasibility of using the proposed approach to probe the composition of the calcifications *in vivo* and hence provide pathology specific information non-invasively, in real time. Using the proposed concept we were able to determine the level of carbonate substitutions through soft tissue phantom samples (total thickness of 5.6 mm). As the level of carbonate substitution has been previously correlated with mid-FTIR to the lesion type, *i.e.* whether benign or invasive or *in situ* carcinoma, the new findings provide a major step forward towards establishing a new capability for diagnosing benign and malignant lesions in breast tissue in a safe and non-invasive manner *in vivo*.

Introduction

The accurate and safe diagnosis of breast cancer is a significant issue, with annual incidence of 44 000 women and around 300 men in the UK. Early diagnosis of the disease allows more conservative treatments and better patient outcomes.¹

Microcalcifications in the breast are an important indicator for cancer, and often the only sign of its presence. Several studies have suggested that the type of calcification formed may act as a marker for malignancy, that its presence may be of biological significance, and that the chemical composition can indicate disease state.^{2–5}

In the breast, two types of microcalcifications are commonly found. Type I consists of calcium oxalate dihydrate (COD) and is mostly associated with benign lesions.^{2,6} Type II consists of calcium phosphate, mostly hydroxyapatite (HAP), and is associated with both benign and malignant pathologies.^{2,3}

Although mammography can, to some extent, detect the presence of calcifications in tissue, it is unable to yield any information on their chemical composition and thus cannot provide a definitive marker for classifying benign and malignant

lesions. This is currently a significant health issue as only 10–25% of mammographically detected lesions are found to be malignant^{7,8} by subsequent needle biopsy.

Our earlier studies have established that the distinctly different types I and II can be detected and separated non-invasively using transmission Raman spectroscopy through up to 27 mm of soft tissue^{9–11} (Fig. 1) providing a basic building block for a non-invasive diagnostic tool based around Raman spectroscopy. As stated above the detection of type I calcifications in such a method would signal the presence of benign lesion. However, if type II calcifications were identified the diagnosis would be ambiguous as both benign or malignant lesion could be present. A study of Haka *et al.*³ has shown that there are significant differences in the level of carbonate substitution in type II calcifications and these can be related to the pathology too; benign proliferative lesions have type II calcifications with higher carbonate levels than those of the HAP found in malignant lesions. Recent work of Baker *et al.*¹² showed that pathology groups could be separated even further to include both invasive and *in situ* breast lesions. This is based on the amide : phosphate ratio and the percentage of carbonate substitution measured with FTIR spectroscopy (Fourier Transform (mid-)Infrared). However, FTIR cannot easily be used *in vivo* because IR light is strongly absorbed by water. Since Raman spectroscopy has been shown to have a considerable potential for being used non-invasively *in vivo*,^{10,11,13–17} accurate analysis of the carbonate levels in type II calcifications with Raman spectroscopy would enable the removal of any ambiguity at mammography in separating the benign and malignant lesions with type II calcifications. By doing this non-invasively through the breast this would eliminate the need for biopsies and thus reduce patient trauma, costs and time delays.

^aBiophotonics Research Unit, Gloucestershire Royal Hospital, Great Western Road, Gloucester, Gloucestershire, GL1 3NN, UK. E-mail: n.stone@medical-research-centre.com

^bCranfield Health, Cranfield University, Cranfield, Bedfordshire, MK43 0AL, UK

^cCentral Laser Facility, Research Complex at Harwell, Science and Technology Facilities Council, Rutherford Appleton Laboratory, Didcot, Oxfordshire, OX11 0QX, UK

† This article is part of a themed issue on Optical Diagnosis. This issue includes work presented at SPEC 2010 Shedding Light on Disease: Optical Diagnosis for the New Millennium, which was held in Manchester, UK June 26th–July 1st 2010.

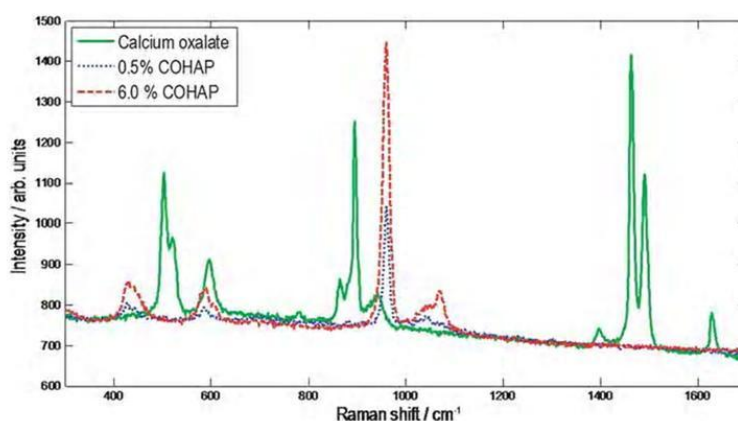


Fig. 1 Raman spectrum of calcium oxalate (type I) and 0.5 and 6.0% carbonate substituted hydroxyapatite (COHAP, type II calcification). As can be seen the carbonate features of the COHAP samples are relatively weak (~ 1042 and ~ 1070 cm^{-1}) compared with the intensity of the phosphate peak (~ 960 cm^{-1}).

Normally, the relative intensities of the intense phosphate band at ~ 960 cm^{-1} and a much weaker carbonate band at ~ 1070 cm^{-1} in Raman experiments are used to quantify the relative amount of carbonate substitution (see Fig. 1). Unfortunately, the carbonate peak has a relatively low intensity and therefore could be hard to measure *in vivo*. This is in contrast with the band at ~ 960 cm^{-1} that has a very high relative intensity. Previous work has demonstrated that the width (full width half maximum—FWHM) of many vibrational bands increases in carbonated phases with the level of carbonate content and therefore the FWHM of the most intense peak at 960 cm^{-1} could be a better quantitative marker for the level of carbonate substitution in deep subsurface studies.^{18–20} A higher FWHM indicates a reduction in crystallinity (*i.e.* an increase in disorder) caused by higher carbonate content. Furthermore, small peak shifts of the same band also indicated in literature^{21,22} appear related to the degree of crystallinity and hence carbonate ion substitution.

The aim of this study is to assess the feasibility of evaluating the amount of carbonate substitution based on properties of the most intense peak at ~ 960 cm^{-1} (width and position) through a layer of tissue, an issue of high clinical relevance.

Materials and methods

Samples

There are three different types of substitution mechanisms possible for the incorporation of carbonate within the lattice for type II calcifications. In A-type substitutions CO_3^{2-} replaces the OH^- lattice ions, in B-type substitutions the CO_3^{2-} takes the position of the PO_4^{3-} , and in L-type (labile) the CO_3^{2-} is within the surface hydration layer of the apatite crystals. Since the carbonate has a charge different from the ions it replaces, the charge has to be compensated by other exchanges, for example Ca^{2+} by Na^+ . It is thought that most, if not all, carbonate substitutions in breast calcifications are B-type.²³ Therefore we have obtained B-type carbonate apatite from Clarkson Chromatography (South Williamsport, PA, USA) to use as standards.

The standards had a carbonate substitution percentage of 0.5, 1.4, 2.0, 2.3, and 3.5, 6.0, and 11.0%, as defined by the manufacturer ($\pm 1\%$) using FTIR and validated by us using X-ray diffraction. The powders were used without further sample pretreatment and placed in quartz cuvettes with a path length of 2 mm (Starna) for the experiments described.

Experimental setup

A scheme of the experimental setup is shown in Fig. 2. The emission from a frequency stabilized laser module (830 nm,

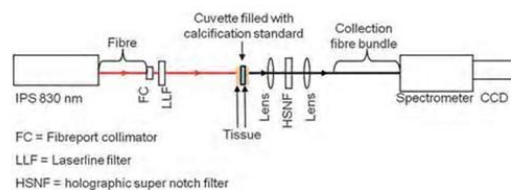


Fig. 2 Illustration of the used setup.

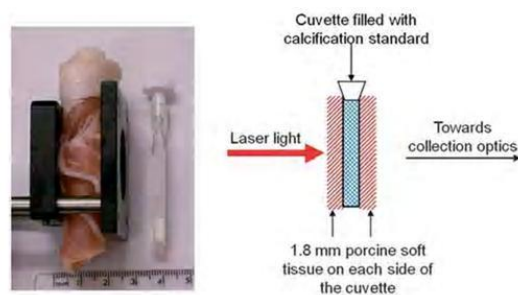


Fig. 3 Details of the experimental setup. Left panel: porcine tissue wrapped around an optical cell was used in the non-invasive experiments. Right panel: schematic representation.

Innovative Photonics Solutions) is sent from a fibre (Ceram-Optec, 'spot to slit line' type bundle assembly, active area spot approximately 2.21 mm, slit line approximately 0.25 mm × 14.95 mm) to a fibre export collimator (Thorlabs) and passed through a laser line filter (FL830-10, Thorlabs) to suppress off-centre spectral emission from the laser line. The sample was illuminated with 130 mW of light in a 4 mm spot. The generated Raman signal was collected in transmission mode using an AR coated lens ($f = 60$ mm, dia. = 50 mm, INGCYS Laser systems). The collimated scattered light was passed through a holographic

super notch filter (HSPF-830.0 AR-2.0, Kaiser Optical Systems) to remove the elastically scattered light and imaged onto a fibre probe bundle by a second lens of the identical parameters to the collection lens. The output end of the fibre probe was placed at the entrance port of a Holospec VPH system spectrograph (Kaiser Optical systems Inc, HSG-917.4 custom). Spectra of the standards were collected with an accumulation time of 20 seconds using a CCD camera cooled to -70 °C (Andor Technology, DU420A-BR-DD, 1024 × 255 pixels). The samples were each measured five times in random order. In a non-invasive

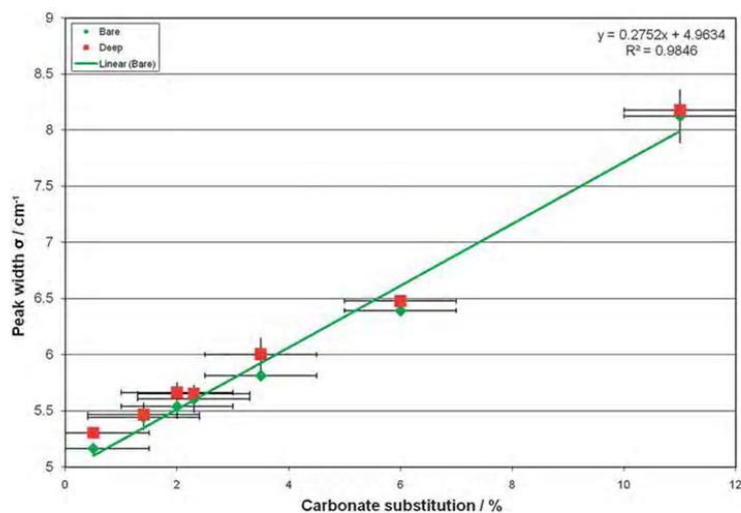


Fig. 4 Peak width versus carbonate substitution; the bare calcification standards are plotted as green diamonds (mean values) and a linear function was fit to provide a calibration function for the standards buried in 3.6 mm of porcine tissue (mean values shown in red squares). Error bars show the uncertainty in the carbonate substitution values provided by the manufacturer and the standard deviation of the replicate values of the spectral peak width.

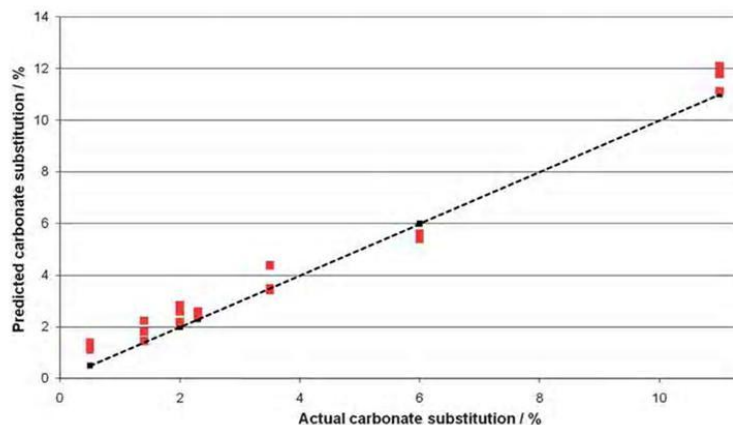


Fig. 5 Predicted versus actual carbonate substitution of the buried material based on the width of the 960 cm^{-1} phosphate peak.

Table 1 Prediction of the percentage carbonate substitution based on the width of the peak

Carbonate substitution according to supplier (quoted as $\pm 1\%$)	Mean predicted carbonate percentage through tissue (± 1 std)	Root mean square error of prediction (% carbonate)
0.5%	1.22 ± 0.14	0.75
1.4%	1.83 ± 0.39	0.54
2.0%	2.55 ± 0.33	0.61
2.3%	2.51 ± 0.07	0.22
3.5%	3.78 ± 0.53	0.52
6.0%	5.51 ± 0.17	0.50
11.0%	11.68 ± 0.50	0.79

proof-of-principle feasibility study the cuvettes were wrapped in porcine tissue (shown in Fig. 3) to evaluate the carbonate substitution through a layer of tissue. Tissue with a mix of fat and protein was chosen to mimic bulk human breast tissue. The thickness of the porcine tissue was 1.8 mm for the proof of principle experiments on both sides of the cuvettes (overall thickness of porcine tissue $3.6 \text{ mm} + 2 \text{ mm cuvette} = 5.6 \text{ mm}$). In this study the signal was accumulated over 5×60 seconds and the cosmic ray removal option of the detector software was used. The system was calibrated using Raman bands of an aspirin tablet (acetylsalicylic acid) and had a spectral resolution of 5.8 cm^{-1} .

Data analysis

All data were loaded into Matlab7 (The Mathworks) in which an in-house written tool fitted a Gaussian to the band located at 960 cm^{-1} and its bandwidth σ (where the FWHM $\approx 2.35\sigma$) and position were evaluated.

Results and discussion

The mean peak width (σ) for each of the bare standard samples (five replicate measurements) was plotted against the calcification substitution percentage. A linear function was fit to these points, shown in Fig. 4, and the mean values for the buried calcifications were also plotted (three replicates). It can be seen that the buried calcification standards have peak widths within a standard deviation of each other (shown with error bars). The equation of the line calculated from the spectra of bare standards was used to provide a prediction of the carbonate substitution percentage of the buried standards. Fig. 5 shows the results plotted against actual concentration determined by the manufacturer with FTIR. Table 1 shows the root-mean-square-error of these predictions.

The mean peak position for each of the bare standard samples (five replicate measurements) was plotted against the calcification substitution percentage. A logarithmic function was fit to these points, shown in Fig. 6, and the mean values for the buried calcifications were also plotted (three replicates). It can be seen that the buried calcification standards have peak positions within a standard deviation of each other (shown with error bars). The logarithmic function was used to provide a prediction of the carbonate substitution percentage of the buried standards. Fig. 7 shows the results plotted against actual concentration. Table 2 shows the root-mean-square-error of these predictions.

As can be seen in Fig. 4 and 6, the width of the peak increases with a higher carbonate substitution, while the position of the phosphate peak moves to lower Raman wavenumber with higher carbonate substitution. There is some subtle variability in the width and position of the phosphate peak between measurements from different areas of the same sample. It is thought to be due to the heterogeneous nature of the apatite standards used. Also, a systematic difference in width between bare and buried samples

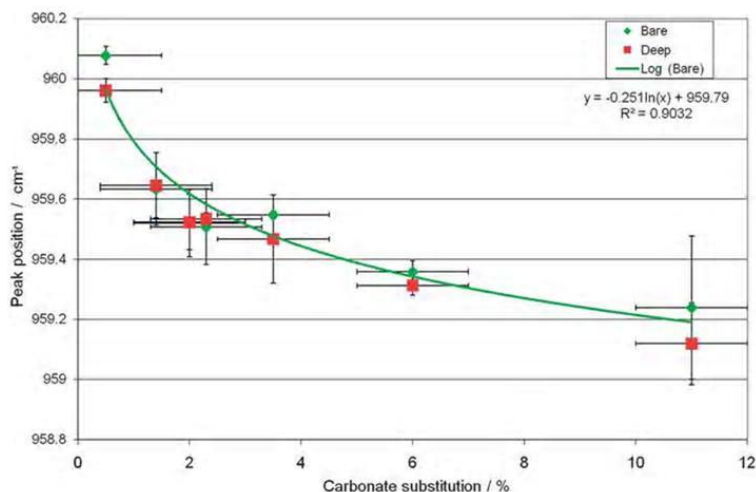


Fig. 6 Peak position versus carbonate substitution; the bare calcification standards are plotted as green diamonds (mean values) and a logarithmic function was fit to provide a calibration function for the standards buried in 3.6 mm of porcine tissue, total thickness 5.6 mm (mean values shown in red squares). Error bars show the uncertainty in the carbonate substitution values provided by the manufacturer and the standard deviation of the replicate values of the spectral peak position.

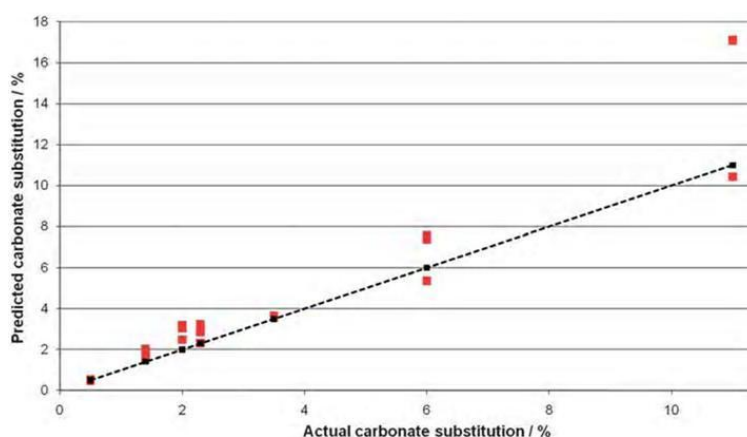


Fig. 7 Predicted *versus* actual carbonate substitution of the buried material based on the position of the 960 cm^{-1} phosphate peak.

Table 2 Prediction of the carbonate substitution based on the peak position

Carbonate substitution according to supplier (quoted as $\pm 1\%$)	Mean predicted carbonate percentage through tissue (± 1 std)	Root mean square error of prediction (% carbonate)
0.5%	0.51 ± 0.04	0.03
1.4%	1.79 ± 0.23	0.43
2.0%	2.91 ± 0.37	0.96
2.3%	2.80 ± 0.46	0.63
3.5%	3.61 ± 0.05	0.12
6.0%	6.77 ± 1.23	1.26
11.0%	14.88 ± 3.85	4.99

can be observed which is believed to be caused by the *S/N* ratio of the buried samples. When signal was acquired for a longer period of time these differences were not observed. The region of interest (clinically relevant area) is between 0.5% and 2.5% and is based on work of Baker *et al.*¹² which indicated that calcifications corresponding to benign pathology have an average carbonate substitution around 2%. This percentage is lower for calcifications corresponding to *in situ* and invasive pathology; where the amount of carbonate substitution is $\sim 1.7\%$ and $\sim 1.4\%$ on average, respectively. The data of these three pathology groups show a spread from 0.5 to 2.5% carbonate substitution.

The relationship between the carbonate substitution and the width in the relevant area seems to be approximately linear. In contrast, the relationship between the carbonate substitution and the position in the clinically relevant area shows a semi-exponential trend. In agreement to the work presented here, it has been reported previously that the width of the 960 cm^{-1} band is linearly correlated to the carbonate concentration in breast calcifications.³ It should be noted that the carbonate substitution can be most accurately predicted using the peak width, although in samples with relatively low carbonate content between 0.5 and 3.5% (the clinically important range for this proposed

application) the peak position has a slightly lower sum of root-mean-squared prediction errors. This is reversed for buried standards with greater than 3.5% carbonate substitution.

In order to use the level of carbonate substitution as a clinical diagnostic tool, more knowledge must be obtained concerning the different types of carbonate substitution in type II breast calcifications and the relationship between this and the width and position of the Raman band at $\sim 960\text{ cm}^{-1}$, as well as other potential sources of broadening. It must be noted that we are not directly measuring the carbonate within the breast calcification standards and are therefore making the assumption that the change in features of the 960 cm^{-1} peak is attributable to the carbonate. This is not unreasonable, and certainly correlates well, however, there are other structural changes that may occur that could also modify the peak—in fact any disordering mechanism could do this.

Conclusions

Samples with different amounts of carbonate substitution can be separated both with the position and the width of the Raman peak located at 960 cm^{-1} . It has also been shown that indication of the carbonate substitution based on the peak located at 960 cm^{-1} is feasible when measured through biological tissue, where porcine tissue was used as a human breast tissue phantom in this study. As part of this feasibility study we also explored the limits under which this method could be used with the described experimental configuration. Peak characteristics were also measured from spectra measured from an overall tissue depth of 16 mm of porcine soft tissue (not shown), with minimal data analysis. Further analysis with chemometric tools such as PCA would be likely to enable greater signal recovery.

This study paves the way towards a new generation of non-invasive breast screening methods based around transmission Raman and spatially offset Raman spectroscopy (SORS). Since the proposed method of pathological discrimination is based upon measuring only the strongest calcification peak, signals

from deeper in the tissue can be used or measurements can be performed in shorter timescales than if the analysis required a conventional calculation of the direct intensity ratio of the weak carbonate and strong phosphate Raman bands.

Acknowledgements

We would like to thank Gavin R. Lloyd for his help with the Matlab fitting routine. Nick Stone holds a Senior (Career Scientist) Research Fellowship funded by the UK National Institute of Health Research. Marleen Kerssens holds a doctoral research fellowship jointly funded by Gloucestershire Hospitals NHS Foundation Trust and the Science and Technology Facilities Council's Biomedical Network (4161234).

References

- 1 NHS, *NHS Breast Screening Programme Annual Review 2008*, 2008.
- 2 M. J. Radi, *Arch. Pathol. Lab. Med.*, 1989, **113**, 1367–1369.
- 3 A. S. Haka, K. E. Shafer-Peltier, M. Fitzmaurice, J. Crowe, R. R. Dasari and M. S. Feld, *Cancer Res.*, 2002, **62**, 5375–5380.
- 4 M. P. Morgan, M. M. Cooke and G. M. McCarthy, *J. Mammary Gland Biol. Neoplasia*, 2005, **10**, 181–187.
- 5 M. P. Morgan, M. M. Cooke, P. A. Christopherson, P. R. Westfall and G. M. McCarthy, *Mol. Carcinog.*, 2001, **32**, 111–117.
- 6 N. Singh and J. M. Theaker, *J. Clin. Pathol.*, 1999, **52**, 145–146.
- 7 A. S. Haka, K. E. Shafer-Peltier, M. Fitzmaurice, J. Crowe, R. R. Dasari and M. S. Feld, *Proc. Natl. Acad. Sci. U. S. A.*, 2005, **102**, 12371–12376.
- 8 A. J. Evans, A. R. M. Wilson, H. C. Burrell, I. O. Ellis and S. E. Pinder, *Clin. Radiol.*, 1999, **54**, 644–646.
- 9 P. Matousek and N. Stone, *Analyst*, 2009, **134**, 1058–1066.
- 10 N. Stone and P. Matousek, *Cancer Res.*, 2008, **68**, 4424–4430.
- 11 P. Matousek and N. Stone, *J. Biomed. Opt.*, 2007, **12**, 024008.
- 12 R. N. Baker, K. D. Rogers, N. Shepherd and N. Stone, *Br. J. Cancer*, 2010, **103**, 1034–1039.
- 13 P. Matousek, I. P. Clark, E. R. C. Draper, M. D. Morris, A. E. Goodship, N. Everall, M. Towrie, W. F. Finney and A. W. Parker, *Appl. Spectrosc.*, 2005, **59**, 393–400.
- 14 M. V. Schulmerich, K. A. Dooley, M. D. Morris, T. M. Vanasse and S. A. Goldstein, *J. Biomed. Opt.*, 2006, **11**, 060502.
- 15 M. V. Schulmerich, J. H. Cole, K. A. Dooley, M. D. Morris, J. M. Kreider, S. A. Goldstein, S. Srinivasan and B. W. Pogue, *J. Biomed. Opt.*, 2008, **13**, 020506.
- 16 N. A. Macleod and P. Matousek, *Appl. Spectrosc.*, 2008, **62**, 291A–304A.
- 17 N. Stone, R. Baker, K. Rogers, A. W. Parker and P. Matousek, *Analyst*, 2007, **132**, 899–905.
- 18 A. Awonusi, M. D. Morris and M. M. J. Tecklenburg, *Calcif. Tissue Int.*, 2007, **81**, 46–52.
- 19 A. Krajewski, M. Mazzocchi, P. L. Buldini, A. Ravaglioli, A. Tinti, P. Taddei and C. Fagnano, *J. Mol. Struct.*, 2005, **744–747**, 221–228.
- 20 F. F. M. de Mul, M. H. J. Hottenhuis, P. Bouter, J. Greve, J. Arends and J. J. ten Bosch, *J. Dent. Res.*, 1986, **65**, 437–440.
- 21 G. Penel, G. Leroy, C. Rey and E. Bres, *Calcif. Tissue Int.*, 1998, **63**, 475–481.
- 22 J. D. Pasteris, B. Wopenka, J. J. Freeman, K. Rogers, E. Valsami-Jones, J. A. M. van der Houwen and M. J. Silva, *Biomaterials*, 2004, **25**, 229–238.
- 23 K. D. Rogers and R. A. Lewis, in *Breast Calcification: a Diagnostic Manual*, ed. A. Evans, S. Pinder, R. Wilson and I. Ellis, Greenwich Medical Media, 2002, pp. 171–189.

Raman spectroscopy has attained much interest as an optical diagnostic technique since high-resolution molecular images can be attained without the need for staining. Application of multivariate analyses and soft modeling methods can allow interpretation of particular structural components from molecular images, representative of the tissue architecture.

Objective: To assess the resolution capabilities of multivariate curve resolution—alternating least squares (MCR-ALS) as a soft modeling method on Raman images of endometrial tissue compared to those of principal component analysis (PCA).

Methods: Snap-frozen tissues for benign and cancer endometrial tissues were obtained. Image maps were acquired using a 785-nm Renishaw Raman spectrometer with spectral pre-processing occurring in the biochemical region (1,800–500 cm^{-1}). PCA and MCR-ALS analysis of image maps was carried out using Renishaw chemometrics software 3.2.

Results: Both analyses identified endometrial glandular epithelia, stroma, glandular lumen, and myometrium. Empty modeling using MCR-ALS alone was able to resolve individual cells and adjacent cellular adhesions. Molecular contrast images of MCR-ALS also demonstrated a superior resolution representative of the unstained tissue architecture in comparison to PCA.

Conclusions: Soft modeling of Raman images using MCR-ALS constructs high-resolution contrast images making tissue architecture interpretation possible without the need for histopathological staining.

Detecting breast cancer by probing micro-calcifications with deep-Raman

Kerssens, M.^{1,2}, Fullerton, R.¹, Matousek, P.³, Rogers, K.², Stone, N.^{1,2}

¹Biophotonics Research Unit, Gloucestershire Hospitals NHS Foundation Trust, ²Cranfield University, ³Central Laser Facility, Rutherford Appleton Laboratory

Background: The accurate and safe diagnosis of breast cancer is a significant issue. Early diagnosis results in more conservative treatments and better patient outcomes. One of the features screened for in the breast screening program is the presence of microcalcifications in the breast. Type I calcifications are mostly associated with benign disease, and type II calcifications are most often present in proliferative lesions.

Objective: Mammography cannot distinguish the two types of calcifications or the chemical differences between

type II calcifications which relate to the state of the disease. Raman spectroscopy has such inherent capability but could, until recently, only be applied to the surface or near-surface of the specimen of interest. Therefore, the disease-specific composition of calcifications is investigated and the ultimate goal is to turn this knowledge into a clinical tool based on deep-Raman spectroscopy, which was recently developed in this context by our team.

Methods: The composition of breast calcifications and the tissue interface from specimens with ‘benign’, ‘in situ’, and ‘invasive’ breast disease (diagnosed by pathologists) were studied with vibrational spectroscopy. The enhanced knowledge was then used to improve deep-Raman techniques for the use of breast screening.

Results: Samples from different pathology groups can be separated based on the chemical differences picked up by vibrational spectroscopy.

Conclusions: Although much work remains to be done, the potential of deep-Raman spectroscopy for breast cancer diagnosis has been successfully demonstrated.

In vitro fluorescent behavior and location of porphyrins in cell lines

Barron, G.A., Woods, J.A., Moseley, H.

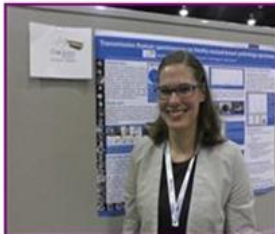
University of Dundee, Photobiology Unit, Ninewells Hospital and Medical School, Dundee

Background: The principle of photodynamic therapy (PDT) involves a photosensitizer (PS) which, when combined with visible light and oxygen, produces reactive oxygen species (ROS), thus leading to cell death. The administration of porphyrin prodrugs, such as 5-aminolevulinic acid (ALA) or its methyl ester (MAL), which bypass the negative feedback mechanism of haem biosynthetic pathway, result in the accumulation of protoporphyrin IX (PpIX); the penultimate molecule in the pathway. PpIX is a highly fluorescent and phototoxic PS that has significantly higher fluorescence intensity in tumor cells than surrounding normal tissue. Consequently, PpIX can also be utilized in photodynamic diagnosis (PDD), which can be used to improve the early detection of cancer.

Objective: These studies aim to determine the fundamental factors influencing the fluorescent behavior and location of porphyrins in normal and cancerous cell lines.

Methods: Cell lines from the epidermis (HaCaT), bladder (HT 1,197), esophagus (OE19), and brain (SH-SY5Y) were incubated with ALA or MAL (1 mM; 4 and 24 h) to induce porphyrin synthesis. Porphyrin fluorescence

International prize for 'no needles' breast cancer diagnosis technique



Marleen Kerssens in front of the poster that she was presenting on Sunday evening in Kansas City.

Currently the abnormalities are seen on mammograms in the form of dots and shadows but can only be identified as malignant or benign through a needle biopsy - the next step. This involves a cut through the skin and tissue and an anxious wait by patients for their results, and in 70-90 percent of cases the calcifications turn out to be benign. Work by Marleen and her team at the Gloucestershire Hospitals NHS Foundation Trust could lead in the next decade, to the biopsy being replaced by a non-invasive screening with instantaneous results. The technique, however, still needs a lot of refinement.

A PhD student co-funded by STFC has won a prestigious award for demonstrating that a technique developed originally at STFC's Central Laser Facility could take away the need for a needle biopsy in breast cancer diagnosis. Marleen Kerssens, also funded by the Gloucestershire Hospitals NHS Foundation Trust has shown that SORS (spatially offset Raman spectroscopy), a method using a laser to see inside objects without making an incision, is viable for detecting if abnormalities found through mammograms are malignant or benign. Currently a needle biopsy is the only way to confirm this. Marleen received the Coblenz Society Student Award, an international prize to recognise young scientists in the area of vibrational spectroscopy, at a conference in Kansas City, USA last night (Sunday 30 September 2012).

The team Marleen is working in at the Gloucestershire Hospitals NHS Foundation Trust has used the SORS method to look at the molecular fingerprints of breast calcifications. The technique involves bouncing light off of the tiny grains of breast tissue and measuring the light scattered at different colours to pick up their molecular signatures which indicate if a cancer is present. This research has shown a correlation between the signature and the type of cancer present and Marleen's work is also looking at how these calcifications form.

Cancer surgeon at the Gloucestershire Hospitals NHS Foundation Trust, Professor Hugh Barr, said: "Marleen is an outstanding translational scientist who has been able to bring vibrational spectroscopy from the laboratory to a potential invaluable clinical diagnostic instrument for patients with breast disease. As a result of her work we now have the prospect of real-time non-invasive diagnosis. She is truly deserving of this great honour and will bring nothing but credit to the Coblenz Society".

Marleen added: "I am honoured to receive this award and for the recognition given by the Coblenz Society for my work. It is a great opportunity to bring this research, with potential for future clinical impact for breast cancer diagnostics, into the spotlight."

Pavel Matousek from STFC's Central Laser Facility based in the Research Complex at Harwell who originally developed the SORS technique will also be given an award this week in Kansas City – he is being awarded a fellowship of the Society for Applied Spectroscopy in recognition of his outstanding service to the field of spectroscopy.

He says:

"This is a well deserved international recognition for Marleen - she put great effort into her research and studies over the last three years that laid firm foundations for the development of a novel non-invasive breast cancer diagnostic tool. For myself, I am just delighted to be part of this exciting field of research that has so much potential in so many different areas of society".

The team is currently working with real samples of excised breast tissue but it is expected to be a decade before this technique could be used routinely in hospitals.

Notes to editors

The purpose of the Coblenz Society, a technical affiliate of the Society for Applied Spectroscopy, is to foster the understanding and application of vibrational spectroscopy.

Marleen is jointly supervised by Professor. Nicholas Stone (Gloucestershire Hospitals NHS Foundation Trust & University of Exeter), Professor Keith Rogers (Cranfield University) and Professor Pavel Matousek (Central Laser Facility, STFC). She is funded by STFC's BioMedical Network and Gloucestershire Hospitals NHS Foundation Trust.

Media contacts:

[Lucy Stone](#)
STFC Press Officer
Email: lucy.stone@stfc.ac.uk
Tel:+44 (0)1235 445627/07920 870125

Staff survey

Throughout October, 850 randomly chosen people across the Trust were sent a Staff Survey asking what it is like to work at our Trust.

A great deal of work has been taking place across the Trust to make things better for staff and we want to find out more about where we are doing well and where we could improve: If you receive a survey this year, please fill it in.

This is our opportunity to make a genuine difference to the way we work and with your help we can find out how much has changed for staff over the last year and where we need to focus our efforts next year.

The surveys are completely anonymous. No individual filling in the questionnaire can be identified by the Trust as an external company (Quality Health) will send out the



questionnaires and gather the responses.

The form has been simplified this year and reduced by four pages so it won't take long to complete. We encourage all staff who receive the form to fill it in and return it as soon as possible.

Find out more by visiting the Staff Survey Pages on the Staff Intranet or contact Emma Dempsey in the Leadership and Organisational Development Department on 08454 226066.

Marleen's international award

A PHD student co-funded by the Trust has won a prestigious award for demonstrating that a technique that could take away the need for a needle biopsy in breast cancer diagnosis.

Marleen Kerssens has shown that SORS (spatially offset Raman spectroscopy), a method using a laser to see inside objects without making an incision, is viable for detecting whether abnormalities found through mammograms are malignant or

benign. Currently a needle biopsy is the only way to confirm this.

Marleen received the Coblenz Society Student Award, an international prize to recognise young scientists in the area of vibrational spectroscopy, at a conference in Kansas City, USA on 30 September 2012.

Marleen previously presented her work to the prestigious Parliamentary and Scientific Committee in Westminster earlier this year.

Taking science to parliament

Marleen Kerssens, a PhD student at GRH, attended Parliament to present her science to a range of politicians and a panel of expert judges, as part of *SET for Britain* this month.

Marleen's poster on research about non-invasive Raman measurements of the calcifications found in breast tissue will be judged against dozens of other scientists' research in the only national competition of its kind. She was short listed from hundreds of applicants to appear in Parliament on the day.

On presenting her science in Parliament, Marleen said: "It is a great opportunity to let people know about the research being undertaken in the UK and its importance to the general public, in my case especially the women involved in the NHS breast screening programme."

Andrew Miller MP, Chairman of the Parliamentary and Scientific Committee, said: "This annual competition is an important date in the parliamentary calendar because it gives



MPs an opportunity to speak to a wide range of the country's best young researchers. These early career scientists are the architects of our future and SET for Britain is politicians' best opportunity to meet them and understand their work."

Marleen's research has been entered into the Physics session of the competition, which will end in a gold, silver and bronze prize-giving ceremony.

Hands-on in Cheltenham

Light is well-established as a tool to help in the diagnosis and treatment of disease. Some of the greatest advances in this field can be found in applications for the areas of oncology, dermatology, ophthalmology, surgery and cardiology. Biophotonics is the development and application of photon (light) based technology to biology and medicine.



So how did the Biophotonics Research Unit participate in hands-on workshops at this year's Cheltenham Science Festival? "The festival was the perfect opportunity to showcase ongoing STFC collaborative research exploiting the potential of light as a diagnostic tool in the early identification of disease. The Biophotonics Research Unit undertakes translational research, knowledge from bench top to bedside, to improve the healthcare of patients within the NHS and enable more successful treatment outcomes." explained Marleen Kerssens from the Biophotonics Research Unit, Gloucester. Gloucestershire Hospitals NHS Foundation Trust hosted the day of workshops giving members of the public a chance to try their hand at various clinical procedures using manikins and simulators.

The Optical Diagnosis session was focussed on a new generation of non-invasive screening with Raman spectroscopy, and specifically Marleen Kerssens' PhD research investigating the use of Deep-Raman spectroscopy in the diagnosis of breast cancer. This is an ongoing project within the Biophotonics Research Unit under the supervision of Professor Nick Stone and in collaboration with Professor Pavel Matousek at STFC's Central Laser Facility. Funding for the session was made available by a small award from STFC's Science in Society programme.

Microcalcifications in the breast are an important indicator for breast cancer and can be separated into two types, apatite and oxalate, of which only apatites are related to disease. Mammography cannot distinguish the different types of microcalcifications, so further tests (including biopsies) have to be done. By incorporating Raman spectroscopy into the diagnostic process it is envisaged that the time delay between screening and diagnosis can be minimised and the number of normal biopsies can be reduced.

In order to get the concept of the research across, several hands-on experiments were available during the Science Festival such as: building a cardboard box spectrometer, investigating the penetration of light with different wavelengths through tissue, and a consensus pathology quiz where groups of visitors examined spectra of different samples and decided whether the patient was healthy or if further tests needed to be done. Furthermore the concept of Raman spectroscopy and the current screening and diagnosis

techniques used were explained with the help of radiologists from the Cheltenham Imaging Centre and the Cobalt Charity.

The other sessions at the 'Medical School on for Dummies' workshop, sponsored by Olympus, included hands-on endoscopy training, a virtual reality simulator to train visitors in diagnosing eye conditions and eye surgery, and a manikin simulator which is used within the Trust for training medical students and doctors in the management of acutely ill patients.



Students enjoying the hands-on demonstrations

STFC run a number of funding schemes for projects aimed at promoting STFC Science and Technology to a wider audience.

The Small Awards Scheme provides funds from £500-£10,000 for small, local or 'pilot' projects promoting STFC science and technology. Anyone can apply, including grant-funded research groups, STFC research facility users, schools, museums, science centres etc.

The Large Awards Scheme provides funds for projects which are expected to have a significant regional or national impact. We offer awards from £10,000 up to £100,000. Almost anyone can apply but project teams must have strong links with STFC's scientific research community.

For more experienced researchers who have a strong track record in both research and outreach, we run the SiS Fellowships scheme where fellows act as champions or ambassadors for STFC's science, technology, engineering and mathematics and work with schools the media and/or public audiences.

For schools wishing to apply for funds up to £500 we operate a scheme with the Institute of Physics which is for projects or events linked to the teaching or promotion of physics and other STFC science areas such as Astronomy, Space Science and the work done at our laboratories.

Further information can be found on the STFC Science in Society webpage. <http://www.stfc.ac.uk/1286.aspx>

Raman imaging gives new hope for cancer diagnosis

10 February 2011

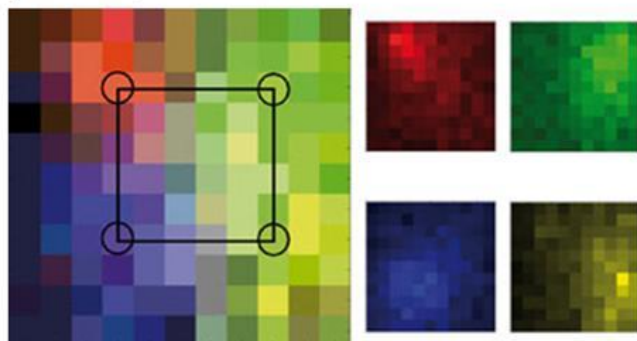
Combining two Raman spectroscopic imaging techniques could offer a valuable tool for future disease diagnosis, say UK scientists.

Surface enhanced Raman scattering (SERS) works by detecting spectroscopic signals of molecules such as cancer antibodies that are in close proximity to metals injected into tissue such as gold or silver nanoparticles.

Nicholas Stone from Gloucester Royal Hospital and colleagues have combined SERS with deep Raman spectroscopy to enable non-invasive analysis of multiple antibodies for different diseases tagged to nanoparticles. The combination allows for the first time antibody detection to a depth of 50mm in tissue samples.

Current methods using SERS and Raman spectroscopy are only able to detect nanoparticles at a maximum depth of 5mm. 'Light doesn't travel too deeply into tissues so it's hard to measure signals from deeper within the body,' explains Sanjiv Sam Gambhir, director of the Molecular Imaging Program at Stanford University, US.

This limits the use of SERS in measuring breast tissue, for example, as mammography screening protocols generally measure signals through a tissue depth of 20 to 50mm. '[Stone's] work solves a limitation of Raman imaging by developing strategies to go from about 5 to 50mm depth penetration,' adds Gambhir.



False colour images of the SERS nanoparticle signals. The left image shows the signals plotted together (with pixel colour mix showing combined signals) with the injection points marked. The right image shows each 'flavour' separately

To demonstrate their method, Stone's team coated gold nanoparticles with four different Raman reporter molecules - molecules that give signals at specific wavelengths - and encapsulated them in a silica shell. They suspended them in water and injected them into a porcine tissue block measuring 20x50x50mm. The signals from each different nanoparticle were then used to produce a false colour image of their locations in the tissue.

Being able to distinguish between different molecules like this means that the technique could be used to detect cancer, monitor treatment and chemosensitivity, provided that the target molecule is known. 'Cancer and other diseases of interest are complex and there is not a single marker which can be used to identify cancer or its susceptibility to treatment,' explains Stone.

Stone now hopes to label the nanoparticles with a wider range of antibodies for use in practical applications. Provided that the nanoparticles' excretion mechanism is found to be safe when injected, Stone thinks that his approach could open up a window to more of the human body.

Erica Wise